Role of HDACs in the regulation of *TERT* in neuroblastoma

DISSERTATION

zur Erlangung des akademischen Grades

Doctor rerum naturalium

(Dr. rer. nat.)

eingereicht an der

Lebenswissenschaftlichen Fakultät der Humboldt-Universität zu Berlin

von

Dipl.-Chem. Sabine Finkler

Präsidentin

der Humboldt-Universität zu Berlin

Prof. Dr.-Ing. Dr. Sabine Kunst

Dekan der Lebenswissenschaftlichen Fakultät

der Humboldt-Universität zu Berlin

Prof. Dr. Bernhard Grimm

Gutachter/innen

1. Prof. Dr. rer. nat. Nils Blüthgen
2. PD Dr. med. Hedwig Elisabeth Deubzer
3. Prof. Dr. rer. nat. Christine Sers

Tag der mündlichen Prüfung: 13. Januar 2021

To my parents.

For giving me roots and wings.

A. Zusammenfassung

Das Neuroblastom ist der häufigste extrakranielle solide Tumor im Kindesalter und hat einen Anteil von etwa 15% an der krebsbedingten Sterberate bei Kindern. Es ist eine heterogene Erkrankung mit einem breiten Spektrum klinischer Verläufe für die Patienten, von vollständiger Remission bis hin zum Fortschreiten der Erkrankung trotz intensiver multimodaler Therapie. Die Therapie der Hochrisikogruppe besteht aus hochdosierter Chemotherapie, Radiotherapie und Stammzelltransplantation. Antineoplastische Substanzen wie Doxorubicin, Vincristin und Carboplatin sind Bestandteil der unspezifischen Medikation. Diese Therapie zeigt jedoch nur begrenzte Effizienz, häufig begleitet von starken Nebenwirkungen. Es besteht eine große Notwendigkeit, neue Vulnerabilitäten dieser Erkrankung aufzudecken und weniger toxische Therapiepläne zu entwickeln. Mehrere genetische Aberrationen wie eine Amplifikation des *MYCN*-Onkogens, eine *ALK*-Mutation oder ein *TERT*-Rearrangement wurden bereits als Risikofaktoren identifiziert. Im Gegensetz zu adulten Tumoren ist die somatische Mutationsrate niedrig, was auf eine Beteiligung von epigenetischen Faktoren bei der Regulation hindeutet. Die Behandlung mit Histondeacetylaseinhibitoren (HDACi) zeigte in klinischen Studien bei Erwachsenen eine Reduktion des malignen Phänotyps. Obwohl die kausalen Regulatoren noch unbekannt sind, stellt die Therapie des Neuroblastoms mit Histondeacetylaseinhibitoren einen potentiellen, vielversprechenden Therapieansatz dar.

Eine kürzlich identifizierte Subgruppe an Hochrisikoneuroblastompatienten zeigt genetische Rearrangements des Gens Telomerase Reverse Transkriptase (*TERT*). Dies resultiert in einer hohen Aktivität der Telomerase und korreliert mit schlechteren Überlebenschancen als bei Patienten ohne *TERT*-Rearrangement. Bislang gibt es keine klinisch erfolgreichen Inhibitoren, die auf *TERT* oder die Telomerase abzielen. Das Ziel dieser Arbeit galt der Evaluierung des niedermolekularen HDAC-Inhibitors Panobinostat (LBH589, Farydak®) in präklinischen Modellen des *TERT*-rearrangierten Neuroblastoms in Mono- und Kombinationstherapie. Die vorliegende Arbeit zeigte, dass in Modellen der Hochrisikogruppe des *TERT*-rearrangierten Neuroblastoms die Behandlung mit HDAC-Inhibitoren zu einer Reprimierung der *TERT* mRNA-Level führt. Bereits nach zweistündiger Behandlung mit Panobinostat nimmt die *TERT*-Expression ab und dieser Effekt verstärkt sich mit zunehmender Behandlungsdauer. Die Inhibierung von HDAC1 und HDAC2 vermittelt die Repression von *TERT* nach Panobinostatbehandlung. Die Telomeraseaktivität wurde nach HDAC-Inhibitorbehandlung herabgesetzt. Dieser Effekt könnte unabhängig vom Onkogen *MYCN* sein, da die Behandlung *TERT*-rearrangierter Neuroblastomzellen mit auf *MYCN* abzielenden Bromodomain and Extra-

Terminal motif (BET)-Inhibitoren keine Regulation der *TERT*-Level und der Telomeraseaktivität zeigte. Die Überexpression von *TERT* resultierte in gesteigerter Resistenz gegenüber dem HDACi-induzierten antitumoralen Phänotyp. *TERT* mRNA-Level, Telomeraseaktivität und Xenografttumorwachstum wurden durch Panobinostatbehandlung in *TERT*-rearrangierten Neuroblastommausmodellen in präventiven und therapeutischen Behandlungsplänen reduziert.

Eine Panobinostatbehandlung reduzierte die Koloniebildung und das Wachstum *TERT*-rearrangierter Neuroblastomzellen. Die Behandlung von *TERT*-getriebenen Neuroblastomzellen mit niedrigen nanomolaren Panobinostatkonzentrationen reduzierte die Zellviabilität in gleichem Maße wie die Behandlung mit mikromolaren Konzentration von spezifischen *TERT*-Inhibitoren. In Übereinstimmung mit diesen Daten reduzierte die Panobinostatbehandlung die metabolische Aktivität in verschiedenen Neuroblastomzelllinien bei einer halbmaximalen inhibitorischen Konzentration im niedrigen nanomolaren Bereich. Durchflusszytometrie- und RNA-Expressionsanalysen von *TERT*-rearrangierten Zelllinien und Xenografttumoren zeigten eine Änderung des Zellzyklusprofils nach Panobinostatbehandlung. Die identifizierten Gene der Gensets E2F und G2M waren nach Panobinostatbehandlung in Zelllinien und Xenografttumoren reduziert exprimiert. Die proteasevermittelte Apoptoseinduktion durch Panobinostatbehandlung wurde anhand der Spaltung von PARP-1 demonstriert. Dieser Effekt wurde partiell durch den Caspaseinhibitor Z-VAD umgekehrt.

In Kombination mit dem proteasomalen Inhibitor Bortezomib zeigte die Panobinostatbehandlung starke synergistische antitumorale Effizienz in 2D- und 3D-Zellmodellen des *TERT*-rearrangierten Neuroblastoms. Eine synergistische Reduktion der *TERT*-mRNA Expression sowie der Telomeraseaktivität nach Kombinationsbehandlung konnte nicht festgestellt werden.

Der genomische Bruchpunkt im 5′-untranslatierten Bereich des *TERT*-Gens und des Rearrangementpartner auf Chromosom 19 wurden in einer *TERT*-rearrangierten Zelllinie ermittelt. Chromatinimmunopräzipitation-Sequenzierung und Analyse von verschiedenen Histonmodifikationen ergab keine wesentliche Veränderung der untersuchten epigenetischen Umgebung am *TERT*-Lokus nach Panobinostatbehandlung. Methylierungsanalysen zeigten eine genomweite Abnahme der Methylierung von CpG-Dinukleotiden, doch wurde das Methylierungsprofil am *TERT*-Lokus nach Panobinostatbehandlung nicht bedeutend verändert.

Auf transkriptioneller Ebene reduzierte die Behandlung mit Panobinostat die Halbwertszeit des *TERT*-Transkriptes nach Inhibierung der *de novo* RNA Synthese. Dies deutet darauf hin, dass die Regulation auf molekularer Ebene durch die Abnahme der Stabilität des *TERT*-Transkriptes vermittelt wird.

Zusammenfassend gibt es bislang keine klinisch erfolgreiche Therapie, die auf *TERT* oder die Telomerase abzielt. Der HDAC-Inhibitor Panobinostat weist antitumorale Effizienz bei einem tolerablen und behandelbaren Nebenwirkungsprofil in klinischen Studien auf. Die Behandlung von *TERT*-rearrangierten Neuroblastomzellmodellen mit dem zugelassenen HDAC-Inhibitor Panobinostat zeigte tumorsupprimierende Eigenschaften und führte zu einer Abnahme der *TERT* mRNA sowie der Telomeraseaktivität. Eine Therapie von Panobinostat in Kombination mit Bortezomib zeigte synergistische antitumorale Effizienz in Zellkulturmodellen und ist ein vielversprechender Ansatz für weitere Studien in Xenograftmausmodellen. Das Abzielen auf *TERT* mit nanomolaren Konzentrationen von HDAC-Inhibitoren wie Panobinostat ist ein vielversprechender Ansatz zur Behandlung von Neuroblastompatienten mit einem *TERT*-Rearrangement, deren Prognose bislang ungünstig ist.

B. Summary

Neuroblastoma is the most common extracranial solid tumor of infancy and accounts for about 15% of cancer-related death in children. It is a heterogenic disease with divert clinical outcome, spanning from complete remission to progressed disease despite intensive multimodal treatment. Therapy concepts for treatment of the high-risk group include high dose chemotherapy, radiotherapy and stem cell transplantation. Antineoplastic drugs like doxorubicin, vincristine and carboplatin are part of the unspecific medication. The current treatment schedules show limited efficacy and frequent and serious side effects. There is an urgent need to identify new vulnerabilities of neuroblastoma and less toxic therapeutic regimens for the treatment of neuroblastoma. Several genomic aberrations like *MYCN* amplification, *ALK* mutation or *TERT* rearrangement are known to drive neuroblastoma progression and malignancy. In contrast to adult cancers, the overall somatic mutation rate is low, suggesting an epigenetic regulation of neuroblastoma. In adult clinical trials, treatment with histone deacetylase inhibitors (HDACi) reduced the malignant phenotype. Although identification of the responsible regulators remains unclear, the application of histone deacetylase inhibitors provides a promising approach for the treatment of neuroblastoma.

A novel subgroup of high-risk neuroblastoma harbors genomic rearrangements of the telomerase reverse transcriptase (*TERT*), resulting in high telomerase activity and poor survival rates. There are no clinically successful inhibitors targeting *TERT* or telomerase. The aim of this study was to assess the potency of the small-molecule HDAC inhibitor panobinostat (LBH589, Farydak®) in preclinical models of *TERT*-rearranged neuroblastoma, in single agent or combination therapy. This study demonstrates that in models of the novel high-risk subgroup of *TERT*-rearranged neuroblastoma, HDAC inhibitor treatment repressed *TERT* mRNA levels. The reduction of *TERT* transcript levels was observed after 2 h of panobinostat treatment, with the effect increasing over time. Inhibition of HDAC1 and HDAC2 was identified to mediate *TERT* repression after panobinostat treatment. Subsequently, telomerase activity was reduced by panobinostat treatment. This effect might be independent of the oncogene MYCN, as *MYCN*-inhibiting Bromodomain and Extra-Terminal motif (BET) inhibitors showed no regulation of *TERT* levels and telomerase activity in *TERT*-rearranged cell lines. Enforced *TERT* expression demonstrated partial rescue of the antitumoral phenotype induced by HDAC inhibitor treatment. *TERT* mRNA level, telomerase activity and xenograft tumor growth was reduced by panobinostat treatment in mouse models of *TERT*-rearranged neuroblastoma in preventive and therapeutic treatment schedules.

Panobinostat treatment resulted in reduction of colony formation capacity and proliferation of *TERT*-rearranged cell lines. Low nanomolar concentrations of panobinostat decreased cell viability as effectively as micromolar concentrations of targeted drugs on telomerase in *TERT*-driven neuroblastoma cell lines. Metabolic activity was reduced in a panel of neuroblastoma cells treated with panobinostat, with low nanomolar half-maximal inhibitory concentrations. Flow cytometry and RNA expression analyses of *TERT*-rearranged cell lines and xenograft tumors revealed alterations of the cell cycle profile after panobinostat treatment. Expression of the identified genes of hallmarks E2F and G2M target genes was reduced after panobinostat treatment in cell lines and xenograft tumors. Protease-mediated induction of apoptosis by panobinostat treatment was demonstrated by cleavage of PARP-1, which was partially rescued by the caspase inhibitor Z-VAD.

In combination with the proteasomal inhibitor bortezomib, panobinostat treatment showed synergistic antitumoral efficacy in 2D and 3D cell models of *TERT*-rearranged neuroblastoma. A synergistic reduction of *TERT* mRNA expression or telomerase activity was not detected after combination treatment.

The DNA breakpoint in the 5'-untranslated region of *TERT* and the rearrangement partner on chromosome 19 were determined in a *TERT*-rearranged cell line. Applying chromatin immunoprecipitation DNA sequencing of different histone marks, the investigated epigenetic landscape of the rearranged *TERT* locus revealed no major changes after panobinostat treatment. Methylation array profiling demonstrated genome-wide demethylation of CpG dinucleotides, but remained the methylation pattern at the *TERT* locus after panobinostat treatment.

On the transcriptional level, RNA stability was impaired by panobinostat treatment. Panobinostat treatment reduced half-life of the *TERT* transcript upon blocking *de novo* RNA synthesis, suggesting reduced *TERT* transcript stability as the underlying mechanism.

In conclusion, there are no clinically successful drugs targeting *TERT* or telomerase. The HDAC inhibitor panobinostat shows antitumoral efficacy at tolerable and manageable side effects in clinical studies. Treatment of *TERT*-rearranged neuroblastoma models with the approved HDACi panobinostat demonstrated tumor-suppressive efficacy and reduction of *TERT* mRNA and telomerase activity. Combination therapy of panobinostat and bortezomib synergistically increased the antitumoral efficacy *in vitro* and is a promising approach for future xenograft mouse studies. Targeting *TERT* by nanomolar doses of HDACi like panobinostat

might be beneficial for neuroblastoma patients presenting with *TERT*-rearranged tumors, still facing poor survival rates today.

C. Table of Contents

D. List of Figures

E. List of Tables

F. Abbreviations

°C	Celsius
µ	Micro
4-C (seq)	Circularized Chromosome Conformation Capture (with high-throughput sequencing)
A	Ampere
A, C, T, G, U, (N)	Adenine, cytosine, guanine, thymine, uracile, (N: any nucleotide)
ADRN	Adrenergic
AFA	Adaptive Focused Acoustics
ALT	Alternative lengthening of telomeres
ALK	Anaplastic lymphoma kinase
AML	Acute myeloid leukemia
Amp	Ampicillin
APS	Ammonium persulfate
ASCT	Autologues stem-cell transplantation
ASF1B	Anti-Silencing Function 1B Histone Chaperone
ATAC-seq	Assay for transposase-accessible chromatin with high-throughput sequencing
ATL	T-cell leukemia/lymphoma
ATP	Adenosine-5´-triphosphat
ATR	Ataxia telangiectasia- and RAD3-related
AURKB	Aurora Kinase B
BAM	Binary alignment map
Bcl-2	B-cell lymphoma 2
BED	Browser extensible data
BET	Bromodomain and extra-terminal motif
BIH	Berlin Institute of Health
BIM	Bcl-2-interacting mediator of cell death
bleyplaby	Homo sapiens spliced coding gene bleyplaby
BMF	Bcl-2-modifying factor
bp	Base pair
BRD4	Bromodomain Containing 4
BSA	Bovine serum albumin
BW	Big wig
CCNA2	Cyclin A2
CDC25A	Cell Division Cycle 25A
cDNA	Complementary DNA
CENPM	Centromere Protein M
ChIP-seq	Chromatin immunoprecipitation coupled with sequencing
chr.	Chromosome
CLL	Chronic lymphocytic leukemia
CLPTM1L	Cleft Lip And Palate Transmembrane Protein 1-Like Protein
CML	Chronic myeloid leukaemia
CMV	Cytomegalovirus
CNV	Copy number variation
CPO	Cellular Phenomics & Oncology Berlin-Buch
CRC	Core regulatory circuitry
CRISPR	Clustered Regularly Interspaced Short Palindromic Repeats

CTCF	CCCTC-Binding Factor
CTCL	Cutaneous T-cell lymphoma
CUBI	Core unit bioinformatics (at the Berlin Institute of Health)
DAPI	4,6-Diamino-2-phenylindol
DEPC	Diethylpyrocarbonate
d	Days
del	Deletion
der	Derivate
DIG	Digoxigenin
DKFZ	Deutsches Krebsforschungszentrum
DMEM	Dulbecco's modified eagle's medium
DMSO	Dimethylsulfoxid
DNA	Desoxyribonucleic acid
DNase	Desoxyribonuclease
DNMT	DNA methyltransferase
DOX	Doxorubicin
dNTP	2'-Deoxyribonucleoside 5'-triphosphate
dsDNA	Double-stranded DNA
DSMZ	Deutsche Sammlung für Microorganismen und Zellkulturen
DTT	Dithiothreitol
E2F	Transcription factor family
E.coli	Escherischia coli
EBF1	EBF Transcription Factor 1
EBRT	External beam radiation therapy
ECACC	European Collection of Authenticated Cell Cultures
ECL	Enhanced chemiluminescence
ECRC	Experimental and Clinical Research Center
EDTA	Ethylendiamintetraacetic acid, Na-salt
EFS	Event-free survival
EGF	Epidermal growth factor
ELISA	Enzyme-linked Immunosorbent Assay
EMA	European Medicines Evaluation Agency, European Union
EMT	Epithelial-mesenchymal transition
EPO	Experimental Pharmacology & Oncology Berlin-Buch
et al.	Et alii (and other)
EtOH	Ethanol
ETS	Erythroblast transformation specific
FA	Formaldehyde
FACS	Fluorescence activated cell sorting
FAK	Focal adhesion kinase
FCS	Fetal calf serum
FDA	Food and Drug Administration, USA
FISH	Fluorescent in situ hybridization
g	Gram
G2M	Transition point between G2- and M-phase in cell cycle
GAGE	Generally applicable gene set enrichment
gDNA	Genomic DNA
GFP	Green fluorescent protein
GINS2	GINS Complex Subunit 2
GPOH	Gesellschaft für pädiatrische Onkologie und Hämatologie

GRHL1	Grainyhead Like Transcription Factor 1
GSEA	Gene set enrichment analysis
h	Hour(s)
H2A/2B/3/4	Histone 2A/2B/3/4
H3K4ac	Acetylation of histone 3 at lysine residue 4
H3K4me1	Monomethylation of histone 3 at lysine residue 4
H3K4me2	Dimethylation of histone 3 at lysine residue 4
H3K4me3	Trimethylation of histone 3 at lysine residue 4
H3K27ac	Acetylation of histone 3 at lysine residue 27
H3K27me3	Trimethylation of histone 3 at lysine residue 27
H3K36me3	Trimethylation of histone 3 at lysine residue 36
H3K9me3	Trimethylation of histone 3 at lysine residue 9
HAT	Histone acetyl transferase
HDAC	Histone deacetylase
HDM	Histone demethylase
HEPES	4-(2-hydroxyethyl)-1-Piperazineethanesulfonic acid
hg19	Human genome 19
hg38	Human genome 38
Hi-C	High-throughput chromosome conformation capture
HMTs	Histone methyltransferases
HR(G)	High-risk (group)
HRP	Horse reddish peroxidase
HRPT	Hypoxanthine Phosphoribosyltransferase
IC_{50}	Half-maximal inhibitory concentration
IgG	Immunoglobulin G
IGV	Integrative Genomics Viewer
INRG	International neuroblastoma risk group
INSS	International neuroblastoma staging system
IP	Immunoprecipitation
K	Lysine
kb	Kilo base
KD	Knockdown
kDa	Kilo dalton
KIF2C	Kinesin Family Member 2C
l	Liter
LB	Luria-Bertani
LMRs	Low methylated regions
lncRNA	Long-noncoding RNA
LOH	Loss of heterozygosity
LR(G)	Low-risk (group)
m	Milli
M	Molar
MACS	Model-based analysis of ChIP-Seq
MARCH11	Membrane Associated Ring-CH-Type Finger 11
Mb	Mega base
Mcl-1	Induced myeloid leukemia cell differentiation protein Mcl-1
MES	Mesenchymal
MIBG	Meta-iodobenzylguanidine
min	Minute(s)
Mio	Million

miRNA	Micro RNA
MIR183	Micro RNA 183
MRD	Minimal residue disease
mRNA	Messenger RNA
MZF1 (*-AS1*)	Myeloid zinc finger 1 (Antisense RNA 1)
n	Nano
NB	Neuroblastoma
NC	Negative control
NCBI	National Center for Biotechnology Information
NP-40	Nonyl phenoxypolyethoxylethanol
NPY	Neuropeptide Y
PAGE	Polyacrylamide gel electrophoreses
PARP-1	Poly (ADP-ribose) polymerase 1
PBS	Phosphate buffered saline
PC(A)	Principle component (analysis)
PCR	Polymerase chain reaction
PD-L1	Programmed death-ligand 1
PDX	Patient-derived xenograft
PI	Propidium iodidie
PIP	Peak incident power
PRRX1	Paired Related Homeobox 1
PTCL	Peripheral T-cell lymphoma
PVDF	Polyvinylidene difluoride
RA	Retinoic acid
rel	Relative
RISC	RNA-induced silencing complex
RNA	Ribonucleic acid
RNAi	RNA-interference
RNA PolIII	RNA polymerase III
RNase	Ribonuclease
ROS	Reactive oxygen species
rpm	Rotation per minute
RPMI1640	Rosvell park memorial institute, medium formulation 1640
RRM2	Ribonucleotide Reductase Regulatory Subunit M2
RT	Room temperature
RTA	Relative telomerase activity
RT-PCR	Reverse transcription reaction followed by PCR
RT-qRT-PCR	Reverse transcription reaction followed by quantitative real-time PCR
SCL6A18	Solute Carrier Family 6 Member 18
SCL6A19	Solute Carrier Family 6 Member 19
SDHA	Succinate dehydrogenase
SDS	Sodiumdodecylsulfat
SE	Super-enhancer
sec	Second(s)
siRNA	Small interfering RNA
SNP	Single nucleotide polymorphism
t	Time
TAD	Topologically associating domain
TAR1	Telomere associated repeat 1
TBS	Tris buffered saline

TE	Tris/EDTA
TEMED	N, N, N´, N´-tetramethylethylendiamin
TMZ	Temozolomide
TERT	Telomerase reverse transcriptase
TF	Transcriptionfactor
TF1	Nuclear Receptor Subfamily 2 Group F Member 1
TH-MYCN	Human *MYCN* gene under the control of tyrosine hydroxylase
THOR	TERT Hypermethylated Oncological Region
TMB	Tetramethylbenzidine
TRAP	Telomerase repeated amplification protocol
tRNA	Transfer RNA
Tris	Tris-(hydroxymethyl)-aminomethan
Triton X-100	Octyl-phenoxy-ethylenoxide
TSS	Transcriptional start site
TTS	Transcriptional termination site
U	Unit (enzyme activity)
UCSC	University of California Santa Cruz
UTR	Untranslated region
UV	Ultraviolet
V	Volt
VPA	Valproic acid
W	Watt
WB	Western blotting
WES	Whole exome sequencing
WGS	Whole genome sequencing
Wnt	Wingless-type MMTV (mouse mammary tumor)
WST	Water-soluble tetrazolium
ZBTB45	Zinc Finger And BTB Domain Containing 45

1 Introduction

1.1 Neuroblastoma

1.1.1 Incidence and biology of neuroblastoma

Neuroblastoma is the most common extracranial solid tumor in childhood with an incidence of about 13 cases per million children in Germany and a total of 130 patients per year (Berthold, 2017). The global incidence of the disease is comparably the same in industrialized nations (Brodeur, 2003). Neuroblastoma occurs spontaneously with low hereditary burden (2%) (Friedman, 2005). The average age at initial diagnosis is 19 month indicating that neuroblastoma is a disease of infancy, with the highest rate of diagnosis in the first month of life (London, 2005). The disease is often diagnosed by coincidence when children are asymptomatic. Otherwise, children present with unspecific symptoms such as pain, fever, hypertension or anemia. Most frequent physical signs of patients presenting in the clinic are occurrence of an abdominal mass, proptosis, periorbital ecchymosis and/or pancytopenia (Pediatric Treatment Editorial Board, 2002). In general, primary tumors are located at the adrenal glands or along the paraspinal sympathetic nerve tissue in the neck, chest, abdomen or pelvis (Figure 1).

Neuroblastoma is a malignant embryonic tumor of the peripheral adrenergic lineage originating from undifferentiated cells of neural crest derivation. During development, neural crest cells give rise to the adrenal medulla and vegetative ganglia (Brodeur, 2003). They delaminate from the neural crest first, migrate ventrally and differentiate into adrenaline- or noradrenaline-producing cells. At the boarder of neural and non-neural ectoderm, neural crest cells are induced during gastrulation by bone morphogenic proteins, fibroblast growth factors, Notch and Wnt signaling (Le Douarin, 2012; Nelms, 2010). Genetic as well as epigenetic events are likely to contribute to the malignant transformation in the process of migration, differentiation and apoptosis. Studying gene expression profiles of neuroblastoma cell lines, Van Groningen and colleagues proposed neuroblastoma to originate from the developing peripheral sympathetic nervous system and to consist of an adrenergic (ADR) type and a mesenchymal (MES) type (van Groningen, 2017). Both cell types can spontaneously interconvert, reflecting the high plasticity and heterogeneity of the disease. Neuroblastoma show clinical heterogeneity in their biological features and response to treatment spanning from rapid progression of the disease to spontaneous regression (Brodeur, 2014; Matthay, 2016).

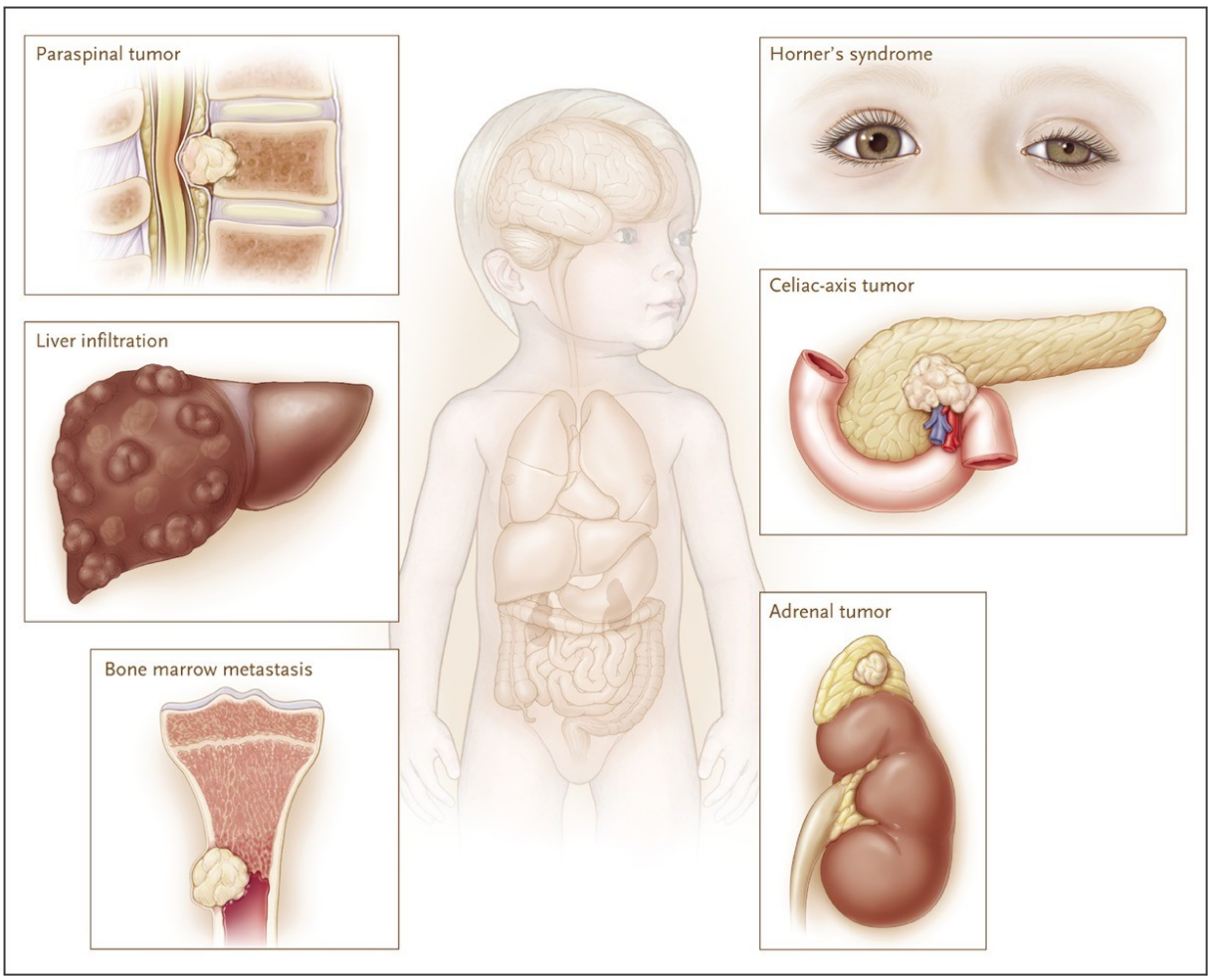

Figure 1: Clinical presentation of neuroblastoma.
From *Maris, 2010*.

Neuroblastoma accounts for 8–15% of cancer-related death in children in Europe and the USA (Althoff, 2015; Brodeur, 2014). Clinical prognostic markers such as age and stage as well molecular markers are used to stratify patients to different risk groups (see section 1.1.2). Several risk factors have been identified to drive neuroblastoma pathogenesis. The most prominent risk factor is the proto-oncogene *MYCN*. Amplification of *MYCN* have been described as major driver in neuroblastoma and to correlate with dismal prognosis. *MYCN* amplification stratifies patients to the high-risk group (Seeger, 1985). *MYCN* amplification is present in 18% of neuroblastoma and other 3% present gain of the *MYCN* gene. Amplification (≥ 8 copies) or gain (3-8 copies) of *MYCN* are associated with increasingly higher rate of unfavorable clinical and biological features (NB2004 trial protocol NCT03042429; Campbell, 2017). *MYCN* status clearly impacts clinical outcome and is used as biomarker for risk stratification (Maris, 2010). *MYCN* is located at chromosome 2p24 and encodes for a transcription factor known to form hetero dimers with the transcription factor MAX (Cascon,

2012). MYC proteins are known for their transforming ability by gene induction via transactivation and chromatin rearrangements (Adhikary, 2005) and have been described to repress tumor suppressor genes (Cheung, 2012). MYCN can be indirectly targeted with bromodomain and extra-terminal motif (BET) inhibitors targeting bromodomains of the BET family. BET proteins are epigenetic readers involved in transcriptional regulation, epigenetic memory and cell growth (Filippakopoulos, 2010). BET inhibitors bind competitively to the acetyl lysine recognition pocket of bromodomains, resulting is the dissociating of N-MYC from its promotor, thereby reducing *MYCN* expression and expression of *MYCN* target genes (Puissant, 2013). BET inhibitors are currently under clinical investigation in adult and pediatric oncology research in brain tumors (NCT03936465), lymphoma (NCT03925428) and solid tumors and hematologic malignancies (NCT02419417) (NIH, 2020).

Another risk factor are chromosomal aberrations and heteroploidy, which are common events in neuroblastoma. About 35% of neuroblastomas harbor deletions of 1p (Attiyeh, 2005; Brodeur, 1977; Caron, 1996). Gain of chromosomal arm 17q is detected in about 60% of neuroblastoma and correlates with dismal prognosis (Bown, 2001). Deletion of 11q is present in 43% of neuroblastoma and correlates with unfavorable prognosis in patients lacking additional 1p deletions and was described to increase the risk for metastatic relapse (Spitz, 2006).

Activating mutations of the anaplastic lymphoma kinase (*ALK*) have been identified as the major cause of hereditary neuroblastoma (Bresler, 2014; Mossé, 2008). Three major residues account for about 85% of *ALK* mutations: R1275 (43%), F1174 (30%), and F1245 (12%) (Bresler, 2014). In a cohort of neuroblastoma tumors, copy number variations (CNV) were detected in about 17% of tumors, with a gain of the *ALK* gene being the most common event. A gain of the *ALK* locus almost exclusively occurs together with *MYCN* amplification, resulting in poor prognosis and inferior outcome with a 5-year overall survival of 23% (Bagci, 2012; Bresler, 2014). ALK is a druggable target and inhibitors of ALK are promising therapeutic agents in neuroblastoma therapy (Carpenter, 2012; Mosse, 2016).

Recent whole genome sequencing studies of neuroblastomas revealed genomic rearrangements of the telomerase reverse transcriptase (*TERT)* gene in about 31% of tumors in the high-risk group (Peifer, 2015; Valentijn, 2015). The importance of *TERT* in neuroblastoma is highlighted in section 1.2. Further risk factors in neuroblastoma are inactivating mutations of *ATRX* and mutations in the *CHD5*, *DOCK8*, *PTPN14*, *PHOX2B*, *HRAS* and *KRAS* genes (Cheung, 2012; Molenaar, 2012; Pugh, 2013; Sausen, 2013).

Patients battling high-risk neuroblastoma experience resistance to first-line therapy in approximately 10% of cases and show frequently resistance to conventional chemotherapy in case of relapse, resulting in progressive disease and eventually early death (Naiditch, 2015). Further, patients of the high-risk subgroup can relapse as late as ten years after completion of the first-line therapy and tumors are often therapy resistant (Pediatric Treatment Editorial Board, 2002; Tonini, 2012; Zage, 2018). Relapses are likely to arise from a small number of clones surviving chemotherapy, called minimal residue disease (MRD) (Maris, 2007; Maris, 2010; van Groningen, 2017). Neuroblastoma cells of the mesenchymal type appear to be more resistant to chemotherapy, eventually giving rise to MRD and relapse (Shibue, 2017; van Groningen, 2017; Ye, 2015). Depending on transcription factor signatures, Van Groningen and colleagues demonstrated that both cell types transdifferentiate, making therapy strategies even more complex (van Groningen, 2017).

1.1.2 Classification of neuroblastoma

Two major classification schemes have been developed to categorize histologic and biologic features of patients to define the different risk groups. The International Neuroblastoma Staging System (INSS) is a postsurgical staging system stratifying patients according to locoregional tumors based on the degree of surgical resection (Monclair, 2009). A second staging system including pre-treatment features of the tumors is the International Neuroblastoma Risk-group (INRG) system, staging patients before therapeutic intervention (Cohn, 2009). There are five stages splitting up into 16 risk groups according to the INRG classification, which help to categorize patients to pre-treatment risk groups and to stratify patients to different therapies (Figure 2). The stratification into different risk groups is based on age at diagnosis, tumor stage, histologic category, grade of tumor differentiation, DNA ploidy, copy-number status of the *MYCN* oncogene and genomic alterations at chromosome 11q (Cohn, 2009; Maris, 2010).

INRG Stage	Age	Histological Category/Grade of Tumor Differentiation	*MYCN*	11q aberration	Ploidy	Pre-treatment Risk Group
L1/L2		GN maturing GNB intermixed				A Very Low
L1		Any, except GN maturing or GNB intermixed	NA			B Very Low
			Amp			K High
L2	<18m	Any, except GN maturing or GNB intermixed	NA	No		D Low
				Yes		G Intermediate
	≥18m	GNB nodular, differentiating NB, differentiating	NA	No		E Low
				Yes		H Intermediate
		GNB nodular, poorly differentiated or undifferentiated NB, poorly differentiated or undifferentiated	NA			H Intermediate
			Amp			N High
M	<18m		NA		Hyperdiploid	F Low
	<12m		NA		Diploid	I Intermediate
	12m-<18m		NA		Diploid	J Intermediate
	<18m		Amp			O High
	≥18 m					P High
MS	<18m		NA	No		C Very Low
				Yes		Q High
			Amp			R High

Figure 2: Pre-treatment classification scheme of neuroblastoma according to the INRG.
GN: ganglioneuroma; GNB: ganglioneuroblastoma; Amp: amplified; NA: not amplified; L1: localized tumor confined to one body compartment and with absence of image-defined risk factors (IDRFs); L2: locoregional tumor with presence of one or more IDRFs; M: distant metastatic disease (except stage MS); MS: metastatic disease confined to skin, liver and/or bone marrow in children < 18 months of age. Adapted from Cohn, 2009 and The International Neuroblastoma Risk INRG, 2020.

About 50% of neuroblastoma patients are stratified to the high-risk group. There are several factors that define a high-risk state including *MYCN* amplification or distant metastasis. Over recent years, the overall prognosis of patients diagnosed with neuroblastoma has improved from about 50% overall survival in 1979 to about 70% in 2004 (Berthold, 2017). The overall survival of patients of the high-risk group remains as low as 40% (Matthay, 2016; Pinto, 2015). The overall survival of patients of the medium-risk group is approximately 80% (Berthold, 2017). A novel mechanistic classification of neuroblastoma into telomere maintaining and non-maintaining tumors was proposed by Ackermann *et al.* in 2018 (Ackermann, 2018). In this study, a subset of tumors harboring telomere maintenance mechanisms and additional mutations in the RAS/TP53 pathway defined an ultra-high-risk group among all telomerase-maintaining neuroblastomas, with event-free survival rates of less than 20% (Ackermann, 2018) (Figure 3). This novel classification is likely to be considered for future categorization and stratification of neuroblastoma patients.

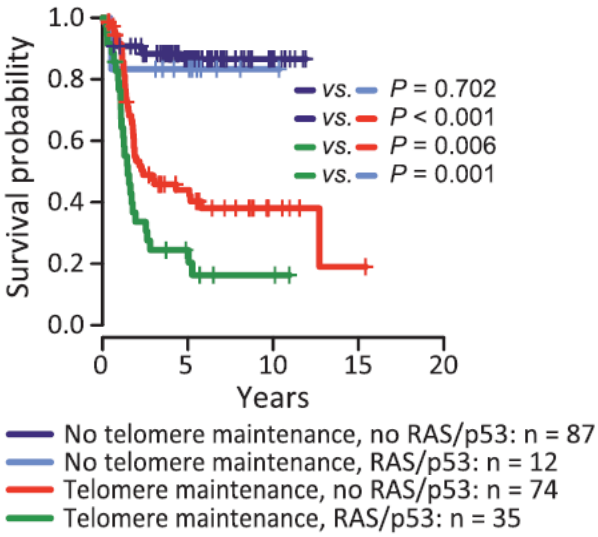

Figure 3: Survival probability of patients depending on telomere maintenance status.
Event-free survival of patients according to the absence or presence of RAS or p53 pathway gene mutations and telomere maintenance activity. From Ackermann, 2018.

1.1.3 Therapeutic strategies in neuroblastoma

One major characteristic of neuroblastoma is the diverse biological behavior necessitating vastly different therapeutic scenarios, ranging from observation only to multimodal concepts including high-dose chemotherapy with autologous stem cell rescue, surgery, radiotherapy and immunotherapeutic targeting of the disialoganglioside GD2 (Maris, 2010; Pinto, 2015; Schulte, 2015; Yu, 2010). Depending on the stratification of the patient, therapy consists of a resection of the tumor with optional mild chemotherapy after recurrence of the disease (very low and low-risk group). For the intermediate-risk group, moderately dosed chemotherapy followed by a surgical resection of the tumor with optional radiation therapy is applied. Patients of the high-risk group are treated with high dose multimodal chemotherapy, radiotherapy and stem cell transplantation. Patients enrolled in the Neuroblastoma NB2004 Trial Protocol (NCT03042429, NIH, 2020) and the subsequent NB2016 Registry in Germany are treated by this multimodal therapy (Figure 4).

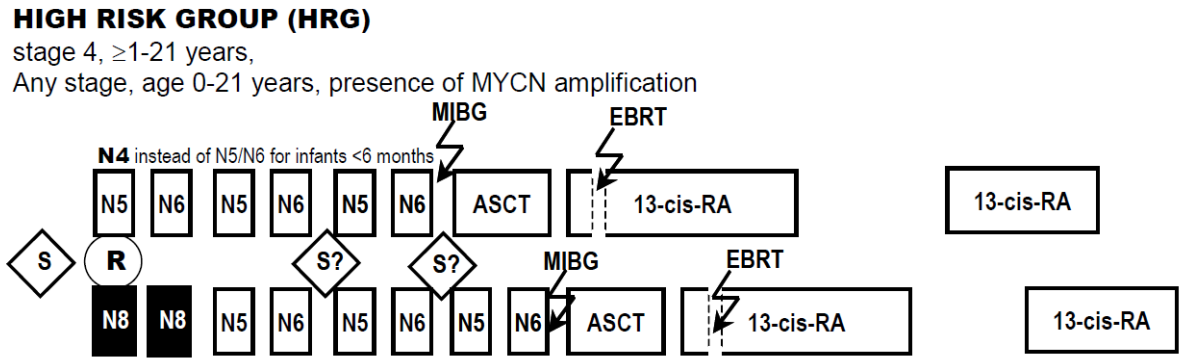

Figure 4: Treatment schedule for the neuroblastoma high-risk group according to the NB2004 trial study NCT03042429.
S: Surgery; R: Randomization; N4/5/6/8: chemotherapy cycles; MIBG: Meta-iodobenzylguanidine treatment; EBRT: External beam radiation therapy; ASCT: autologous stem-cell transplantation; 13-cis-RA: 13-cis-retinoic acid. From the study protocol NCT00410631.

Multiple cycles with antineoplastic chemotherapeutic drugs such as doxorubicin, vincristine and carboplatin are part of this treatment recommendation. A phase II study recruiting relapsed high-risk neuroblastoma patients in Germany is the RIST-rNB-2011 protocol (NCT01467986, NIH, 2020). Therapy of patients randomized to the experimental arm consists of treatment with dasatinib, rapamycin, irinotecan and temozolomide. Treatment regimens are accompanied by unwanted side effects such as pancytopenia, hearing loss, infertility and potentially secondary malignant neoplasms. Targeted therapeutics matching to the individual tumor genotype of each patient are urgently required and are likely to be combined with standard chemotherapeutics to minimize the risk of resistance development and to yield optimal antitumoral efficacy.

1.2 TERT and telomerase

1.2.1 TERT and telomerase in neuroblastoma

A novel subgroup of high-risk neuroblastoma was identified to harbor rearrangements at the *TERT* locus (Peifer, 2015; Valentijn, 2015). An estimate of about 30% of high-risk cases present genomic *TERT* rearrangements, resulting in high *TERT* levels and active telomerase. The *TERT* rearrangement was analyzed in a cohort of neuroblastoma patient samples of different risk groups (Peifer, 2015; Valentijn, 2015). Rearrangements of the *TERT* locus were shown to occur in a region upstream of *TERT*, termed the “breakpoint region” (Figure 5). In these tumors, the rearrangement was found to be located 50 kb upstream of the transcriptional start site (TSS) of *TERT* without affecting the gene or its promoter and resulting in proximity of *TERT* to super-enhancer elements.

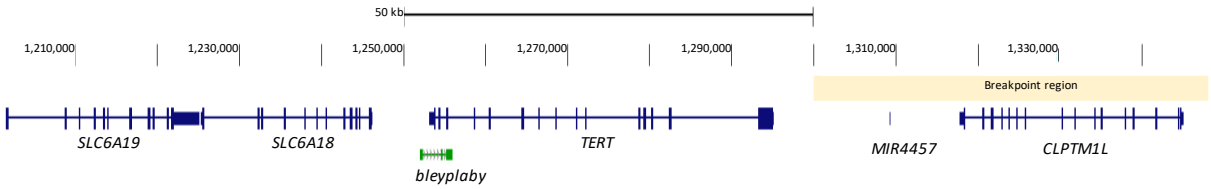

Figure 5: The TERT genomic region.
The *TERT* genomic region including the predicted breakpoint region as described in Peifer, 2015.

The *TERT* gene is surrounded by genes *SLC6A19*, *SLC6A18* and *bleyplaby* at the distal side and *CLPTM1L* proximal of the gene locus. *TERT*-rearranged neuroblastoma show increased expression of *SLC6A19*, *SLC6A18* and *bleyplaby* compared to *MYCN*-amplified neuroblastoma or tumors lacking a *TERT* rearrangement and *MYCN* amplification. In contrast, *CLPTM1L* is equally expressed in *TERT*-rearranged, *MYCN*-amplified or in tumors lacking a *TERT* rearrangement and *MYCN* amplification (Peifer, 2015). In *MYCN*-amplified tumors from this study, only *TERT* and the overlapping gene *bleyplaby* show upregulated gene transcription, demonstrating a silencing of gene expression in this chromosomal region and a selective upregulation of *TERT* by transcriptional activation by amplified *MYCN* (Peifer, 2015). In a second cohort of *TERT*-rearranged neuroblastomas, only *TERT* expression was increased with no alterations in *SLC6A19*, *SLC6A18*, *bleyplaby* or *CLPTM1L* expression compared to non-*TERT*-rearranged samples (Valentijn, 2015). The neuroblastoma cell lines GI-ME-N and CLB-GA carry rearrangements of *TERT* without harboring amplification of *MYCN*. The high *TERT* expression is mediated via enhancer hijacking, putting the *TERT* locus under the control of super enhancers (Peifer, 2015; Gartlgruber, 2018; Valentijn, 2015; Zhao, 2009). Although several copies of *TERT* were detected in *TERT*-rearranged cell line models, the high *TERT* expression in *TERT*-rearranged cell lines is most likely enabled by the rearranged chromatin environment of the locus and not be copy number alterations (Gartlgruber, 2018; Peifer, 2015; Valentijn, 2015). In a cohort of colorectal carcinomas, there was no correlation between *TERT* copy number and its expression level or telomerase activity (Palmqvist, 2005). The *MYCN*-amplified cell line Kelly was demonstrated to harbor a *TERT* rearrangement whereas LAN-2 was presumed to carry a *TERT* rearrangement (Gartlgruber, 2018). In *TERT*-rearranged CLB-GA and Kelly cells, Assay for transposase-accessible chromatin (ATAC) sequencing revealed enriched peaks in the *TERT* locus and surrounding genes, indicative of an open chromatin state (Gartlgruber, 2018). In the patient cohorts by Peifer *et al*. and Valentijn *et al*., *TERT* rearrangements occur almost mutually exclusive with *MYCN* amplification or *ATRX*

mutation, juxtaposing the *TERT* coding sequence under the control of strong super-enhancer elements, resulting in transcriptional upregulation of *TERT* (Peifer, 2015; Valentijn, 2015). The occurrence of *TERT* rearrangements correlates with unfavorable patient survival, even stronger than *MYCN* amplification (Figure 6).

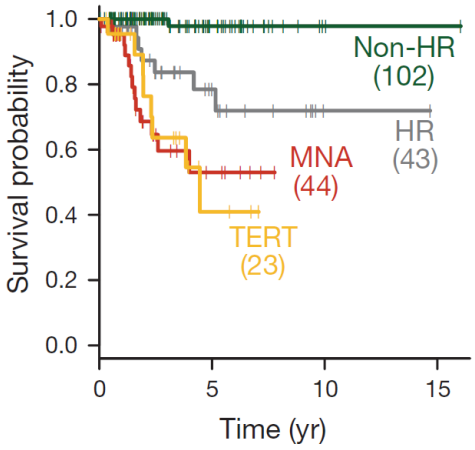

Figure 6: Overall survival of neuroblastoma patients of different risk-groups.
TERT: *TERT* rearrangements, MNA: *MYCN* amplification, HR: high-risk disease without these alterations, non-HR: low-risk or intermediate-risk disease. Numbers indicate patients per group. From Peifer, 2015.

1.2.2 Telomere biology

The *TERT* gene is located on the minus strand of chromosome 5p15.33 and consists of 16 exons (Figure 7). Several isoforms have been discovered but only the full-length transcript shows catalytic activity (Saeboe-Larssen, 2006). The coding sequence consists of 41,901 bp translating into a protein of 127 kDa.

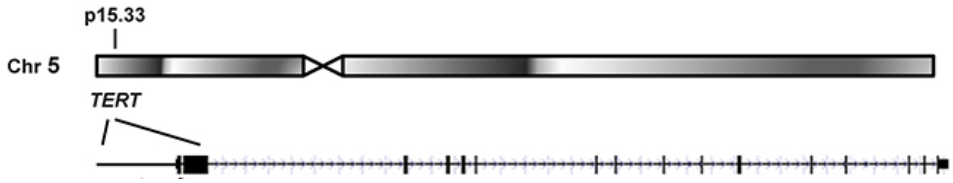

Figure 7: The TERT gene is localized on the distal part of chromosome 5.
The gene is located on chr5, p15.3 and is composed of 16 exons (adapted from Wang, 2016).

The TERT protein is major component of the telomerase holoenzymatic complex and is responsible for its catalytic reverse transcriptase DNA polymerase function (Figure 8) (Counter, 1998). Other components of the complex such as the RNA template TERC or the telomerase-

associated protein *TEP1* did not influence telomerase activity in breast cancer cells (Rubis, 2013). TERT is most commonly localized in the nucleus, but also found in mitochondria and the cytosol (Ahmed, 2008; Singhapol, 2013). Telomeres consist of tandem repeats of the sequence TTAGGG in vertebrates at distal ends of eukaryotic chromosomes, stabilizing them during mitosis and protecting chromosomal ends from degradation. After each cell division, telomeres are shortened progressively resulting in successive degradation of chromosomal ends. When telomeres have reached a critical length, tumor suppressor p53 becomes activated and mediates entering of replicative senescence and cell death (Shay, 1991).

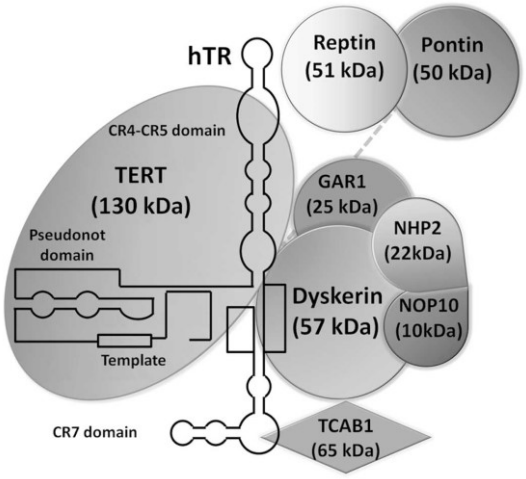

Figure 8: Schematic illustration of the telomerase holoenzymatic complex.
The core components of the telomerase complex. The molecular weight is shown in parentheses. From Gomez, 2012.

The single-stranded 3′-telomeric overhang at chromosomal ends is the substrate of telomerase. Telomerase adds the sequence TTAGGG to chromosomal ends, protecting cells from entering replicative senescence and escaping from the “end replication problem” (Olovnikov, 1996). The telomerase ribonucleoprotein enzyme complex functions as a reverse transcriptase and consists of two major components that ensure catalytic activity: TERT (or hTERT) and the RNA template TERC (or hTR) (Figure 8). TERT adds telomeric repeats to chromosomal ends by using TERC as a template for extension (Figure 9) (Greider, 1985). Besides these core components, the proteins TCAB1, Dyskerin, Reptin, Pontin, telomerase Cajal body protein 1, NHP2, NOP10 and GAR1 are associated with the telomerase complex (Artandi, 2010).

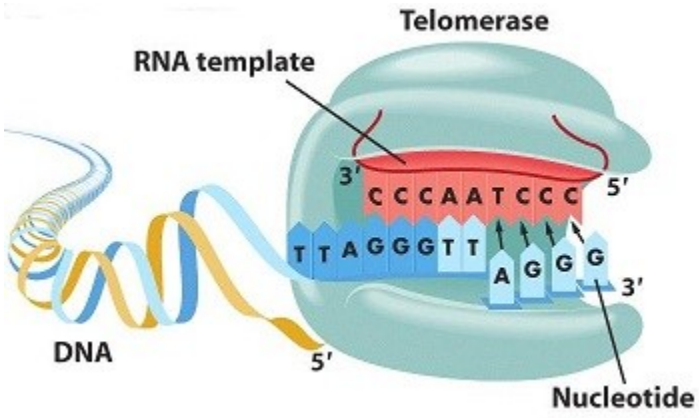

Figure 9: Telomerase adds repeats of the TTAGGG sequence to telomeric ends.
Illustration of the enzymatic activity of telomerase at chromosomal ends (from English Wikibooks, 2008).

The replicative aging concept is considered to be an important anti-cancer mechanism since cells accumulate oncogenic mutations over time (Yuan, 2019). In humans, *TERT* expression is silenced in somatic tissue so that only very low levels of telomerase are detectable, whereas TERC is expressed ubiquitously (Yuan, 2019). In stem cells and germline cells, telomerase is active since these cells replicate indefinitely without entering senescence and apoptosis (Kim, 1994b; Wright, 1996). The importance of *TERT* and telomerase in healthy individuals is evidenced by pathological alterations of the *TERT* gene as demonstrated in breast, prostate and pancreas cancer (Walsh, 2019). About 80-90% of cancer cells display *TERT* expression resulting in active telomerase promoting cell division and proliferation (Cortez-Gonzalez, 2007). Activation of telomerase is an early key event in malignant transformation with activated *TERT* expression together with two oncogenes (SV40 T-antigen and mutant RAS) showing to be sufficient to promote tumorigenesis (Hahn, 1999). Many cancer cells show (re-)activation of telomerase, enabling those cells to divide indefinitely and become replicative immortal. Re-activation of telomerase was sufficient to extend the lifespan of cultured non-cancerous cells by maintaining telomeres (Bodnar, 1998). Telomerase activity *per se* is not tumorigenic, but enables cancer cells to become replicative immortal and proliferate continuously (Park, 2009). *TERT* overexpression is used to disable entry of senescence and to immortalize cell lines in culture (Counter, 1998; Hahn, 1999; Henssen, 2017). Nevertheless, cancer cells show shorter telomeres than surrounding healthy tissue, reflecting the increased proliferation rate of cancer cells (Engelhardt, 1997). Mice have longer telomeres than humans with telomerase being active throughout life. Mice carrying hyper-long telomeres had an increased lifespan without increase in spontaneous tumor formation (Muñoz-Lorente, 2019). Beside their roles in telomeric homeostasis, *TERT* and telomerase have been demonstrated to be involved in additional non-

canonical pathways including regulation of mitochondrial activity (Gordon, 2010; Indran, 2011; Mukherjee, 2011), cell proliferation and apoptosis (Bodnar, 1998; Kang, 2004; Ren, 2001), WNT/β-catenin and NF-κB signaling (Choi, 2008; Ghosh, 2012b; Park, 2009) as well as DNA-damage repair (Beliveau, 2007; Chenette, 2009; Masutomi, 2005; Tamakawa, 2010) and chromatin remodeling (Masutomi, 2005). Cancer cells maintain their telomeres via expression of *TERT* or a recombination-based alternative lengthening of telomeres (ALT) mechanism. In cancer cells, the cell has either active *TERT* transcription (85%) or activated ALT (15%) to maintain its telomeres (Bryan, 1995). Both telomere maintenance mechanisms can occur in the same tumor, but are mutually exclusive in the same cell as demonstrated in various cancers including neuroblastoma (De Vitis, 2018; Pezzolo, 2015). Switching between active telomerase and ALT to maintain the telomeres was reported (Hu, 2016). A remarkable observation was made in a subset of neuroblastoma undergoing spontaneous regression, which failed to up-regulate telomerase (Hiyama, 1995).

1.2.3 Regulation of TERT

The *TERT* locus is highly repressed in most human somatic cells (Wright, 1996). Expression of *TERT* is detected during embryogenesis and is subsequently silenced during cell differentiation. The *TERT* promotor consists of E-boxes, GC-motifs and ETS domains (Figure 10), enabling binding of transcription factors such as MYC, SP1 and NF-κB but also estrogen, AP-1, p53 and E2F factors were demonstrated to influence *TERT* expression (Akincilar, 2016; Colebatch, 2019; Cong, 1999; Kyo, 2000). In neuroblastoma, *MYCN* amplification results in an active transcription of *TERT* as a downstream target of *MYCN* (Mac, 2000). In consequence, *TERT* expression is increased in comparison to non *MYCN*-amplified neuroblastoma (Peifer, 2015; Valentijn, 2015). Several mutations of *TERT* or its promotor are described to mainly activate *TERT* expression in somatic tissue, potentially contributing to malignant transformation (Colebatch, 2019). *TERT* promoter mutations resulting in increased *TERT* expression and telomerase activity are associated with metastasis and reduced survival (Heidenreich, 2017) as described in melanoma (Populo, 2014), thyroid carcinomas (Melo, 2014) and gliomas (Killela, 2013).

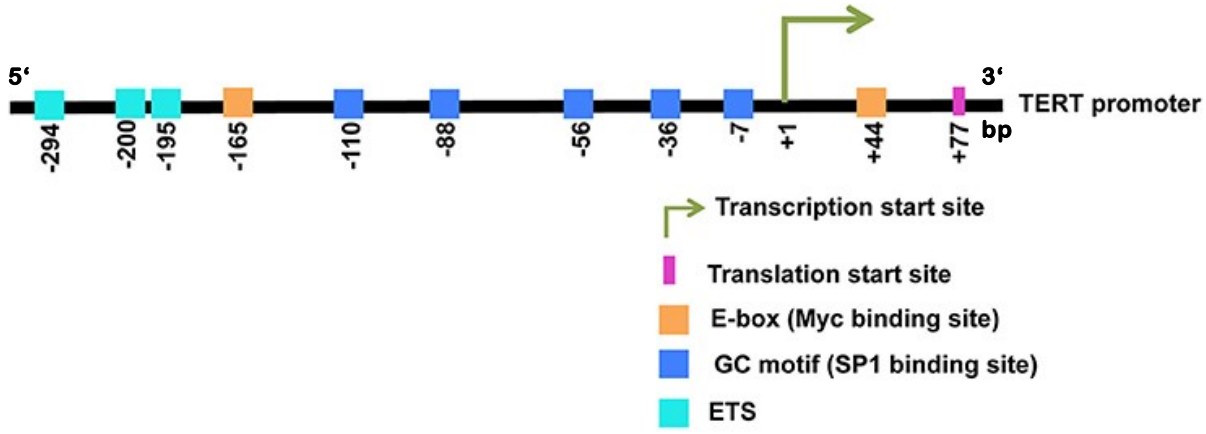

Figure 10: Schematic overview of the TERT promotor site.
Regulatory motifs of the *TERT* region. Numbers indicate distance in base pairs to transcriptional start site. Not true to scale. Bp: base pair; ETS: erythroblast transformation specific (binding site). Adapted from Khattar, 2017.

In *TERT*-rearranged neuroblastoma, the promotor and gene body of *TERT* are not found to be mutated (Peifer, 2015; Valentijn, 2015). Genomic rearrangements result in translocation of the *TERT* locus, thereby putting *TERT* under the control of super-enhancers (Peifer, 2015; Valentijn, 2015). These regulatory elements are collectively bound by an array of transcription factors, inducing high transcription of subsequent target genes (Peifer, 2015; Gartlgruber, 2018). Many cancer cells acquire super-enhancers at key oncogenes ("enhancer hijacking"), strongly driving gene transcription (Northcott, 2014). When *TERT* is actively transcribed, massive chromatin remodeling is necessary since the *TERT* locus is tightly repressed in most somatic tissues (Yuan, 2019). Epigenetic modifications such as histone modifications, methylation status and non-coding RNA (miRNA, lncRNA) have been associated to influence *TERT* levels (Jie, 2019).

1.2.4 Epigenetic regulation of *TERT*

1.2.4.1 Histone modifications

Several epigenetic modifications are associated to influence *TERT* expression, although the regulation depends on the cellular context (Zhu, 2010). Methylation at lysine 4 on histone H3 (H3K4) and acetylation of histones are generally considered as marks for active gene transcription (Kim, 2005b). Triple methylation of lysine 9 (H3K9me3) and of lysine 27 on histone H3 (H3K27me3) repress gene transcription and are less prominent in cancer cells (Boros, 2014). In telomerase-positive tumor cells, highly triple methylated lysine 4 on histone H3 (H3K4me3) seems to activate transcription of *TERT* (Atkinson, 2005). The high methylation

status is mediated by SET and MYND domain-containing protein 3 (SMYD3). SMYD3 is a specific H3K4 dimethyl- and trimethyltransferase, which regulates trimethylation of H3K4 within the *TERT* core promotor (Liu, 2007). Treatment with HDAC or DNA methyltransferase (DNMT) inhibitors re-activates *TERT* expression in non-malignant cells by keeping high levels of histone acetylation and DNA demethylation (Cong, 1999). In high-risk neuroblastoma tumors and cell lines presenting high *TERT* expression, histone marks standing for active gene expression were enriched at the *TERT* locus and repressive histone marks were less abundant, compared to low *TERT*-expressing tumors and cell lines (Peifer, 2015; Gartlgruber, 2018; Valentijn, 2015). In *TERT*-rearranged neuroblastoma, activating histone marks indicative of an active promoter (H3K4me3 and H3K27ac) and transcriptional elongation (H3K36me3) were enriched at the *TERT* TSS and the gene body. Enrichment of H3K27me3 and H3K9me3 marking repressed gene transcription were also detected in *TERT*-rearranged neuroblastoma tumors (Gartlgruber, 2018; Peifer, 2015). Another pathway to activate *TERT* is mediated via β-catenin (Hoffmeyer, 2012). The protein binds to the TCF motif within the *TERT* promotor and recruits methyltransferase SETD1a, resulting in trimethylation of H3K4 and activation of *TERT* gene transcription. It was also shown that TCF1, TCF4 and KLF4 might participate in the β-catenin-mediated *TERT* transcription (Hoffmeyer, 2012; Zhang, 2012). Another pathway to regulate *TERT* transcription was demonstrated via the two catalytic subunits of the SWI/SNF chromatin remodeling complex, BRD1 and BRM (Ito, 2008).

1.2.4.2 DNA methylation

Methylation adds a methyl group to the C5 position of cytosines in CpG dinucleotide DNA sequences. Three DNA methyltransferases are described in humans: DNMT1, DNMT3a and DNMT3b (Deaton, 2011). Methylation of cytosine at CpG islands near gene promotor regions is considered to mediate epigenetic silencing of gene transcription (Medvedeva, 2014). For the *TERT* locus, there is recent evidence that methylation of a region proximal to *TERT* termed THOR (TERT hypermethylated oncological region) is enabling gene transcription across cancer entities (Lee, 2019). THOR is a 433-bp genomic region containing 52 CpG sites located upstream of the *TERT* core promoter (Lee, 2019). In contrast to the general assumption that DNA methylation correlates with gene repression, it has been suggested that the unmethylated *TERT* promoter favors binding of transcriptional repressors in non-cancerous cells and that methylation enhances *TERT* gene transcription and subsequent malignant transformation (Lee, 2019). The HDAC inhibitor vorinostat was shown to reduce methylation in Non-Small Cell

Lung Cancer Cells (Li, 2011). In neuroblastoma tumors highly expressing *TERT*, methylation array profiling revealed a consistent increase in CpG methylation across the *TERT* locus, compared to tumors with low *TERT* expression (Peifer, 2015).

1.2.4.3 Non-coding RNA

Non-coding RNAs such as micro RNA (miRNA) or long-noncoding RNA (lncRNA) are encoded throughout the genome and add additional complexity to the process of gene transcription (Buckingham, 2013). The most prominent non-coding RNA to be involved in the regulation of *TERT* are miRNAs (Farooqi, 2018). They play important roles in post-transcriptional regulation of target genes by binding to the 3' untranslated region (UTR) of transcripts (Ali Syeda, 2020). Several miRNA have been described to target *TERT* transcripts in cancer, resulting in reduced translational rates such as miR-491-5p (Zhao, 2015), miR-1182 (Zhang, 2015), miR-1207-5p and miR-1266 (Chen, 2014). The lncRNAs compete with miRNAs and inhibit their binding to miRNA recognizing elements (MRE), resulting in protection of target RNAs (Buckingham, 2013). Only a few lncRNA have been associated to influence *TERT* transcription: long-noncoding RNA BC032469 is overexpressed in gastric cancer resulting in higher abundance of TERT (Lu, 2016).

1.2.5 Therapies targeting *TERT* or telomerase

Inhibitors of *TERT* or telomerase have proven efficacy in preclinical research but failed in clinical trials due to severe side effects (Relitti, 2020). A telomerase-targeted therapy represents a promising option for a variety of cancer entities. The likelihood to acquire resistance is considered minor, since *TERT* is encoded by a non-redundant gene. ALT-positive tumors maintain telomeres independent of telomerase activity. A selection for ALT-positive tumor cells or a switch to ALT activation under therapy is still possible (Cortez-Gonzalez, 2007; Hu, 2016; Shay, 2012). It might become necessary to target both pathways to arrest telomere maintenance. Nevertheless, treatment with *TERT* or telomerase-specific agents should be specifically target tumor cells at low toxicity towards stem cells or germline cells. Several approaches to target telomerase have been developed: inhibition of telomerase with small molecules, active immunotherapy, telomere-disrupting agents, suicide gene therapy and inhibition of telomerase expression or biogenesis (Harley, 2008). Studies in multiple myeloma, erythroid leukemia and gastric cancer show that bortezomib treatment reduces *TERT* expression

and telomerase activity (Ci, 2015; Weiss, 2012). Several small molecule inhibitors of telomerase have been developed to interfere with the binding of telomerase to its native template TERC. One of the most promising inhibitors for telomerase is the N3′-P5′-thio-phosphoramidate imetelstat (GRN163L), developed by Gereon Corp. It was administered to patients having cancer including multiple myeloma, non-small cell lung cancer and metastatic breast cancer within the framework of a clinical trial. These studies showed that imetelstat treatment was generally well-tolerated by the patients, but had limited therapeutic efficacy (Recagni, 2020). In non-small cell lung cancer, treatment with imetelstat was accompanied by several side effects and did not prolong the progression-free survival of the patients (Chiappori, 2015; Relitti, 2020). Until recently, telomerase inhibitors applied to young patients with central nervous malignancies failed in the clinical setting due to severe side effects and toxicity (Salloum, 2016). An indirect targeting of *TERT* and telomerase using small-molecule inhibitors that have proven safety in clinical trials could serve as a valuable therapeutic option to repress *TERT* expression and/or telomerase activity. According to the proposed novel classification of neuroblastoma into telomere maintaining and non-maintaining tumors (Ackermann, 2018), targeting *TERT* and telomerase in *TERT*-rearranged neuroblastoma is highly desirable and could offer cure to patients considered incurable today.

1.3 Histone deacetylases

1.3.1 Biology and classification of HDACs

The DNA strand of eukaryotes is organized in nucleosomes. Each nucleosome consists of histone proteins H2A, H2B, H3 and H4, forming the core structure of the nucleosome. The core is formed of two H2A-H2B dimers and one H3-H4 tetramer, around which the DNA strand is wrapped, resulting in a tight compensation of DNA (Roth, 2001). Each core particle binds 146 base pairs, with linker histone H1 sitting at the front and the end of the DNA strand, locking the DNA in place. The core histone possesses a long, N-terminal tail, protruding into the nucleoplasm. These tails are highly post-transcriptionally modified and influence accessibility of DNA. There are several histone modifications described in humans: acetylation, methylation, ubiquitination, sumoylation, propionylation, citrullination and phosphorylation of specific amino acids within the histone protein (Weaver, 2018). Epigenetic modifications are reversible marks at histone proteins, mainly at lysine moieties of histones H3 and H4, or at cytosine nucleobases without affecting the DNA sequence. These modifications on histone proteins influence the shift between euchromatin and heterochromatin formation, thereby regulating

gene transcription (Baylin, 2006). The condensed heterochromatin disables gene transcription while euchromatin is a more open chromatin structure and correlates with enabled gene transcription (Cann, 2011). One characteristic of epigenetic marks is the reversibility of modifications. Writing or erasing a covalently set mark is a dynamic process mediated by, for example histone deacetylases (HDAC), histone acetylases (HAT) or DNA methyltransferases (DNMT). These non-genetic modifications can be inherited and influence later generations gene transcription (Slatkin, 2009).

Histone deacetylases play important roles in epigenetic modifications of histone and non-histone proteins. Up to date, eleven Zn^{2+}-dependent "classical" HDACs and seven NAD^{+}-dependent sirtuins are known. Based on structural similarities, HDACs are categorized into four different classes (Table 1).

Table 1: Classification of histone deacetylases into four major classes.

Group	Class	Name	Location
Zn^{2+}-dependent	I	HDAC1	Nucleus/Cytoplasm
		HDAC2	
		HDAC3	
		HDAC8	
	IIa	HDAC4	Nucleus/Cytoplasm
		HDAC5	
		HDAC7	
		HDAC9	
	IIb	HDAC6	Cytoplasm
		HDAC10	
	IV	HDAC11	Nucleus/Cytoplasm
NAD^{+}-dependent	III	SIRT1-7	Nucleus/Cytoplasm/Mitochondria

Class I HDACs are most closely to the yeast Rpd3 and are ubiquitously expressed. HDACs 1-3 are located in the nucleus with only HDAC8 additionally being found in the cytosol (Yang, 2008b). HDAC1 and HDAC2 share 82% amino acid identity and have overlapping functions. Since they form common complexes, they compensate each other in their function (Montgomery, 2007). HDACs 1-3 act in multi-protein complexes including Sin3A, NcoR/SMRT, Co-REST, Mi2/NuRD and EST1B (de Ruijter, 2003; Zhang, 2014). HDAC1 and HDAC2 suppress hyperacetylation of tumor suppressor p53 in the embryonic epidermis

(LeBoeuf, 2010). Class II HDACs are homologues to the yeast *HDA1*, and their expression and function is more tissue specific (Yang, 2008b). Class IIa HDACs can be translocated to the cytosol whereas class IIb HDACs are exclusively found in the cytosol (de Ruijter, 2003; Yang, 2008b). The class III HDACs are called sirtuins, referring to homologues of yeast *SIR2*. All seven sirtuins have a distinct subcellular localization: SIRT1, SIRT6 and SIRT7 are localized in the nucleus, SIRT2 in the cytosol, and SIRT3, SIRT4 and SIRT5 in the mitochondria. Sirtuins are involved in cancer, aging and neurodegenerative diseases (Donmez, 2013; Hall, 2013). Class IV has only one member HDAC11, which is mainly located in the nucleus (Gao, 2002). HDAC11 has been proposed as a drug target in cancer therapy (Deubzer, 2013).

The well-studied role of HDACs is their function as epigenetic modifiers in deacetylating histones. Histone tails carry positive charges due to amine groups at lysine and arginine amino acids, increasing the binding affinity to the negatively charged phosphate backbone of DNA (Seto, 2014). Acetyl moieties for acetylation of lysines are transferred from acetyl-coenzyme A (Figure 11). Introduction of acetyl groups by histone acetyl transferases reduces the positive charge of histone tails, diminishes the interaction of histones and DNA resulting in a more open chromatin state (Seto, 2014). Acetylation of proteins changes the physicochemical features of modified lysines from basic to polar. This change in polarity can influence the features of the protein regarding its structure, stability and function. Acetylation of lysine hinders further modification of lysine such as methylation, ubiquitinylation, sumoylation and others (Yang, 2008a).

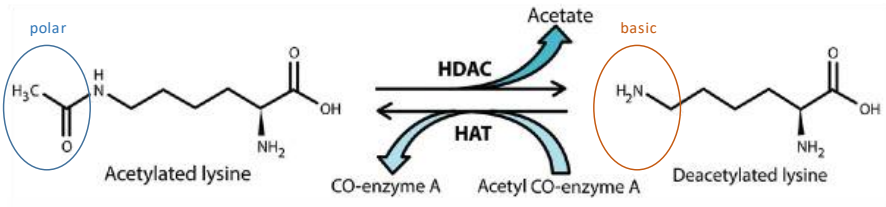

Figure 11: (De-)Acetylation of lysine is catalyzed by HDACs and HATs.
Enzymatic activity of HDACs and HATs at lysine (modified from Sanaei, 2019).

Acetylation of histones is considered a prerequisite for enabled gene transcription. Histone deacetylases cleave the covalently bound acetyl moieties from ε-amino-groups of histone tails and non-histone proteins, thereby increasing binding affinity of histone tails to DNA (Haberland, 2009; Witt, 2009b; Yang, 2008a). Acetylation and deacetylation of histones and non-histone proteins form a dynamic equilibrium and can influence activity, stability and interaction of proteins (Figure 12) (Seto, 2014).

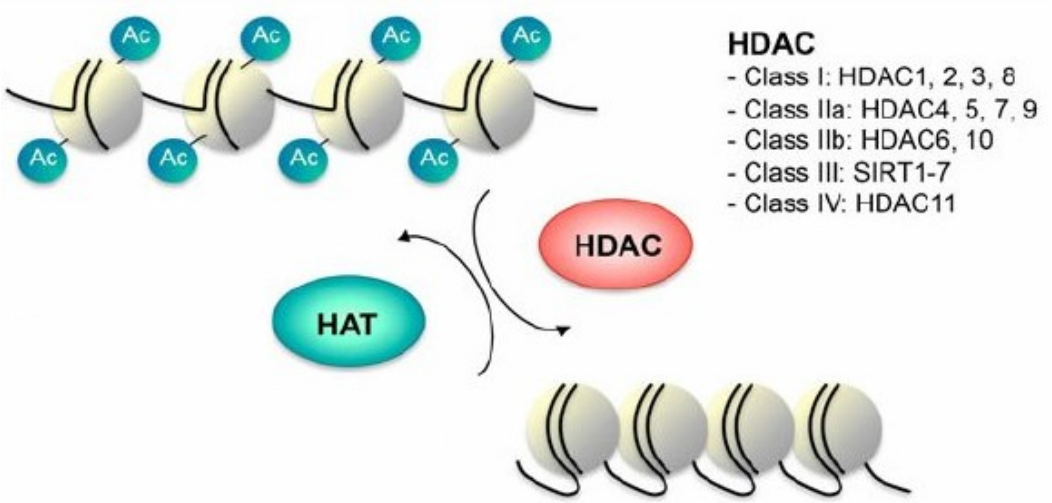

Figure 12: Acetylation of histone tails is a dynamic process mediated by HDACs and HATs.
HDACs of classes I-IV remove acetyl moieties from histone tails. Adapted from Schneider, 2013.

1.3.2 HDACs in neuroblastoma

In healthy somatic tissue, there is a balance between acetylation and deacetylation level of histones and non-histone proteins. This balance is often altered in cancer with many tumor suppressors being transcriptionally silenced (Kazanets, 2016). In numerous cancers, differential expression and activity of HDACs have been reported (Bolden, 2006; Mei, 2004; Sanaei, 2019). HDACs were reported to influence chromatin structure and fundamental pathways such as gene expressing, cell differentiation, cell cycle arrest and cell death (Kramer, 2001). Additional substrates undergoing dynamic acetylation and deacetylation are signal transduction mediators, cytoskeletal proteins, molecular chaperones, nuclear import factors, and viral proteins (Glozak, 2005). These HDAC substrates are directly or indirectly involved in numerous important cell pathways including control of gene expression, regulation of cell proliferation, differentiation, migration, and death (Zhang, 2014). In neuroblastoma, it was reported that several HDACs harbor specific and non-redundant oncogenic functions. HDAC2 cooperates with MYCN to repress tumor suppressor miR-183 (Lodrini, 2013). Induced miR-183 expression resulted in cell death and reduced proliferation of xenograft tumors (Lodrini, 2013). The transcription factor grainyhead-like 1 (GRHL-1) mediates expression of tumor suppressive elements and is transcriptionally repressed by HDAC3 and MYCN (Fabian, 2014). Expression of HDAC8 was

described to correlate with advanced stages of disease, and reduced HDAC8 expression resulted in induction of differentiation and apoptosis (Oehme, 2009a; Oehme, 2009b). HDAC10 was reported to promote autophagy-mediated neuroblastoma cell survival (Oehme, 2013). Elevated HDAC11 expression was detected in neuroblastomas and depletion of HDAC11 was sufficient to cause apoptosis and to inhibit metabolic activity in different cancer cell lines including neuroblastoma (Deubzer, 2013; Thole, 2017). This data underlines the importance of HDACs in neuroblastoma and have led inhibitors of HDACs to become interesting anticancer agents.

1.3.3 Histone deacetylase inhibitors

Most of the developed histone deacetylase inhibitors (HDACi) target the classical HDACs of classes I, II and IV. Within a class of HDACs, there are structural similarities which makes it difficult to synthesize specific HDAC inhibitors. For example, HDAC1 and HDAC2 share 82% amino acid identity and have overlapping functions (Ma, 2012; Montgomery, 2007). Inhibitors of HDACs might not be specific and additionally inhibit other HDACs as well. Additionally, target specificity depends on the applied concentration. Many HDAC inhibitors were isolated from natural compounds or organisms. Several chemical motifs inhibiting HDACs were identified and served as building blocks for development of novel synthetic HDAC inhibitors (Olzscha, 2016; Pavlik, 2013):

- Hydroxamates (trichostatin A, vorinostat, panobinostat, WT161, Santacruzamate A)
- Cyclic peptides (trapoxin B, romidepsin)
- Benzamides (entinostat, mocetinostat)
- Electrophilic ketones
- Aliphatic fatty acids (phenylbutyrate, valproic acid).

HDAC inhibitors share structural similarities and consist of three major building blocks: cap group, linker and functional group (Figure 13). The cap group is often made of cyclic aromatics, enhancing structure recognition of the molecule. The linker defines the space between the cap group and the functional group, thereby ensuring proximity of the functional group to the binding site. The functional group is designed to have strong affinity to Zn^{2+} cations, the catalytic active site of the HDACs (Ficner, 2009). Oxygen and nitrogen atoms owning a free electron pair are commonly used to chelate Zn^{2+}. Therefore, Zn^{2+}-chelating HDACi specifically target HDACs of class I, II and IV and not the sirtuins (Wu, 2011).

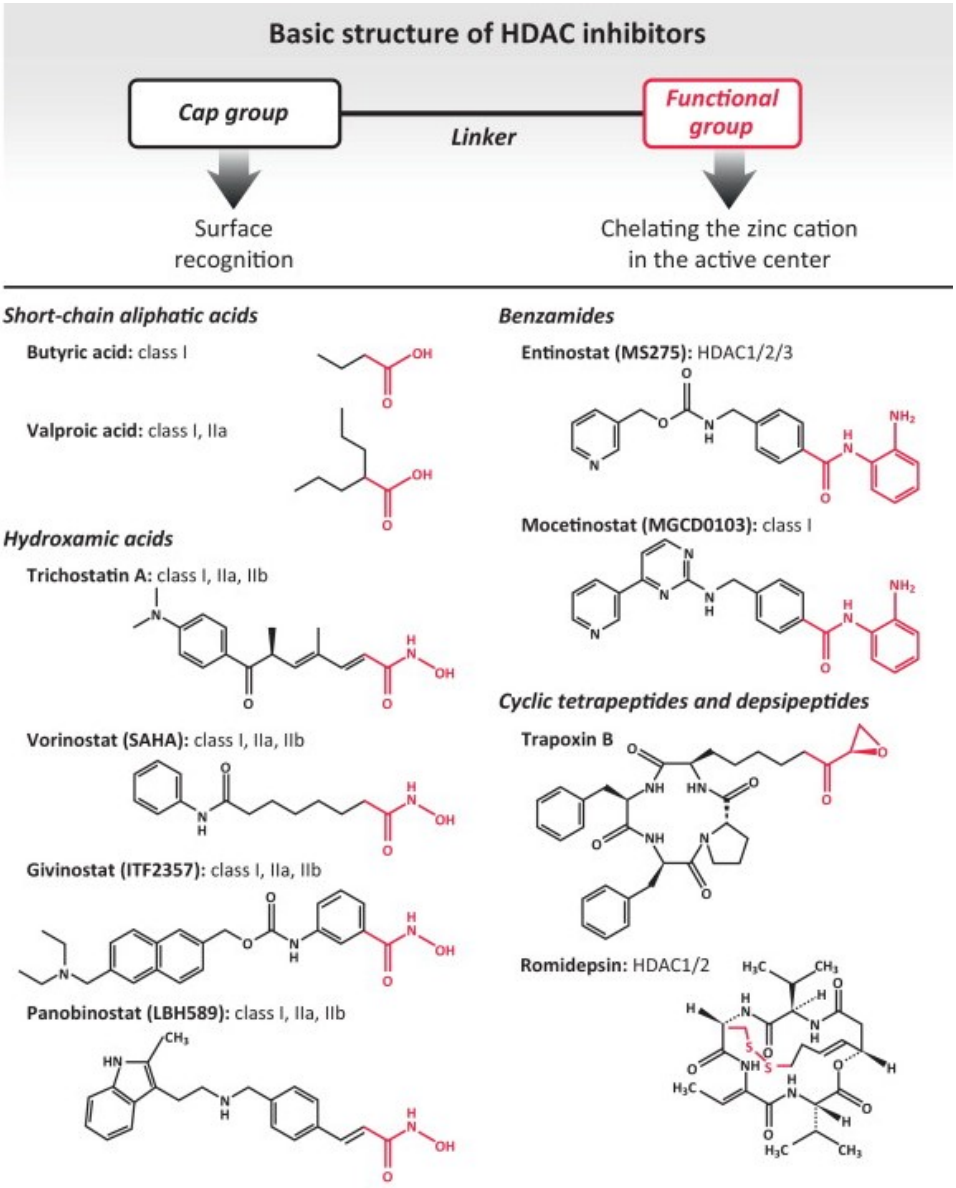

Figure 13: Structural properties of HDAC inhibitors.
The red moieties highlight the functional group responsible for classification (from Shirakawa, 2013).

Hydroxamates often target multiple HDACs (pan-HDACi) while benzamides are more selective for class I HDACs. Many of these derivatives directly target the catalytic site of the enzyme by chelating Zn^{2+} ions. Since HDACs are involved in many different pathways, inhibition of HDACs has severe impact on downstream mechanisms such as angiogenesis, cell cycle and apoptosis (Anne, 2013; Seto, 2014) (Figure 14). This could explain their cytotoxicity and antitumoral effects.

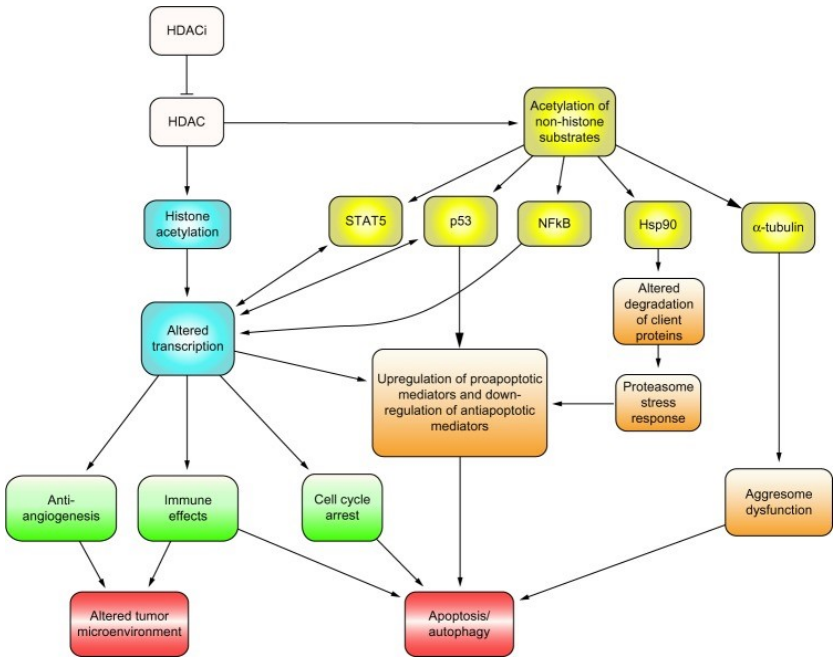

Figure 14: HDAC inhibition affects multiple essential cellular pathways.
HDACs are involved in many different pathways regulating transcription, cell cycle and apoptosis (from Anne, 2013).

HDACi treatment causes cell cycle arrest (Yamaguchi, 2010) and disrupts DNA repair in various ways including double-strand break stabilization, reduced expression of DNA repair factor and accumulation of reactive oxygen species (ROS) causing cellular stress and damage (Khan, 2008b). HDACi demonstrate a relative specificity in targeting cancer cells. In contrast to cancer cells, normal cells harbor multiple epigenetic regulatory mechanisms. Proper maintenance of a set of key genes required for survival and growth is mediated by HDACs, suggesting HDAC inhibition as promising vulnerability of cancer cells (Dawson, 2012). Mechanisms of anticancer effects of HDAC inhibitors are not uniform and may differ in the types of cancer, dependent on the individual HDAC inhibitor, its dose and/or some other factors to result in the divert phenotypes (Eckschlager, 2017). Over the last years, HDAC inhibitors became approved by the US *Food and Drug Administration* (FDA) and the *European Medicines Agency* (EMA) for application as anti-cancer agents. The pan-HDAC inhibitor vorinostat (SAHA; Merck; 2006) was the first HDACi approved by the FDA for the treatment of cutaneous T-cell lymphoma. Romidepsin (FK228; Celgene; 2009) was approved for cutaneous T-cell lymphoma (CTCL), belinostat (Beliodaq; Spectrum Pharmaceuticals; 2014) for peripheral T-cell lymphoma (PTCL), and panobinostat (LBH589, Farydak®; Novartis; 2015) for multiple myeloma (Singh, 2016). Up to now, there is no approved HDACi for pediatric application.

1.3.4 Panobinostat

Panobinostat (LBH589) is an orally bioavailable hydroxamic acid-derived pan-HDACi approved for treatment of multiple myeloma in 2015 and is one of the most promising HDACi in clinical trials. It is used in combination therapy with the proteasomal inhibitor bortezomib and dexamethasone in refractory or relapsed multiple myeloma and is under clinical investigation in various adult cancer entities including acute myeloid leukemia (NCT01242774), non-small cell lung cancer (NCT01336842), lymphoma (NCT00967044) and others (NIH, 2020). Few pediatric phase I and II studies are currently being investigated in pediatric leukemia (NCT01321346), glioma (NCT03566199) or Hodgkin's Lymphoma (NCT01169636) (NIH, 2020). In preclinical models of neuroblastoma, treatment with HDACi showed to induce differentiation, cell cycle arrest, apoptosis and arrested xenograft tumor growth (Deubzer, 2008; Kolbinger, 2018; Lodrini, 2013; Oehme, 2009b; Witt, 2009a). These promising reports give rise for future clinical application of HDACi in neuroblastoma therapy. Pan-HDACi inhibitor treatment is accompanied by a broad spectrum of side effects and a more defined therapy will contribute to reduce side effects of the treatment. Since inhibition of HDACs results in extensive changes in cancer cells expression profiles, identification of distinct vulnerabilities in neuroblastoma induced by HDACi treatment need to be further investigated.

1.4 Aims of the project

Treatment of high-risk neuroblastoma patients remains a challenge in pediatric oncology. Survival rates have not improved much during the last years for this group of patients. The recently identified sub-group of high-risk neuroblastoma patients carry *TERT* rearrangements resulting in high telomerase activity, which is considered as one of the hallmarks of cancer. A novel classification of neuroblastoma into telomere-maintaining and non-maintaining tumors underlines the importance of *TERT* and telomerase in neuroblastoma. Hence, there is an urgent clinical need for targeting *TERT*. Up to now, there are no clinically successful therapeutics targeting *TERT* or telomerase due to severe side effects of the therapy. An indirect targeting of *TERT* using HDAC inhibitors could circumvent limitations of current strategies and open up new application for epigenetic agents. As epigenetic modifications induced by HDAC inhibitors are pharmacologically reversible, they can serve as attractive targets for non-genotoxic treatment approaches. Panobinostat is an approved pan-HDAC inhibitor in adult cancer therapy. As it has demonstrated antitumoral efficacy in preclinical models of high-risk neuroblastoma, panobinostat could serve as a valuable therapeutic option for the *TERT*-rearranged neuroblastoma patients. The aims of this study were:

- Assess the potency of the small-molecule inhibitor panobinostat (LBH589, Farydak®) in preclinical model systems of *TERT*-rearranged neuroblastoma on *TERT* expression and telomerase activity.
- Define the antitumoral efficacy of panobinostat therapy in neuroblastoma cell lines and xenograft mouse models.
- Dissect the molecular pathways and regulatory networks of HDAC inhibition to gain a deeper understanding of the underlying mechanism on the regulation of *TERT*.
- Investigate potential combination treatment of panobinostat with the proteasomal inhibitor bortezomib in *TERT*-rearranged neuroblastoma models.

2 Materials

2.1 Organisms

Table 2: Organisms.

Microorganism	Name	Supplier
E.coli	X10GOLD	Agilent Technologies, Santa Clara, USA
Nude mice	NMRI-Foxn1$^{nu/nu}$, female	Janvier Labs, Le Genest-Saint-Isle, France

2.2 Cell lines

Table 3: Neuroblastoma cell lines.

Cell line	Identifier	Genotype			Source
GI-ME-N	RRID: CVCL_1232)	*TERT* rearrangement		1p del	DSMZ, Braunschweig, Germany
CLB-GA	RRID: CVCL_9529	*TERT* rearrangement	ALK^{R1275Q} mut	1p del	Matthias Fischer, Universitätsklinikum Köln, Germany
BE(2)-C	RRID: CVCL_V006	*MYCN* amplification		1p LOH	ECACC, Salisbury, UK
IMR-5/75	RRID: CVCL_M473	*MYCN* amplification			Matthias Fischer, Universitätsklinikum Köln, Germany
LAN-6	RRID: CVCL_1363				DSMZ, Braunschweig, Germany
SK-N-FI	RRID: CVCL_1702				Matthias Fischer, Universitätsklinikum Köln, Germany

2.3 Inhibitors

Table 4: Inhibitors.

Inhibitor	Synonym	Supplier
Actinomycin D		Sigma-Aldrich Chemie GmbH, Steinheim, Germany
BIBR1532		Biozol Diagnostica Vertrieb GmbH, Eching, Germany
Bortezomib		Selleck Chemicals, Houston, USA
Bufexamac		Selleck Chemicals, Houston, USA
Compound 2		Selleck Chemicals, Houston, USA
Costunolide		Biozol Diagnostica Vertrieb GmbH, Eching, Germany
Doxorubicin		Selleck Chemicals, Houston, USA
Entinostat	MS-275	Selleck Chemicals, Houston, USA
I-BET762		Selleck Chemicals, Houston, USA
Mocetinostat		Selleck Chemicals, Houston, USA
Oxaliplatin		Selleck Chemicals, Houston, USA
Panobinostat	LBH589	Selleck Chemicals, Houston, USA
Romidepsin		Selleck Chemicals, Houston, USA

Santacruzamate A		Biozol Diagnostica Vertrieb GmbH, Eching, Germany
Temozolomide		Selleck Chemicals, Houston, USA
Valproic acid		Selleck Chemicals, Houston, USA
Vorinostat	SAHA	Selleck Chemicals, Houston, USA
Z-VAD		Thermo Fisher Scientific, Waltham, USA

2.4 Reagents

Table 5: Chemicals and enzymes.

Chemical/Reagent	**Comments**	**Manufacturer**
Agarose	Biozym Scientific GmbH, Hessisch Oldendorf, Germany LE agarose	Biozym Scientific GmbH, Hessisch Oldendorf, Germany
Alkaline phosphatase Alkaline phosphatase buffer	rAPid Alkaline Phosphatase	Roche, Rotkreuz, Switzerland
Ammonium persulfate		Sigma-Aldrich Chemie GmbH, Steinheim, Germany
Ampicillin		Sigma-Aldrich Chemie GmbH, Steinheim, Germany
Bovine Serum Albumin	Fraction V	Carl Roth, Karlsruhe, Germany
Bradford reagent	Roti-Quant	Carl Roth, Karlsruhe, Germany
Chloramphenicol	34 mg/ml	Sigma-Aldrich Chemie GmbH, Steinheim, Germany
Crystal violet		Sigma-Aldrich Chemie GmbH, Steinheim, Germany
CutSmart buffer		New England BioLabs, Ipswich, Massachusetts, USA
dNTPs		Thermo Fisher Scientific, Waltham, USA
DMEM medium	DMEM (4.5g/l glucose) with 1 mM Na-pyruvate, 584 mg/l L-glutamine	Thermo Fisher Scientific, Waltham, USA
DMSO	>99.5% bioscience grade	Carl Roth, Karlsruhe, Germany
DNase		Qiagen, Venlo, The Netherlands
DNA ladder	GeneRuler™, 100 bp	Thermo Fisher Scientific, Waltham, USA
DNA ladder, 1 kb	GeneRuler 1kb DNA ladder	Thermo Fisher Scientific, Waltham, USA
DpnI		New England BioLabs, Ipswich, Massachusetts, USA
dNTP Mix	my-budget dNTP mix	Bio-Budget Technologies GmbH, Krefeld, Germany
Western Lightning Plus-ECL detection solution		Perkin Elmer, Waltham, USA
EcoRI		New England BioLabs, Ipswich, Massachusetts, USA
Effectene®	Transfection reagent	Qiagen, Venlo, The Netherlands
Ethanol		Carl Roth, Karlsruhe, Germany
Ethidium bromide	0.5% solution	Carl Roth, Karlsruhe, Germany

Fetal calf serum	Superior	Merck, Darmstadt, Germany
p-Formaldehyde	37%	Carl Roth, Karlsruhe, Germany
Formalin	4%	Th. Geyer, Renningen, Germany
Glucose		Sigma-Aldrich Chemie GmbH, Steinheim, Germany
Isopropanol		Carl Roth, Karlsruhe, Germany
LB	For molecular biology	Carl Roth, Karlsruhe, Germany
Lipofectamine™ RNAiMAX	Transfection reagent	Thermo Fisher Scientific, Waltham, USA
Lithium chloride		Sigma-Aldrich Chemie GmbH, Steinheim, Germany
Non-essential amino acids	100x	Biochrom, Berlin, Germany
Magnetic beads	SureBeads™, Protein A coupled	Bio-Rad, Hercules, USA
2-Mercaptoethanol		Sigma-Aldrich Chemie GmbH, Steinheim, Germany
Magnesiumdichloride		Merck, Darmstadt, Germany
Magnesiumsulfate		Sigma-Aldrich Chemie GmbH, Steinheim, Germany
Matrigel™	Basement membrane-like matrix, Phenol Red-Free	Corning Life Science, Tewksbury, USA
Milk powder	Skimmed milk powder	Carl Roth, Karlsruhe, Germany
Opti-MEM™ medium	Opti-MEM™ reduced medium, w/o HEPES; with L-Glutamine, w/o Phenol Red	Thermo Fisher Scientific, Waltham, USA
P1 buffer	Resuspension buffer for DNA purification	Qiagen, Venlo, The Netherlands
P2 buffer	Lysis buffer for DNA purification	Qiagen, Venlo, The Netherlands
P3 buffer	Neutralization buffer for DNA purification	Qiagen, Venlo, The Netherlands
Paraffin	Paraplast	Leica Biosystems, Leider Lane, USA
PEG 3000		Sigma-Aldrich Chemie GmbH, Steinheim, Germany
Phusion DNA polymerase Phusion HF buffer	Phusion Hot Start II High Fidelity DNA Polymerase	Thermo Fisher Scientific, Waltham, USA
Polyacrylamide		Carl Roth, Karlsruhe, Germany
Propidium iodide		Thermo Fisher Scientific, Waltham, USA
Protein Ladder	PageRuler™, 10-18 kDa	Thermo Fisher Scientific, Waltham, USA
Q5 DNA Polymerase Q5 buffer	Q5® High-Fidelity DNA Polymerase	New England BioLabs, Ipswich, Massachusetts, USA
RNase		Qiagen, Venlo, The Netherlands
RNase A		Thermo Fisher Scientific, Waltham, USA
RNase-free water		Qiagen, Venlo, The Netherlands
RPMI medium	RPMI Medium 1640, w/o HEPES; with L-Glutamine, Phenol Red	Thermo Fisher Scientific, Waltham, USA

Sodium acetate		Carl Roth, Karlsruhe, Germany
Sodiumchloride		Carl Roth, Karlsruhe, Germany
Sodiumdodecylsulfate		Carl Roth, Karlsruhe, Germany
SYBR green mastermix	Fast Start Essential Mastermix	Roche, Rotkreuz, Switzerland
T4 ligase T4 ligase buffer		New England BioLabs, Ipswich, Massachusetts, USA
Tetramethylethylendiamin		Sigma-Aldrich Chemie GmbH, Steinheim, Germany
Trypan Blue Solution	0.4%	Thermo Fisher Scientific, Waltham, USA
Trypsin	1x Trypsin, 0,05% EDTA, Phenol Red	Thermo Fisher Scientific, Waltham, USA
Tryptone		Sigma-Aldrich Chemie GmbH, Steinheim, Germany
Tween 20		Sigma-Aldrich Chemie GmbH, Steinheim, Germany
WST-1 reagent		Roche, Rotkreuz, Switzerland
XhoI		New England BioLabs, Ipswich, Massachusetts, USA
Xylene		VWR International, Radnor, USA
Yeast extract		Sigma-Aldrich Chemie GmbH, Steinheim, Germany

2.5 Expendable goods, laboratory equipment

Table 6: Expendable goods and general laboratory equipment.

Expendable good	**Comments**	**Supplier**
AFA® tubes	2 ml, for sample sonification	Covaris Inc, Woburn, USA
Assay tubes	Qubit™	Thermo Fisher Scientific, Waltham, USA
Beakers	200 ml, 500 ml	Schott AG, Mainz, Germany
Biopsy punch	5 mm diameter	Kai Industries Co., Ltd., Seki, Japan
Blades	X50 Blade MX35 Ultra LP	Thermo Fisher Scientific, Waltham, USA
Cell culture dish	10 cm, 15 cm	Corning Life Science, Tewksbury, USA®
Cell culture flasks	T25, T75, T175	Corning Life Science, Tewksbury, USA®
Cell scrapers		Sarstedt, Nümbrecht, Germany
Cryo Pure Tube	1.6 ml	Sarstedt, Nümbrecht, Germany
Embedding cassettes	40 x 28 x 6.8 mm	Carl Roth, Karlsruhe, Germany
FACS tubes	FACS-tubes Polystyrol, 6 ml, 12x75 mm	Corning Life Science, Tewksbury, USA
Corning Life Science, Tewksbury, USA™ Conical Centrifugation Tubes	*Falcon* tubes 15 ml, 50 ml	Corning Life Science, Tewksbury, USA
Glass bottles	100 ml, 200 ml, 500 ml, 1 l	Schott AG, Mainz, Germany
Microcentrifuge tubes	0.5 ml, 1.5 ml, 2 ml, 5 ml	Eppendorf, Hamburg, Germany Sarstedt, Nümbrecht, Germany

Mortar, Pestle		Waldenwanger, Berlin, Germany
Multiply®-µStrip 0.2ml chain		Sarstedt, Nümbrecht, Germany
Multiwell cell culture plates	6-, 96-well	Corning Life Science, Tewksbury, USA
Multiwell cell culture plates	16-well	ACEA Biosciences Inc., San Diego, USA
Neubauer cell counting chamber	0.0025 mm²	Carl Roth, Karlsruhe, Germany
Parafilm™ M Sealing Film	10 cm x 38 m	Bemis Company, Neenah, USA
PCR well plates FrameStar®	96-well Semi-Skirted PCR Plate 0.1 ml	4titude Limited, Surrey, UK
PCR plate seal	96-well,(140 x 77 mm	4titude Limited, Surrey, UK
PCR tube lids	8-lid chain	Sarstedt, Nümbrecht, Germany
Pipette filter tips SurPhob	10 µl, 100 µl, 1000 µl	Biozym Scientific GmbH, Hessisch Oldendorf, Germany
Pipette filter tips SurPhob SafeSeal	10 µl, 100 µl, 1000 µl	Biozym Scientific GmbH, Hessisch Oldendorf, Germany
Pipette filter tips ep Dualfilter T.I.P.S.®	5 ml	Eppendorf, Hamburg, Germany
Pipette tips Combitips advanced®	0.5 ml, 1 ml, 5 ml, 10 ml, 25 ml	Eppendorf, Hamburg, Germany
PVDF Membrane		Sigma-Aldrich Chemie GmbH, Steinheim, Germany
SafeSeal Microtubes	1.5 ml, 2 ml	Sarstedt, Nümbrecht, Germany
Scalpel Disposable, sterile	No. 11	Swann-Morton Ltd., Sheffield, UK
Serological pipettes	5 ml, 15 ml, 25 ml	Sarstedt, Nümbrecht, Germany Corning Life Science, Tewksbury, USA
Syringe with needle	Omnican 100 (30 G,0,3 mm x 12 mm)	Braun, Melsungen, Germany
Whatman Paper		GE Healthcare, Chalfont St Giles, UK

2.6 Antibodies

Table 7: Antibodies for western blot and ChIP sequencing.

Antibody	**Function**	**Cat. No.**	**Origin**	**Dilution**	**Supplier**
Anti-CASP3	Primary antibody	9662	Mouse	1:1000	Cell Signaling Technology, Cambridge, UK
Anti-GAPDH	Primary antibody	MAB374	Mouse	1:100,000-200,000	Merck, Darmstadt, Germany
Anti-HDAC1	Primary antibody	ab7028	Rabbit	1:10,000	Abcam PLC, Cambridge, UK
Anti-HDAC2	Primary antibody	sc-81599	Mouse	1:10,000	Santa Cruz Biotechnology Inc., Dallas, USA
Anti-PARP1	Primary antibody	9542S	Rabbit	1:1000	Cell Signaling Technology, Cambridge, UK
Anti-TERT	Primary antibody	ab183105	Rabbit	1:2000	Abcam PLC, Cambridge, UK
Anti-rabbit IgG	Secondary antibody	111-035-003	Goat	1:5000	Dianova GmbH, Hamburg, Germany
Anti-mouse IgG	Secondary antibody	115-035-003	Goat	1:5000	Dianova GmbH, Hamburg, Germany

Anti-$H_3K_4Me_1$	ChIP antibody	ab8895	Rabbit	1 µg / Mio. cells	Abcam PLC, Cambridge, UK
Anti-$H_3K_4Me_3$	ChIP antibody	ab8580	Rabbit	1 µg / Mio. cells	Abcam PLC, Cambridge, UK
Anti-$H_3K_{27}Ac$	ChIP antibody	ab4729	Rabbit	1 µg / Mio. cells	Abcam PLC, Cambridge,UK
Anti-$H_3K_{36}Me_3$	ChIP antibody	ab9050	Rabbit	1 µg / Mio. cells	Abcam PLC, Cambridge, UK
Anti-$H_3K_9Me_3$	ChIP antibody	ab8898	Rabbit	1 µg / Mio. cells	Abcam PLC, Cambridge, UK
Anti-$H_3K_{27}Me_3$	ChIP antibody	39155	Rabbit	1 µg / Mio. cells	Active Motif Inc, Carlsbad, USA

2.7 Buffers

Table 8: Composition of buffers.

Buffer	**Composition**
Blocking Buffer BSA	30.3 g 1 M Tris, 3 g BSA powder in 50 ml BST-T
Blocking Buffer Milk	30.3 g 1 M Tris, 5 g low fat milk powder in 50 ml BST-T
ChIP dilution buffer	100 µl 20% SDS, 2.2ml Triton X-100, 480 µl 0.5 M EDTA pH=8.0, 3.34 ml 1 M Tris-HCl pH=8.1, 6.68 ml 5 M NaCl, ad 200 ml ddH_2O, autoclave
Complete protease inhibitor	1 tablet of cOmplete® to 2 ml PBS
EDTA buffer 0.5 M	14.6 g EDTA in 100 ml ddH_2O, pH adjusted to 8.0 with 40% NaOH
High salt immune complex wash buffer	1 ml 20% SDS, 2 ml Triton X-100, 800 µl 0.5 M EDTA pH=8.0, 4 ml 1 M Tris-HCl pH=8.1, 20 ml 5 M NaCl, ad 200 ml ddH_2O, autoclave
Laemmli buffer 2x for western blot	12.5 ml 0.5 M Tirs-HCl pH=6.5, 5 ml 20% SDS, 5 ml glycerol, 2.5 ml 2-mercaptoethanol, 1 spatula's tip of bromophenol blue
LB agar	35 g LB, 10 g NaCl, 10 g tryptone and 5 g yeast extract in 1 l ddH_2O, add 20 g Agar, autoclave
LB medium	35 g LB in 1 l ddH_2O, autoclave
LiCl immune complex washing buffer	50 ml 1 M LiCl, 2 ml NP40, 2.12 g (Na)Deoxycholate, 400 µl 0.5 M EDTA pH=8.0, 2 ml 1 M Tris-HCl pH=8.1, ad 200 ml ddH_2O, autoclave
Low salt immune complex wash buffer	1 ml 20% SDS, 2 ml Triton X-100, 800 µl 0.5 M EDTA pH=8.0, 4 ml 1 M Tris-HCl pH=8.1, 6 ml 5 M NaCl, ad 200 ml ddH_2O, autoclave
Lysis buffer for western blot	1 ml 1 M Tris-HCl pH=8.5, 21 g urea, 0.5 ml Triton X-100, 5 ml 1 M DTT, 2 ml 1 M $MgCl_2$, 2 tablets cOmplete® protease inhibitor cocktail, ad 50 ml ddH_2O
PBS	80.0 g NaCl, 11.6 g Na_2HPO_4, 2 g KH_2PO_4 and 2 g KCl in 10 l ddH_2O, pH adjusted to 7.0 with acetic acid
SDS 20%	20 g SDS, ad 100 ml ddH_2O
SDS-Lysis Buffer	10 ml 20% SDS, 4 ml 0.5 M EDTA pH=8.0, 10 ml 1 M Tris-HCl pH=8.1, ad 200 ml ddH_2O, autoclave
SDS-Running buffer 10x (SDS-PAGE)	30.3 g Tris, 144 g Glycine and 50 ml 20% SDS (w/w) in 1 l ddH2O
SDS-Transferbuffer 10x (SDS-PAGE)	30.3g Tris and 144 g Glycine in 1 l ddH_2O
Separation gel buffer (SDS-PAGE)	45.4 g 1.5 M Tris in 250ml ddH_2O, pH adjusted to 8.8
Separation gel 10% (SDS-PAGE)	4 ml ddH_2O, 3.3 ml 30% Polyacrylamide, 2.5 ml 1.5 M Tris (pH 8.8), 0.1 ml 10% SDS, 0.1 ml 10% APS and 0.004 ml TEMED
SOC medium	20 g tryptone, 5 g yeast extract, 0.5 g NaCl, 10 ml 1M $MgCl_2$, 10 ml 1 M $MgSO_4$ and 20 ml 20 % glucose in 1 l ddH_2O
Stacking gel buffer (SDS-PAGE)	30.3 g 1.5 M Tris-HCl in 250ml ddH_2O, pH adjusted to 6.8

Stacking gel (SDS-PAGE)	3.4 ml ddH_2O, 0.83 ml 30 % Polyacrylamide, 0.63 ml 1.5 M Tris pH=8.8, 0.05 ml 10% SDS, 0.05 ml 10 % APS and 0.005 ml TEMED
TAE buffer 50x	242.28 g Trizma-base, 59 ml glacial acetic acid, 100 ml 0.5 M EDTA in 1 l ddH_2O
TBS buffer 10x	60.6 g Tris, 87.6 g NaCl in 1 l ddH_2O, pH adjusted to 7.6
T-BST buffer 1x	100 ml 10x TBS-Buffer, 1 ml Tween-20 in 900 ml ddH_2O
TE buffer for ChIP	400 µl 0.5 M EDTA pH=8.0, 2 ml 1 M Tris-HCl pH=8.1, ad 200 ml ddH_2O, autoclave
TE buffer 1x	10 ml 1 M Tris HCl pH 7.4, 2 ml EDTA buffer pH=8.0 in 1 l ddH_2O
Versene	2 ml 0.5 EDTA pH=8.0, ad 1 l ddH_2O, pH adjusted to 7 with HCl
Transfer buffer western blot 10x	30.3 g Trizma-base, 144 g Glycine, ad 1000 mL ddH_2O, add 20% MeOH prior to use
Tris-HCl buffer 1M	121.14 g Trizma-base in 1 l ddH_2O, pH adjusted to 8.1 or 6.5 with HCl

2.8 Kits

Table 9: Kits.

Kit	**Supplier**
CellTiter-Glo® Luminescent Cell Viability Assay	Promega, Madison, Wisconsin, USA
First-Strand cDNA Synthesis Kit	Thermo Fisher Scientific, Waltham, USA
Ligation Sequencing Kit	Oxford Nanopore Technologies Ltd., UK
MagAttract HMW DNA Kit	Qiagen, Venlo, The Netherlands
NucleoBond®Xtra Maxi kit	Macherey-Nagel, Düren, Germany
QIAamp DNA Mini Kit	Qiagen, Venlo, The Netherlands
QIAquick® Gel Extraction Kit	Qiagen, Venlo, The Netherlands
QIAquick® PCR Purification Kit	Qiagen, Venlo, The Netherlands
QIAprep® Spin Miniprep Kit	Qiagen, Venlo, The Netherlands
Qubit™ dsDNA HS assay kit	Thermo Fisher Scientific, Waltham, USA
RNeasy Mini Kit	Qiagen, Venlo, The Netherlands
T4 DNA ligation kit	New England BioLabs, Ipswich, Massachusetts, USA
TeloTAGGG™ Telomerase PCR ELISA Plus	Roche, Rotkreuz, Switzerland

2.9 Nucleic acids

2.9.1 Small interfering RNAs

Table 10: Small interfering RNAs.

Target	Comment	Cat. No.	Supplier
Negative control	siTOOLS negative control pool siRNA		siTOOLs Biotech GmbH, Planegg, Germany
HDAC1	siTOOLS pool siRNA HDAC1	3065	siTOOLs Biotech GmbH, Planegg, Germany
HDAC2	siTOOLS pool siRNA HDAC2	3066	siTOOLs Biotech GmbH, Planegg, Germany

2.9.2 Oligonucleotides

Table 11: Oligonucleotide primer applied in qRT-PCR analysis.

Gene	Forward 5'-3'	Reverse 5'-3'	Ref./ Supplier
Bleyplaby	CAGGATGGAGTAGCAGAGGG	CCTCTCAGGTTTCACGCATG	
HDAC1	TGACGAGTCCTATGAGGCCATT	CCGCACTAGGCTGGAACATC	Oehme, 2009b
HDAC2	TGTGAGATTCCCAATGAGTTGC	GGTAACATGCGCAAATTTTCAA	Oehme, 2009b
HRPT	TGACACTGGCAAAACAATGCA	GGTCCTTTTCACCAGCAAGCT	Fischer, 2005
KIF2C	GATCTATGCCATGGCCTCCC	CAGAACCTGTCCCAGCTCAG	
MYCN	CCACGTCCGCTCAAGAGTGT	CCCTGAGCGTGAGAAAGCTG	Thole, 2020
RPS18	GAGGATGAGGTGGAACGTGT	TCTTCAGTCGCTCCAGGTCT	Thole, 2017
SDHA	TGGGAACAAGAGGGCATCTG	CCACCACTGCATCAAATTCATG	Fischer, 2005
TERT	GTCTGGAGCAAGTTGCAAAG	CGATGCTGCCTGACCTCT	
QuantiTect Primer Assays Qiagen (Hilden, Germany)			
ASF1B			QT00007224
AURKB			QT00067403
CCNA2			QT00014798
CDC25A			QT00001078
CENPM			QT00044499
GINS2			QT00068208
RRM2			QT00039480
TK1			QT00083874

Table 12: Oligonucleotides applied in gene technology.

Gene	Forward 5'-3'	Reverse 5'-3'	Ref./ Supplier
pBABE5'	CTTTATCCAGCCCTCAC		GATC
TERT Sequencing Primer 1	CTGGTGGCTCCCAGCTGCGC		
TERT Sequencing Primer 2	TTCCAGGCCCTGGATGCCAG		

TERT Sequencing Primer 3	TACCTTGACAGACCTCCAGC		
TERT Sequencing Primer 4		ACACCTGGTTGCTGACTAAT	
TERT Mutagenesis primer leading strand	GCCAAGCGCAGTCCCGCACGCTC		
TERT Mutagenesis primer lagging strand	GAGCGTGCGGGACTGCGCTTGGC		
*TERT*_EcoRI Mutagenesis primer	CCTTTATCCAGCCCTCACTC		
*TERT*_XhoI Mutagenesis primer		CACGCTGAACAGTGCCTTC	
TERT Mutation site	GAGCGTGCGGGACTGCGCTTGGC TGCG	GCCAAGCGCAGtCCCGCACG CTCATCTTC	

Table 13: Oligonucleotide primers applied in ChIP-PCR.

Gene	**Forward 5'-3'**	**Reverse 5'-3'**	**Ref./Supplier**
MIR183	CGTAGGGCCACTGGACGA	TTGTCCCCATTCCAGCCCTG	Lodrini, 2013
GRHL1	AGAAGGGACATTCCGGAGAC	GTCTCACCTCTCGGTTCTCG	Fabian, 2014

2.9.3 Plasmids

Table 14: Plasmids.

Plasmid	**Name**	**Selection marker**	**Source**
TERT	pBABE-neo-hTERT, Addgene ID 1774	Ampicillin	Plasmid was a gift from Anton Henssen, Bob Weinberg (Counter, 1998)
Empty vector	pBABE-neo, Addgene ID 1767	Ampicillin	Plasmid was a gift from Anton Henssen, Bob Weinberg (Counter, 1998)

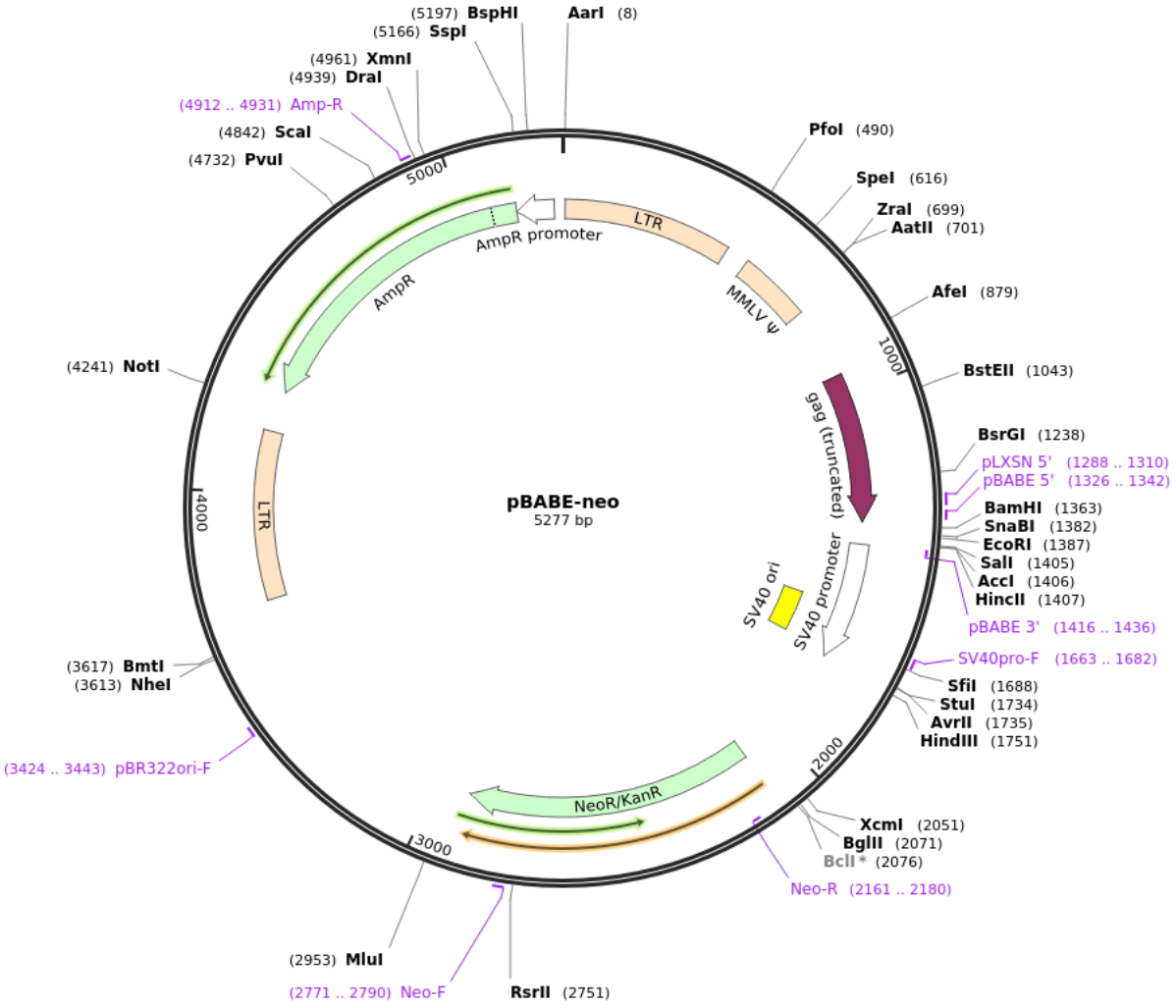

Figure 15: Vector map of pBABE-neo plasmid.
Created with SnapGene.

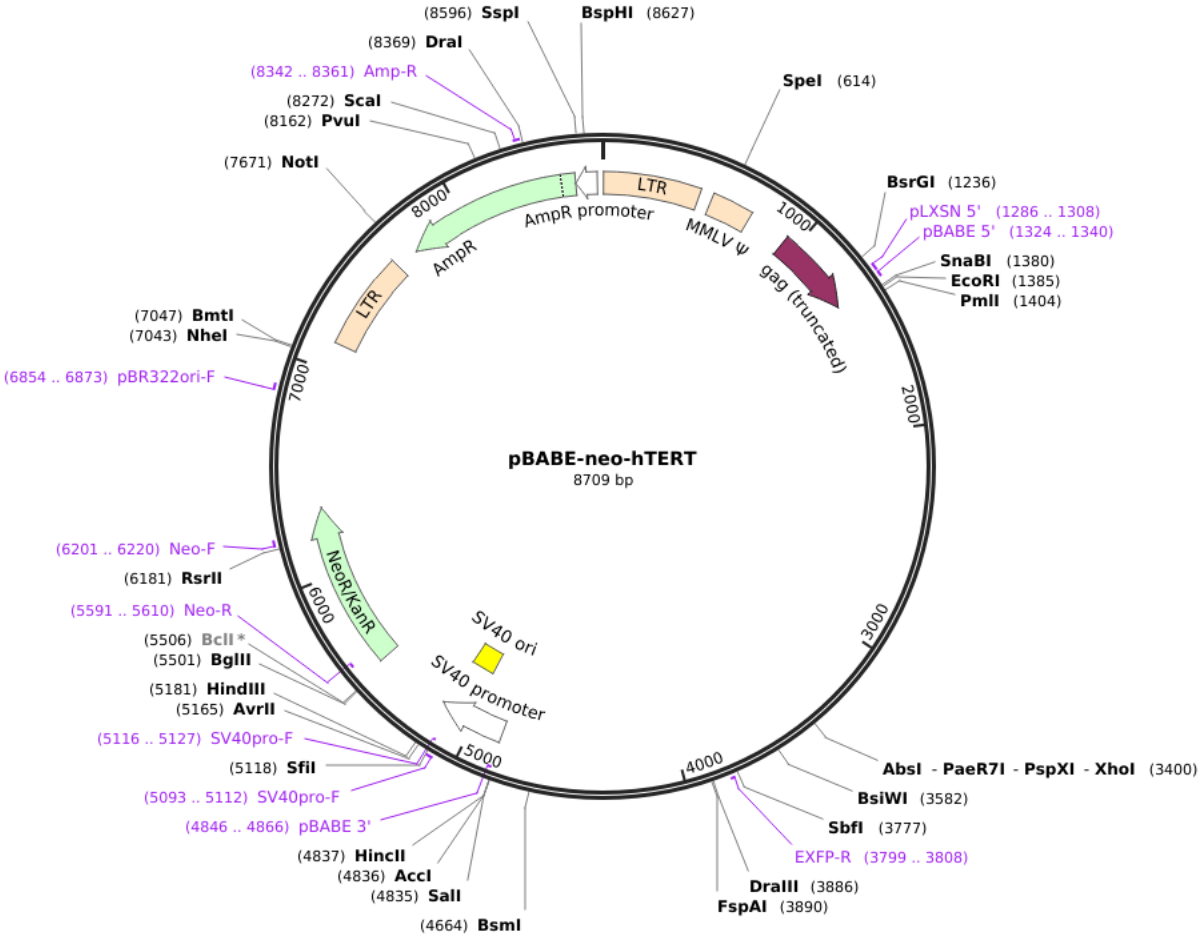

Figure 16: Vector map of pBABE-neo-hTERT plasmid.
Created with SnapGene.

2.10 Instruments

Table 15: Technical laboratory equipment.

Device	Comments	Manufacturer
Bio Photometer	Spectrophotometer	Eppendorf, Hamburg, Germany
Centrifuge 5415 D		Eppendorf, Hamburg, Germany
Centrifuge 5424		Eppendorf, Hamburg, Germany
Centrifuge 5810 R		Eppendorf, Hamburg, Germany
Centrifuge Heraeus Biofuge Primo R		Thermo Fisher Scientific, Waltham, USA
Centrifuge Megafuge 1.0R		Thermo Fisher Scientific, Waltham, USA
Centrifuge Mini Star silverline		VWR International, Radnor, USA
Centrifuge PerfectSpin Mini		PEQLAB, Erlangen, Germany
Centrifuge Rotina 46		Gemini BV, Apeldoorn, The Netherlands
Centrifuge Sorvall LYNX 4000	Used with the F14-6x250y rotor	Thermo Fisher Scientific, Waltham, USA
Centrifuge Universal 320 R		Andreas Hettich GmbH & Co. KG, Tuttlingen, Germany

Covaris Inc, Woburn, USA S220	Ultra sonicator	Covaris Inc, Woburn, USA
Doc-Print VX5	Gel documentation system	VWR INTERNATIONAL, RADNOR, USA
Cryostat	CryoStar™ NX70 Cryostat	Thermo Fisher Scientific, Waltham, USA
Epoch	Spectrophotometer	BioTek Instruments Inc., Vinooski, USA
Electrophoresis chamber vertical	Mini-PROTEAN® Series, for western blot	Bio-Rad, Hercules, USA
Electrophoresis chamber horizontal	Wide Mini-Sub Cell GT Systems, for DNA	Bio-Rad, Hercules, USA
Flow Cytometer LSR-Fortessa X-20		Becton, Dickinson and Company, BD Biosciences, San Jose, USA
Fridge FKUv 1610 Index 21J/001	4°C	Liebherr, Bulle FR, Switzerland
Freezer LCv4010eez	-20°C	Carl Roth, Karlsruhe, Germany
Freezer LKexv 3910	-4°C	Carl Roth, Karlsruhe, Germany
Freezer HeraFreeze T series HFU400TV63	-80°C	Thermo Fisher Scientific, Waltham, USA
Hybridization oven	6/12 V	UniEquip, Martinsried, Germany
Ice machine AF80		Scotsman, Vernon Hills, USA
Incubator HERATHERM	For bacteria plates and digests	Thermo Fisher Scientific, Waltham, USA
Incubator HERAcell240i	CO_2 Incubator for cell culture	Thermo Fisher Scientific, Waltham, USA
Incubator HERAcell2 Midi40	CO_2 Incubator for cell culture	Thermo Fisher Scientific, Waltham, USA
Magnetic rack	24 tubes	Bio-Rad, Hercules, USA
Microscope Axiovert A1		Carl Zeiss, Oberkochen, Germany
Microscope Axiovert 40 CFL		Carl Zeiss, Oberkochen, Germany
Microwave	800 W	Severin Elektro, Sundern, Germany
MinION flowcell	R9.4.1 FLO-MIN106	Oxford Nanopore Technologies Ltd., UK
Mini Trans-Blot®	Wet/Tank blot transfer system	Bio-Rad, Hercules, USA
NanoDrop 2000	Spectrophotometer	Thermo Fisher Scientific, Waltham, USA
Nitrogen tank Arpege 100		VWR INTERNATIONAL, RADNOR, USA International
PCR cycler C100 Touch™ Thermal Cycler		Bio-Rad, Hercules, USA
Pipettes Research (Plus)	0.5-2.5 µl, 1-10 µl, 10-100 µl, 100-1000 µl	Eppendorf, Hamburg, Germany
Pipette Multipette® E3	1 µl – 50 ml	Eppendorf, Hamburg, Germany
Pipettor		Hirschmann Laborgeräte GmbH & Co. KG, Eberstadt, Germany
PowerPac™ Basic	Electrophoresis power supply	Bio-Rad, Hercules, USA
qPCR Cycler	StepOne Plus	Thermo Fisher Scientific, Waltham, USA
qPCR Cycler	Quant Studio 3	Thermo Fisher Scientific, Waltham, USA
Quantum ST5	Gel documentation system	Vilber Lourmat, Marne-la-Vallée, France
Qubit 2.0 Qubit 3.0	Fluorometer	Thermo Fisher Scientific, Waltham, USA
Rotator	SB3	Cole-Parmer, Staffordshire, UK
Safety cabinet Safe 2020	Laminar airflow bench	Thermo Fisher Scientific, Waltham, USA
Scale Kern EW		Kern & Sohn GmbH, Balingen, Germany
Scanner	Epson Perfection V700 Photo	Seiko Epson Corporation, Suwa, Japan
Tapestation 4200	Automated electrophoresis tool	Agilent Technologies, Santa Clara, USA
Trans-Blot Turbo	Semi-dry transfer system	Bio-Rad, Hercules, USA
Shaker G24 Environmental Incubator		New Brunswick Scientific Co., Inc., Enfield, USA
Shaker innova™ 4300 incubator		New Brunswick Scientific Co., Inc., Enfield, USA
Shaker KS 4000 I control		IKA®-Werke GmbH & CO. KG, Staufen, Germany

Suction pump AC02		Carl Roth, Karlsruhe, Germany
ThermoMixer C	For 1.5 or 2 ml tubes	Eppendorf, Hamburg, Germany
Vi-CELL™ XR	Automated cell counting system	BeckmanCoulter, Brea, USA
Vortexer Minishaker MS1		IKA®-Werke GmbH & CO. KG, Staufen, Germany
Vortexer Reax top		Heidolph Instruments, Schwabach, Germany
Waterbath GFL 1086		GFL Gesellschaft für Labortechnik mbH, Burgwedel, Germany
Waterbath WNB 7		Memmert GmbH & Co. KG, Schwabach, Germany
xCelligence™	Real-time cell impedance analyzer	ACEA Biosciences Inc., San Diego, USA

2.11 Software

Table 16: Software.

Name	**Source**
ApE – A plasmid editor v2.0.47	M. Wayne Davis, University of Utah, USA
Endnote X8	Clarivate Analytics, Philadelphia, USA
Epson Scan v 5.1.1f2	Seiko Epson Corporation, Suwa, Japan
FlowJo v10.2	Becton, Dickinson and Company, BD Biosciences, San Jose, USA
Gen5 v2.04	BioTek Instruments Inc., Vinooski, USA
GraphPad Prism v7	GraphPad Software Inc., San Diego, USA
Integrative genome viewer v2.6.3.	Broad Institute and the Regents of the University of California, San Diego, USA
ImageJ v1.48	National Institutes of Health, Bethesda, USA
Microsoft Office 2016	Microsoft Corporation, Redmond, USA
QuantStudio v1.5.1	Thermo Fisher Scientific, Waltham, USA
RTCA v1.0.0.0134	ACEA Biosciences Inc., San Diego, USA
SnapGene v5.0.7	GSL Biotech LLC, Chicago, USA
StepOne Software v2.3	Thermo Fisher Scientific, Waltham, USA
Synergyfinder (https://synergyfinder.fimm.fi)	Institute for Molecular Medicine Finland (FIMM), University of Helsinki, Finland
VisionCapt v16,11a	Vilber-Lourmat, Marne-la-Vallée, France

3 Methods

3.1 Animal experiments

Animals (RRID: MGI:5653040) were purchased from Janvier Labs, France, and housed in a pathogen-free animal facility. For xenograft inoculation, 5-20x10^6 tumor cells were suspended in 100 µl Matrigel™ (Corning Life Science, USA) and injected subcutaneous into the right flank of 8-week-old female athymic nude mice (NMRI-Foxn1$^{nu/nu}$). Tumor size was measured daily using a caliper and tumor volume was calculated by tumor volume = π/6 (d1 x d2 x d3) where d1 is the largest and d3 the smallest tumor diameter. Animals were randomized when tumor sizes reached about 150 mm³ (preventive treatment schedule) or 300 mm³ (therapeutic treatment schedule). Animals were treated with 7.5-15 mg/kg/d panobinostat or solvent (each dissolved in 5% glucose in water) by intraperitoneal injection 5 d/week starting at randomization. Special wet food was offered to animals from onset of treatment to counteract potential bodyweight loss under treatment. Animal handling and care conformed to national and EU regulatory standards in accordance with the "Guidelines for accommodation and care of laboratory animals" by the Council of Europe and by the *Forschungseinrichtungen für Experimentelle Medizin*, *Charité Universitätsmedizin Berlin*. Experiments were approved by the local institutional ethics commission for animal experimentation *Landesamt für Gesundheit und Soziales Berlin*.

Combination therapy experiments were performed by the company EPO (*Experimental Pharmacology & Oncology*, Berlin). In total, 18 x10^6 CLB-GA cells were suspended in 100 µl Matrigel™ (Corning Life Science, USA) and injected subcutaneous into the right flank of 8-week-old female athymic nude mice (NMRI-Foxn1$^{nu/nu}$). Tumor size was daily measured using a caliper, and tumor volumes were calculated by tumor volume = π/6 (d1 x d2 x d3) where d1 was the largest and d3 the smallest tumor diameter. Animals were randomized when tumor sizes reached 100 mm³. Animals were treated with 15 mg/kg/d panobinostat or solvent (each dissolved in 5% glucose in water) by intraperitoneal injection 5 d/week and/or with 0.5 mg/kg/d bortezomib or solvent (0.9% sodium chloride) by intravenous injection 3 d/week starting at randomization. Special wet food was offered to animals from onset of treatment to counteract potential bodyweight loss under treatment. Animal handling and care conformed to national and EU regulatory standards and experiments were approved by *Landesamt für Gesundheit und Soziales Berlin*.

3.2 Methods in mammalian cell culture

3.2.1 Cultivation of cells

The neuroblastoma cell lines GI-ME-N (RRID: CVCL_1232), CLB-GA (RRID: CVCL_9529), BE(2)-C (RRID: CVCL_V006), IMR-5/75 (RRID: CVCL_M473), LAN-6 (DSMZ Cat# ACC-674, RRID: CVCL_1363) and SK-N-FI (ICLC Cat# HTL97020, RRID: CVCL_1702) representing different neuroblastoma risk groups were used in this study. The GI-ME-N and LAN-6 cell lines were purchased from the *Deutsche Sammlung für Mikroorganismen und Zellkulturen* (DSMZ, Germany). The CLB-GA, IMR-5/75 and SK-N-FI cell lines were kindly provided by Matthias Fischer, *Kinderkrankenhaus der Universität Köln*, Germany. The BE(2)-C cell line was purchased from the *European Collection of Authenticated Cell Cultures* (ECACC, UK). Identity of cell lines was checked at least once a year using the cell authentication services of *Multiplexion* (Germany) or the *Deutsche Sammlung von Mikroorganismen und Zellkulturen* (DSMZ, Germany) applying single nucleotide polymorphism (SNP)-typing. GI-ME-N, IMR-5/75 and SK-N-FI cells were cultured in RPMI cell culture medium, CLB-GA, LAN-6 and BE(2)-C cells were cultured in DMEM cell culture medium cultivated at 37°C in a humidified atmosphere of 5% CO_2. Media were supplemented with 10% FCS and 1% non-essential amino acids. For the LAN-6 cells, 20% FCS was added to cell culture media. Percentage of FCS supplementation was adjusted to 10% few days prior to experimental use of LAN-6 cells. For each count, 10 µl of cell suspension was mixed with 10 µl trypan blue (0.4%) vital cell stain and a volume of 10 µl of the mixture was applied to a Neubauer cell counting chamber. Four quadrants were counted for each cell suspension and vital cell number was calculated according to formula:

*Number of vital cells per ml = (number of counted cells / 4) * dilution factor*

Cell number counts for treatment experiments were performed using the Vi-Cell™ XR cell viability analyzer for automated trypan blue stained cell counting (Beckman Coulter, USA).

3.2.2 Infection and contamination control

Cells were regularly monitored for mycoplasma infection using the HEK-Blue™-2 Mycoplasma Sensor Cell-based Plasmo Test™ (Invivogen, USA). Conditioned medium was

heated at 100°C for 15 min according to the manufacturers intruction. A volume of 50 µl was added to a 96-well plate always including supplied positive and negative controls. The HEK-Blue™ cell suspension was mixed with prewarmed detection medium and added to a total volume of 200µl to each well. The plate was incubated at 37°C and 5% CO_2 in an incubator overnight. The presence of mycoplasma was detected with the Epoch™ spectrophotometer (BioTek, USA) at 620-655 nm. Mycoplasma screenings were performed by Jasmin Wünschel.

3.2.3 Inhibitors

Panobinostat, vorinostat, entinostat, bufexamac, compound 2, romidepsin, doxorubicin, oxaliplatin, temozolomide and I-BET762 were purchased from Selleck Chemicals, USA, and Z-VAD (Thermo Fisher Scientific, USA), actinomycin D (Sigma-Aldrich, Germany), Santacruzamate A, BIBR1532 and costunolide (Biozol, Germany) were prepared as stock solutions in dimethyl sulfoxide (DMSO). A complete list of all used chemicals for this study is to be found in section 2.3, Table 4.

3.2.4 Plasmid transfection

Transient transfection of GI-ME-N cells was performed using the plasmids pBABE-neo for empty vector transfection and pBABE-neo-hTERT to obtain high-expressing *TERT* cells. Plasmids were kindly provided by Anton Henssen, *Charité Universitätsmedizin Berlin*, Germany. Cells were seeded 24 h prior to transfection to 10 cm cell culture dishes in 10 ml cell culture medium. The transfection was performed using the Effectene® transfection reagent (Qiagen, The Netherlands) following the manufacturers protocol. Cell culture medium was reduced to 3 ml per 10 cm plate. The transfection mixture was prepared as followed: 200 µl EC buffer, 1 µg plasmid DNA and 4 µl Enhancer were mixed and incubated for 5 min at room temperature. A volume of 15 µl Effectene® transfection reagent was added and incubated for 30 min at room temperature. Subsequently, solution was mixed with 1000 µl Opti-MEM™ reduced serum medium (Thermo Fisher Scientific, USA) and was added dropwise to cells. After 24 h incubation, the medium was replaced with 10 ml fresh cell culture medium. Transfection efficacy was measured via *TERT* mRNA expression analysis using qRT-PCR.

3.2.5 Transfection with pooled small interfering RNA

Transient small interfering (si)RNA-mediated knockdown of HDACs was performed in GI-ME-N cells to silence target RNA processing. Cells were seeded 24 h prior to transfection

in 10 cm cell culture dishes in 10 ml cell culture medium. The transfection was performed using the Lipofectamine™ RNAiMAX transfection reagent (Thermo Fisher Scientific, USA) following an optimized manufacturers protocol. Mock and a pooled siRNA negative control were included in each experiment. Cell culture medium was reduced to 2 ml per 10 cm plate. The transfection mixture was prepared as followed: 20 µl transfection reagent and 980 µl Opti-MEM™ reduced serum medium were mixed in a reaction tube. In a separate reaction tube, 40 µl of pooled siRNA (20 nM) and 960 µl Opti-MEM™ reduced serum medium were mixed. Both mixtures were united and incubated for 5 min at room temperature. Subsequently, the suspension was added dropwise to cells. After 24 h incubation, the medium was replaced with 10 ml fresh cell culture medium. RNA expression was measured using quantitative real-time polymerase chain reaction (qRT-PCR).

3.2.6 Cell viability assays

Automated trypan blue cell counting:

The number of dead cells was quantified using trypan blue staining and automated cell counting. Cell viability was quantified using the Vi-CELL^{TM} XR Cell Viability Analyzer (Beckman Coulter, USA). Cells were seeded to 6-well plates or 10 cm cell culture dishes (Table 17). Optional transfection of cells was performed 24 h after seeding according to section 3.2.4. After 24 h incubation, cells were treated for 72 h before they were harvested for cell count. To harvest the cells, first the supernatant was transferred into a 15 ml *Falcon* tube, centrifuged for 4 min at 300 *x g* and supernatant was removed. The remaining cell pellet was united with the adherent cells harvested with 1 ml trypsin (0.05%) and 5 ml medium. The cells were centrifuged again, the supernatant was removed and the cell pellet was washed with 3 ml PBS. The centrifuged cell pellet was resuspended in 1 ml cell culture medium and cell number was measured with the Vi-CELL™ XR for automated cell counting.

Table 17: Cell numbers for automated trypan-blue cell counting.

Cell line	Cell number 6-well plate	Cell number 10 cm cell culture dish
GI-ME-N	20,000	150,000
CLB-GA	80,000	500,000

Semi-automated medium throughput screening:

Drug screenings in 2D and 3D cell cultures were performed in a semi-automated system by the company CPO (*Cellular Phenomics & Oncology*, Berlin). For the 2D drug screening, 1,000 GI-ME-N and 7,500 CLB-GA cells were seeded to each well of a 384-well plate and were incubated 24 h before treatment was applied. Read-out was performed after 72 h in a 6-point curve using the CellTiter-Glo® Luminescent Cell Viability Assay (Promega, USA). For the 3D cell culture model, 1,000 GI-ME-N and 10,000 CLB-GA cells were suspended in Matrigel™ and seeded to a 384-well plate. Small organoids were grown in well plates and showed similar proliferation as in the 2D models. After several days of pre-culture, treatment was applied for 72 h and read-out was performed using the CellTiter-Glo® Luminescent Cell Viability Assay.

Impedance real-time measurements:

Impedance was measured in panobinostat treated GI-ME-N, LAN-6 and IMR-5/75 cells using the real-time cell impedance analyzer xCelligence™ (ACEA Biosciences Inc., USA). Growth behavior of adherent cells can be correlated with continuously measured impedance of cell culture medium towards a microelectrode sensor. A weak electronic current was applied and impedance was measured every 15 min. A number of 10,000 GI-ME-N cells, 15,000 IMR-5/75 and 60,000 LAN-6 were seeded in 200 µl cell culture medium to 16-well plates and cultured for 24 h before treatment was applied for several days. At latest after 72 h, treatment was refreshed to ensure stable drug concentration over the time-course. Cell proliferation curves were analyzed using the RTCA software 1.0.0.0134.

3.2.7 Colony formation assay

Anchorage-dependent ability of cancer cells to form colonies from single cell levels is considered as one of the hallmarks of cancer and can be quantified with the colony formation assay (Menyhárt, 2016). Cells were seeded to 6-well plates in 3 ml medium 24 h before treatment. Treatment was applied and cells were incubated for nine days. After incubation, supernatant was removed and cells were fixed using 1.5 ml of a 1:1 mixture of ice-cold methanol/acetone for 5 min incubation time at room temperature. Wells were carefully washed with 2 ml cold PBS. Colonies were stained with 1 ml of a 0.005% crystal violet solution and incubated for 30 min. Stain was removed and cells were carefully washed twice with 2 ml deionized distilled water. Well plates were scanned on a Epson Perfection V700 Photo scanner using the following settings: Doc Type: Film, Film Type: Positive Film, 1200 dpi, 24 bit, TIFF, Unsharp Mask. Quantification was done using ImageJ Software v1.48. TIFF files were copied

to the mask and converted into 8-bit. A binary image was created and stained colonies were counted in each well applying the implemented particle count function.

3.2.8 Metabolic activity assay

The water-soluble tetrazolium (WST-1) assay (Roche, Switzerland) uses a substrate that will be converted by mitochondrial enzymes thereby changing its color. No change in color is observed when mitochondrial integrity is altered. The WST-1 assay was used to quantify metabolic activity according to manufacturer's instructions. Cells were seeded to 96-well plates and treated with panobinostat or solvent for 72 h. Equivalent amount of WST-1 reagent was added to each well and read-out was performed after 1-2 h incubation time at 37°C with Epoch™ spectrophotometer (BioTek, USA) at 450 nm and for reference at 650 nm wavelength.

3.2.9 Determination of *TERT* mRNA half-life

To determine the half-life and the stability of target mRNA after panobinostat treatment, treatments with actinomycin D were performed. Actinomycin D is an agent that inhibits *de novo* RNA synthesis. GI-ME-N cells were seeded to 10 cm plates 24 h before treatment. Solvent (DMSO) or 30 nM panobinostat was applied for 2 h and cells were subsequently treated with actinomycin D (5 µg/ml). Cells were harvested after 0, 6, 10, 14, 18 and 24 h of combination treatment. Levels of mRNA were measured using qRT-PCR analysis. Half-life of mRNA was determined via linear regression fit of transformed data using *GraphPad Prism* (GraphPad Software Inc., USA).

3.3 Methods in bacterial culture

3.3.1 Plasmids

The *TERT* over-expressing plasmid pBABE-neo-hTERT (RRID: Addgene_1774) and the corresponding empty vector (RRID: Addgene_1767) were deposited by the laboratory of Bob Weinberg and kindly provided from Anton Henssen, *Charité Universitätsmedizin Berlin*, Germany and Bob Weinberg (Counter, 1998). The *TERT* plasmid encoding the full-length human *TERT* cDNA sequence was used and 1 µg DNA was transfected via lipofection (3.2.4). The pBABE-neo plasmids contain resistance cassettes against ampicillin in prokaryotes and neomycin in eukaryotes. The pBABE-neo-hTERT plasmid was sequenced by Sanger sequencing before use (section 3.3.2.12) and was aligned to the reference sequence at the

National Center for Biotechnology Information (NCBI). One nucleobase did not match with the reference sequence. According to the reference genome, the nucleobase adenine at plasmid position 2982 was mutated to guanine (A_{2982}→G). This point mutation was re-mutated by overlap-extension PCR and the corrected sequence was re-ligated into the plasmid. All cloning experiments were advised by and performed under the supervision of Annika Winkler.

3.3.2 Re-mutation of *TERT* plasmid

3.3.2.1 Amplification of *TERT* region covering mutation site

To re-mutate the point mutation of the plasmid back into the reference sequence, Overlap Extension PCR was applied. Two primers containing the desired reference sequence were designed to cover the region of the mutated nucleobase. Each was used with another primer containing restriction sites for *EcoRI* or *XhoI* to amplify parts of the *TERT* cDNA, thereby generating two fragments of *TERT* with a sequence-corrected overhang (Figure 17).

Figure 17: Overlap extension PCR generates fragment with corrected TERT sequence of the insert.
Amplification of up- and downstream part around TERT mutation site with correcting primer pair (PCR1 & PCR2). Red letter: Mutated nucleobase; green letter: corrected nucleobase. Modified from A. Winkler.

For every PCR reaction, conditions were optimized prior to performing the assay. Each condition consisted of six individual reactions which were pooled after amplification (Table 18; Table 19). All reagents were added to a microreaction tube, sealed with a cap and loaded onto a PCR cycler C100 (BioRad, USA).

Table 18: PCR 1 mix to amplify TERT region of the plasmid.

	1x
Buffer 5x Phusion HF	4 µl
dNTPs 20 mM (200 µM)	0.2 µl
Primer *TERT* Mut rev 100 µM (0.5 µM)	0.1 µl
Primer *EcoRI* for 100 µM (0.5 µM)	0.1 µl
DNA approx. 100 ng	0.5 µl
DMSO	0.6 µl
Phusion Polymerase	0.2 µl
Nuclease-free water ad 20 µl	14.3 µl

Table 19: PCR 2 mix to amplify TERT region of the plasmid.

	1x
Buffer 5xQ5 (1x)	5 µl
dNTPs 20 mM (200 µM)	0.25 µl
Primer *XhoI* rev 100 µM (0.5 µM)	0.125 µl
Primer *TERT* Mut for 100 µM (0.5 µM)	0.125 µl
DNA approx. 100 ng	0.5 µl
Q5 Polymerase	0.25 µl
Nuclease-free water ad 25 µl	18.75 µl

Table 20 summarizes the PCR program used for amplification. For the different primer pairs from PCR1 and PCR2, two different annealing temperatures were chosen.

Table 20: PCR program applied for PCR 1 and PCR 2 amplification.

	Temperature	Duration	Cycles
	98°C	30 sec	1
Denaturation	98°C	10 sec	35
Annealing	60°C PCR1 68°C PCR2	30 sec	
Extension	72°C	120 sec PCR1 30 sec PCR2	
	72°C	10min	1

The obtained PCR products were each pooled.

3.3.2.2 PCR purification

The obtained PCR products were purified using the QIAquick® PCR Purification Kit (Qiagen, The Netherlands). Five volumes PB buffer were added to the pooled PCR products and 10 µl of 3 M sodium acetate, the samples were mixed and 750 µl were loaded to a QIAquick spin column. Samples were centrifuged at 15,871 ×g at room temperature for 1 min. Flow-through was discarded. This procedure was repeated until all sample was loaded onto the column. 750 µl PE buffer was added to wash the column, followed by centrifugation and removal of flow-through. To remove residual buffer, columns were again centrifuged for 1 min. The collection tube was then replaced with a fresh microcentrifuge tube. To elute the DNA, 44 µl of RNase-

free water was added to the middle of the column, incubated for 10 min and subsequently centrifuged for 2 min to collect the DNA extract.

3.3.2.3 Digestion of DNA fragments

Before overlap PCR can be performed, purified PCR products were digested with *DpnI*, to degrade residual template plasmid backbone. For that, 5 µl of CutSmart Buffer and 1 µl of *DpnI* enzyme were added to each purified PCR product and incubated overnight at 37°C. The next day, DNA products were purified by agarose gel purification.

3.3.2.4 Agarose Gel purification

To obtain the desired DNA product, a 1% agarose gel was freshly prepared for sample separation and purification. A volume of 150 ml TAE buffer was cooked with 1.5 g agarose powder. When the gel was cooled down to about 60°C, 200 µl of a 0.05% ethidium bromide solution was added. The gel was poured into a cartridge, provided with a polycomb and eliminated for air bubbles. After 20 min, the gel was loaded into the electrophoresis chamber containing 1x TAE buffer and the polycomb was carefully removed. Samples were mixed with loading dye before electrophoresis. A volume of 15 µl DNA ladder (GeneRuler) was used to identify fragment sizes. After 90 min of electrophoresis at 100 V, the gel was analysed using a UV light source. The fragment of digested PCR1 product is expected at 1.6 kb length, of PCR2 at 0.4 kb length. The agarose gel containing the fragment of interest was cut out using a scalpel and was transferred into a 2 ml microcentrifuge tube for agarose gel extraction.

3.3.2.5 Agarose Gel extraction

The QIAquick® Gel Extraction Kit (Qiagen, The Netherlands) was applied to extract and purify DNA fragments after gel electrophoresis. A volume of 1.2 ml QG buffer was added to the gel pieces incubated at 50°C and 600 rpm until the gel was completely dissolved. After that, 400 µl isopropanol and 10 µl 3 M sodium acetate were added and the sample was mixed. The mixture was loaded onto a QIAquick spin column. Samples were centrifuged at 15,871 ×g at room temperature for 1 min. Flow-through was discarded. This procedure was repeated until all sample was loaded onto the column. A volume of 750 µl PE buffer was added to wash the column, followed by centrifugation and removal of flow-through. To remove residual buffer,

columns were centrifuged for 1 min. The collection tube was replaced with a fresh microcentrifuge tube. To elute the DNA, 40 µl of RNase-free water was added to the middle of the column, incubated for 10 min and subsequently centrifuged for 2 min to collect DNA. The DNA concentration was quantified using the NanoDrop™ spectrophotometer (Thermo Fisher Scientific, USA). After obtaining purified DNA, the overlap extension PCR was performed to generate the full insert for ligation.

3.3.2.6 Overlap extension PCR

The overlap extension PCR was performed in quadruplicates to achieve a sufficient yield of DNA product (Figure 18).

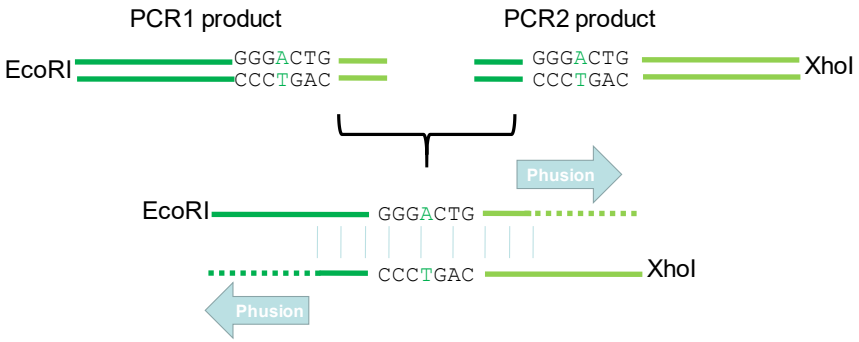

Figure 18: Scheme of the overlap extension PCR to create the corrected TERT insert.
Green letter: corrected nucleobase. Modified from A. Winkler.

All reagents were added to a microreaction tube, sealed with a cap and loaded onto the PCR cycler C100 (BioRad, USA) applying the following program (Table 21):

Table 21: PCR 3 mixture to amplify corrected DNA fragment for insertion.

	1x
Buffer Phusion HF (1x)	10 µl
dNTPs 10 mM (0.5 mM)	2 µl
PCR Product 1 200 ng	1.7 µl
PCR Product 2 200 ng	1.7 µl
Phusion Polymerase	0.5 µl
DMSO	0.8 µl
Nuclease-free water ad 50 µl	33.5 µl
Add after prior PCR: Primer *EcoRI* for and *XhoI* rev 100 µM (0.5 µM)	Each 0.25 µl

The overlap extension reaction was performed according to the following program (Table 22):

Table 22: PCR program applied for amplification of corrected DNA fragment.

	Temperature	Duration	Cycles
	98°C	2 min	1
Denaturation	98°C	10 sec	10
Annealing	65°C	30 sec	
Extension	72°C	5 min	
	72°C	10 min	1

After this prior step, the primers covering restriction sites of *EcoRI* (forward) and *XhoI* (revers) were added to each reaction mixture. Subsequently, the final PCR was performed following the program listed above to generate the full-length fragment for insertion (Table 23):

Table 23: PCR program applied to obtain full-length fragment for insertion.

	Temperature	Duration	Cycles
	98°C	30 sec	1
Denaturation	98°C	10 sec	35
Annealing	66°C	30 sec	
Extension	72°C	2.5 min	
	72°C	10 min	1

The PCR product was analyzed via agarose gel electrophoresis (section 3.3.2.4) and purified according to section 3.3.2.10 with 40 µl RNase-free water to elute DNA. The obtained PCR product was digested with 5 µl Buffer 3 and 2 µl of each restriction enzyme *EcoRI* and *XhoI*, filled up with RNase-free water to 50 µl total volume. In a second reaction, 10 µl of the mutated pBABE-neo-hTERT plasmid was added to 5 µl Buffer 3, 31 µl RNase-free water and 2 µl of each restriction enzyme *EcoRI* and *XhoI*. The digestion was performed at 37°C overnight. The following day, the digested mutated pBABE-neo-hTERT vector was dephosphorylated to avoid spontaneous re-circularization of the opened plasmid. For that, the 50 µl digestion mixture was added to 6 µl of alkaline phosphatase buffer and 4 µl alkaline phosphatase and incubated at 37°C for 30 min. The alkaline phosphatase was subsequently heat-inactivated at 72°C for 10 min. The full-length PCR product and the opened plasmid were purified via agarose gel electrophoresis according to section 3.3.2.4. The desired fragment of the full-length fragment

is 2.1 kb long and of the opened plasmid 6.6 kb. These bands were cut out with a scalpel and purified (section 3.3.2.5). The fragment was inserted into the open plasmid by subsequent ligation reaction. The DNA was measured with the NanoDrop™ spectrophotometer (Thermo Fisher Scientific, USA).

3.3.2.7 Ligation

For the ligation reaction, a 1:3 or 1:5 ratio of vector (6.6 kb) to insert (2.1 kb) were chosen. The amount of DNA (Insert) was calculated with the formula with n=3 or 5:

$$ng\ (Insert) = ng\ (Vector) * (bp\ Insert / bp\ Vector) * n$$

The reactions were set up like shown in the table below and incubated at 16°C overnight. Two negative controls were included leaving out either the insert or the vector (Table 24).

Table 24: Different ligation reactions applied for ligation of corrected DNA fragment into plasmid.

	1:3	1:5	W/o Insert	W/o Vector
Insert	7.8 µl	13 µl	--	7.8 µl
Vector	2 µl	2 µl	2 µl	--
T4 10x	2 µl	2 µl	2 µl	2 µl
T4 Ligase	1 µl	1 µl	1 µl	1 µl
H_2O ad 20 µl	7.2 µl	2 µl	15 µl	9.2 µl

The ligation preparation was completely used up for transformation of chemically competent *E.coli* bacteria to obtain the re-mutated pBABE-neo-hTERT plasmid.

3.3.2.8 Chemically competent bacteria

Plasmid DNA was amplified in chemical competent *E. coli* X10GOLD cells. To obtain enough plasmid DNA for cell transfection experiments, the re-mutated pBABE-neo-hTERT and the ready pBABE-neo plasmids were amplified by using *E.coli* as a host organism. To generate competent *E.coli*, fresh bacteria was taken from frozen glycerol stocks and incubated in 50 ml LB- medium supplemented with 10 mM $MgCl_2$ and 50 µl chloramphenicol (34 µg/ml) overnight at 37°C in an agitation shaker at 200 rpm. An aliquot of 500 µl of the culture was

taken to inoculate 300 ml LB medium supplemented with 10 mM $MgCl_2$ and 300 µl chloramphenicol (34 µg/ml) at 37°C and 200 rpm agitation for 3 to 4 h until the bacteria culture reached an optical density between 0.4 and 0.6 at 600 nm. The culture was aliquoted into six precooled 50 ml *Falcon* tubes and incubated for 15 min on ice. They were subsequently centrifuged for 15 min at 867 × *g* at 4°C in a precooled centrifuge. The supernatant was discarded and each pellet was dissolved in 1 ml transformation buffer consisting of 1 g PEG 3000 dissolved in 8 ml LB medium, 10mM $MgCl_2$, 10mM $MgSO_4$, 0.5 ml DMSO and filled up to 10 ml with LB medium. All tubes were pooled and incubated for 30 min on ice. Aliquots of 200 µl were immediately used for transformation or stored at -80°C.

3.3.2.9 Transformation of chemically competent bacteria

Chemically competent *E.coli* were thawn on ice for 30 min (section 3.3.2.8). Either 20 µl Ligation mix or 1 µg of plasmid were added to 200 µl of cells. The mix was incubated for 30 min on ice, than for 90 sec at 42°C in a pre-heated water bath and again cooled for 2 min on ice. Subsequently, 800 µl SOC medium was added and cell suspension was incubated at 37°C in an agitation shaker at 550 rpm for 1 h. Bacteria were centrifuged at 3,466 *x g* at room temperature and supernatant was discarded, leaving a small volume of supernatant behind. Cells were suspended in residual supernatant and all of culture was plated to LB agar plates containing 100 µg/ml ampicillin and incubated at 37°C overnight. The following day, clones from each condition were picked and incubated in 5 ml LB medium supplemented with 100 µg/ml ampicillin at 37°C in an agitation shaker at 200 rpm overnight. A replica plate was prepared in parallel. The next day, glycerol stocks from the bacterial cultures were prepared by taking 500 µl of the bacterial culture and adding them to 500 µl of a 50% glycerol solution and subsequent storage at -80°C. Replica plates were sealed with Parafilm and stored at 4°C until use. Plasmid DNA was isolated from residual culture using the QIAprep® Spin Miniprep Kit (Qiagen, The Netherlands) as described in section 3.3.2.10 and the full insert was analyzed by Sanger sequencing (section 3.3.2.12).

3.3.2.10 Plasmid preparation and purification of small DNA amount

To obtain small amounts of desired plasmid DNA, colonies from the replica plate were picked and incubated in 5 ml ampicillin-containing LB medium (3.3.2.9). Cells were pelleted at 3,466 *x g* and supernatant was discarded. For DNA isolation and purification, the QIAprep®

Spin Miniprep Kit was used. Cells were suspended in 250 µl P1 buffer and transferred to a 1.5 ml microcentrifuge tube. A volume of 250 µl P2 buffer was added and suspension was inverted several times until the solution became clear. Then, 350 µl N3 buffer was added and tube was inverted several times for mixing. Tube was centrifuged at 17,900 *x g* for 10 min. Supernatant was loaded onto a purification column and centrifuged at 17,900 *x g* for 1 min. Flow-through was discarded and column was washed using 500 µl PB buffer and tube was centrifuged at 17,900 *x g* for 1 min. Subsequently, 750 µl PE buffer was used for additional washing and tube was centrifuged at 17,900 *x g* for 1 min. After removal of the flow-through, column was again centrifuged at 17,900 *x g* for 1 min to remove residual buffer. The column was placed in a clean 1.5 ml microcentrifuge tube. To elute DNA, 50 µl RNase-free water was placed to the center of the spin column, incubated for 1 min, and centrifuged for 1 min at 17,900 *x g*. DNA concentration was determined using the NanoDrop™ spectrophotometer (Thermo Fisher Scientific, USA) and samples were subsequently validated using Sanger sequencing (section 3.3.2.12). One positive clone containing the full re-mutated *TERT* cDNA sequence was selected for transfection experiments. Of this clone, plasmid DNA was amplified to obtain sufficient amounts of DNA for *in vitro* experiments.

3.3.2.11 Plasmid preparation and purification of larger DNA amount

To obtain sufficient amount of plasmid DNA, the selected transformed clone from 3.3.2.10 and the empty vector were picked from their replica plates and cultured in 200 ml LB medium supplemented with 100 µg/ml ampicillin. Cultures were incubated at 37°C in an agitation shaker at 200 rpm overnight. Cells were centrifuged at 2,468 *x g* at 4°C for 20 min and cell pellets were pooled. DNA isolation and purification was performed by using the NucleoBond®Xtra Maxi kit (Machery-Nagel, France). Following an optimized protocol based on the manufactures instructions, the pellets were resuspended in 24 ml RES buffer and lysed by adding 24 ml LYS buffer followed by thoroughly shaking the tubes. An incubation step at room temperature for 5 min was performed before adding 24 ml NEU buffer. The solutions were mixed until they became clear. The filter columns were equilibrated with 25 ml EQU buffer and the cell lysates were loaded onto the columns. After the lysates had passed the filter, the residual samples were washed with 15 ml EQU buffer. For the next step, the filters were discarded and the columns were washed with 25 ml pre-warmed WASH buffer. The washed columns were placed onto a 50 ml *Falcon* tube and plasmid DNA was eluted with 15 ml pre-warmed ELU buffer. After the buffer had completely run through, the DNA was precipitated

with 10.5 ml isopropanol. DNA was pelleted at 3,466 *x g* at 4°C for 1 h. The supernatants were carefully discarded and the residual cell pellets were washed with 5 ml 70% ethanol. Again, the DNA was pelleted at 3,466 *x g* at 4°C for 1 h. The supernatants were discarded and the pellets were air-dried. To resuspend the plasmid DNA, 500 µl RNase-free water was added and mixed until DNA was dissolved. The DNA was subsequently stored at -20°C until use. DNA concentrations were determined using the NanoDrop™ spectrophotometer (Thermo Fisher Scientific, USA) and samples were validated using Sanger sequencing (sections 3.3.2.12).

3.3.2.12 Sanger sequencing of plasmids

To check for the correct *TERT* cDNA insert and the empty vector, purified plasmid DNA was prepared for Sanger sequencing at *GATC*/*Eurofins*. A total volume of 20 µl of plasmid DNA (100 ng/µl) and 20 µl of primers (10 pmol/µl) were used for analysis. Results were aligned to the *TERT* reference sequence (NM_198253) and the vector maps (plasmids #1774 for the *TERT* plasmid and #1767 for the empty vector) using the software *ApE*. The vector maps of pBABE-neo-hTERT and pBABE-neo are shown in section 2.9.3.

3.4 Methods in molecular biology

3.4.1 DNA extraction from eukaryotic cells

Genomic DNA was isolated from eukaryotic cell lines using the QIAamp DNA Mini Kit (Qiagen, The Netherlands). Cells were detached from cell culture plates by adding 0.05% trypsin. The reaction was quenched with 5 ml medium and cells were centrifuged at 300 *x g* for 4 min. The cell pellet was washed with 3 ml phosphate-buffered saline (PBS) and centrifuged again, the supernatant was discarded. The cell pellet was resuspended in 200 µl PBS and transferred to a 1.5 ml microcentrifuge tube. A volume of 20 µL Proteinase K and 200 µL AL buffer were added to the cell pellet, mixed vigorously for 15 sec and incubated at 56°C for 10 min. Subsequently, 200 µl ethanol p.a. was added and lysate was mixed vigorously. The lysate was loaded onto the spin columns placed in a 2 ml collection tube. The samples were centrifuged at 6,000 *x g* at room temperature for 1 min. The collection tube was replaced with a fresh microcentrifuge tube. A volume of 500 µl AW1 buffer was added to wash the sample and samples were centrifuged at 6,000 *x g* at room temperature for 1 min. The collection tube was replaced with a fresh microcentrifuge tube. 500 µl of AW2 buffer was added to wash the sample. The samples were centrifuged at 20,000 *x g* at room temperature for 3 min. The

collection tube was replaced with a fresh microcentrifuge tube and centrifuged again to remove residual buffer for 1 min. The spin column was placed into a fresh microcentrifuge tube. To elute the DNA, 2x50 µl of RNase-free water was added to the middle of the column, incubated for 1 min and subsequently centrifuged for 1 min to collect DNA. The DNA concentration was quantified using the NanoDrop™ spectrophotometer (Thermo Fisher Scientific, USA) as described in section 3.4.3.1.

3.4.2 RNA extraction

Total RNA was isolated from cell lines using the RNeasy Mini Kit (Qiagen, The Netherlands) and RNA concentrations were measured using the NanoDrop™ system (Thermo Fisher Scientific, USA) as described in section 3.4.3.1. RNA from adherent cells was harvested with 600 µl RLT buffer supplemented with 6 µl β-mercaptoethanol, scraped from cell culture plates and stored at -80°C until isolation. If tumor tissue was used, powdered tissue was lysed in 600 µl RLT buffer supplemented with 6 µl β-mercaptoethanol and pipetted up and down until roughly dissolved. For both sample types, one volume of 70% ethanol was added to each sample, mixed by pipetting and 700 µl of lysate was loaded onto the RNeasy spin columns placed in a 2 ml collection tube. The samples were centrifuged at 15,871 *x g* at room temperature for 1 min. Flow-through was discarded. This procedure was repeated until all sample was loaded onto the column. A volume of 700 µl RW1 buffer was added to wash the column, followed by centrifugation and removal of flow-through. Subsequently, 500 µl of RPE buffer were added to the columns and they were centrifuged for 1 min. The flow-through was discarded. Another 500 µl of RPE buffer was added to the columns followed by subsequent centrifugation. To remove residual buffer, columns were put into a fresh collection tube and centrifuged for 1 min. The collection tube was replaced with a fresh microcentrifuge tube. To elute the DNA, 2x15 µl of RNase-free water was added to the middle of the column, incubated for 1 min and subsequently centrifuged for 1 min to collect RNA. The RNA concentration was quantified using the NanoDrop™ spectrophotometer (Thermo Fisher Scientific, USA) as described in section 3.4.3.1.

3.4.3 Nucleic acid quantification

3.4.3.1 Measurement of RNA or DNA concentration with NanoDrop™

To determine the RNA or DNA concentration, the absorbance spectrum was measured with the NanoDrop™ 2000c spectrophotometer (BioTek). The device was blanked with RNase-free water and 1 µl of purified RNA or DNA was taken for analysis and was loaded to the sample plate. The NanoDrop™ software calculates nucleic acid concentrations by analyzing the absorption spectra at 260 und 280 nm.

3.4.3.2 Measurement of DNA concentration with Qubit™

For sensitive measurements of DNA for the ChIP and WGS Sequencing and the methylation array, the Qubit® fluorometer (Thermo Fisher Scientific, USA) was applied. The working solution was prepared by diluting the Qubit® dsDNA HS Reagent 1:200 in Qubit® dsDNA HS Buffer. For the two supplied calibration standards, 190 µl of working solution and 10 µl of standard were mixed. For each sample, 199 µl of working solution was mixed with 1 µl of sample DNA. Samples were incubated at room temperature for 2 min. Standards were measured from 300-1000 nm wavelength and samples at 260 nm. Concentration of samples was calculated as followed:

$$Concentration\ of\ sample = Measured\ value \times 200$$

3.4.4 Reverse transcription

The First-Strand cDNA Synthesis Kit (Thermo Fisher Scientific, USA) was used to transcribe complementary DNA (cDNA) from RNA for qRT-PCR analysis. Per reaction, 0.1-1 µg of total RNA was diluted with RNase-free water to a total volume of 10 µl, subsequently 1 µl of random hexamer primer mix was added. The annealing of primers to RNA was performed at 65°C for 5 min in a PCR cycler. Next, 4 µl 5x reaction buffer, 1 µl RiboLockTM RNase Inhibitor (20 u/µl), 2 µl of 10 mM dNTP Mix and 2 µl of M-MuLV Reverse Transcriptase (20 u/µl) were added to each reaction. The cDNA synthesis was performed in accordance to described PCR program (Table 25) and complementary DNA was stored at -20°C until use.

Table 25: PCR program applied for cDNA synthesis.

	Temperature	Duration
Incubation	25°C	5 min
Synthesis	37°C	60 min
Denaturation	70°C	5 min

3.4.5 Quantitative real-time polymerase chain reaction

Relative gene expression was measured using SYBR Green Dye (Roche, Switzerland) on a StepOne Plus or QuantStudio 3 real-time PCR system (Thermo Fisher Scientific, USA), and was normalized to the averaged expression of *18S*, *HRPT* or *SDHA* (Fischer, 2005). All primers used in this study are summarized in Table 11. For quantitative real-time polymerase chain reaction (qRT-PCR) analysis, 18 µl of master mix was added to each 96-well. The composition of master mixes was adapted to corresponding primer type (Table 26). Complementary DNA was diluted 1:10 with RNase-free water and 2 µl of the diluted cDNA was used for analysis.

Table 26: Reaction mixture for qRT-PCR analysis.

	Self-designed Primer (100 pmol) 1x	Quantitect Primer (forward & reverse Mix) 1x
PCR Mix 2x	10 µl	10 µl
RNase-free H_2O	7.84 µl	5.8 µl
Primer	Forward: 0.08 µl Reverse: 0.08 µl	2.2 µl
cDNA 1:10	2 µl	2 µl

The quantitative real-time PCR was performed using the following temperature protocol (Table 27):

Table 27: PCR program applied for qRT-PCR analysis.

	Temperature	Duration	Cycles
	50°C	2 min	1
Denaturation	95°C	10 min	1
Annealing	60°C	1 min	40
Extension	95°C	15 sec	
	95°C	15 sec	1
Melt curve	60-95°C		+ 0.3°C increments

Data was analyzed using StepOne™ v2.3 or QuantStudio™ v1.5.1 Software (Thermo Fisher Scientific, USA). Changes in expression were calculated using the $\Delta\Delta C_t$ method for the cell culture experiments or the standard curve method for *in vivo* experiments. Each primer was validated before use and tested by using the standard curve method (VanGuilder, 2008).

3.5 Methods in biochemistry

3.5.1 Telomerase activity assay

To quantify telomerase activity, the TeloTAGGG™ Telomerase PCR ELISA^{PLUS} Kit (Roche, Switzerland) was used according to manufacturer's instructions. Adherent cells were harvested with Versene, counted and 200.000 vital cells were harvested and centrifuged at 3000 *x g* at 4°C for 10 min. Supernatant was completely removed and residual liquid was carefully soaked up using Whatman Paper. For tumor samples, punch biopsies of 5 mm diameter were asservated and 20 cryosections of 10 µm thickness were used for lysis. Preparation of tumor slices was performed by Daniela Tiburtius and Jeannette Mothes using a CryoStar™ NX70 (Thermo Fisher Scientific, USA). Cells or cryosections were frozen in liquid nitrogen after collection and stored at -80°C until lysis. For lysis, the pellets were kept on ice and were lysed in 200 µl ice-cold lysis buffer for 20 min, followed by centrifugation at 16,000 *x g* at 4°C for 30 min. Supernatants were flash-frozen in liquid nitrogen until use. The assay consists of two major steps: the telomerase repeated amplification protocol (TRAP) assay followed by hybridization and enzyme-linked immunosorbent assay (ELISA) (Figure 19).

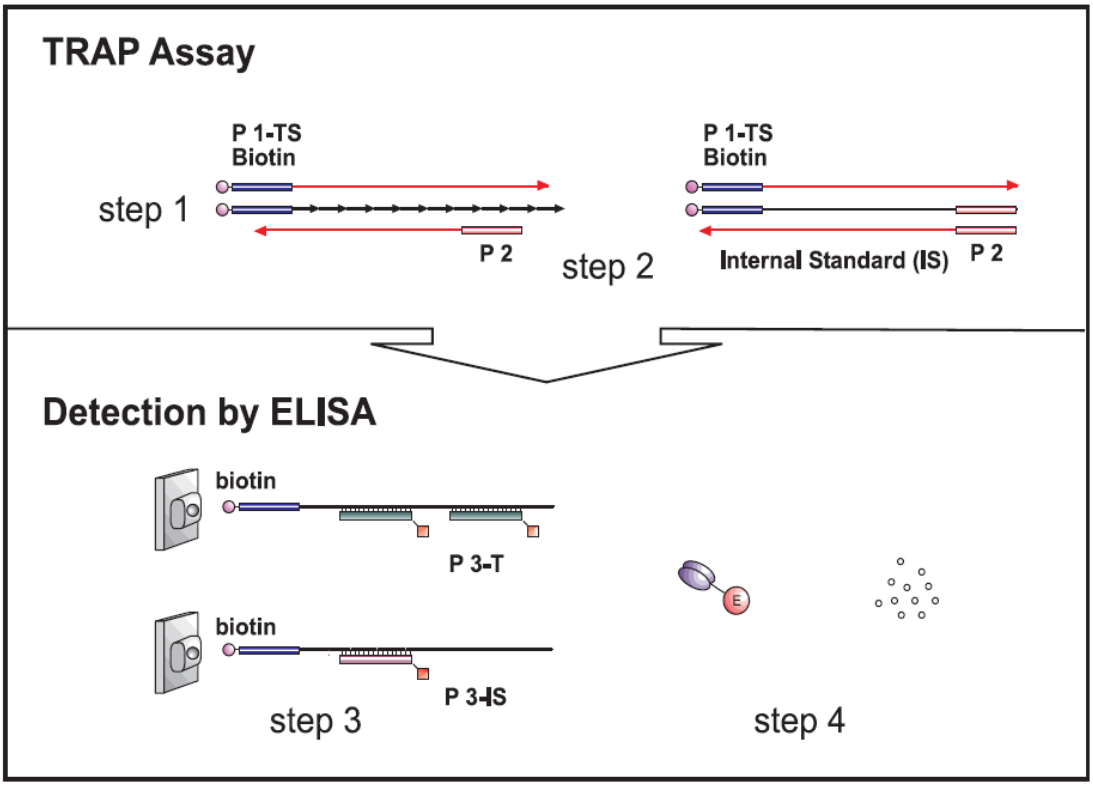

Figure 19: Assay principle of the TeloTAGGG™ ELISA.
P: Primer; TS: template synthetic; IS: internal standard; T: template; E: enzyme (HRP). From the manufacturer's instruction handbook (Roche, Switzerland).

For the first step of the protocol, 3 µl of sample lysate or control was used for each TRAP reaction. To obtain heat-treated negative controls, solvent treated cell lysates were used and exposed to 85°C for 15 min to disintegrate the telomerase enzyme complex. For each TRAP reaction, a master mix of 25 µl reaction mixture and 5 µl internal standard solution was prepared. A volume of 3 µl of sample or of 1 µl of the supplied positive control ("control high") was added to the master mix and filled up with RNase-free water to 50 µl total volume. The telomerase DNA polymerase reaction followed by PCR amplification of products was performed according to Table 28 (step 1).

Table 28: PCR temperature gradient for TeloTAGGG™ ELISA.

	Temperature	Duration	Cycles
Primer elongation	25°C	30 min	1
Telomerase inactivation	94°C	5 min	1
Denaturation	94°C	30 sec	30
Annealing	50°C	30 sec	
Polymerization	72°C	90 sec	
	72°C	10 min	1
Hold	4°C		infinite

A volume of 2.5 µl of PCR product was taken for subsequent denaturation and hybridization. For that, 10 µl of denaturation reagent was each pipetted into two separate reaction tubes. A volume of 2.5 µl PCR product was added, mixed and incubated for 10 min at room temperature. Afterwards, 100 µl supplied sample solution was added to one of the tubes and 100 µl of internal standard solution was added to the other tube. These two hybridization mixtures are necessary to exclude intra-assay variations of samples after TRAP reaction. For heat-treated negative control samples, only one hybridization with sample solution was performed. The samples were mixed and incubated at 37°C and 300 rpm for 2 h (step 2). After the hybridization step, samples were immobilized to a streptavidin-coated 96-well plate and incubated at 37°C for 1 h (step 3). The wells were washed three times with 250µl washing buffer. A solution of 2 µl anti-DIG-HRP antibody (10 mU/ml) was prepared in 98 µl conjugate dilution buffer and added to each well. The mixture was incubated at room temperature on a shaker at 300 rpm for 30 min. After incubation, the wells were washed five times with 250µl washing buffer. Prewarmed TMB substrate solution was added to each well and incubated at room temperature on a shaker at 300 rpm for 20 min. When the TMB substrate was converted by peroxidase, wells turned blue (step 4). Subsequently, 100 µl stop reagent was added and read-out was performed after 10 min incubation at room temperature. Addition of the stop reagent resulted in a color change to yellow. Absorbance was detected at 450 nm and for reference at 690 nm wavelength using the Epoch™ spectrophotometer (BioTek, USA). Normalization was done according to control high template results and compared between the corresponding solvent-treated samples or drug-treated samples. Samples are to be considered as telomerase-positive if the difference in absorbance ($\Delta A = A_{450\ nm} - A_{690\ nm}$) is higher than the twofold background activity (background

activity is the value of negative control or heat-treated sample). Samples were considered negative if extinction < 0.25 ($A_{450\ nm}$ - $A_{690\ nm}$). The relative telomerase activity (RTA) was calculated using the equation:

$$RTA = \frac{(AS - AS,0)/AS,IS}{(ATS8 - ATS8,0)/ATS8,IS} * 100$$

AS: absorbance of sample

AS,0: absorbance of heat- or RNase-treated sample

AS,IS: absorbance of Internal Standard (IS) of the sample

ATS8: absorbance of Control template (TS8)

ATS8,0: absorbance of Lysis buffer

ATS8,IS: absorbance of Internal Standard (IS) of the Control template (TS8)

3.5.2 Western blotting

Preparation of whole cell protein extracts

Proteins from cell extracts can be analyzed by this antibody-based detection method. Cells were harvested with Versene, centrifuged at 300 *x g* for 4 min and supernatant was completely removed. Cell pellets were lysed one ice for 5-10 min in buffer containing 20 mM Tris-HCl, 7 M urea, 0.01% Triton X-100, 100 mM DTT, 40 mM $MgCl_2$ and cOmplete® protease inhibitor cocktail (Roche, Switzerland). Lysate was centrifuged at 18,000 *x g* for 1 min, supernatant was transferred to a fresh microcentrifuge tube and stored at -80°C until use.

Protein quantification

Total protein content of cell extracts were quantified using the colorimetric Bradford assay (Roti®-Quant by Carl Roth). The assay is based on the dye Coomassie Brilliant Blue-G250, which changes color from brown to blue if basic amino acids are present. Absorption was detected at 595 nm wavelength using the Epoch™ spectrophotometer (BioTek, USA) and plotted against a bovine serum albumin (BSA) standard curve.

SDS polyacrylamide gel electrophoresis

For each sample, 10-15 µg (PARP-1, HDAC1, HDAC2), 25 µg (TERT) or 15-30 µg (CASP-3) of protein was mixed with 2x Laemmli buffer to a total volume of 15-20 µl, depending on the target protein and gel layout. Samples were denatured for 5 minutes at 100°C in a thermo block and were stored at -20°C until further use. The proteins were separated by gel electrophoresis on 8% (TERT), 10% (PARP-1, HDAC1, HDAC2) or 15% (CASP-3) sodium dodecyl sulfate

(SDS) polyacrylamide gels. A protein ladder (Page Ruler™, Thermo Fisher Scientific, USA) was included to determine protein sizes.

Semi dry blot

After the electrophoresis, proteins were transferred to a polyvinylidene difluoride (PVDF) membrane using the BioRad Trans-Blot® semi-dry system with the following parameters: max. 1.0 A, 25 V, 30 min. Antibodies used in this study are listed in Table 7. Anti-GAPDH detection was measured as loading control. Membranes were blocked for 1 h at room temperature with 5% powdered milk BST-T blocking buffer followed by incubation with the primary antibodies at 4°C overnight in 5% powdered milk PBS buffer.

Wet blot

TERT was transferred via wet blot for 90 min at 300 mA in the cold to a polyvinylidene difluoride (PVDF) membrane using the BioRad Mini Trans-Blot® system. Membranes were blocked for 1 h at room temperature with 3% BSA BST-T blocking buffer followed by incubation with the primary antibody at 4°C overnight in 0.3% BSA.

Detection

After incubation with the primary antibodies, membranes were washed three times with BST-T buffer and subsequently incubated with corresponding peroxidase-conjugated secondary antibodies (anti-rabbit IgG or anti-mouse IgG) for 1 h at room temperature. Membranes were washed three times with BST-T buffer and chemoluminescence detection was performed using Western Lightning Plus-ECL detection solution (Perkin Elmer, USA) and measured on a Quantum ST5 imaging system (Vilber Lourmat, France).

3.5.3 Flow cytometry

Fluorescence activated cell sorting (FACS) analyses were performed on a LSR Fortessa™ X-20 (BD Biosciences, USA), and data was analyzed using FlowJo™ V10 software (BD Biosciences, USA). Cells were harvested with 0.05% trypsin and 5 ml medium and centrifuged together with the supernatant at 300 *x g* for 5 min at 4°C. Supernatant was discarded and cell pellets were washed with 2 ml cold PBS, transferred into FACS tubes and centrifuged again. Cells were fixed with 70% cold ethanol and incubated for 30 min. Tubes were centrifuged at 300 *x g* for 5 min at 4°C, supernatant was discarded and cells were washed with 2 ml ice-cold PBS followed by subsequent centrifugation at 300 *x g* for 5 min at 4°C. Supernatant was discarded, 50 µl RNase A solution (100 µg/ml) and 400 µl propidium iodide solution (50 µg/ml)

were added and incubated at room temperature for 10 min in the dark. Unstained cells were always included as controls for parameter setting.

3.6 Transcriptomic and (epi)genomic analyses

3.6.1 RNA sequencing

RNA was isolated from cell cultures or tumor tissues as described in section 3.4.2. Library preparation and total RNA sequencing were performed at the DKFZ High Throughput Sequencing Core Facility, Germany. Libraries were prepared with the Illumina TruSeq mRNA stranded protocol (500 ng input) following the manufacturers' instructions. Six libraries were pooled on one lane Hiseq 4000 and sequenced in 100 paired end mode. This resulted in a minimum of 48 million read pairs per library.

3.6.2 ChIP sequencing

The chromatin immunoprecipitation (ChIP) protocol was modified based on the manufacturers ChIP protocol (ChIP Assay Kit, Millipore) and performed as previously described (Lee, 2006). Cells were seeded to 15 cm plates to obtain sufficient amount of cells. Five million cells were used for each antibody. Cell culture medium was reduced to 10 ml before harvest. All steps to harvest the cells were performed by two people in parallel to ensure correct incubation times. DNA and proteins were cross-linked using 270 µl of a 37% formaldehyde solution (total: 1% formaldehyde per plate) at room temperature, plates were stacked on a shaker and rotated horizontally. Cross-linking was stopped after 10 min with 1.25 ml of 1 M glycine (125 mM) and incubated on a horizontal shaker for 5 min. Supernatant was removed, cells were put on ice and washed three times with 10 ml of cold PBS to remove residual reagent. Afterwards, 2 ml PBS solution containing cOmplete® protease inhibitor (Roche, Switzerland) was added to each plate. Cells were scraped from plates and lysed for 1 h at 4°C with ChIP lysis buffer containing 50 mM Tris-HCl, pH 8.1, 1% SDS, 10 mM EDTA and cOmplete® protease inhibitor cocktail to achieve a concentration of 35 Mio cells in 1750 µl lysis buffer per condition.

DNA was fragmented using the Covaris S220 ultra sonicator to obtain fragments of 200–800 bp DNA. Using 2 ml Adaptive Focused Acoustics (AFA) tubes, an optimized program was applied for sonification at 4-8°C: Duty Factor: 5; PIP: 140; 200 Burst/cycle; Permanent sonification;

46 cycles (~23 min), run the program twice (~46 min). DNA fragments were analyzed on a 1.5% agarose gel as described in section 3.3.2.4.

Protein A coupled magnetic beads (SureBeads™, BioRad, USA) were used for sample enrichment and purification. In between, 100 µg beads per immunoprecipitation (IP) were washed three times with ChIP dilution buffer. Supernatant was discarded. Sheared DNA samples were centrifuged at 18,000 *x g* at 4°C for 10 min. Sheared DNA was diluted 1:10 with ChIP dilution buffer. The input samples (1%) were taken from that solution and frozen at -20°C until use. The diluted DNA was added to the washed beads and incubated on a rotator at 4°C for 1 h. After pre-clearing of cell lysates, the beads were immobilized and supernatants were transferred to fresh microcentrifuge tubes. A total amount of 1 µg of each antibody was used per million cells for pull-down overnight at 4°C on a rotator. The antibodies used for ChIP sequencing listed in Table 7 were successfully used by other laboratories and were not further validated.

The next day, 100 µl of fresh beads were washed and prepared for each sample. The immunoprecipitated DNA lysates were added to the beads and incubated on a rotator at 4°C for 1 h. After incubation, the beads were immobilized using a magnetic rack and were subsequently washed with 1 ml low salt buffer, 1 ml high salt buffer, 1 ml LiCl buffer and 2x 1 ml TE-buffer. Elution of chromatin from magnetic beads was performed by adding 2x 250 µl of elution buffer to each sample at each incubation step on a rotator for 15 min at room temperature. Magnetic beads were immobilized and supernatant was transferred to a fresh microcentrifuge tube. De-crosslinking of the DNA-protein complexes was achieved by adding 5 M NaCl to eluates and incubated overnight at 65°C. Input controls were thawn and 5 M NaCl was added.

The next day, proteins were digested using a mixture of 0.5 M EDTA, Tris-HCl pH=6.6 and 10 mg/ml proteinase K (20 mg/ml) at 45°C for 1 h. DNA was isolated with the QIAamp DNA Purification Kit (Qiagen, The Netherlands) as described in section 3.4.1 and quantified using the Qubit™ fluorometer (Thermo Fisher Scientific, USA) as described in section 3.4.3.2. Immunoprecipitated DNA was analyzed by qRT-PCR using primers at *MIR183* and *GRHL-1* locus as positive controls (Table 13).

To ensure high quality of samples, only samples that showed reduced *TERT* mRNA levels after panobinostat treatment and additionally an enrichment (in active chromatin marks) or decrease (in repressive chromatin marks) at *MIR183* and *GRHL1* were included for sequencing. Corresponding solvent (DMSO) treated samples and input controls completed the sample set.

For most of the samples, it was possible to sequence technical replicates. Library preparation and sequencing were performed at the DKFZ High Throughput Sequencing Core Facility, Germany. Libraries were prepared with the NEBNext® ChIP-Seq Library Prep Reagent Set for Illumina (10 ng input) following the manufacturers' instructions. A size selection step for fragments of 300 bp length was performed after library preparation. Pools of six to seven libraries were sequenced on one lane HiSeq 4000 in 50 single read mode.

3.6.3 Methylation array

To investigate the methylation status of the rearranged *TERT* region, methylation profiling analysis was performed. Adherent cells were harvested with 0.05% trypsin and centrifuged at 300 *x g* for 4 min. Supernatant was removed, cell pellet was washed with 2 ml PBS and centrifuged again. Supernatant was removed and DNA was isolated using the QIAamp DNA Purification Kit (Qiagen, The Netherlands) as described in section 3.4.1 and DNA was quantified using the Qubit™ fluorometer (Thermo Fisher Scientific, USA) as described in section 1.4.4. Methylation array was performed at the DKFZ Genomics and Proteomics Core Facility, Germany. A total amount of 350-500 ng genomic DNA from each sample was bisulfite converted using the EZ-96 DNA Methylation Kit (Zymo Research Corporation, USA) according to the manufacturer's recommendation. Bisulfite converted DNA was amplified, fragmented and hybridized to Illumina Infinium Human MethylationEPIC BeadChip using standard Illumina protocol. Microarrays were scanned using the Illumina iScan-Scanner according to "Standard Illumina Scanning Protocol".

3.6.4 Nanopore sequencing

To identify the breakpoint and fusion partner in GI-ME-N cells, DNA sequencing using the Nanopore platform was performed to obtain the exact sequence of the *TERT* region. Sample preparation and Nanopore sequencing were performed by Rocío Chamorro González at the *Experimental and Clinical Research Center* (ECRC), Berlin. High molecular weight DNA was extracted using the MagAttract HMW DNA Kit (Qiagen, The Netherlands). DNA content was measured with a Qubit 3.0 Fluorometer (Thermo Fisher Scientific, USA) and sample quality control was performed using a 4200 TapeStation System (Agilent Technologies, USA). Libraries were prepared using the Ligation Sequencing Kit (SQK-LSK109, Oxford Nanopore

Technologies Ltd., UK) and sequenced on a R9.4.1 MinION flowcell (FLO-MIN106, Oxford Nanopore Technologies Ltd., UK).

Data analysis was performed by Kerstin Haase and Konstantin Helmsauer at the *Experimental and Clinical Research Center* (ECRC), Berlin. Raw data was basecalled using Guppy 2.3.7 (Oxford Nanopore Technologies Ltd., UK) with default parameters. Adapters were trimmed using qcat 1.0.1 (Oxford Nanopore Technologies Ltd., UK). Quality control was performed using NanoPlot 1.0.0 (De Coster, 2018). Reads were aligned to hg19 using minimap2 2.16-r922 (Li, 2018) with default parameters. Individual split reads in the *TERT* promotor region were identified manually and supplementary alignments inspected, focusing on alignments to chromosome 19, taking evidence for a *TERT*-chr19-fusion from 4C-seq and FISH into account (Gartlgruber, 2018). Mappings were lifted over to hg38 using CrossMap v0.4.1 for visualization.

To sustain the analysis of the DNA breakpoint in the *TERT* genomic region, published targeted sequencing data (Peifer, 2015) was quality controlled (FASTQC 0.11.8) and adapters were trimmed (BBMap 38.58). Reads were aligned to hg19 using BWA-MEM 0.7.15 (Li, 2009) with default parameters and duplicate reads were removed (Picard 2.20.4). Coverage tracks were generated using bamCoverage (bin size 20bp, normalization using counts per million) from Deeptools 3.3.0. Copy number alterations were called using Control-FREEC 11.4 (Boeva, 2012) with default parameters. Structural variants were called using SvABA 1.1.1 (Wala, 2018) in germline mode (discarding regions blacklisted in https://data.broadinstitute.org/snowman/svaba_exclusions.bed). Unfiltered SvABA calls were inspected for breakpoints involving the *TERT* promotor region.

3.6.5 Data deposition

Chromatin immunoprecipitation sequencing and methylation profiling data are available at NCBI's Gene Expression Omnibus (Edgar, 2002) under the accession number GSE155707. Whole-genome sequencing data have been deposited at NCBI's Sequence Read Archive under the accession number SRR12476600.

3.7 Statistical analyses

Data was illustrated and analyzed using the *GraphPad Prism* software package (version 7) from GraphPad Software Inc., USA, unless stated otherwise. P-values ≤0.05 were considered significant.

3.7.1 Cell culture experiments

In vitro experiments were performed in at least three independent biological replicates unless indicated otherwise. Relative values were compared to the control used for normalization applying the one-sample t-test. Relative values compared to each other and absolute values were analyzed using unpaired two-tailed t-test. RNA stability experiments were analyzed using linear regression of $\log_2$ transformed expression values, which were normalized to the initial expression.

3.7.2 Animal experiments

In vivo effects of panobinostat treatment on mRNA expression and telomerase activity were analyzed using unpaired two-tailed t-test. Growth curves were quantified using area under the curve analysis. Kaplan-Meier survival curves were analyzed via Mantel-Cox test.

3.7.3 Transcriptomic and epigenomic analyses

3.7.3.1 RNA sequencing

Data analysis was performed at the *Core Unit Bioinformatics* (CUBI) at the *Berlin Institute of Health* (BIH), Berlin by Benedikt Obermayer. Reads were mapped with STAR (v2.6.1) (Dobin, 2012) to the hg38 genome and quantified using featureCounts (v1.6.3; Liao, 2013) with the Gencode v25 reference. Differential expression analysis was performed using DESeq2 (v1.18.1, Love, 2014) testing for treatment effects in the two cohorts separately. GO term enrichment was performed using topGO (v2.30.1) and GAGE (v2.28.2, Luo, 2009) was used with gene sets taken from MSigDB (Liberzon, 2015) for additional gene set enrichment.

3.7.3.2 ChIP Sequencing

Data analysis was performed at the *Core Unit Bioinformatics* (CUBI) at the *Berlin Institute of Health* (BIH), Berlin by January Weiner. Reads were aligned using the R package Rsubread (Liao, 2019) to the GRCh38 genome assembly and filtered for properly paired reads. Alignment coverage was calculated with the bamCoverage program from the deepTools package (Ramirez, 2014). ChIPQC (Carroll, 2014) was used for quality control. DiffBind was applied separately to each of the probes with the parameter minOverlap=2. Peak annotation was done with ChIPseeker. The annotatePeak function from the ChIPseeker package was used (Yu). The function assigns peaks to genes only based on their respective location on the genome (e.g., intergenic region, transcriptional start site, TSS, region, promoter etc.). The TSS region was defined as 3 kb up- and downstream from the TSS. Differential occupancy analysis (DOA) was performed using the DESeq2 package. In the separate analysis, DiffBind was used to select identified peaks for each probe separately. In a DESeq2 analysis for a given probe, only peaks relevant for that probe were taken into account. For histone mark H3K4me1 only one sample per experimental group was obtained, and thus no direct comparison could be made. For alignment visualization and peak inspection, the program Integrative genome Viewer was used (Thorvaldsdottir, 2013). For the results and visualization of peaks in the rearranged *TERT* region, reads of the *TERT* region and of the rearrangement region on chromosome 19 were combined. Coverage was calculated with bamCoverage. Data was scaled to the maximum value in the whole region.

3.7.3.3 Methylation array

Data analysis was performed at the Core Unit Bioinformatics (CUBI) at the *Berlin Institute of Health* (BIH), Berlin by January Weiner. Illumina data files were read and processed using the minfi R package (Aryee, 2014). The arrays were normalized using the quantile algorithm (Touleimat, 2012). Probes with detection p-values above 0.01 as well as probes known to be unreliable due to cross-reactivity or containing variants (Pidsley, 2016) were removed (in total, 44916 probes were removed). The IlluminaHumanMethylationEPICanno.ilm10b4.hg19 R package (Hansen, 2017) was used for probe annotation. Probe-wise differential methylation analysis was done using the limma R package (Smyth, 2005) using the M-values, while beta-values were used for visualization (Du, 2010). For prediction of differentially methylated regions, the package DMRcate (Peters, 2015) was used.

3.7.4 Synergy analysis

Data obtained from cell viability assays including concentrations and phenotypic response is calculated as mean of four replicates and loaded into a defined online mask (https://synergyfinder.fimm.fi/). As phenotypic response, the parameter “Inhibition” was selected and the Bliss model was chosen for overall synergy calculation as the deviation of phenotypic responses compared to the expected values, averaged over the full dose–response matrix. The average synergy score is displayed and individual synergy score at each dose combination can be displayed by hovering the mouse across the 3D plot in the online application (Ianevski, 2017).

4 Results

4.1 Histone deacetylase inhibition suppresses *TERT* transcript levels and telomerase activity in *TERT*-driven neuroblastoma cells

Histone deacetylase inhibitors (HDACi) induce epigenetic modifications and show antitumoral efficacy towards neuroblastoma cells (Deubzer, 2008; Lodrini, 2013; Muhlethaler-Mottet, 2008; Oehme, 2009b). A novel subgroup of high-risk neuroblastoma patients were identified to harbor rearrangements of the telomerase reverse transcriptase (*TERT*) gene, correlating with a malignant phenotype and poor prognosis (Ackermann, 2018; Peifer, 2015; Valentijn, 2015). Therefore, treatment of *TERT*-rearranged neuroblastoma with HDACi was investigated in models of high-risk neuroblastoma.

4.1.1 Histone deacetylase inhibition suppresses *TERT* transcript levels in *TERT*-driven neuroblastoma cells

Treatment of *TERT*-rearranged cell line with HDACi provides a promising strategy to target *TERT*. To investigate the epigenetic approach to use HDAC inhibitors for the treatment of high-risk *TERT*-rearranged neuroblastoma, two high-risk neuroblastoma cell lines GI-ME-N and CLB-GA were used. Both cell lines show high *TERT*-expression and telomerase activity as result of the genomic rearrangement (Peifer, 2015; Valentijn, 2015). These are the only confirmed *TERT*-rearranged, not *MYCN*-amplified neuroblastoma cell lines. GI-ME-N cells harbor six copies of *TERT*: two of chromosome 5 derivatives, two of a derivative chromosome 6 and two of a derivative chromosome 16. CLB-GA owns three copies of *TERT*: two of different chromosome 5 derivatives and one of a derivative chromosome 20 (Gartlgruber, 2018). GI-ME-N and CLB-GA cell lines were treated with the pan-HDACi panobinostat (Khan, 2008a) and *TERT* mRNA expression was analyzed after treatment by qRT-PCR. Treatment was applied for 0-120 h to analyze the kinetic of *TERT* expression after treatment and CLB-GA cells were treated with 15 nM panobinostat and GI-ME-N cells were treated with 30 nM panobinostat. The lower concentration used for CLB-GA was chosen since treatment with higher concentrations of panobinostat impeded the analysis due to few remaining adherent cells after treatment. Both applied concentrations lie in the spectrum of clinically relevant patient

plasma concentrations of about 5 ng/ml (Rathkopf, 2010a). This patient plasma concentration corresponds to 15 nM panobinostat as applied in the cell culture models.

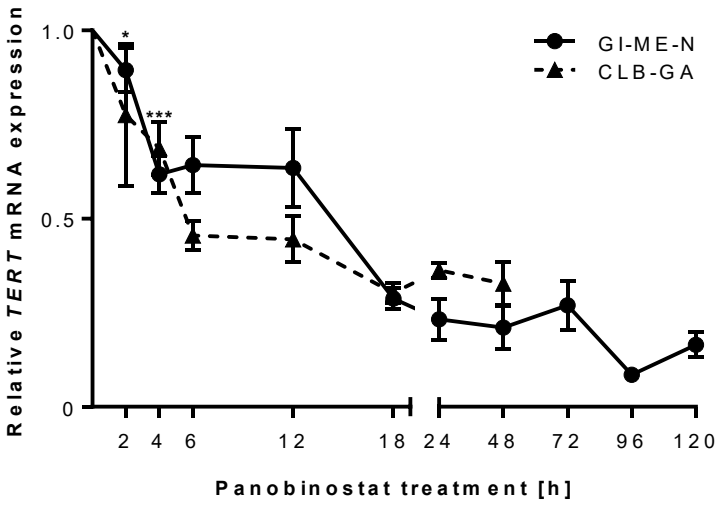

Figure 20: TERT mRNA expression is decreased after panobinostat treatment.
Kinetic of *TERT* mRNA expression in GI-ME-N (30 nM panobinostat) and CLB-GA (15 nM panobinostat) cells after 2-120 h treatment. *TERT* expression was analyzed by qRT-PCR (mean fold change over solvent ± SD; n≥3). The first significant data point is marked with an asterix, all subsequent time points show significantly reduced *TERT* levels with p ≤ 0.001-0.05, *P≤0.05, ***P≤0.001.

Due to the strong cell death induction of panobinostat treatment, RNA expression in CLB-GA cells treated for longer than 48 h could not be analyzed. RNA expression analysis revealed that *TERT* mRNA levels were significantly decreased after 2 h of treatment to 89% in GI-ME-N and after 4 h to 78% in CLB-GA cells and RNA levels further declined under treatment (Figure 20). After 120 h treatment, *TERT* mRNA expression was reduced to 16% in GI-ME-N cells and after 48 h treatment to 30% in CLB-GA cells. Panobinostat showed to be a potent HDACi, reducing *TERT* levels to less than 50% after about 15 h of treatment at low nanomolar concentrations (Figure 20).

To investigate whether the repression of *TERT* is a common effect of HDAC inhibition, and to narrow down the HDACs involved in the regulation of *TERT*, different pan-HDAC and specific HDAC inhibitors were selected for treatment. Valproic acid (VPA), vorinostat (SAHA) and entinostat (MS-275) inhibit all classical eleven HDACs (Khan, 2008a). Mocetinostat inhibits HDACs 1, 2, 3 and 11 (Boumber, 2011), romidepsin HDACs 1 and 2 (Furumai, 2002), Santacruzamate A HDAC2 (Pavlik, 2013), bufexamac HDACs 6 and 10 (Bantscheff, 2011) and compound 2 selectively inhibits HDAC8 (Krennhrubec, 2007).

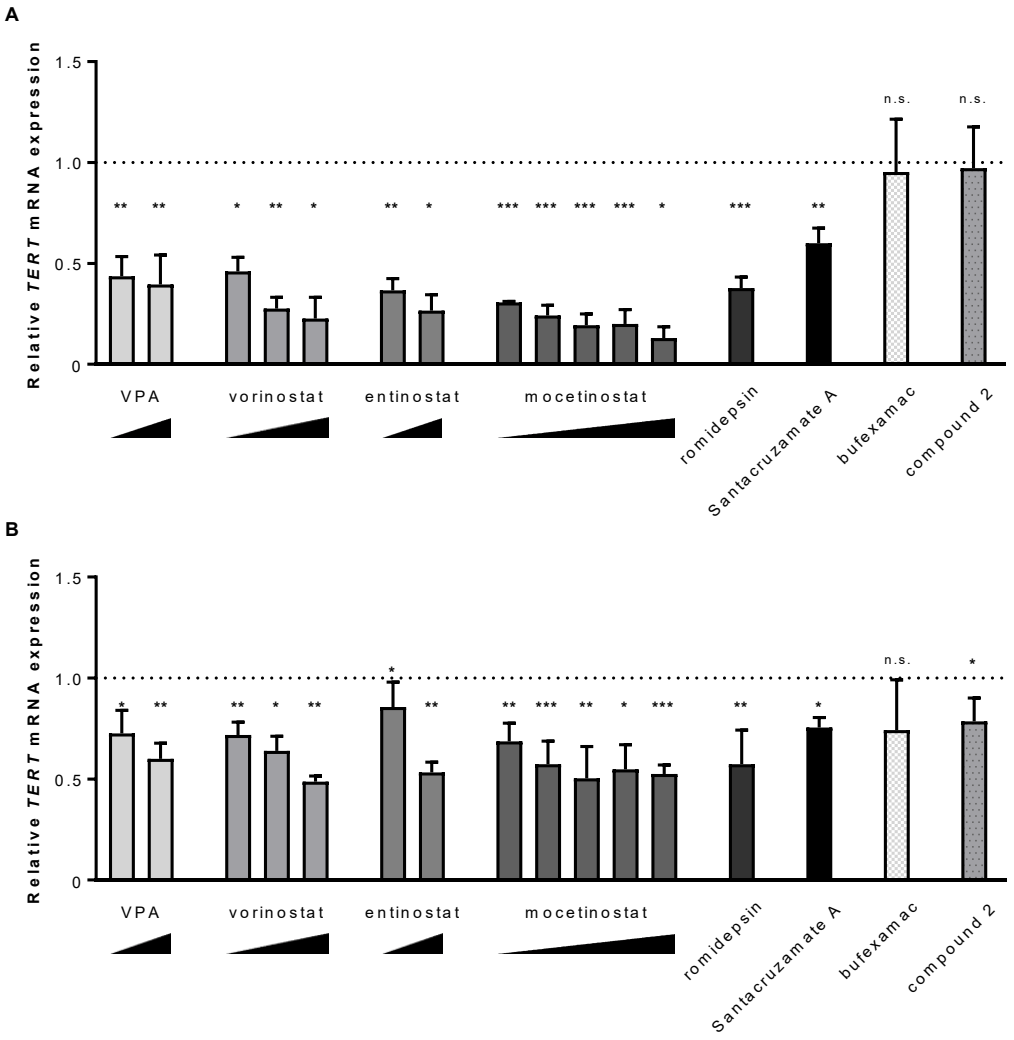

Figure 21: TERT mRNA expression is reduced by HDACi treatment.
A, GI-ME-N and (**B**) CLB-GA cells were treated for 48 h with valproic acid (VPA) (1, 2 mM), vorinostat (0.5, 1, 2 µM), entinostat (0.25, 0.5 µM), mocetinostat (0.1, 0.25, 0.5, 0.75, 1 µM), romidepsin (3 nM), Santacruzamate A (1 nM), bufexamac (30 µM) or compound 2 (20 µM). *TERT* expression was analyzed by qRT-PCR (mean fold change over solvent ± SD; n≥2). Dotted lines indicate control value. *P≤0.05, **P≤0.01, ***P≤0.001, n.s.: not significant.

TERT mRNA expression was reduced to 13-60% in GI-ME-N and to 49-86% in CLB-GA after HDACi treatment with VPA, vorinostat, entinostat, mocetinostat, romidepsin and Santacruzamate A (Figure 21 A and B). HDAC inhibitors bufexamac and compound 2 merely affected *TERT* mRNA levels. Moreover, the inhibitors specifically targeting HDAC1 and HDAC2 such as mocetinostat, romidepsin and Santacruzamate A downregulate *TERT* expression at low nanomolar concentrations (Figure 21 A, B). Together, the repression of *TERT* mRNA level is not a specific effect of panobinostat treatment but a common event upon HDACi

treatment, and is mediated by clinically approved HDAC1 and HDAC2 inhibitors such as vorinostat, romidepsin and panobinostat.

4.1.2 Histone deacetylase inhibition suppresses telomerase activity in *TERT*-driven neuroblastoma cells

Reduced *TERT* mRNA levels may translate into less activity of the telomerase holoenzymatic complex. To assess whether treatment with HDACi results in reduced activity of telomerase, a PCR-based ELISA was used to quantify telomerase activity. Panobinostat or mocetinostat treatment was applied to GI-ME-N cells for 96-144 h and to CLB-GA cells for 24-72 h. HDACi treatment suppresses telomerase activity in *MYCN*-amplified cell lines, where MYCN regulates the expression of its downstream target *TERT* (Deubzer, 2008; Shahbazi, 2016). To compare telomerase levels after HDACi treatment in *TERT*-rearranged and in *MYCN*-amplified neuroblastoma cell lines, the *MYCN*-amplified cell lines BE(2)-C and IMR-5/75 were included in the panel and treated with 15 nM panobinostat for 48 h. The non *MYCN*-amplified, not *TERT*-rearranged cell line LAN-6 has little telomerase activity and served as a control.

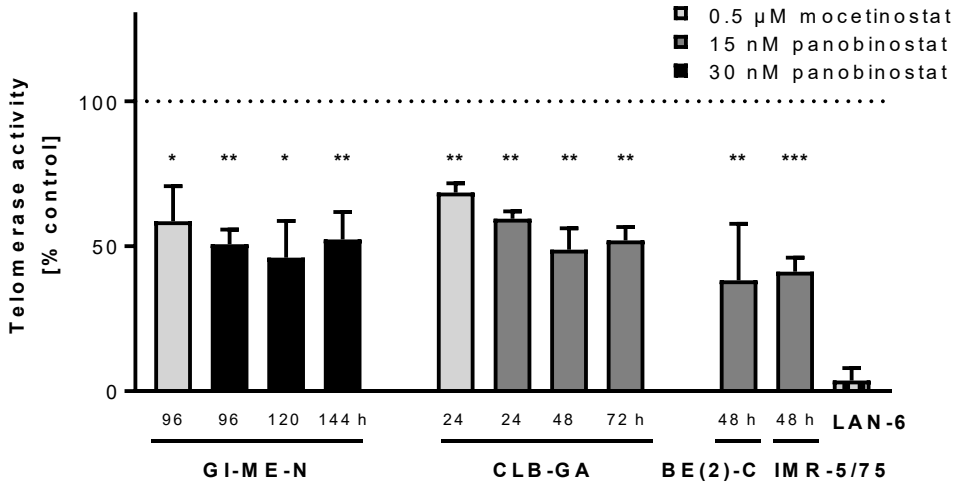

Figure 22: Telomerase activity is decreased after HDACi treatment.
Cell lines were treated with mocetinostat or panobinostat, LAN-6 cells were harvested untreated and normalized to internal control. Telomerase activity was measured by ELISA (mean % over solvent/internal control ± SD; n≥3). Dotted line indicates control value. *P≤0.05, **P≤0.01, ***P≤0.001.

Panobinostat treatment resulted in a 2-fold reduction of telomerase activity in GI-ME-N and CLB-GA cell lines after several days of treatment (Figure 22). Mocetinostat reduced telomerase activity to 59% after 96 h in GI-ME-N and to 69% after 24 h in CLB-GA. Telomerase activity

in BE(2)-C was reduced to 38% and to 41% in IMR-5/75 cell lines (Figure 22). Untreated LAN-6 cells showed a low level of 4% telomerase activity (Figure 22). These data show that HDAC inhibition induces a decrease of telomerase activity in *TERT*-rearranged neuroblastoma cells, and that the repression of telomerase activity after HDACi treatment was similar in the *MYCN*-amplified cell lines BE(2)-C and IMR-5/75, where MYCN regulates the expression of its downstream target *TERT*.

4.1.3 Enforced *TERT* expression partially rescues the anti-proliferative effect of HDAC inhibition

HDAC inhibitor treatment results in strong antitumoral effects across cancer entities including neuroblastoma (Lodrini, 2013; Fabian, 2014). To investigate the phenotypic consequences of *TERT* repression by HDAC inhibition on neuroblastoma cells, a rescue experiment in GI-ME-N cells was performed using a *TERT* plasmid and its respective empty vector control. The plasmid used to transiently enforce *TERT* expression harbored a point mutation in the coding sequence. The nucleobase adenine at plasmid position 2982 was mutated to guanine (A2982→G). To exclude possible effects of this point mutation, the sequence was re-mutated back to the reference sequence (section 3.3.2). After successful cloning, the plasmid and the corresponding empty vector (pBABE-neo) were used for transfection. Efficacy of the plasmid was tested by analysis of *TERT* mRNA expression and telomerase activity in untreated GI-ME-N and CLB-GA cells (section 6.2.2). For subsequent transfection experiments, the treatment period of 72 h after transfection was used to ensure high *TERT* levels and telomerase activity in transfected cells throughout the experiment (section 6.2.2). Three different HDACi were used for treatment to investigate the effect of this substance class on transfected neuroblastoma cells. Since HDAC inhibitors have a severe impact on divert pathways and show strong antitumoral effects at clinically relevant concentrations, the inhibitor concentrations were decreased to reduce unspecific effects of the treatment. GI-ME-N cells were transfected with the *TERT* expressing plasmid, and 24 h post transfection the cells were treated for 72 h with HDAC inhibitors panobinostat, entinostat or mocetinostat, all targeting class I HDACs. Empty vector transfected cells were used as control. Cell viability was measured by automated trypan blue stained cell counting (Figure 23, upper panel). To control transfection efficacy in transfected and treated cells, *TERT* mRNA levels were measured by qRT-PCR.

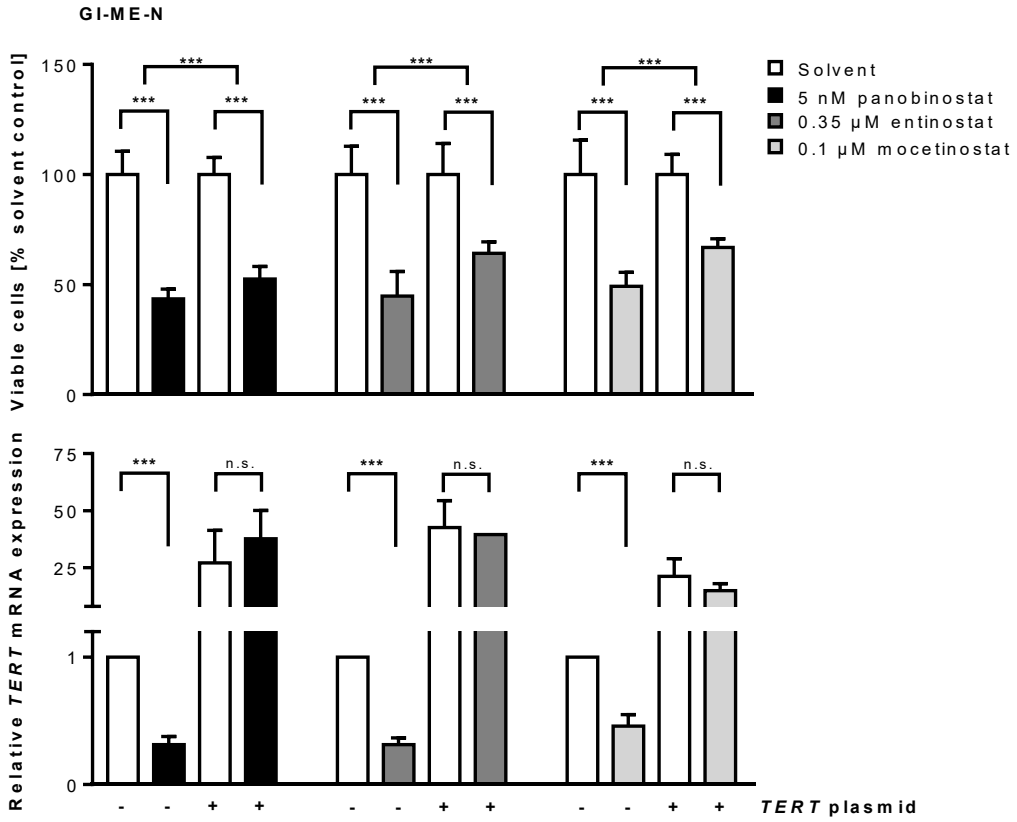

Figure 23: Enforced TERT expression partially rescues HDACi induces antitumoral phenotype.
GI-ME-N cells were transfected with either empty vector or *TERT* plasmid. Cells were treated for 72 h with panobinostat, entinostat or mocetinostat. (A) Viable cell numbers by semi-automated trypan blue staining (mean % over solvent ± SD; n≥3) and (B) *TERT* mRNA expression analyzed by qRT-PCR (mean fold change over solvent ± SD; n≥3). ***P≤0.001, n.s.: not significant.

Panobinostat treatment reduced cell viability to 43% in empty vector transfected cells and this reduction in cell viability was rescued to 55% after enforced *TERT* expression (Figure 23, lower panel). Treatment with entinostat decreased cell viability to 45%, which was rescued to 64% after enforced *TERT* expression. Mocetinostat treatment resulted in a decrease of cell viability to 49% in empty vector transfected cells and increased to 67% in cells transfected with the *TERT* plasmid. *TERT* mRNA transcript levels induced by plasmid transfection were not changed by HDACi treatment. These experiments demonstrate that enforced *TERT* expression partially rescued the HDACi induced antitumoral phenotype and increased cell viability under HDACi treatment. This observation stresses the importance of *TERT* expression in GI-ME-N neuroblastoma cell viability and underlines the need for therapeutic interventions targeting *TERT*.

4.2 HDAC1 and HDAC2 inhibition mediates *TERT* repression

Treatment with pan-HDAC inhibitors panobinostat, valproic acid and vorinostat results in downregulation of *TERT* expression. The specific class I HDAC inhibitor mocetinostat, the HDAC1 and HDAC2 specific inhibitor romidepsin and the specific HDAC2 inhibitor Santacruzamate A showed repressive effects on *TERT* levels. To investigate the role of HDAC1 and HDAC2 in the regulation of *TERT*, transient knockdown of HDAC1 and HDAC2 using pooled small interfering RNA (siRNA) was performed in GI-ME-N cells. Commercially available siRNA pools of 30 optimally designed siRNAs were used for each target. Transfection with mock or negative control (NC) siRNA were included. Expression measured by qRT-PCR and western blot analysis were performed 72 h post transfection.

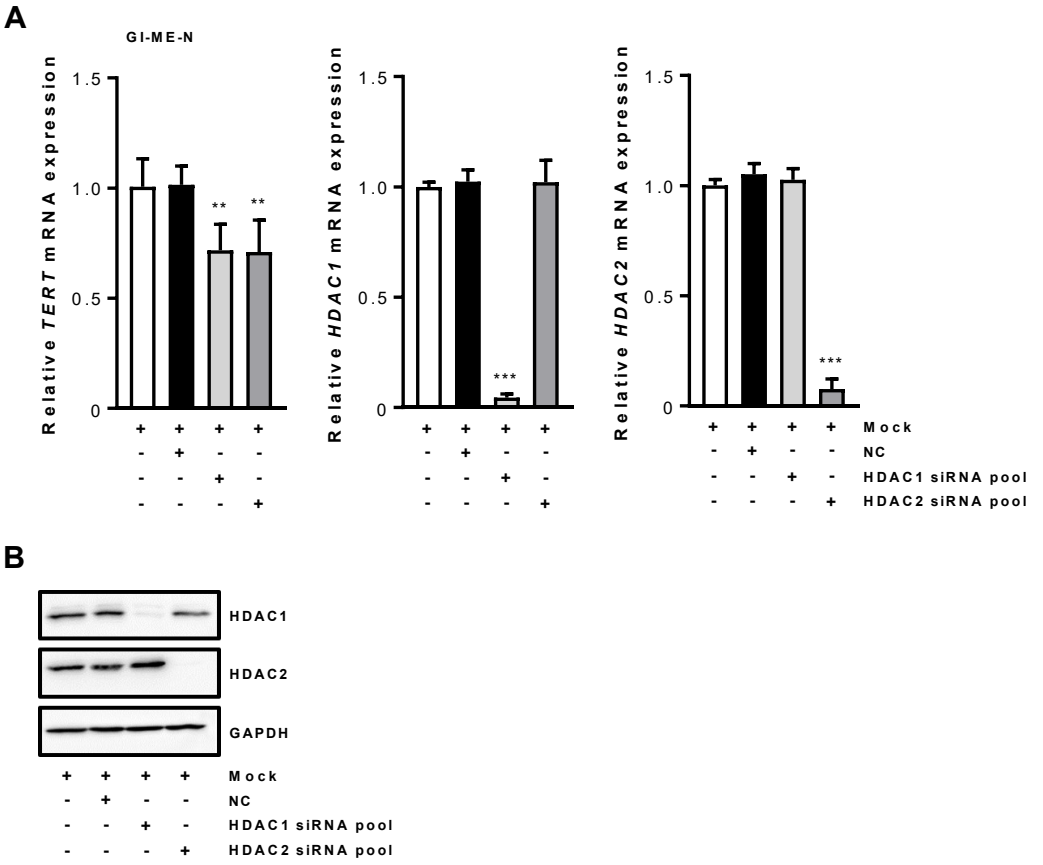

Figure 24: Knockdown of HDAC1 and HDAC2 results in reduction of TERT mRNA levels.
Analysis of *TERT* and *HDAC* expression in GI-ME-N cells after transfection with pooled siRNA or controls and western blot analysis of HDAC1 and HDAC2. **A**, Expression was analyzed 72 h after transfection with siRNA by qRT-PCR (mean fold change over mock control ± SD; n≥4). **B**, Representative western blot analysis of GI-ME-N cells 72 h after transfection with siRNA (20 nM) (lanes 3-4) or controls (lanes 1-2). GAPDH served as a loading control. NC: Negative control. **P≤0.01, ***P≤0.001.

Knockdown with pooled siRNAs resulted in knockdown efficacies of 95% for *HDAC1* and of 92% for *HDAC2* after 72 h (Figure 24 A, right panels). Western blot analysis of HDAC1 and

HDAC2 after transfection with siRNA revealed reduction of protein levels after targeted knockdown after 72 h (Figure 24 B). RNA expression analysis revealed that *TERT* mRNA levels were significantly decreased after knockdown of *HDAC1* to 72% and of *HDAC2* to 71% after 72 h (Figure 24 A, left panel). In conclusion, this data shows that inhibition of HDAC1 and HDAC2 mediates the repression of *TERT* mRNA in *TERT*-rearranged neuroblastoma cells.

4.3 Influence of conventional chemotherapeutics and targeted drugs on telomerase activity in *TERT*-driven neuroblastoma cells

4.3.1 Chemotherapeutics or targeted drugs do not repress telomerase

To investigate whether standard-of-care or targeted drugs reduce *TERT* expression or telomerase activity, a panel of chemotherapeutic or targeted agents for treatment of *TERT*-rearranged neuroblastoma cell lines was analyzed. Topoisomerase II inhibitor doxorubicin (DOX), DNA-binding agent oxaliplatin, and the alkylating agent temozolomide (TMZ) were selected as representatives for chemotherapeutic or targeted agents used in neuroblastoma therapy. Temozolomide is used in the study protocol RIST-rNB-2011 for treatment of high-risk neuroblastoma patients (NCT01467986, NIH, 2020). Doxorubicin is used in N6 cycle and cis-platin is used in N5 cycle of the NB2004 trial protocol for treatment of medium risk and high-risk groups (Figure 4) (NCT03042429, NIH, 2020). As alternative for cis-platin, the platin-based drug oxaliplatin was used instead since it reacts less with DMSO, which is used as dissolvent in the *in vitro* experiments in this study (Hall, 2014). I-BET762 was chosen as representative of bromodomain and extra-terminal motif (BET) inhibitors, which showed promising effects in *MYCN*-amplified neuroblastoma and are being investigated in preclinical models of pediatric cancer (Wyce, 2013). BETi indirectly downregulate *MYCN* levels, resulting in less expression of its downstream target *TERT*. Treatment of GI-ME-N and CLB-GA cells was performed for 48 h at clinically relevant concentrations. Since doxorubicin and oxaliplatin have a strong antitumoral effect on the CLB-GA cell line, lower concentrations were used for treatment. *TERT* expression and telomerase activity were quantified by qRT-PCR and telomerase activity assay after treatment.

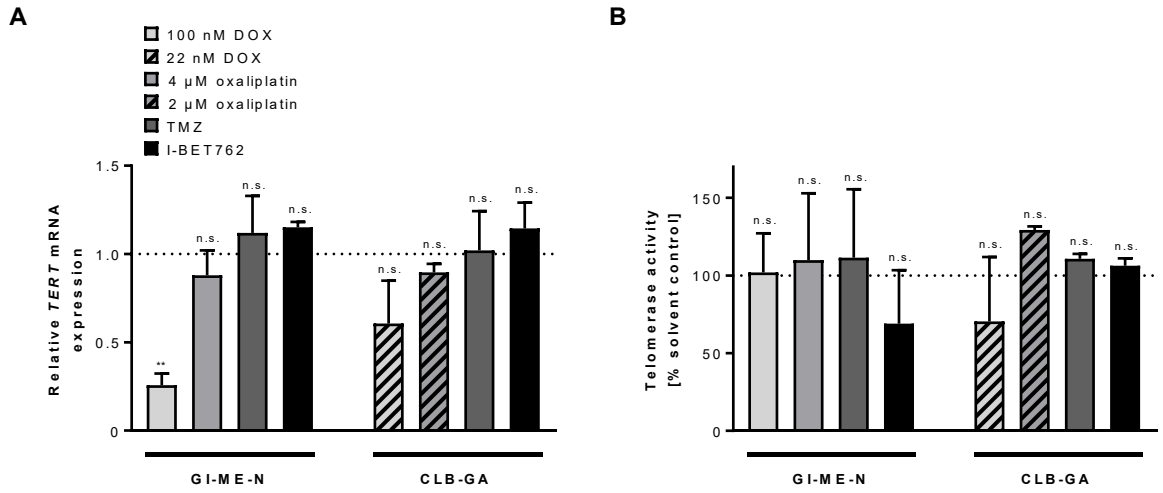

Figure 25: Telomerase activity is not decreased by treatment with chemotherapeutic or targeted agents.
GI-ME-N and CLB-GA cells were treated for 48 h with doxorubicin (DOX), oxaliplatin, temozolomide (TMZ) or I-BET762. **A**, *TERT* mRNA expression analysis after 48 h and (**B**) telomerase activity assay after 96 h (GI-ME-N) and 24 h (CLB-GA). *TERT* expression was analyzed by qRT-PCR (mean fold change over solvent ± SD; n≥3) and telomerase activity was measured by ELISA (mean % over solvent ± SD; n≥3). Dotted lines indicate control value. **P≤0.01, n.s.: not significant.

Treatment of GI-ME-N cells with doxorubicin resulted in decreased *TERT* levels to 26% (Figure 25 A). None of the other treatments with standard therapeutics or targeted drugs tested resulted in a significant downregulation of *TERT* mRNA. These drugs might still have an impact on telomerase activity. Subsequently, telomerase activity was assessed after treatment with doxorubicin, oxaliplatin, temozolomide or I-BET762 in GI-ME-N (96 h) and CLB-GA (24 h) cells. Telomerase activity was not reduced in GI-ME-N and CLB-GA cells by treatment with these compounds (Figure 25 B), showing that none of the drugs tested changed telomerase activity in *TERT*-rearranged neuroblastoma cell lines. To summarize, the tested clinically relevant therapeutics do not reduce telomerase activity as achieved by HDACi treatment with panobinostat.

4.3.2 Panobinostat and telomerase inhibitor treatment reduces cell viability of *TERT*-rearranged cell lines

Enforced expression of *TERT* increased cell viability and partially rescued the antitumoral phenotype after HDAC inhibitor treatment. To compare the antitumoral effect of panobinostat with specific telomerase inhibitors, cell viability after treatment was assessed. There are no clinically successful telomerase inhibitors (Ait-Aissa, 2016). From the commercially available

in vitro inhibitors that directly target telomerase, BIBR1532 and costunolide were used for the analyses. GI-ME-N and CLB-GA cells were treated with BIBR1532, costunolide or panobinostat for 72 h. The number of dead cells was quantified using trypan blue staining and automated cell counting.

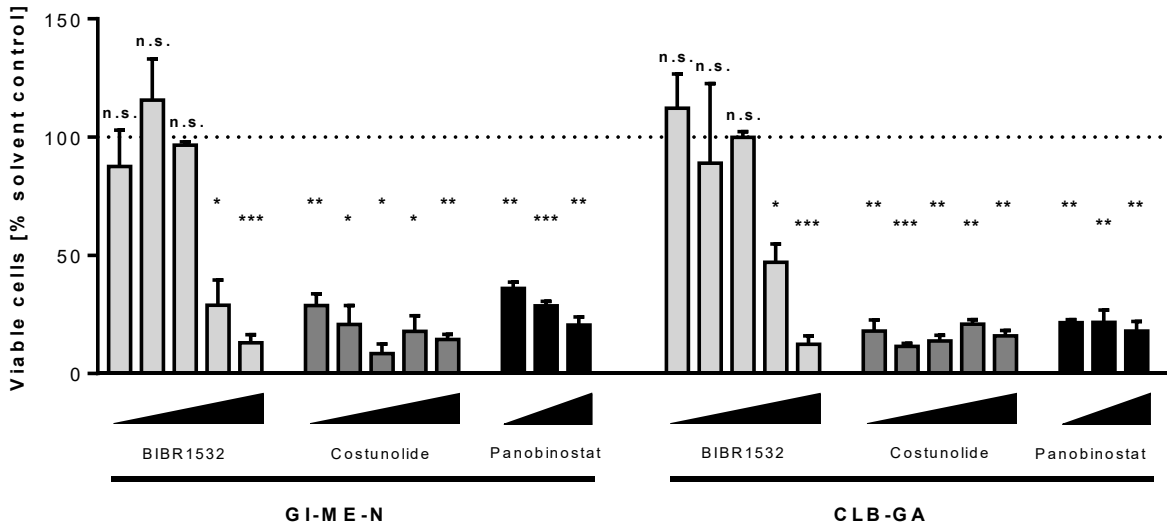

Figure 26: Cell viability decreases after telomerase inhibitor or panobinostat treatment in GI-ME-N and CLB-GA cells.
GI-ME-N or CLB-GA cells were treated for 72 h with BIBR1532 (5, 10, 25, 50, 100 µM), costunolide (5, 10, 25, 50, 100 µM) or panobinostat (7.5, 15, 30 nM). Viable cell number count by semi-automated trypan blue staining (mean % over solvent ± SD; n≥3). Dotted line indicates control value. *P≤0.05, **P≤0.01, ***P≤0.001, n.s.: not significant.

A concentration of 100 µM BIBR1532 resulted in a decrease of cell viability to 13% in GI-ME-N and to 12% in CLB-GA cells (Figure 26). Treatment with 100 µM costunolide reduced cell viability to 14% in GI-ME-N and to 16% in CLB-GA cells. Treatment with panobinostat reduced cell viability to 20% in GI-ME-N and to 18% in CLB-GA cells at 30 nM (Figure 26). Low nanomolar concentrations of panobinostat decreases cell viability as effectively as micromolar concentrations of targeted drugs on telomerase in *TERT*-driven neuroblastoma cell lines. Taken together, *in vitro* telomerase inhibitors BIBR1532 and costunolide reduce cell viability as achieved by panobinostat treatment.

4.4 Evaluation of panobinostat in preclinical *in vivo* models of *TERT*-driven neuroblastoma

4.4.1 Panobinostat treatment suppresses *TERT* transcript levels and telomerase activity in xenografted tumors in mice in a preventive treatment schedule

Panobinostat treatment reduces cell *TERT* mRNA level and telomerase activity in cell culture models of *TERT*-rearranged high-risk neuroblastoma. To investigate the influence of panobinostat treatment on *TERT* expression and telomerase activity *in vivo*, neuroblastoma xenograft mouse models of *TERT*-rearranged neuroblastoma were established. From previous studies, an effective application method at patient plasma concentration could be adapted (Lodrini, 2013; Wong, 2019). Mouse experiments were performed by Annika Sprüssel and Daniela Tiburtius. GI-ME-N and CLB-GA cells were used for xenotransplantation into the right flank of immunosuppressed 8-week-old athymic female NMRI-Foxn1$^{nu/nu}$ nude mice. For the GI-ME-N xenograft model, 5 x10^6 cells per animal were suspended in Matrigel™ for tumor cell inoculation, for the CLB-GA xenograft model 20 x10^6 cells were used. In a preventive treatment schedule, animals were treated when tumors reached a volume of about 150 mm³. Animals were randomized and treated with solvent (DMSO) or panobinostat 15 mg/kg/d bodyweight, each dissolved in 5% glucose solution applied via intraperitoneal injection. Treatment was applied for five consecutive days followed by two days offset of treatment to counteract potential weight loss under therapy (Figure 27). Tumor volume determination using a caliper and bodyweight were measured daily. Animals were sacrificed when tumor volume reached 1500 mm³.

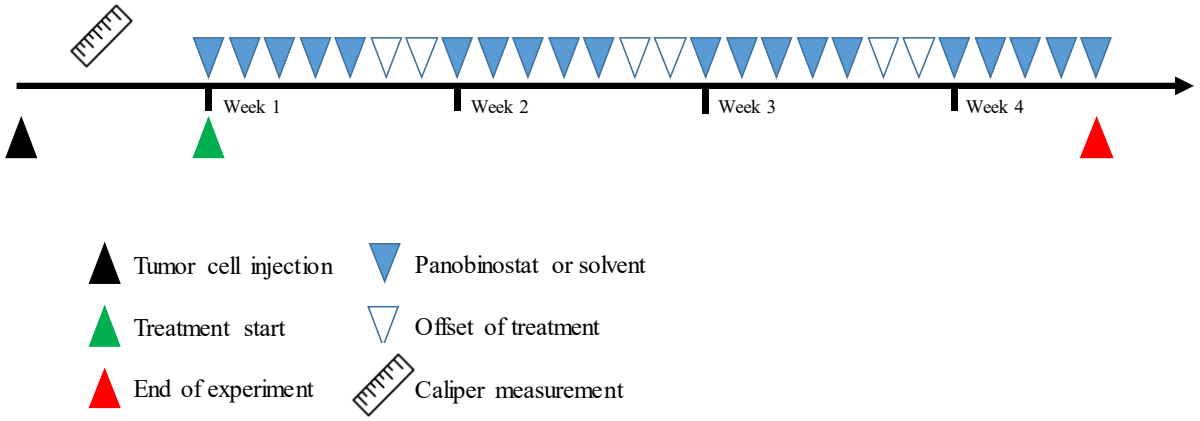

Figure 27: Panobinostat treatment schedule in TERT-driven neuroblastoma xenograft mouse models.
Solvent or 15 mg/kg/d panobinostat was applied to xenografted mice for five consecutive days, followed by two days offset of treatment. Animals were treated for a maximum of four weeks.

GI-ME-N xenografted mice were treated for a maximum of 25 days. The GI-ME-N tumors showed a slow engraftment and mice carrying GI-ME-N xenograft tumors showed ulcerations at tumor sites, which was treated with application of wound healing ointment. After 25 days, the experiment was terminated in accordance with animal welfare laws. Xenograft tumor growth was reduced after panobinostat treatment in the GI-ME-N xenograft model compared to solvent-treated controls (Figure 28 A). Solvent treated GI-ME-N xenograft tumors had an average size of 685 mm^3 at the end of the experiment compared to 352 mm^3 in the panobinostat treated tumors (Figure 29 A).

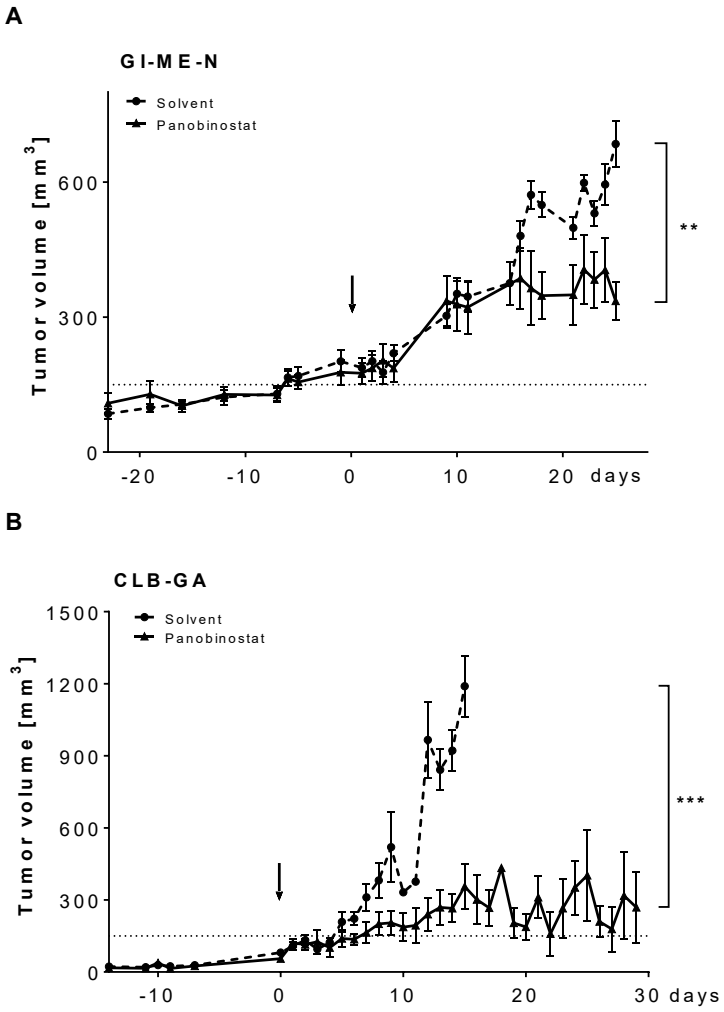

Figure 28: Panobinostat treatment reduces xenograft tumor growth in GI-ME-N and CLB-GA mouse models in a preventive treatment schedule.
Xenograft tumor growth of the GI-ME-N and CLB-GA neuroblastoma mouse models in a preventive treatment schedule. Tumor volume was measured daily (mean ± SEM, n≥6). **A**, GI-ME-N xenograft tumors treated with panobinostat 15 mg/kg/d (n=7) or solvent (DMSO) (n=6). **B,** CLB-GA xenograft tumors treated with panobinostat 15 mg/kg/d (n=8) or solvent (DMSO) (n=7). Dotted lines indicate tumor volumes at onset of treatment. Arrows indicate onset of treatment. For statistical analysis, tumor volumes at day 25 for the GI-ME-N model and at day 15 for the CLB-GA model were compared. Statistical testing via area under the curve analysis after termination of solvent treated cohort. **P≤0.01, ***P≤0.001.

CLB-GA xenografted mice were treated for a maximum of 29 days. Xenograft tumor growth was inhibited under panobinostat treatment in the CLB-GA xenograft model (Figure 28 B). Solvent treated CLB-GA xenograft tumors had a final average tumor volume of 1162 mm³ compared to 309 mm³ in the panobinostat treated cohort (Figure 29 B). Together, the final tumor volumes of panobinostat treated xenograft tumors compared to solvent treated xenograft tumors demonstrated smaller tumors in the panobinostat treated cohort.

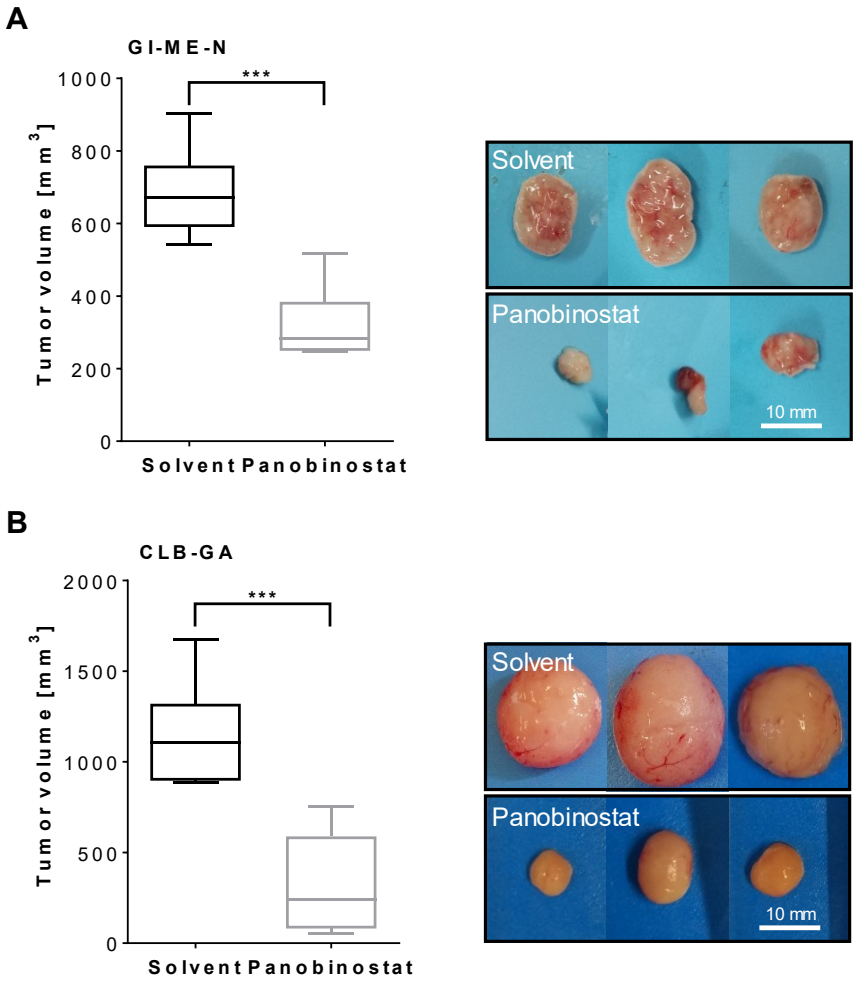

Figure 29: Panobinostat treatment reduces tumor volumes in xenograft tumor volumes in GI-ME-N and CLB-GA mouse models in a preventive treatment schedule.
Xenograft tumor volumes at termination of experiment or when maximum tumor volume was reached are depicted as box plots (mean ± SEM, n≥6), and exemplarily shown as pictures. **A**, GI-ME-N xenograft tumors treated with panobinostat 15 mg/kg/d (n=7) or solvent (DMSO) (n=6) and photographed tumors after explantation. **B**, CLB-GA xenograft tumors treated with panobinostat 15 mg/kg/d (n=8) or solvent (DMSO) (n=7) and photographed tumors after explantation. For statistical analysis, tumor volumes at day 25 for the GI-ME-N model and at day 29 for the CLB-GA model were compared. ***P≤0.001.

For the CLB-GA model of the preventive treatment schedule, Kaplan-Meier survival curves were generated. Kaplan-Meier survival analysis of CLB-GA xenografted animals showed that panobinostat treatment resulted in extended survival of animals compared to solvent-treated controls (Figure 30).

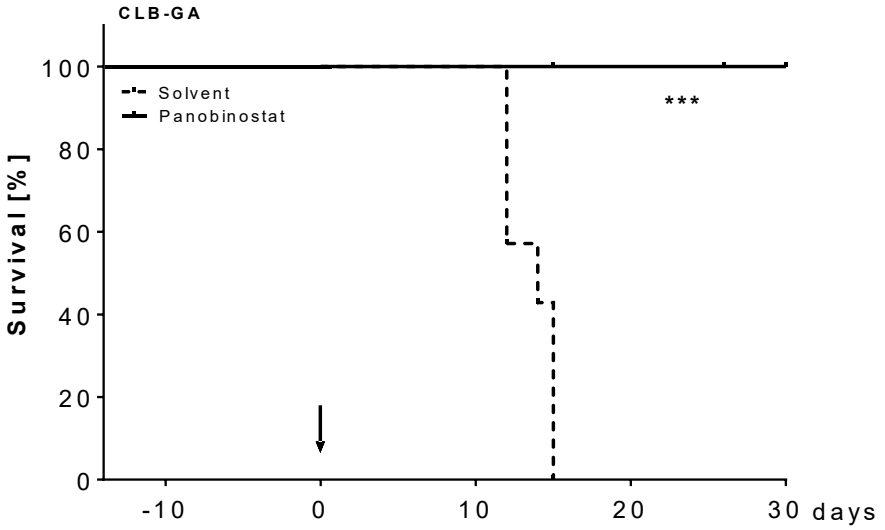

Figure 30: Panobinostat treatment increases survival of CLB-GA xenografted mice.
Kaplan-Meier analysis of overall survival of CLB-GA xenografted mice (mean, n≥7). CLB-GA xenograft mice were treated with panobinostat 15 mg/kg/d (n=8) or solvent (DMSO) (n=7). Arrow indicates onset of treatment. ***P≤0.001.

Punch biopsies from each xenograft tumor were taken for further analyses. For the molecular analyses, cryosections of the tumors were prepared and lysed. To measure *TERT* mRNA levels, qRT-PCR expression analysis was performed. *TERT* expression was reduced to 61% in animals treated with panobinostat in GI-ME-N xenograft tumors compared to solvent-treated animals (Figure 31). In CLB-GA xenografted mice, *TERT* expression was reduced to 56% after panobinostat treatment compared to solvent-treated controls (Figure 31).

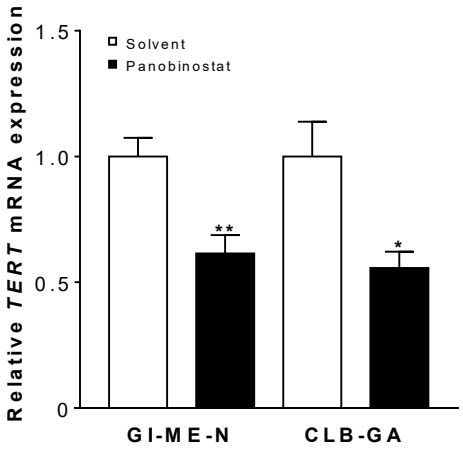

Figure 31: TERT mRNA expression is reduced in xenograft tumors treated with panobinostat in GI-ME-N and CLB-GA mouse models in a preventive treatment schedule.
TERT mRNA expression analysis in GI-ME-N xenograft tumors treated with panobinostat 15 mg/kg/d (n=7) or solvent (DMSO) (n=6) and in CLB-GA xenograft tumors treated with panobinostat 15 mg/kg/d (n=8) or solvent (DMSO) (n=7). *TERT* expression was analyzed by qRT-PCR (mean fold change over solvent ± SEM; n≥6). *P≤0.05, **P≤0.01.

Subsequently, telomerase activity was quantified in xenograft tumors. Telomerase activity was reduced to about 10% in GI-ME-N xenograft tumors after panobinostat treatment compared to solvent-treated animals (Figure 32). In CLB-GA xenografted mice receiving panobinostat, telomerase activity was reduced to 23% compared to solvent-treated control animals (Figure 32). Reduction of telomerase activity *in vivo* was stronger reduced than in the *in vitro* cell culture models.

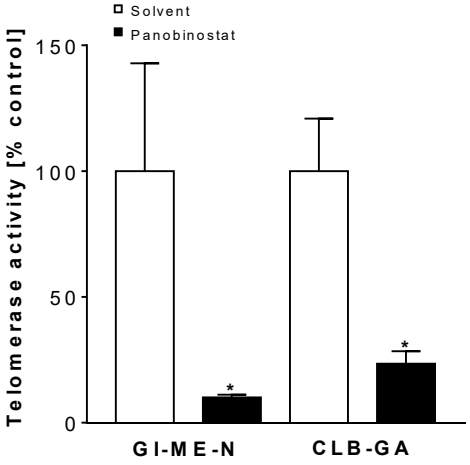

Figure 32: Telomerase activity in xenograft tumors in GI-ME-N and CLB-GA mouse models in a preventive treatment schedule.
Telomerase activity in GI-ME-N xenograft tumors treated with panobinostat 15 mg/kg/d (n=7) or solvent (DMSO) (n=6) and in CLB-GA xenograft tumors treated with panobinostat 15 mg/kg/d (n=8) or solvent (DMSO) (n=7). Telomerase activity was measured by ELISA (mean % over solvent ± SEM; n≥6). *P≤0.05, **P≤0.01.

Reduced xenograft tumor growth, *TERT* expression and telomerase activity after panobinostat treatment were reproduced in a second animal study applying the preventive treatment schedule and confirmed the previous results in independent cohorts of each model (data not shown). Taken together, panobinostat treatment represses *TERT* mRNA expression and telomerase activity in xenograft models of *TERT*-rearranged high-risk neuroblastoma, and has strong antitumoral efficacy in a preventive treatment schedule.

4.4.2 Panobinostat treatment reduces *TERT* transcript levels and telomerase activity in xenografted tumors in mice in a therapeutic treatment schedule

Patients initially presenting with neuroblastoma often show progressed disease. Therefore, a therapeutic treatment schedule was investigated in the CLB-GA xenograft model to investigate how panobinostat treatment affects *TERT* transcript levels and telomerase activity in highly proliferating tumors. Since the GI-ME-N xenograft model showed slow tumor engraftment, low tumor take rates and triggered an inflammatory response, the CLB-GA model was chosen for further analyses. Mouse experiments were performed by Annika Sprüssel and Daniela Tiburtius. To investigate the dose-efficacy of the treatment, a lower concentration of 7.5 mg/kg/d panobinostat was included. For each xenotransplantation, 20 $x10^6$ CLB-GA cells were transplanted into the right flank of immunosuppressed 8-week-old athymic female NMRI-Foxn1$^{nu/nu}$ nude mice. In a therapeutic treatment schedule, animals were treated when tumors reached a volume of about 300 mm³. Animals were randomized and treated with 7.5-15 mg/kg/d panobinostat or solvent (DMSO), each dissolved in 5% glucose solution applied via intraperitoneal injection. Treatment was applied for five consecutive days followed by two days offset of treatment (Figure 27). Tumor volume determination using a caliper and bodyweight were measured daily. All animals were sacrificed at day eleven of treatment when tumor volume of control animals reached 1500 mm³.

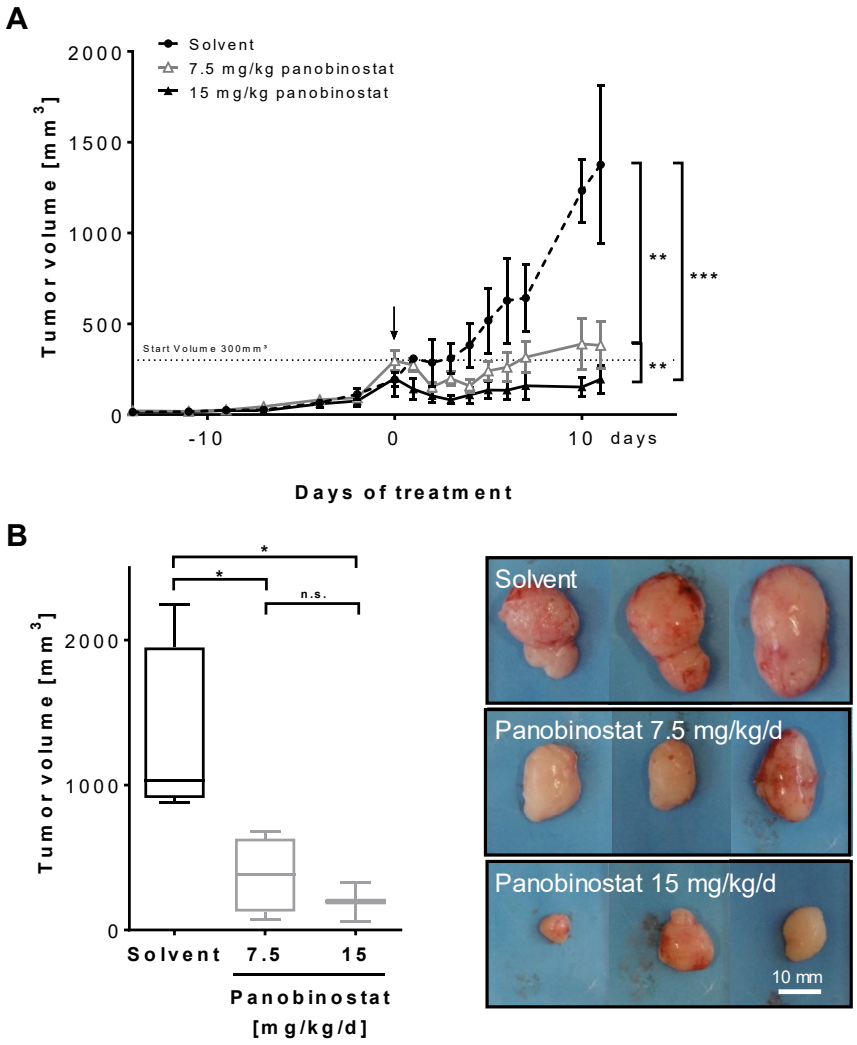

Figure 33: Panobinostat treatment reduces xenograft tumor growth in a CLB-GA mouse model in a therapeutic treatment schedule.
Xenograft tumor growth of the CLB-GA neuroblastoma mouse model in a therapeutic treatment schedule and tumor volumes depicted as box plot and exemplarily shown as pictures. Tumor volume was measured daily (mean ± SEM, n≥3). **A**, Tumor volumes of CLB-GA xenograft tumors treated with 15 mg/kg/d panobinostat (n=3) and 7.5 mg/kg/d panobinostat (n=4) or solvent (DMSO) (n=4). **B**, Xenograft tumor volumes are depicted as box plots at day 11 (mean ± SEM, n≥3) and photographed tumors after explantation. Dotted line indicates tumor volume at onset of treatment. Arrow indicates onset of treatment. Statistical testing of tumor growth via area under the curve analysis. *P≤0.05, **P≤0.01, ***P≤0.001, n.s.: not significant.

Tumor growth and tumor volumes were significantly reduced after panobinostat treatment (Figure 33). Solvent treated CLB-GA xenograft tumors had an average size of 1297 mm³ compared to 382 mm³ in the 7.5 mg/kg/d panobinostat and to 194 mm³ in the 15 mg/kg/d panobinostat treated cohorts. Punch biopsies from each xenograft tumor were taken for further analyses. For the *in vitro* assays, cryosections of the tumors were prepared and lysed. To measure *TERT* mRNA levels, qRT-PCR expression analysis was performed. *TERT* expression was reduced to 58% in the 7.5 mg/kg/d cohort and to 47% in animals treated with 15 mg/kg/d

panobinostat compared to animals receiving solvent treatment (Figure 34). After panobinostat treatment, telomerase activity decreased to 17% in the 7.5 mg/kg/d panobinostat cohort and to 22% in xenograft tumors treated with 15 mg/kg/d panobinostat compared to solvent-treated animals (Figure 34).

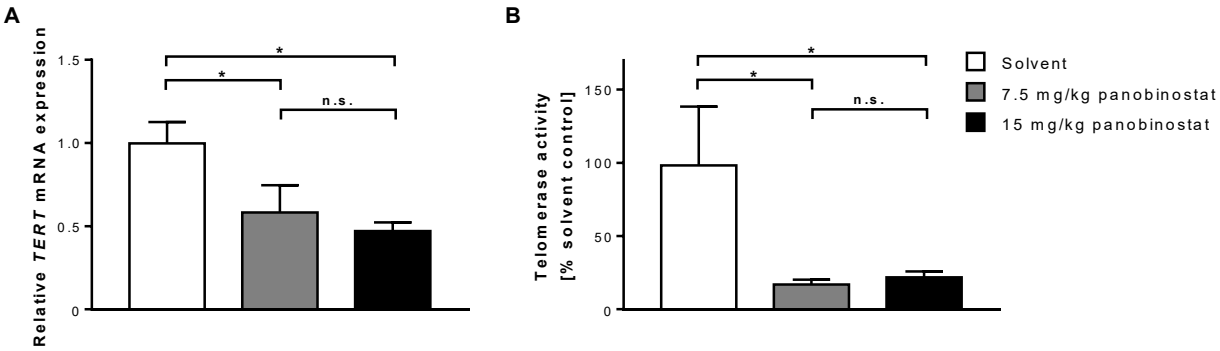

Figure 34: TERT expression and telomerase activity are reduced in xenograft tumors treated with panobinostat in a CLB-GA mouse model in a therapeutic treatment schedule.
A, *TERT* mRNA expression analysis in CLB-GA xenograft tumors treated with panobinostat 15 mg/kg/d (n=3), panobinostat 7.5 mg/kg/d (n=4) or solvent (DMSO) (n=4). *TERT* expression was analyzed by qRT-PCR (mean fold change over solvent ± SEM; n≥3). **B**, Telomerase activity in CLB-GA xenograft tumors treated with panobinostat 15 mg/kg/d (n=3) and 7.5 mg/kg/d (n=4) or solvent (DMSO) (n=4). Telomerase activity was measured by ELISA (mean % over solvent ± SEM; n≥3). *P≤0.05, n.s.: not significant.

As in the preventive treatment schedule, telomerase activity was stronger reduced than *TERT* mRNA levels following the therapeutic treatment schedule. There was no significant difference between the 7.5 mg/kg/d panobinostat and the 15 mg/kg/d panobinostat cohorts regarding tumor volume, *TERT* expression and telomerase activity after eleven days of treatment. These results are in line with previous observations in the preventive approach and demonstrate that panobinostat treatment reduces *TERT* expression and telomerase activity in xenograft mouse models of *TERT*-rearranged neuroblastoma in a therapeutic treatment schedule.

4.5 Epigenomic analyses reveal no major changes at the *TERT* locus by panobinostat treatment

Panobinostat treatment decreases *TERT* levels and telomerase activity in models of *TERT*-rearranged high-risk neuroblastoma. HDAC inhibition is generally considered to result in a more open chromatin state, thereby enabling gene transcription (de Ruijter, 2003; Roth, 2001). Epigenetic remodeling towards an activated chromatin state was described showing histone

marks H3K27ac and H3K4me1to be often enriched at super-enhancer elements (Chipumuro, 2014; Loven, 2013), which was also described in *TERT*-rearranged neuroblastoma (Gartlgruber, 2018; Peifer, 2015; Valentijn, 2015). To gain inside the epigenetic regulation after panobinostat treatment, the individual profile of the rearranged *TERT* region was identified (section 6.1) and subsequently chromatin immunoprecipitation (ChIP) sequencing and methylation array profiling were performed.

4.5.1 Panobinostat treatment triggers no major changes in chromatin marks associated with the *TERT* locus

Epigenetic modifications such as histone marks or methylation status of CpG islands regulate DNA accessibility and gene transcription. The epigenetic agent panobinostat might influence the chromatin state and mediate reduction of *TERT* expression by formation of condensed chromatin at the *TERT* locus. To understand how panobinostat influences expression of the *TERT* gene, ChIP sequencing analysis was performed. Because the reduction of *TERT* levels after panobinostat treatment is stronger in GI-ME-N than in CLB-GA cells, GI-ME-N cells were used for the analysis. The four histone modifications acetylation of histone 3 at lysine residue 27 (H3K27ac), trimethylation of histone 3 at lysine residue 4 (H3K4me3), trimethylation of histone 3 at lysine residue 36 (H3K36me3) and monomethylation of histone 3 at lysine residue 4 (H3K4me1) were selected for the analyses of histone marks. These marks represent histone modifications indicative of an open chromatin structure and enabled gene transcription. In addition, the two histone modifications standing for a condensed chromatin state and disabled gene transcription trimethylation of histone 3 at lysine residue 27 (H3K27me3) and trimethylation of histone 3 at lysine residue 9 (H3K9me3) were chosen for the analyses (Peifer, 2015; Henrich, 2016). *TERT* mRNA expression is reduced to about 50% after 18 h of panobinostat treatment in GI-ME-N cells (section 4.1.1). This rather early time-point was chosen for subsequent ChIP sequencing analysis to capture early events after panobinostat treatment and to reduce further effects of elongated treatment. Cells were treated with solvent (DMSO) or 30 nM panobinostat for 18 h. Fragmentation of precipitated DNA was controlled by agarose gel electrophoresis.

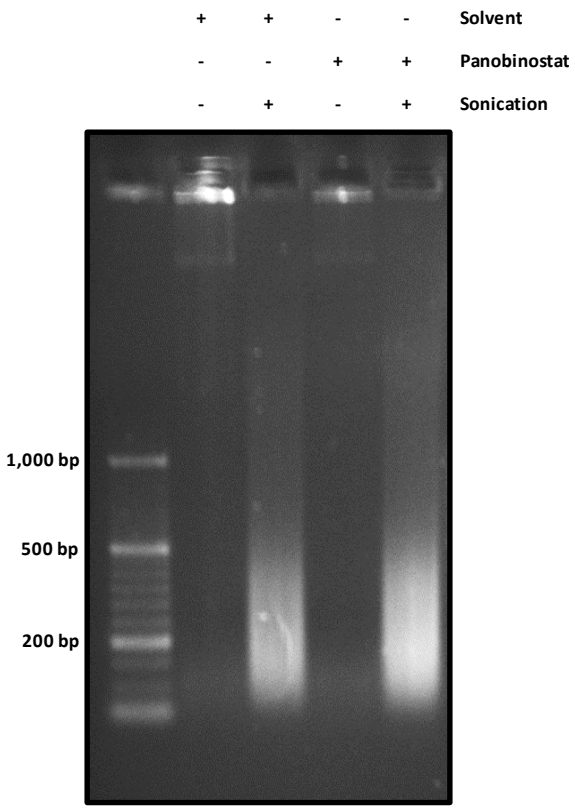

Figure 35: Sonication of precipitated DNA results in fragments of 100-300 base pair length.
DNA from sonicated samples and unsonicated controls were analyzed by agarose gel electrophoresis. DNA was stained using ethidiumbromide. The bulk of fragments had a length between 100 to 300 base pairs.

Fragmentation of precipitated DNA resulted in fragments of 100-300 bp length, as recommended for ChIP sequencing (Figure 35). Immunoprecipitation of histone mark H3K4me1 resulted in small amounts of precipitated DNA of desired quality. To control the downregulation of *TERT* in the ChIP experiment, *TERT* mRNA was analyzed in parallel using qRT-PCR. Induction of tumor suppressors *MIR183* and *GRHL-1* was demonstrated after panobinostat treatment in neuroblastoma (Fabian, 2014; Lodrini, 2013). Validation of chromatin remodeling at tumor suppressor *MIR183* and *GRHL-1* loci was performed by qRT-PCR analysis of precipitated DNA fragments.

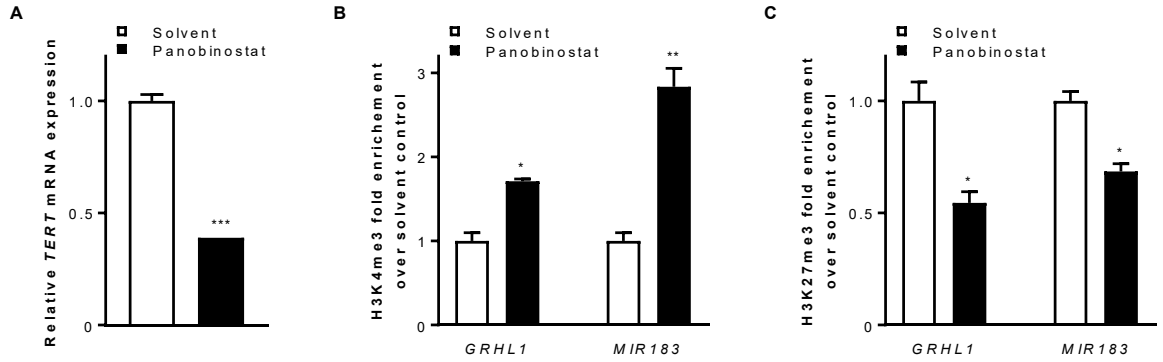

Figure 36: Technical validation of samples for ChIP experiments.
Validation analyses of ChIP sequencing experiment. GI-ME-N cells were treated with panobinostat 30 nM or solvent for 18 h. **A**, Expression of *TERT* mRNA in GI-ME-N cells. *TERT* expression was analyzed by qRT-PCR (mean fold change over solvent ± SD; n≥2). **B**, Enrichment of H3K4me3 at *GRHL1* and *MIR183* loci after panobinostat treatment. **C**, Enrichment of H3K27me3 at *GRHL1* and *MIR183* loci after panobinostat treatment. Bars represent mean relative enrichment above the solvent control (±SD; n≥2), detected by qRT-PCR. *P≤0.05, **P≤0.01, ***P≤0.001.

After panobinostat treatment, *TERT* mRNA expression was reduced to 40% (Figure 36 A). Enrichment of activating mark H3K4me3 at *GRHL1* (1.7-fold) and *MIR183* (2.8-fold) loci was detected after panobinostat treatment (Figure 36 B). Depletion of repressive mark H3K27me3 at *GRHL1* (0.5-fold) and *MIR183* (0.7-fold) loci was detected after panobinostat treatment (Figure 36 C). In total, one replicate for H3K4me1, three replicates for H3K4me3, H3K27ac, H3K36me3 and H3K9me3 and four replicates for H3K27me3 were sequenced for each condition and analyzed for altered patterns of histone marks after panobinostat treatment.

Sequencing was performed at the DKFZ High Throughput Sequencing Core Facility and data analysis was performed by January Weiner at the *Berlin Institute of Health* (BIH). First, a correlation analysis was performed to check sample quality and clustering of the different samples. Subsequently, principal component analysis (PCA) was performed to reveal the internal structure of the data in a way that best explains the variance in the sequencing data.

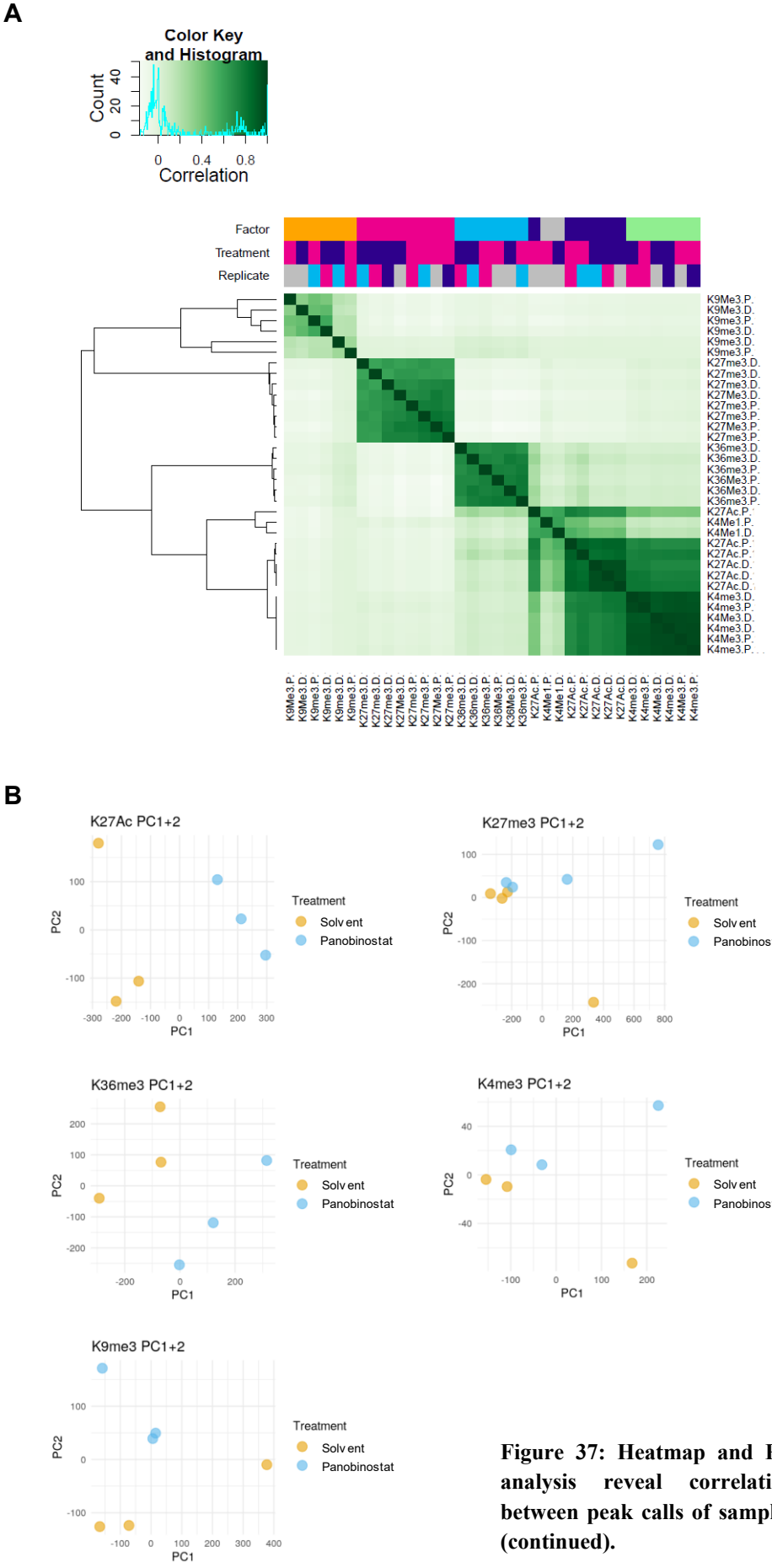

Figure 37: Heatmap and PC analysis reveal correlation between peak calls of samples (continued).

Figure 37: Heatmap and PC analysis reveal correlation between peak calls of samples.
Continued. **A**, Heat-map depicting the correlation of samples sorted by histone mark and condition. GI-ME-N cells were treated for 18 h with 30 nM panobinostat or solvent (DMSO). Antibodies H3K4me1, H3K4me3, H3K27ac, H3K36me3, H3K9me3 and H3K27me3 were used for immunoprecipitation. **B**, Principal component analysis performed separately for each probe. For histone mark H3K4me1, no analysis was possible due to small sample size. Yellow circles: Solvent treated samples; blue circles: panobinostat treated samples; D: DMSO (solvent), P: panobinostat. Reads were aligned to the GRCh38 genome assembly (hg38).

The correlation analysis between peak-calls in the analyzed samples showed that the six histone marks in the different groups cluster together (Figure 37 A). Principal component analysis of PC1 and PC2 revealed that active enhancer mark H3K27ac as well as H3K36me3 and H3K9me3 showed a separation of the two conditions tested, in contrast to most of the other marks, indicating that the H3K27ac modification is strongly influenced by panobinostat treatment (Figure 37 B). Histone marks H3K27me3 and H3K4me3 showed no clear clustering of the two conditions in PC1 and PC2 (Figure 37 B). Since only one single sample per condition could be sequenced for histone mark H3K4me1, no principal component analysis was performable with the applied method. The genome-wide number of peaks with significant differences between the tested conditions at different p-value cutoffs was summarized in a table.

Table 29: Panobinostat treatment changes epigenetic marks in GI-ME-N cells.
Overview of the results of the separate genome-wide analysis. Numbers indicate the total number of results below at different p-value cutoffs. Differential abundance of histone marks H3K27ac, H3K27me3, H3K36me3, H3K4me3 and H3K9me3 after panobinostat treatment. For histone mark H3K4me1, no analysis was possible due to small sample size.

	K27Ac	K27me3	K36me3	K4me3	K9me3
0.050	41782	468	431	1038	26
0.010	26206	108	133	467	13
0.001	13936	0	43	216	7

The most strongly significantly altered histone mark after panobinostat treatment is H3K27ac; 41,182 H3K27ac marks were changed with a p-value ≤ 0.05 (Table 29). Of that, 13,936 marks had p-values ≤ 0.001. In total, 468 H3K27me3 marks were changed with a p-value ≤ 0.05 and for 108 marks, p ≤ 0.01 was calculated (Table 29). Trimethylated histone 3 K36 (H3K36me3) standing for transcriptional elongation was altered in 431 peaks at p-values of 0.05 and 43 peaks showed a lower p-value of ≤ 0.001. Trimethylated histone 3 K4 (H3K4me3) showed 1,038 peaks with p ≤ 0.05 and 216 peaks with p ≤ 0.001. Repressive histone mark H3K9me3 showed

genome-wide alterations of 26 marks with a p-value ≤ 0.05 and 7 marks with p ≤ 0.001. Since only one single sample per condition could be sequenced for histone mark H3K4me1, no differential abundance of peaks could be analyzed with the applied method.

Subsequently, the *TERT* genomic region at chromosome 5 and the rearrangement partner on chromosome 19 was further analyzed (section 6.1). In the following, the rearranged *TERT* region is defined as the result of combining the *TERT* region downstream of the putative rearrangement (chr5, 1195067–1295066) and the region chr19, 58507053–58607052.

Table 30: The epigenetic marks of the rearranged TERT region are not strongly altered by panobinostat treatment.
Differential abundance of histone marks H3K27ac, H3K27me3, H3K36me3, H3K4me3 and H3K9me3 after panobinostat treatment in the *TERT* region. The table represents results from the defined *TERT* region (chr5, 1195067–1295066 and chr19, 58507053–58607052) showing the number of peaks with significant differences between the tested conditions at different p-value cutoffs. The p-values are corrected for multiple testing within all results in the recombined region for a given probe. The numbers indicate the total number of differentially bound peaks at a given p-value threshold in relation to total number of peaks. In parentheses: number of peaks differentially bound in the *TERT* region, number of peaks bound in the upstream recombined region. For histone mark H3K4me1, no analysis was possible due to small sample size.

	K27Ac	K27me3	K36me3	K4me3	K9me3
Total peaks	13	8	33	8	28
Peaks in the TERT region	1	0	21	1	28
Peaks in the upstream region	12	8	12	7	0
0.050	8 (0/8)	1 (0/1)	0 (0/0)	0 (0/0)	0 (0/0)
0.010	8 (0/8)	1 (0/1)	0 (0/0)	0 (0/0)	0 (0/0)
0.001	5 (0/5)	1 (0/1)	0 (0/0)	0 (0/0)	0 (0/0)

In the rearranged *TERT* region the most significantly altered histone mark was H3K27ac showing 8 peaks with p-values ≤ 0.05 and 5 peaks with p-values ≤ 0.001 (Table 30). The second most altered histone mark after panobinostat treatment was H3K27me3, with 1 peak showing p-value ≤ 0.001. For histone marks H3K36me3, H3K4me3 and H3K9me3, there were no histone marks identified to be significantly altered by panobinostat treatment (Table 30). Since only one single sample per condition could be sequenced for histone mark H3K4me1, no differential abundance of peaks was analyzed with the applied method.

A graphical overview of the rearranged *TERT* region in GI-ME-N including all assigned peaks was generated.

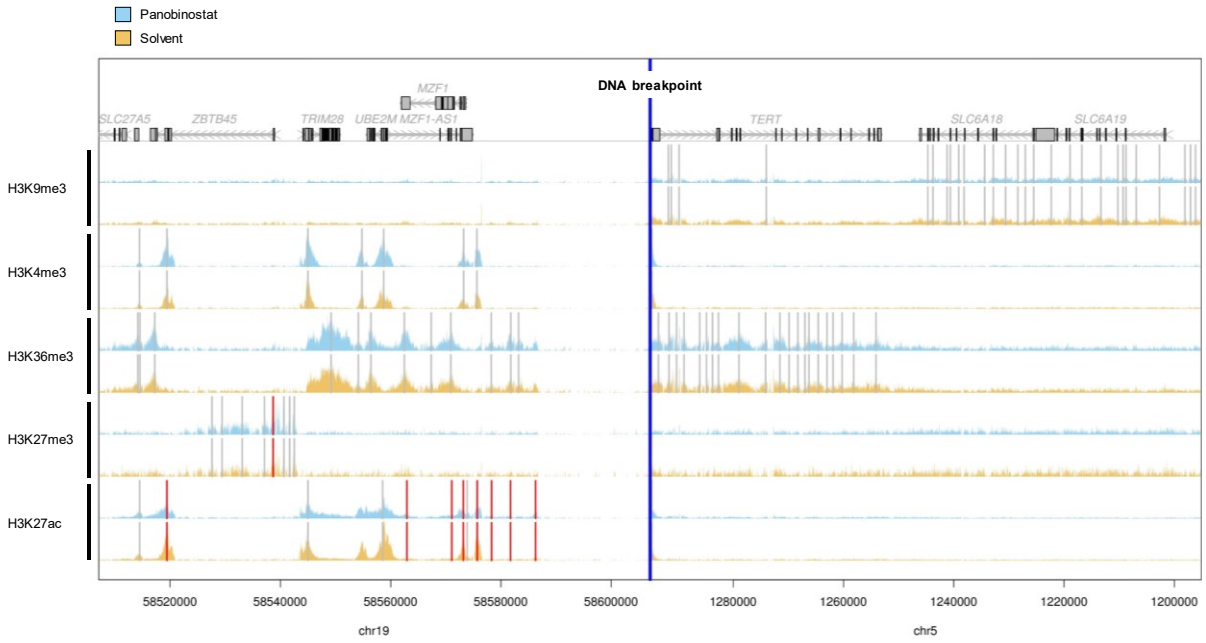

***Figure 38: Histone marks at the rearranged TERT genomic region in GI-ME-N* cells.**
GI-ME-N cells were treated for 18 h with panobinostat (30 nM) or solvent (DMSO) (n≥3). Survey of the five histone marks in the rearranged *TERT* region with the peaks shown for each probe. Grey vertical lines indicate peaks identified in the samples. Red vertical lines indicate peaks which show a significant difference between solvent (n≥1) and panobinostat (n≥1) for the given mark. Peaks of the defined *TERT* region (chr5, 1195067-1295066) and the rearrangement partner (chr19, 58507053–58607052) are shown for H3K9me3, H3K4me3, H3K36me3, H3K27me3 and H3K27ac. ChIP sequencing reads were aligned to the GRCh38 genome assembly (hg38) and visualized with the Integrative Genomics Viewer (IGV). For histone mark H3K4me1, no analysis was possible due to small sample size. Yellow tracks: Solvent (DMSO); blue tracks: panobinostat; blue vertical line: DNA breakpoint. Reads were aligned to the GRCh38 genome assembly (hg38).

The significant peaks for H3K27ac were all assigned to regions and genes Zinc Finger And BTB Domain Containing 45 (*ZBTB45*) and Myeloid zinc finger 1 (Antisense RNA 1) (*MZF1*(-A*S1*)) upstream of *TERT* (Figure 38). The sole significantly changing H3K27me3 peak was assigned to the *ZBTB45* upstream of *TERT* (Figure 38). For histone marks H3K36me3, H3K4me3 and H3K9me3, there were no histone modifications identified to be significantly altered by panobinostat treatment (Figure 38). These modifications are not likely to explain the strong repression of *TERT* after panobinostat treatment. To summarize, results from ChIP sequencing analysis revealed that the most strongly significantly altered histone marks are H3K27ac and H3K4me3 looking at genome-wide histone modifications. The rearranged *TERT* region undergoes minor changes after panobinostat treatment, and repression of *TERT* mRNA levels does not result from changes in the investigated chromatin marks.

4.5.2 Panobinostat treatment induces reduction of genome-wide methylation

The *TERT* region is alternatively methylated during carcinogenesis (Lee, 2019). Massive methylation of the *TERT* promotor region was described to enable active *TERT* transcription (Lee, 2019) and increased methylation in the *TERT* region was demonstrated in *TERT*-rearranged neuroblastoma (Peifer, 2015). To investigate putative changes in methylation status of the rearranged *TERT* region after panobinostat treatment, methylation profiling analysis was performed. *TERT* mRNA expression is reduced to about 50% after 18 h of panobinostat treatment (section 4.1.1). This rather early time-point was chosen for subsequent methylation array profiling to capture early events after panobinostat treatment and to reduce further effects of elongated treatment. Cells were treated with solvent (DMSO) or 30 nM panobinostat for 18 h. To control the downregulation of *TERT* in the methylation profiling experiment, *TERT* mRNA was analyzed in parallel using qRT-PCR (data not shown). Three replicates were analyzed for each condition. DNA from treated cells was isolated, bisulfite-converted and amplified prior to being loaded on the BeadChip. The methylation array was performed at the DKFZ Genomics and Proteomics Core Facility and data analysis was performed by January Weiner at the *Berlin Institute of Health* (BIH). The quality control of samples did not show outliers or low quality arrays.

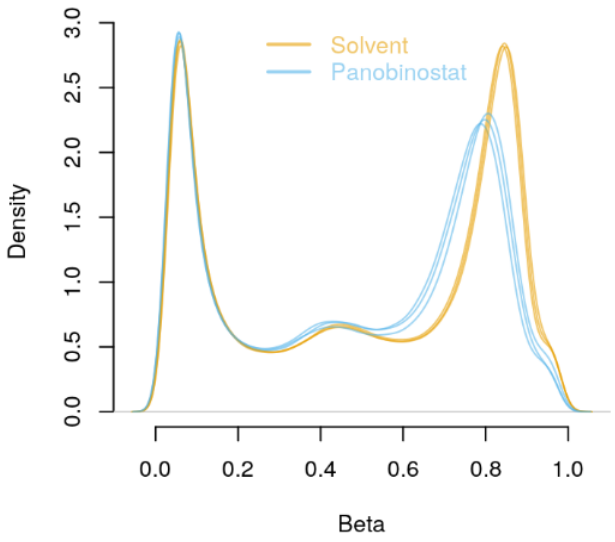

Figure 39: Panobinostat treatment induces genome-wide demethylation of CpG sites.
GI-ME-N cells treated for 18 h with panobinostat (30 nM) or solvent (DMSO). Density plot showing the distribution of signals for each sample (n=3). Samples were processed using raw normalization. Yellow lines: Solvent (DMSO); blue lines: panobinostat

Average methylation of CpG sites is indicated by Beta values of the mono-methylated (Beta=1) and non-methylated (Beta=0) state. Genome-wide methylation decreased after panobinostat treatment as demonstrated by an average shift to smaller beta values (Figure 39). Reduction of methylated CpG sites of panobinostat treated samples was observed in all replicates. Subsequently, analysis of CpG sites in the rearranged *TERT* region on chromosome 5 with the rearrangement partner on chromosome 19 was performed.

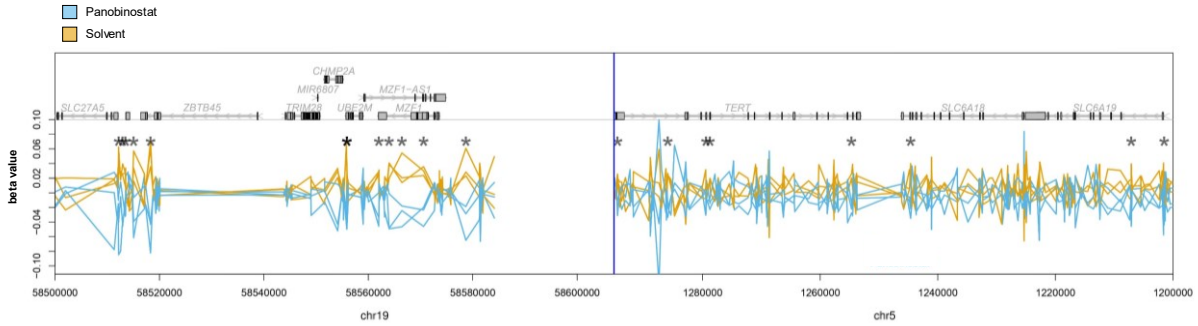

Figure 40: Minor changes in the methylation status of the rearranged TERT locus in GI-ME-N cells.
GI-ME-N cells were treated for 18 h with panobinostat (30 nM) or solvent (DMSO) (n=3). Methylation status of the defined *TERT* region (chr5, 1195067–1295066 and chr19, 58507053–58607052). Stars indicate CpG sites that are significantly different between solvent and panobinostat treatment. Each track corresponds to a single sample. Yellow tracks: Solvent (DMSO); blue tracks: panobinostat; blue vertical line: DNA breakpoint. Visualization referred to the GRCh38 genome assembly (hg38).

Few sites in the *TERT* gene and the rearranged *TERT* locus were less methylated after panobinostat treatment (Figure 40). The actual effect size in differences between mean methylation in both sample groups was small (data not shown). These alterations in CpG methylation are not likely to explain the strong repression of *TERT* after panobinostat treatment. Taken together, methylation status of CpG sites in the rearranged *TERT* region revealed no major changes after panobinostat treatment and does not explain the repression of the *TERT* mRNA.

4.6 Panobinostat treatment reduces the stability of the *TERT* transcript

TERT mRNA levels decline after 2-4 h of panobinostat treatment in GI-ME-N and CLB-GA cells (section 4.1.1). To investigate whether the decrease in mRNA expression is due to a decrease in mRNA stability, expression of *TERT* mRNA was analyzed in cells treated with actinomycin D, a transcriptional inhibitor. The half-life of *TERT* mRNA in GI-ME-N and

CLB-GA cells was determined upon actinomycin D treatment. Actinomycin D blocks *de novo* gene transcription by forming stable complexes with double-stranded DNA. To ensure valid quantification, GI-ME-N cells were treated at maximum for 30 h and CLB-GA cells for 24 h, since transcriptional inhibition is toxic to cells and results in detachment from cell culture plates.

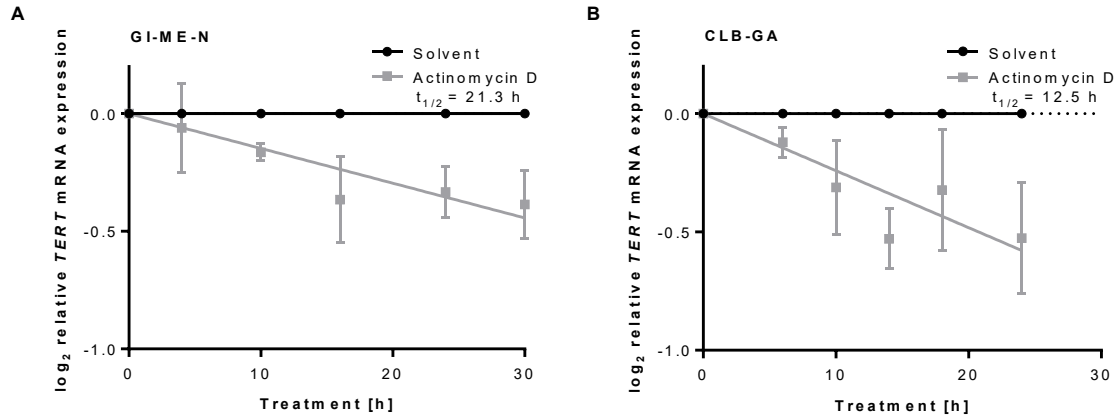

Figure 41: TERT half-life is determined after transcriptional inhibition with actinomycin D.
Expression of *TERT* upon actinomycin D treatment. **A**, GI-ME-N cells treated with actinomycin D (5 µg/ml) or solvent (DMSO) for 1-30 h. *TERT* expression was analyzed by qRT-PCR (mean log fold change over solvent ± SD; n≥2). **B**, CLB-GA cells treated with actinomycin D (5 µg/ml) or solvent (DMSO) for 1-24 h. *TERT* expression was analyzed by qRT-PCR (mean log fold change over solvent ± SD; n≥3). Half-life of *TERT* mRNA was determined via linear regression fit of transformed data.

Half-life of *TERT* mRNA was determined to about 21.3 h in GI-ME-N cells (Figure 41 A). In CLB-GA cells, *TERT* mRNA half-life was determined to about 12.5 h (Figure 41 B). To investigate the *TERT* mRNA stability of after panobinostat treatment, combination treatment of panobinostat and actinomycin D was performed. GI-ME-N and CLB-GA cells were treated first with solvent (DMSO) or panobinostat 2 h prior to actinomycin D treatment. Treated cells were harvested after 0, 6, 10, 14, 18 and 24 h after combination treatment and RNA levels were measured by qRT-PCR.

The half-life of *TERT* mRNA in GI-ME-N cells was reduced from 24.4 h to 13 h (Figure 42 A), and from 12 h to 8.4 h in CLB-GA cells after panobinostat treatment (Figure 42 B), suggesting reduced *TERT* transcript stability as the underlying molecular mechanism.

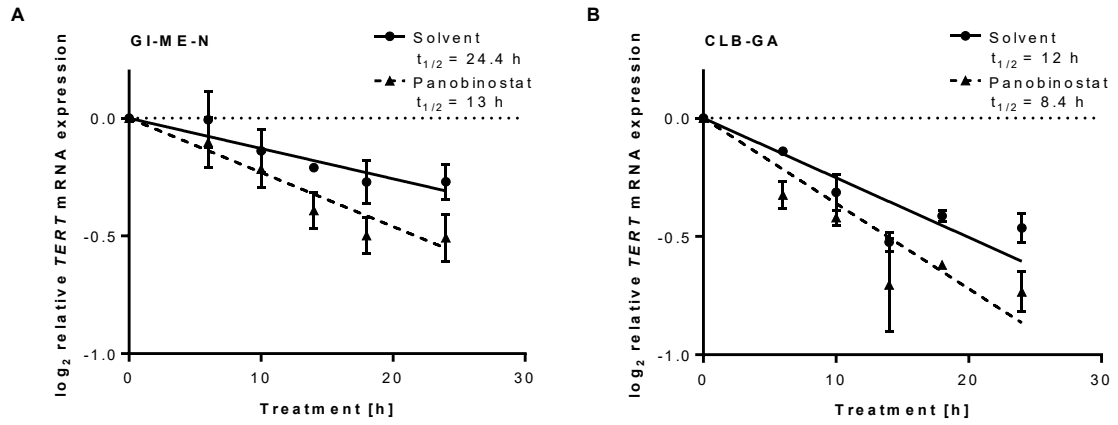

Figure 42: Half-life of the TERT transcript is decreased by panobinostat treatment.
Expression of *TERT* upon actinomycin D treatment alone or in combination with panobinostat. **A**, *TERT* expression of GI-ME-N cells co-treated with actinomycin D (5 µg/ml) and panobinostat (30 nM) or solvent (DMSO). *TERT* expression was analyzed by qRT-PCR (mean log fold change over start expression ± SD; n≥2). **B**, *TERT* expression of CLB-GA cells co-treated with actinomycin D (5 µg/ml) and panobinostat (30 nM) or solvent (DMSO). *TERT* expression was analyzed by qRT-PCR (mean log fold change over start expression ± SD; n≥2). Half-life of *TERT* mRNA was determined via linear regression fit of transformed data. Dotted line indicates control value.

4.7 Evaluation of synergistic drug combinations with panobinostat

4.7.1 Selection of chemotherapeutics or targeted compounds for combination with panobinostat

Panobinostat treatment reduces tumor growth in preventive and therapeutic xenograft mouse models of *TERT*-rearranged high-risk neuroblastoma (section 4.4). In cancer therapy, application of monotherapy will most likely result in acquired therapy resistance of tumor cells since they can adapt to the selective pressure of monotherapy (Jagadeeshan, 2019). To optimize treatment success and to search for synergisms, combination therapy with panobinostat was investigated with standard chemotherapeutic agents used in neuroblastoma treatment protocols or targeted compounds. The classical first-line chemotherapeutic agents doxorubicin and oxaliplatin were used for the combination therapy. The platinum derivative cytostatic oxaliplatin was used instead of cisplatin, since oxaliplatin is less deactivated by DMSO that it used as solvent in the analyses here (Hall, 2014). The RIST-rNB 2011 study is a multimodal molecular targeted therapy to treat relapsed or refractory high-risk neuroblastoma patients (NCT01467986, NIH, 2020). Dasartinib, rapamycin, irinotecan and temozolomide are administered to patients enrolled in this study, combining molecular targeted drugs (rapamycin and dasatinib) with conventional chemotherapy (irinotecan and temozolomide). In multiple

myeloma, panobinostat is used in combination with the proteasomal inhibitor bortezomib and dexamethasone, significantly increasing progression-free survival of patients (Richardson, 2016). In addition, proteasomal inhibition with bortezomib triggered cell death of neuroblastoma cell lines (Pilchova, 2017). Lorlatinib was used as exemplary inhibitor of anaplastic lymphoma kinase (ALK), a frequent target of genetic alteration in advanced neuroblastoma. The CLB-GA cell line harbors a gain-of-function point mutation in the *ALK* gene (R1275Q), which can be targeted by ALK-inhibitor lorlatinib (Trigg, 2018). Further, I-BET762 was used as exemplary BET inhibitor. BETi indirectly reduce expression of *MYCN* and *MYCN* target genes such as *TERT*, and are promising preclinical candidates for treating *MYCN*-amplified neuroblastoma (Henssen, 2016, Huang, 2020). The drug concentrations applied for the testing were either derived from patient plasma levels (Infarinato, 2016; Choo, 2013; Christopher, 2008; Tan, 2018), preclinical experiments (Mustafi, 2019) or as recommended by CPO, Berlin and adapted to *in vitro* application (Table 31). To calculate dose-response curves using the software *Synergyfinder* (Ianevski, 2017), a concentration series of six data points was measured for each compound. Due to technical settings of the screen, most of the compounds were diluted with solvent in a 1:3 ratio.

Table 31: Concentrations of chemotherapeutic and targeted compounds for synergistic drug testing with panobinostat.

Grey filled columns highlight published drug concentrations and translated *in vitro* concentrations. The third highest concentration represents the medium plasma concentration or concentration applied in preclinical models. For doxorubicin and bortezomib, the applied concentrations were decreased in both cell lines.

	In vitro / In vivo concentration [ng/ml]	Assay concentrations [ng/ml]						Comment	Source
Panobinostat	5.1	0.2	0.6	1.7	5	15	45		Rathkopf, 2010
Irinotecan	4000	180	560	1670	5000	15,000	45,000		CPO, Berlin
Temozolomid	7000	370	1110	3300	10,000	30,000	90,000		CPO, Berlin
Rapamycin	14.4	0.6	1.7	5	15	45	135		Choo, 2013
Dasatinib	247	9	28	83	250	750	2250		Christopher, 2008
Doxorubicin	600	2	6	19	56	167	500	GI-ME-N	CPO, Berlin
		0.02	0.1	0.48	2	12	60	CLB-GA	
Oxaliplatin	1440	56	167	500	1500	4500	13,500		CPO, Berlin
Bortezomib	106	0.4	1	4	11	33	100	GI-ME-N	Tan, 2018
		0.001	0.006	0.032	0.16	0.8	4	CLB-GA	
Lorlatinib	569	20	61	183	550	1650	4950		Infarinato, 2016; Shaw, 2017
I-BET762	111	4	11	33	100	300	900		Mustafi, 2019

To assess the concentration range of the nine selected compounds in *TERT*-rearranged cell lines GI-ME-N and CLB-GA, cell viability experiments were performed by Alessandra Silvestri and Guido Gambara at CPO, Berlin. GI-ME-N and CLB-GA cells were treated with the selected agents for 72 h with the concentrations outlined in Table 31. Treatment with doxorubicin and

bortezomib showed strong toxicity towards both cell lines at published concentrations, impeding the analysis of cell viability after treatment (data not shown). Therefore, concentrations of doxorubicin and bortezomib were decreased for each cell line (Table 31). For the CLB-GA cells, lower concentrations as for the GI-ME-N cell line were applied for treatment.

4.7.2 Combination therapy of panobinostat with bortezomib identifies synergistic reduction of cell viability in 2D and 3D neuroblastoma *in vitro* models

After the analyses of the effective concentration range in GI-ME-N and CLB-GA cells at clinically relevant concentrations or below, combination treatment with panobinostat was performed in 2D cell culture. The identification of synergistic combinations investigating cell viability and induction of protease-mediated apoptosis based on Table 31 was investigated in the medical dissertation of Rasmus Linke.

Combination therapy with panobinostat identified several synergistic combinations that reduced cell viability and induced protease-mediated apoptosis in both cell lines (R. Linke, Medical Dissertation, work in progress). The combination of panobinostat and bortezomib was among the top 3 combinations that synergistically reduced cell viability in GI-ME-N and CLB-GA cell lines (R. Linke, Medical Dissertation, work in progress). Since bortezomib was shown to reduce *TERT* expression and telomerase activity (Ci, 2015; Weiss, 2012), the combination of panobinostat and bortezomib was further investigated. Cell viability was measured in 3D spheroids of GI-ME-N and CLB-GA cells after combination treatment. The applied concentration range was chosen according to Table 31. Cell viability experiments of the combination therapy in 2D cell cultures were performed by Rasmus Linke, combination therapy in 3D cell cultures were performed by Alessandra Silvestri and Guido Gambara at CPO, Berlin. GI-ME-N and CLB-GA cells were treated with solvent, panobinostat and/or bortezomib for 72 h at different concentrations. Synergy analysis of the combination treatment was performed using the software *Synergyfinder* (Ianevski, 2017). A three-dimensional hypersurface was generated, identifying concentration areas of high synergy by calculating Bliss synergy scores (δ-scores).

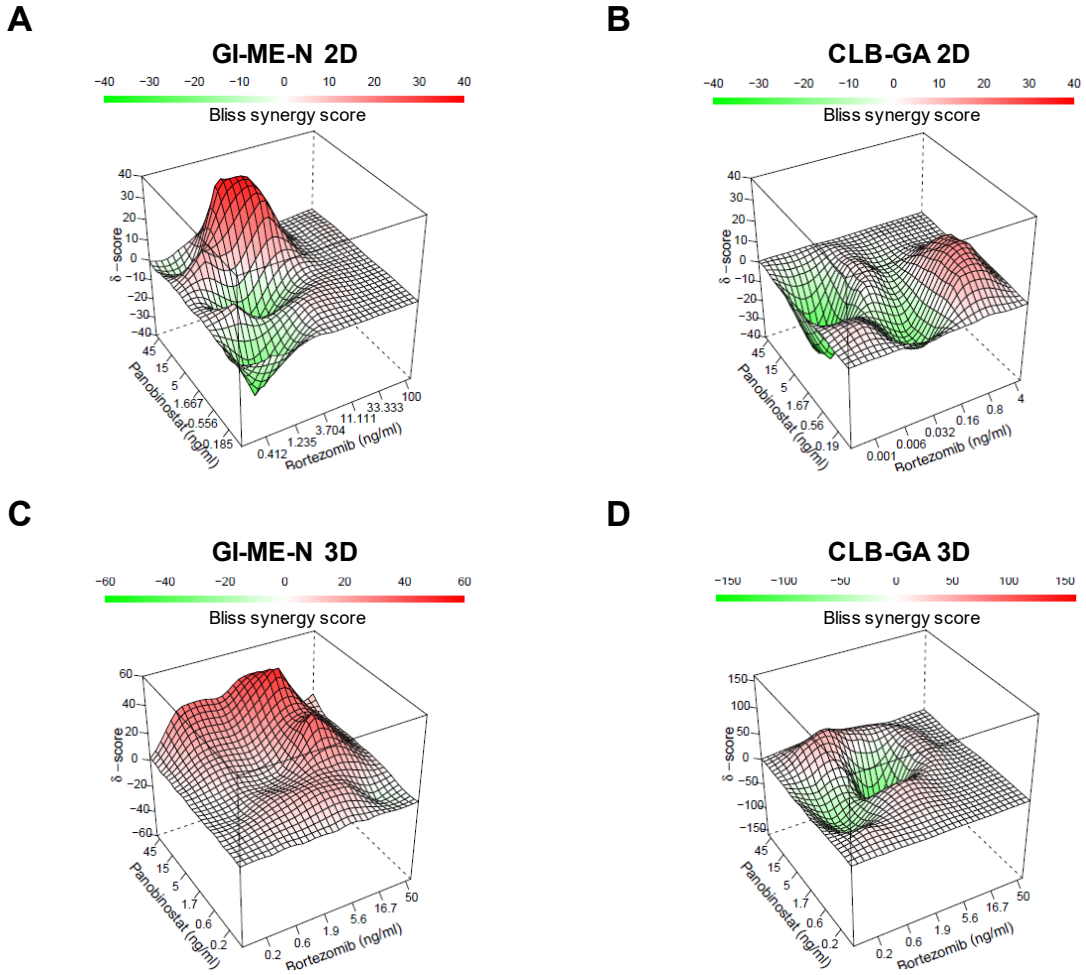

Figure 43: Panobinostat and bortezomib synergistically reduce cell viability in 2D and 3D models of TERT-rearranged high-risk neuroblastoma.
Synergy plots of GI-ME-N and CLB-GA cells treated with panobinostat and bortezomib combination therapy for 72 h in 2D and 3D cell culture models. **A**, Synergy plots of GI-ME-N in 2D and (**C**) 3D models. **B**, Synergy plots of CLB-GA in 2D and (**D**) 3D models. Areas with δ-scores ≥ 1 are considered as synergistic, δ-scores ≤ 1 as antagonistic. Viable cell numbers by luminescence-based assay (mean % over solvent control; n=4). Bliss synergy scores were calculated using the Synergyfinder web application. Red: synergistic effect, green: antagonistic effect. 2D experiments were performed by Rasmus Linke, 3D experiments were performed by CPO.

The calculated overall δ-scores of 14.1 (2D) (Figure 43 A) and 30.3 (3D) (Figure 43 C) in the GI-ME-N models are considered as strongly synergistic and were detected in a wide range of concentrations. In the CLB-GA models, the calculated overall δ-scores were 8.1 (2D) (Figure 43 B) and 7.2 (3D) (Figure 43 D). Synergistic effects in the CLB-GA models were observed at few concentrations, but overall showed no or antagonistic effects. Taken together, combination therapy of panobinostat with bortezomib results in strong synergistic reduction of cell viability in the 2D and 3D GI-ME-N cell line models of *TERT*-rearranged high-risk neuroblastoma at clinically relevant concentrations.

4.7.3 No synergistic effect on protease-mediated apoptosis by combined panobinostat/bortezomib treatment

The combination of panobinostat and bortezomib revealed synergistic anti-tumoral potential in 2D and 3D models of *TERT*-rearranged high-risk neuroblastoma. To investigate if protease-mediated apoptosis is synergistically induced after combination treatment, PARP-1 western blot analysis was performed in GI-ME-N and CLB-GA cells. Specific fragmentation of PARP-1 is considered as indication for active caspase signaling and active proteases unique in cell death programs. GI-ME-N and CLB-GA cells were treated with solvent, panobinostat and/or bortezomib for 24 h. The applied concentrations were chosen according to synergy calculations of the combination treatment, revealing strong decrease of cell viability as shown in section 4.7.2.

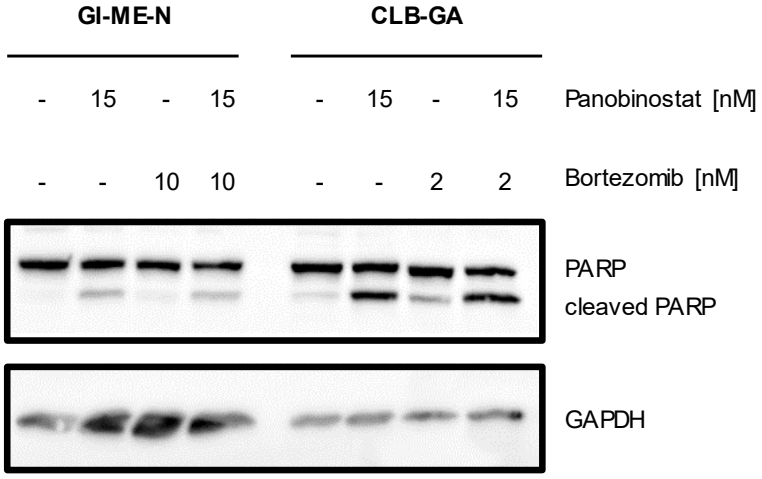

Figure 44: Panobinostat and bortezomib do not synergistically induce protease-mediated apoptosis in GI-ME-N and CLB-GA cells.
Representative western blot analysis of GI-ME-N (left side) and CLB-GA cells (right side) 24 h after solvent, panobinostat (15 nM), bortezomib (GI-ME-N: 10 nM, CLB-GA: 2 nM) or combination treatment. GAPDH served as a loading control.

GI-ME-N cells treated with panobinostat showed an increase in cleaved PARP-1 protein level after panobinostat treatment (Figure 44, lanes 1-4). A small increase of cleaved PARP-1 was observed after bortezomib treatment. CLB-GA cells treated with panobinostat and/or bortezomib showed an increase in cleaved PARP-1 protein level (Figure 44, lanes 5-8). The cleavage of PARP-1 was stronger in CLB-GA than in GI-ME-N cells. Combination treatment with panobinostat and bortezomib revealed no synergistic effects on PARP-1 and cleaved PARP-1 levels. This experiment suggests that panobinostat and bortezomib do not synergistically induce apoptosis via active protease signaling in GI-ME-N and CLB-GA cells.

4.7.4 No synergistic effect on *TERT* expression and telomerase activity by combined panobinostat/bortezomib treatment

Panobinostat reduces *TERT* mRNA expression and telomerase activity *in vitro* and *in vivo* models of *TERT*-rearranged neuroblastoma models. Subsequently, the combination of panobinostat and bortezomib was investigated to assess whether this combination synergistically downregulates *TERT* expression and telomerase activity. GI-ME-N cells were treated for 24 h for RNA expression analysis and for 48 h for telomerase activity assay with solvent, 15 nM panobinostat and/or 10 nM bortezomib. CLB-GA cells were treated for 24 h with solvent, 15 nM panobinostat and/or 2 nM bortezomib in both assays. The applied concentrations were chosen according to the synergy calculations of the combination treatment quantified by δ-score ≥ 1 as shown in section 4.7.2.

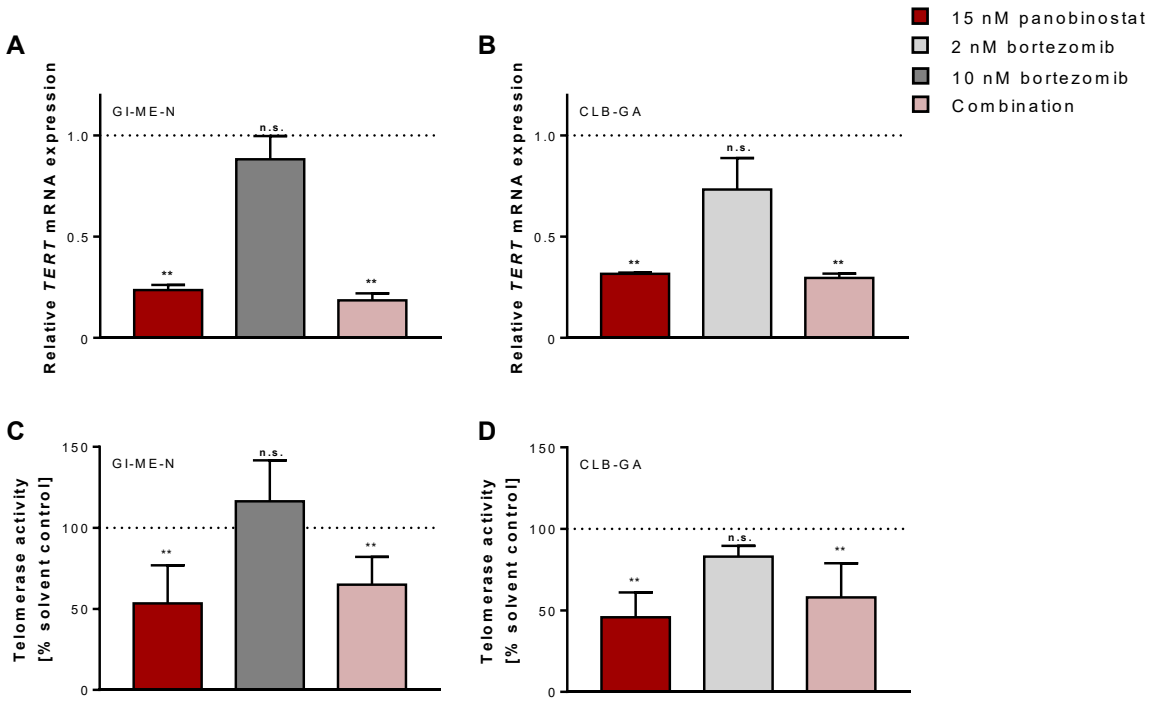

Figure 45: Combination treatment of panobinostat and bortezomib has no synergistic effect on TERT expression and telomerase activity.
GI-ME-N and CLB-GA cells were treated for 24 or 48 h with solvent, panobinostat (15 nM), bortezomib (2, 10 nM) or combination. *TERT* expression analysis after 24 h treatment in (**A**) GI-ME-N and (**B**) CLB-GA was analyzed by qRT-PCR (mean fold change over solvent ± SD; n≥3). Telomerase activity in (**C**) GI-ME-N after 48 h and (**D**) CLB-GA after 24 h treatment was measured by ELISA (mean % over solvent ± SD; n≥2). Dotted lines indicate control value. **P≤0.01, n.s.: not significant.

TERT expression was reduced after panobinostat treatment to 24% in GI-ME-N cells (Figure 45 A) and to 32% in CLB-GA cells (Figure 45 B). Bortezomib treatment revealed no significant

reduction of *TERT* mRNA levels and no synergistic effect was detected on *TERT* expression after combination treatment (Figure 45 A and B). Telomerase activity was decreased after panobinostat treatment to 53% in GI-ME-N cells (Figure 45 C) and to 46% in CLB-GA cells (Figure 45 D). Treatment with bortezomib alone showed no reduction of telomerase activity. The combination of bortezomib with panobinostat revealed no synergistic effect on telomerase activity (Figure 45 C and D). Taken together, the combination treatment of panobinostat and bortezomib showed no synergistic reduction of *TERT* mRNA levels and telomerase activity in models of *TERT*-rearranged high-risk neuroblastoma.

4.7.5 Preliminary study testing the synergistic efficacy of combined panobinostat/bortezomib treatment in subcutaneous xenografts in mice in a preventive treatment schedule

The combination therapy of panobinostat and bortezomib showed strong synergistic antitumoral potential in 2D and 3D models of *TERT*-rearranged neuroblastoma *in vitro* models and was further analyzed for *in vivo* efficacy. Since the GI-ME-N xenograft model showed slow tumor engraftment, low tumor take rates and triggered an inflammatory response, the CLB-GA model was chosen for further analyses. Mouse experiments were performed by Dennis Gürgen at EPO, Berlin. The panobinostat concentration was adapted from previous mouse studies (section 4.4) and the bortezomib concentration was chosen following standard protocols applied by EPO, reflecting achievable patient plasma levels (Tan, 2018). CLB-GA cells were xenotransplanted into the right flank of immunosuppressed 8-week-old athymic female NMRI-Foxn1nu/nu nude mice. About 18 x10^6 cells per animal were suspended in Matrigel™ for tumor cell inoculation. In a preventive treatment schedule, animals were treated when tumors reached a volume of about 100 mm³. Animals were randomized and treated with 15 mg/kg/d panobinostat or solvent (each dissolved in 5% glucose solution) by intraperitoneal injection 5 d/week, and/or with 0.5 mg/kg/d bortezomib or solvent (each dissolved in 0.9% sodium chloride solution) by intravenous injection 3 d/week starting at randomization. Treatment was applied for five consecutive days followed by two days offset of treatment (Figure 46). Tumor volume determination using a caliper and bodyweight were measured daily. Animals were sacrificed when tumor volume reached about 1500 mm³.

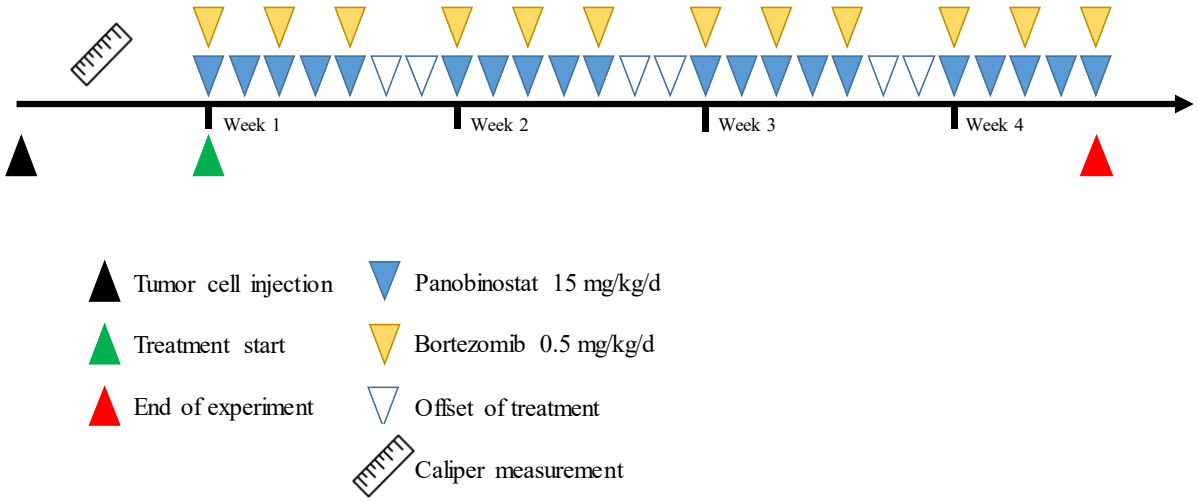

Figure 46: Combination treatment scheme with panobinostat and bortezomib in a high-risk neuroblastoma xenograft mouse model.
Solvent or 15 mg/kg/d panobinostat was applied to xenografted mice for five consecutive days, followed by two days offset of treatment. Three days a week, 0.5 mg/kg/d bortezomib treatment was applied in parallel. Animals were treated for a maximum of four weeks.

Four animals were randomized to each group and treatment. Treatment was applied for a maximum of 19 days. Group A was treated with solvent control, group B with panobinostat, group C with bortezomib and group D received treatment with panobinostat and bortezomib. The treatment schedule could not be followed as outlined due to transient weight loss of two mice of the combination treatment cohort (group D). For that cohort, treatment was paused from day 8 until day 12. Other cohorts were treated according to schedule (Figure 46).

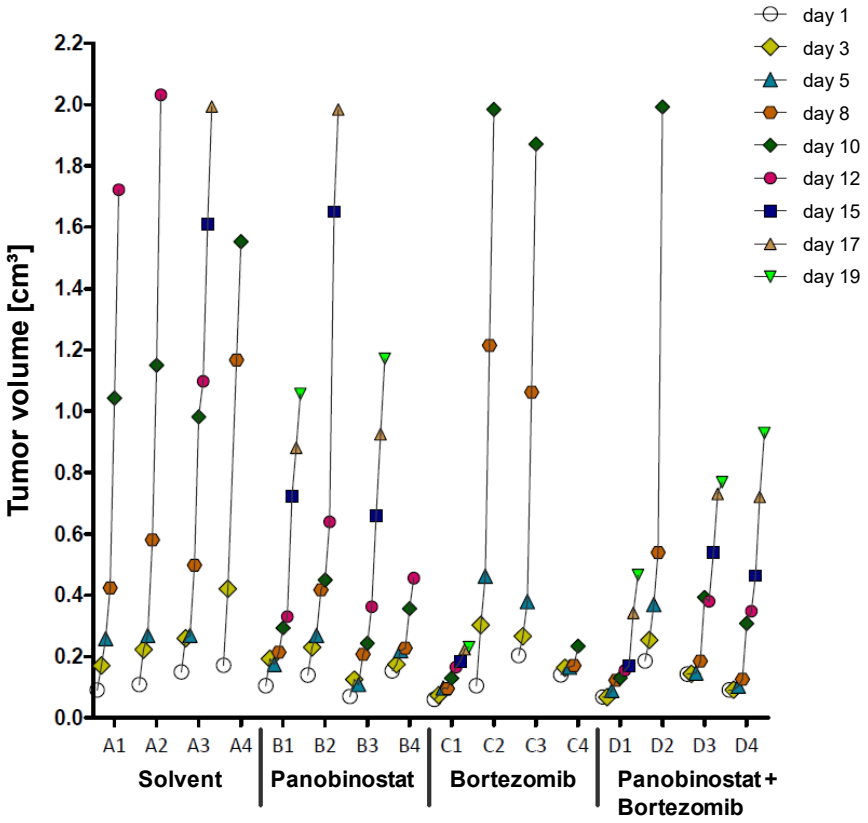

Figure 47: Combination treatment of panobinostat and bortezomib in a CLB-GA mouse model following a preventive treatment schedule.
Individual CLB-GA xenograft tumor growth in a preventive treatment schedule shown for each day under therapy. Tumor volume was measured daily and animals were treated with solvent (DMSO, group A), panobinostat 15 mg/kg/d (group B), bortezomib 0.5 mg/kg/d (group C) or combination (group D). Experiment was performed by and graphic was adapted from EPO.

Xenograft tumor growth was comparable to previous CLB-GA mouse studies and showed progressive tumor growth of the solvent treated cohort (Figure 47). Individual animals were taken out of the study when tumors reached the maximal allowed volume of about 1500 mm³. Due to high variance in tumor volumes in each group, averaged growth curves were highly affected when individual animals were taken out of the study (data not shown). Treatment with panobinostat reduced xenograft tumor growth but could not arrest proliferation of tumors (Figure 47). Bortezomib treatment resulted in reduction of tumor growth in half of the animals from that cohort, with progressive tumor growth in animals of the other half (Figure 47). The combination therapy of panobinostat and bortezomib revealed a reduction of tumor growth in 3 out of 4 animals of that cohort (Figure 47). The small cohort size of four animals per cohort does not allow to identify outliers or non-responders. Regarding the technical limitations of the study, no clear conclusion can be drawn of the synergistic efficacy of the combination treatment

of panobinostat and bortezomib in this pilot study in a *TERT*-rearranged high-risk neuroblastoma xenograft mouse model following a preventive treatment schedule.

5 Discussion

The prognosis of high-risk neuroblastoma patients is still unfavorable despite intensive therapeutic intervention and multimodal treatment. Neuroblastoma patients with tumors maintaining their telomeres show poor survival rates and may define a novel high-risk group of the disease (Ackermann, 2018; Peifer, 2015; Valentijn, 2015). Irreversible side effects of the cytotoxic therapy reduce the quality of life of surviving patients. Novel targeted therapeutic options are of enormous importance for the treatment of neuroblastoma patients in the future. Upon malignant transformation and carcinogenesis, epigenetic silencing of tumor suppressive genes are frequent events, putting epigenetic modifiers like HDACs in the focus of current research (Baylin, 2006; Esteller, 2007; Sanaei, 2019; Zhang, 2017a). Although aberrant expression of HDACs in cancer remains largely correlative, histone deacetylase inhibitors demonstrated their potential as anticancer agents in divert adult cancer entities like leukemia, multiple myeloma or lymphoma (Bolden, 2006; Catley, 2003; Duan, 2005; He, 2001; Hideshima, 2005; Rosato, 2003). In neuroblastoma, the relevance of histone deacetylases regarding malignancy, cell cycle progression, cell differentiation and autophagy was highlighted (Deubzer, 2008; Lodrini, 2013; Oehme, 2009b; Oehme, 2013). In preclinical models of neuroblastoma, the pan-HDACi panobinostat (LBH589, Farydak®) was shown to inhibit the malignant properties of neuroblastoma cells (Fabian, 2014; Lodrini, 2013; Waldeck, 2016). Since there are no clinically successful inhibitors targeting *TERT* or telomerase, HDACi like panobinostat offer an interesting approach to overcome current limitations of the therapy. Although a wide range of side effects was associated with HDACi treatment (Al-Hamamah, 2019; Bruserud, 2007), a better understanding of the underlying molecular mechanisms could help to optimize their use as therapeutic agents. This study aimed to evaluate the potential of panobinostat treatment to target *TERT* and telomerase in models of *TERT*-rearranged high-risk neuroblastoma, and to decipher the underlying regulatory mechanisms. Panobinostat treatment could provide a valuable therapeutic option for the subgroup of *TERT*-rearranged high-risk neuroblastoma patients.

5.1 Histone deacetylase inhibitor treatment decreases TERT levels and telomerase activity

Active *TERT* expression is detected in about 80-90% of tumors across cancer entities and is commonly associated with poor prognosis (Kim, 1994a; Shay, 1997). Telomere maintenance is

mandatory for cancer cell's survival, and activation or reactivation of *TERT* enables tumor cells to overcome the Hayflick limit to achieve replicative immortality, which is considered as a central hallmark of cancer (Hayflick, 1965). In earlier studies of neuroblastoma, telomerase activity has been correlated with unfavorable outcome (Hiyama, 1995). More recently, in about 30% of high-risk neuroblastoma, genomic *TERT* rearrangements have been described as a major driver of malignancy by demonstrating a strong correlation between high *TERT*-expression and telomerase activity and poor survival rates (Ackermann, 2018; Peifer, 2015; Valentijn, 2015). As demonstrated in colorectal carcinomas and neuroblastoma, there was no correlation between *TERT* copy number and its expression levels or telomerase activity, indicating that the high *TERT* expression is caused by the genomic repositioning and subsequent transcriptional upregulation of *TERT*, rather than by gain of *TERT* copy numbers (Palmqvist, 2005; Peifer, 2015; Valentijn, 2015). The lack of telomere maintenance mechanisms in neuroblastoma tumors correlates with a more benign prognosis (Ackermann, 2018). The study presented here reveals that treatment of *TERT*-rearranged neuroblastoma models highly expressing *TERT* with the pan-HDACi panobinostat reduced *TERT* expression by 2-4.5-fold. The on-target effect of HDACi treatment on *TERT* expression was demonstrated by treatment with structurally different pan-HDACi and HDAC1/2 inhibitors, showing that *TERT* repression is a common event upon HDAC inhibition in *TERT*-rearranged neuroblastoma cell lines. In normal human renal cortical epithelial cells and foreskin fibroblasts, trichostatin A treatment transcriptionally activated *TERT* expression and induced telomerase activity (Takakura, 2001). *TERT* downregulation after treatment with HDACi trichostatin A was shown in prostate cancer (Suenaga, 2002), liver cancer (Nakamura, 2001) and brain tumor cell lines (Rahman, 2010). Treatment with HDACi B1 repressed telomerase in lung adenocarcinoma cells via downregulation of STAT3, a transcription factor known to regulate *TERT* expression (Cheng, 2017b). Together, this points to a major role of HDACs in the regulation of *TERT* in healthy and malignant tissue.

In this study, TERT protein levels were demonstrated to decrease after panobinostat treatment. Although several publications present TERT immunoblotting (Bui, 2019; Iannilli, 2013), western blot analysis of the full length protein of about 127 kDa is technically challenging. The protein seems to degrade easily in absence of its native template TERC and was shown to form functional dimers, impeding analysis of the TERT monomer (Sauerwald, 2013). By using a *TERT* overexpressing plasmid, antibody specificity was validated. Decreasing TERT levels were demonstrated after pan-HDACi treatment in rat aortic vascular smooth muscle cells (Qing, 2016). More importantly, the functional consequence of decreasing TERT levels after HDACi

treatment was demonstrated here by detection of reduced activity of the telomerase holoenzymatic complex.

Telomere maintenance is a major driver of malignancy in neuroblastoma (Ackermann, 2018) and the pharmacologic targeting of *TERT* and telomerase with small-molecules is currently under clinical investigation (Relitti, 2020; Salloum, 2016; Thompson, 2013). Most of these inhibitors directly bind to the catalytic center or the periphery of TERT or the telomerase holoenzymatic complex (Lavanya, 2018; Yan, 2019). Imetelstat (GRN163L) is a specific and one of the most developed telomerase inhibitors in phase I and II clinical trials targeting the *TERC* RNA. In a clinical phase II study in children with recurrent CNS malignancies, treatment with imetelstat before surgical resection of the tumors resulted in grade 3/4 toxicities including thrombocytopenia, lymphopenia and neutropenia, and overall proved too toxic (Salloum, 2016). During embryogenesis and development, *TERT* and telomerase are important for normal development, but in most adult somatic tissue, *TERT* expression and telomerase activity are repressed and are only detectable in stem and germline cells (Collins, 2002). There are additional cell survival and stress resistance beneficial roles of telomerase in the cell, which are abrogated after its repression, probably explaining the observed toxicities upon pharmacological inhibition of telomerase (Ahmed, 2008). For neuroblastoma patients harboring *TERT*-rearranged tumors with high *TERT* levels and telomerase activity, HDACi treatment presents a promising therapeutic option to reduce *TERT* expression and telomerase activity. In this study, telomerase repression was similar in the *TERT*-rearranged and *MYCN*-amplified neuroblastoma cell lines treated with panobinostat, suggesting that panobinostat treatment could also be beneficial for patients with tumors harboring *MYCN* amplification.

TERT is the major component of the telomerase holoenzymatic complex and contains the catalytic subunit. In breast cancer cells, transient knockdown of *TERT* expression resulted in reduced telomerase activity, while knockdown of other telomerase subunits as the RNA template TERC or *TP1* was not decreasing activity of the complex (Rubis, 2013). Telomerase repression was demonstrated in liver cancer cells treated with HDACi (Nakamura, 2001) and in brain tumor cells treated with HDACi trichostatin A, with no toxicity to normal brain tissue function (Rahman, 2010). This highlights the potential utility of panobinostat treatment in patients presenting with telomerase-positive tumors. Reduced activity of the telomerase complex might result in limited ability of cancer cells to undergo cell division and replicative immortality may be lost, reducing tumorigenicity. In this study, telomerase activity was stronger repressed after panobinostat treatment in *TERT*-rearranged xenograft tumors than in

the cell culture models, although reduction of *TERT* mRNA expression was comparably reduced in the *TERT*-rearranged *in vitro* and *in vivo* neuroblastoma models. There might be additional factors like posttranscriptional modifications of the TERT protein or of other subunits of the telomerase complex (Kharbanda, 2000; Kim, 2005a), probably explaining the strong reduction of telomerase activity after several weeks of panobinostat treatment. The xenograft tumors were treated for about three to four weeks with panobinostat, whereas this long treatment was not applicable in cell culture at comparable concentrations. Post-transcriptional and -translational modifications, targeted decay of the TERT protein, repression of further subunits of the telomerase complex or other factors might contribute to reduced telomerase activity after long-term treatment with panobinostat. As demonstrated in breast cancer cells, alternative splicing events result in a product termed β-deletion of the *TERT* transcript, coding for a truncated TERT protein that lacks most of the reverse transcriptase activity (Listerman, 2013; Wong, 2013). Phosphorylation (Kharbanda, 2000) or ubiquitination (Kim, 2005a) of TERT were found to be associated with decreased telomerase activity. Alternative splicing or post-translational modifications of TERT might contribute to decreasing *TERT* and telomerase levels after HDACi treatment. Further studies investigating the fate of the *TERT* mRNA transcript are necessary to address these possible regulatory pathways induced by panobinostat treatment. Taken together, the evidence obtained here demonstrate the reduction of *TERT* levels and telomerase activity by panobinostat treatment *in vitro* and *in vivo* models of *TERT*-rearranged neuroblastoma. Panobinostat treatment could present a potential way to target telomerase in neuroblastoma patients presenting with telomerase-positive tumors. As telomere maintenance is given in most cancers and generally considered as one of the hallmarks of cancer, it would be worthwhile to investigate if panobinostat treatment reduces *TERT* levels and telomerase activity in other telomerase-positive cancer entities as well.

5.2 HDAC1 and HDAC2 mediate *TERT* repression

Treatment with broad-spectrum pan-HDACi is accompanied by divert side effects like neutropenia, thrombozytopenia, diarrhea or fatigue (Afifi, 2015; Eckschlager, 2017). Application of more selective HDACi could help to reduce these undesired side effects. Downregulation of *TERT* mRNA was mediated by inhibition of HDAC1 and HDAC2, as demonstrated by mocetinostat, romidepsin and Santacruzamate A treatment. Additionally, transient knockdown of HDAC1 and HDAC2 significantly reduced *TERT* expression. Nevertheless, it might still be possible that the other HDACs have further minor contributions

in the regulation of *TERT*. Since HDACs also deacetylate non-histone proteins like p53, GATA4, E2F1 and NF-κB, the inhibition of HDACs might also trigger pathways independent of their function as epigenetic erasers (Kelly, 2013). HDAC knockdown induces different phenotypes dependent on the respective cell line (Turtoi, 2015). The participation of HDAC1 and HDAC2 as subunits of the Sin3B and CoREST corepressor complex were shown to repress *TERT* expression in normal fibroblasts, with trichostatin A treatment inducing *TERT* expression (Cheng, 2017a). As subunits of the chromatin binding complexes SIN3A/B, NuRD and CoREST, HDAC1 and HDAC2 are essential for global gene transcription and their inhibition has severe impact on gene expression (Kelly, 2013; Zhao, 2014). In cancer, HDAC expression is dysregulated with class I HDACs and HDAC6 found to be predominantly upregulated (Bolden, 2006; Ropero, 2007). Sharma and colleagues identified HDAC1 and HDAC2 to influence global mRNA stability. Reduced protein deacetylation mediated by HDAC1/2 inhibition resulted in acetylated CAF1 of the CCR4-CAF1-NOT deadenylase complex, and active degradation of poly(A) tails of global RNA pools (Sharma, 2016). The involvement of HDAC1/2 in the acetylation of the CAF-1 subunit after panobinostat treatment should be further elucidated and could help to explain the reduction of *TERT* levels after HDACi treatment. Structural similar HDAC1 and HDAC2 were shown to compensate each other in their function (Montgomery, 2007). After transient knockdown of either HDAC1 or HDAC2, no response in RNA or protein levels of the other HDAC was observed in this study. Examining a connection of individual HDACs on the regulation of *TERT* expression, the role of HDACs in the regulation of *TERT* is highly complex with multiple signaling pathways possibly mediating its repression. In conclusion, HDACi treatment revealed a major participation of HDAC1 and HDAC2 in the regulation of *TERT* expression in *TERT*-rearranged neuroblastoma cells. Further analysis of HDAC1 and HDAC2 at the *TERT* locus could shed light on the regulation of *TERT* after panobinostat treatment, for example by applying chromatin immunoprecipitation of HDAC1 and HDAC2 followed by sequencing. Application of more specific HDACi for the treatment of neuroblastoma patients could help to diminish unspecific side effects and toxicities of the therapy.

Since cancer cells have shorter telomeres than somatic cells due to their enhanced proliferation rate, evaluation of telomere length after panobinostat treatment could provide further insides into telomere maintenance in neuroblastoma (Okamoto, 2019). Disabling cancer cells to maintain their telomeres via TERT or telomerase inhibition could provide a promising approach to induce senescence and apoptosis in these cells. In addition, induction of the second pathway of telomere maintenance termed alternative lengthening of telomeres (ALT), might become

activated after telomerase inhibition, and circumvent entering replicative crisis (Hu, 2012). In a clinical perspective, it might become necessary to target both pathways to induce telomeric crisis. Ataxia telangiectasia- and RAD3-related (ATR) protein inhibitors are promising candidates to target ALT and could be applied in combination with TERT/telomerase inhibitors (Deeg, 2016; Flynn, 2015). Short-term treatment of liver cancer cells with HDACi did not show telomere shortening (Nakamura, 2001), and did not increase telomere length in ALT-positive transformed cell lines (Jung, 2013). Whether panobinostat treatment reduces telomere lengthening and prevents activation of ALT in long-term experiments remains to be investigated. In summary, inhibition of HDAC1 and HDAC2 reduces *TERT* expression and telomerase activity in models of *TERT*-rearranged neuroblastoma.

5.3 Enforced *TERT* expression attenuates HDACi induced antitumoral phenotype

TERT expression resulting in telomerase activation enables cancer cells to replicate indefinitely (Akincilar, 2016). Telomere maintenance is proposed as novel mechanistic classification correlating with poor prognosis of neuroblastoma patients (Ackermann, 2018). Since *TERT* expression is detected in stem cells and germline cells that have long or indefinite lifespan, its expression *per se* is not sufficient to induce malignant transformation (Boehm, 2005). Increasing *TERT* levels with overexpressing plasmids has been investigated to promote number of cell divisions and to increase lifespan of non-mutagenic and neuroblastoma cell lines (Bodnar, 1998; Samy, 2012). Enforced *TERT* expression enhances cell proliferation rate and increases telomerase activity (Artandi, 2002; Ramunas, 2015). HDACi treatment did not influence *TERT* expression of the plasmid used in this study, enabling to dissect the role of *TERT* expression on cell viability in the cell line model. This study reveals that upon HDACi treatment, transient enforced *TERT* expression resulted in increased cell viability and number of cells, partially rescuing the anti-tumor effects induced by HDAC inhibitor treatment, underlining the importance of *TERT* for cell viability in *TERT*-rearranged neuroblastoma cancer cells. Telomere shortening induces senescence or apoptosis after multiple replication cycles, when the telomeric ends fall below the critical length. *S*hort-term inhibition of *TERT* had no impact on telomere length, but induced cell cycle arrest and apoptotic response (Celeghin, 2016). The proposed novel classification of neuroblastoma highlights the importance of telomere maintenance in tumor progression and treatment success, but an upcoming number of reports demonstrate the participation of TERT in pathways independent of its telomerase

function (Ackermann, 2018). Several reports on the non-canonical functions of *TERT* moonlight its role in resistance response to several lethal stresses (Lee, 2008), induction of cell proliferation in resting stem cells (Sarin, 2005) or as mediator of the Wnt/β-catenin and NF-κB signaling pathways (Ghosh, 2012a; Park, 2009). Genetically modified cancer cells with abolished *TERT* expression might rely on essential pathways in cancer mediated by *TERT*, independent of its role in telomere maintenance (Koh, 2015). In a model of *MYCN*-amplified neuroblastoma, abolished telomerase activity resulted in less tumorigenic cells that were more prone to apoptosis and attenuated xenograft tumor growth in long-term experiments (Samy, 2012). *TERT* knockdown or knockout models could augment current understanding of the role of *TERT* expression in neuroblastoma. Together, this study demonstrates that enforced *TERT* expression attenuates the HDACi induced antitumoral phenotype in *TERT*-rearranged high-risk neuroblastoma cells.

5.4 Chemotherapeutics or targeted drugs do not repress *TERT* and telomerase

Chemotherapy is a harsh therapeutic option, which remains the gold standard in most cancer entities. Chemotherapeutic agents like platinum derivatives, anthracyclines or taxanes act unspecific on mitotic cells and affect somatic cells as well as cancer cells (Agarwal, 2016). Common side effects of chemotherapy such as nausea, fatigue and impairments of the nervous system can be addressed by supportive therapy but remain a challenge. Targeted agents could help to reduce side effects of the treatment and increase selectivity towards cancer cells. In this study, temozolomide and doxorubicin from the RIST and NB2004 study protocols for treatment of neuroblastoma patients were used for the analyses. In addition, oxaliplatin as first-line chemotherapeutic and the preclinical compound I-BET762 were investigated as representatives for chemotherapeutic or targeted compounds used in first-line therapy or in preclinical models of high-risk neuroblastoma. Treatment of *TERT*-rearranged neuroblastoma cells with these compounds did not impair *TERT* expression or telomerase activity at clinically relevant concentrations, except for doxorubicin reducing *TERT* expression in GI-ME-N cells. Although reducing the cell viability, these agents display their cytotoxic potential independent of *TERT*.

The *TERT*-rearranged GI-ME-N cells are classified as mesenchymal-like neuroblastoma cells, whereas CLB-GA cells reflect an adrenergic-like cell profile (Boeva, 2017). Mesenchymal cells were demonstrated to be more resistant to chemotherapy and to probably account for minimal

residue disease, probably giving to relapse after therapeutic intervention (van Groningen, 2017). The antitumoral effect induced by treatment with the selected chemotherapeutic or targeted compounds showed to be more effective towards CLB-GA cells than GI-ME-N cells, and lower concentrations were used for treatment of CLB-GA cells. This could correlate with the observation that mesenchymal-like cells show to be more resistant to drugs applied in neuroblastoma therapy such as cisplatin, doxorubicin or etoposide, than an adrenergic counterpart (van Groningen, 2017). The importance of *TERT* in regard to therapy resistance was shown in osteosarcoma cells, where *TERT* was reported to inhibit cisplatin-induced apoptosis (Zhang, 2017b). Targeting *TERT* could increase vulnerability of cancer cells towards chemotherapeutic or target therapy. In pancreatic cancer, regulators of epithelial-mesenchymal transition (EMT) maintain drug resistance against chemotherapeutic agents and could serve as an interesting target for therapeutic intervention (Arumugam, 2009). It would be interesting to investigate the role of *TERT* repression after HDAC inhibition on regulators of EMT in preclinical models of high-risk neuroblastoma, and if resistant clones potentially giving rise to MRD can be diminished by targeting *TERT* and telomerase with HDACi treatment. Further, differentiation of neuroblastoma cells into benign forms is highly desirable and can be mediated by treatment with 13-*cis*-retinoic acid (Haas, 1988; Reynolds, 2003; Sidell, 1982; Thiele, 1985). *TERT* is expressed in human stem cells, while repression of *TERT* during cell differentiation is observed (Liu, 2004). In neuroblastoma, inhibition of HDAC1/2 was shown to induce cell differentiation (Frumm, 2013), and in high-risk neuroblastoma, *TERT* expression was demonstrated to be reduced after induced cell differentiation, potentially contributing to reduce malignancy (Bui, 2019; Das, 2009). In this study, it was observed that the mesenchymal-like GI-ME-N cells changed their morphology towards a more differentiated phenotype after HDACi treatment (data not shown). It would be interesting to investigate whether inhibition of HDAC1/2 induces differentiation in mesenchymal-like *TERT*-rearranged neuroblastoma cells towards an adrenergic profile. This would open up new perspectives for subsequent combination therapy, as adrenergic cell lines are more vulnerable towards treatment with chemotherapeutic agents. Together, this study revealed that the analyzed standard antineoplastic and targeted agents applied in clinical or preclinical neuroblastoma treatment showed no reduction of *TERT* levels and telomerase activity in *TERT*-rearranged cell lines.

5.5 Panobinostat treatment represses *TERT* and telomerase in *TERT*-driven neuroblastoma xenograft mouse models

The assessment of novel drugs as stand-alone or combination therapy requires preclinical models that closely resemble the primary tumors. The antitumoral efficacy of panobinostat and other HDACi has been demonstrated in various cancer models including *MYCN*-amplified neuroblastoma (He, 2001; Helland, 2016; Lodrini, 2013). Xenograft mouse models of *TERT*-rearranged GI-ME-N and CLB-GA cells are underrepresented in neuroblastoma xenograft studies (Mandriota, 2015). This study demonstrates that panobinostat treatment reduces xenograft tumor growth, *TERT* expression and telomerase activity in *TERT*-rearranged xenograft models. This sustains data from the *in vitro* experiments of this study. The results of the GI-ME-N and CLB-GA xenograft mouse studies were confirmed in a second independent cohort of each model, highlighting the efficacy of panobinostat treatment on *TERT* and telomerase repression in *TERT*-rearranged high-risk neuroblastoma models. Reduced expression of *TERT* was also observed in *MYCN*-amplified xenograft tumors treated with panobinostat (Lodrini, 2013), highlighting the *TERT*-repressive efficacy of panobinostat in other telomerase-positive neuroblastoma high-risk groups (data not shown).

Mesenchymal-like neuroblastoma cells were demonstrated to be more resistant to chemotherapy and to probably account for minimal residue disease (van Groningen, 2017). Regarding the different transcription profiles of the cell models, the mesenchymal-like GI-ME-N xenograft model showed good response to panobinostat therapy, offering a prospect to diminish the risk of relapse. Whether panobinostat treatment reduces the risk of relapse is to be investigated in future long-term experiments.

Panobinostat is one of the most potent pan-HDACi in clinical application, presented here to reduce *TERT* expression and telomerase activity *in vitro* and *in vivo* models of *TERT*-rearranged neuroblastoma. It has a long elimination time and causes prolonged hyperacetylation of histone proteins (Singh, 2016; Tate, 2012). Long-term treatment of panobinostat has been investigated in models of *MYCN*-amplified high-risk neuroblastoma. In the *TH-MYCN* mouse model, terminal-differentiation of tumors to benign ganglioneuromas after nine weeks of treatment and prolonged survival were demonstrated (Waldeck, 2016). The continuous treatment with panobinostat questions current therapy schedules including only short-period treatment with HDACi. Further, hydroxamate-based HDACi like panobinostat have been described to induce DNA mutations (Al-Hamamah, 2019; Munakata, 1980; Prince, 2009; Wang, 1977). Up to now, hydroxamates are a major class of HDACi because of their high zinc-chelating capability,

isoform selectivity, and *in vivo* efficacy (Shen, 2016). Applying mutagen therapeutics to patients needs a careful risk-benefit assessment and their medical use should be weighted against the hazards of carcinogenesis. Panobinostat has been applied in preclinical models of neuroblastoma, but its application in models of the *TERT*-rearranged high-risk subgroup had not been evaluated before. Currently, there are several pediatric applications of panobinostat under investigation in clinical phase I-II trials (NIH, 2020), but its mutagenic potential still needs to be carefully evaluated. Addressing that issue, whole exome sequencing (WES) analyses of xenograft tumors of the preventive treatment schedules are currently under investigation in our laboratory. Alternatively, structurally different HDACi like the cyclic peptide romidepsin could serve as non-mutagenic therapeutic option. Specific HDACi targeting HDAC1/2 like romidepsin, mocetinostat and Santacruzamate A were demonstrated here to reduce *TERT* expression *in vitro*. Applying selective HDACi for the treatment of *TERT*-rearranged neuroblastoma provides an interesting approach to target *TERT* and telomerase on the one hand and reduce the toxic side effects of the treatment on the other hand.

Potential therapeutics often fail when translated from *in vitro* to *in vivo* models. A changed microenvironment, reduced uptake and metabolization of drugs diminish plasma levels and therapeutic success. Here, it was demonstrated that a reduction of the initial 15 mg/kg/d panobinostat to half of the dose resulted in comparable outcome, reducing toxic side effects of the treatment. The chosen concentration of 15 mg/kg/d panobinostat is in the spectrum of therapeutically effective doses of 5-25 mg/kg/d (Helland, 2016; Hennika, 2017; Shahbazi, 2016; Waldeck, 2016) and is achievable in patient plasma levels (Rathkopf, 2010b; Van Veggel, 2018). Upon panobinostat treatment, the observed side effects in xenografted mice here were weight loss of a maximal of about 5% and mild diarrhea, as described in previous studies (Floris, 2009; Hennika, 2017). In contrast, no significant bodyweight loss was described in mouse models receiving 7.5-15 mg/kg/d panobinostat (Helland, 2016). Reduction of bodyweight upon treatment may be strain-specific and might additionally depend on the administration route. Compared to other drugs used in cancer therapy, the side effects of panobinostat treatment are manageable and are usually reversible (Greig, 2016).

GI-ME-N xenograft tumor growth was slow and tumor engraftment was successful three month after transplantation, impeding the experimental schedule. This maybe explains that GI-ME-N xenograft models are underrepresented in the literature and showed slow growth in control-transfected GI-ME-N xenograft tumors (Mandriota, 2015). CLB-GA xenograft models have been investigated in few studies (Huang, 2020; Provost, 2016; Regairaz, 2016). Many studies

use xenograft tumor volumes of 50 mm³ at onset of treatment, but this may overestimate a potential effect of the treatment (Wong, 2019). On the one hand, smaller tumors might not have reached their replicative potential and show slow progression in cell cycle, being more vulnerable to external stressors. On the other hand, in large and highly proliferating tumors a potential effect of the drug might be extinguished. In the preventive treatment schedule of this study, a tumor volume of about 150 mm³ was chosen for induction of treatment, assuring successful tumor engraftment. In the therapeutic treatment schedule, tumor volumes of about 300 mm³ were used to investigate highly proliferating tumors. Each condition represented a balanced mean reflecting the desired clinical outset upon therapeutic intervention. Although tumors were larger and highly proliferative at onset of the therapeutic treatment schedule, panobinostat treatment repressed *TERT* expression and telomerase activity and arrested xenograft tumor growth.

Patient derived xenograft (PDX) models reflect the heterogeneous biology of patient tumors much closer than established cell culture models (Jung, 2018). In this study, a *TERT*-rearranged neuroblastoma PDX could not be investigated due to insufficient tumor growth. Instead, subcutaneous xenograft mouse models of *TERT*-rearranged neuroblastoma cells were evaluated. Further experiments in PDX models generated from patient tumor material could help to assess the *TERT* repressive phenotype and antitumoral efficacy of panobinostat in these heterogeneous models of patient tumors. In summary, this study demonstrates that panobinostat treatment represses *TERT* expression, telomerase activity and harbors antitumoral efficacy in *TERT*-rearranged high-risk neuroblastoma models following preventive and therapeutic treatment schedules. These effects of panobinostat treatment have not been previously described in models of *TERT*-rearranged high-risk neuroblastoma and might be translated to patients with *TERT*-rearranged neuroblastoma still facing poor survival rates today.

5.6 Panobinostat and bortezomib synergistically reduce cell viability in models of *TERT*-rearranged neuroblastoma

In cancer therapy, application of monotherapy will most likely result in acquired therapy resistance of tumor cells since they can adapt to the selective pressure of monotherapy (Jagadeeshan, 2019). Therefore, the efficacy of combinatorial intervention combining panobinostat and established treatment elements such as conventional anti-neoplastic chemotherapeutic agents, or targeted (preclinical) drugs in 2D and 3D cell culture models was

investigated. Investigation of 3D cell culture models reflects better the environment of a solid tumor, and can built a rationale for subsequent *in vivo* analyses. In an unbiased screen of FDA-approved therapeutics, the proteasome was identified to be a promising target in *MYCN*-driven neuroblastoma (Wang, 2019). The proteasomal inhibitor bortezomib (Velcade®) in combination with panobinostat is approved for treatment of relapsed or refractory multiple myeloma and showed prolonged survival of patients (Afifi, 2015). The combination of panobinostat and bortezomib resulted in synergistic decrease of cell viability in *TERT*-rearranged neuroblastoma cell line models (R. Linke, Medical Dissertation, work in progress). Reduced *TERT* mRNA expression and telomerase activity after bortezomib treatment were described in multiple myeloma, erythroid leukemia and gastric cancer (Ci, 2015; Weiss, 2012). Moreover, the combination of HDACi valproic acid and bortezomib was shown to reduce *TERT* expression and telomerase activity in myeloid leukemia cells (Nie, 2012). In contrast, this study in *TERT*-rearranged neuroblastoma cells revealed that bortezomib treatment alone had no major effect on *TERT* levels and telomerase activity, and showed no synergistic effect on *TERT* expression and telomerase activity when combined with panobinostat. As demonstrated in glioblastoma stem-like cells and ovarian cancer cells, the combination of HDACi and bortezomib act synergistically on cell viability, sustaining the results of this study (Asklund, 2012; Janyst, 2018). RNA sequencing studies of the combination therapy approach in GI-ME-N and CLB-GA are currently under investigation in our laboratory, contributing to the identification of pathways alternatively regulated by panobinostat and bortezomib treatment.

In this study, a pilot xenograft mouse study assessing the combination of panobinostat with bortezomib was performed. The treatment schedule was not implemented by the company as outlined by our laboratory. Accordingly, tumor growth of individual animals within one study group showed strong discrepancies. Nevertheless, no severe toxicities of the combination treatment were observed in this first investigation. Future studies in xenograft or PDX models are necessary to assess the potency of the combination therapy of panobinostat and bortezomib in preclinical models of *TERT*-rearranged high-risk neuroblastoma.

Telomere maintenance mechanisms define a novel subgroup of high-risk neuroblastoma patients (Ackermann, 2018). Additional alterations of RAS and/or p53 signaling pathways worsen the prognosis and form the ultra high-risk group with a high likelihood of death from disease (Ackermann, 2018). Compounds targeting RAS/p53 pathway show promising effects in preclinical models of neuroblastoma and represent a therapeutic option worthwhile investigating in *TERT*-rearranged high-risk neuroblastoma (Hart, 2017; Infarinato, 2016).

Inhibitors of ALK are currently under clinical investigation to impair RAS signaling pathway, although resistance to therapy is one major risk of the treatment (Dagogo-Jack, 2018). The investigated CLB-GA cell line harbors an ALK R1275Q mutation. Recent studies demonstrate a good response of ALK inhibitors combined with p53-restoring agents, which might be enhanced in combination with panobinostat treatment (Miyazaki, 2018). Panobinostat in combination with Wee1 inhibitor adavosertib (MK-1775), cisplatin, doxorubicin or etoposide are further interesting candidates shown to synergistically reduce neuroblastoma tumor cell viability (Hanmod, 2015; van Groningen, 2017; Wang, 2013; Zareifar, 2019). High-risk neuroblastoma xenograft tumors showed good response to combination therapy of panobinostat and THZ1, a CDK7 inhibitor (Wong, 2019), and in *MYCN*-amplified neuroblastoma, combined treatment with panobinostat and the BETi JQ1 showed synergistic induction of anticancer effects (Shahbazi, 2016). In addition, GI-ME-N and CLB-GA cells express programmed death-ligand 1 (PD-L1) antigen on their cell surface (data not shown), a druggable target applying PD-L1 inhibitors. Immunotherapy could augment current treatment schedules and help improving patient survival rates. Aiming for an optimized therapy schedule including pre-treatment or co-treatment with HDACi like panobinostat, combination therapy can result in a stronger response to therapy than single agent treatment, reduce the risk of resistance against therapeutics and might be applied at less toxic doses, reducing undesired side effects of the therapy. Optimization of current neuroblastoma treatment protocols including panobinostat presents a rationale for future investigations to identify synergistic combinations to reduce dose and toxicity of the treatment. In this study, the proteasomal inhibitor bortezomib in combination with panobinostat was demonstrated to synergistically reduce cell viability in models of *TERT*-rearranged neuroblastoma.

5.7 BET inhibitor treatment has no influence on *TERT* levels and telomerase activity in *TERT*-rearranged neuroblastoma cells

Amplification of the *MYCN* gene stratifies neuroblastoma patients to the high-risk subgroup, with currently no convincing therapy inhibiting MYCN in a clinical setting (Moreno, 2017). Treatment with BET inhibitors results in reduced *MYCN* expression in *MYCN*-amplified neuroblastoma models (Henssen, 2016). *MYCN* expressing neuroblastoma are characterized by high *TERT* expression and telomerase activity, with *TERT*-rearranged neuroblastoma showing even higher levels of *TERT* expression and telomerase activity (Peifer, 2015). This study revealed that *TERT* and *MYCN* mRNA expression were reduced after panobinostat treatment in

TERT-rearranged cell lines (data not shown), sustaining data in neuroblastoma cells without a *TERT* rearrangement that HDACi treatment suppresses *MYCN* (Deubzer, 2008; Shahbazi, 2016; Wong, 2019). Downregulation of telomerase activity driving neuroblastoma malignancy provides a promising treatment approach, not limited to the *TERT*-rearranged subgroup. Interestingly, in this study it was demonstrated that BET inhibitor treatment at clinically relevant concentrations applying JQ1, I-BET762 and OTX015 did not influence *TERT* mRNA expression in *TERT*-rearranged neuroblastoma cell lines, supporting the assumption that *TERT* expression is not primarily dependent on *MYCN* in this subgroup. Further, telomerase activity was not altered after treatment with BRD2-4 inhibitor I-BET762 in these models. BRD4 is an epigenetic reader recognizing chromatin and lysine-acetylated histones. In fibroblasts and HeLa cells, telomerase activity was not altered after BRD4 inhibition but telomeres were shortened in long-term experiments (Wang, 2017). In contrast, a recent study presents BET inhibitors JQ1 and AZD5153 to downregulate *TERT* expression in *TERT*-rearranged neuroblastoma models, mediated by BRD4 inhibition (Huang, 2020). In the study presented here, there was no evidence that BRD4 inhibition influences *TERT* levels in the CLB-GA neuroblastoma cell line, that was also used in the study by Huang and colleagues (Huang, 2020). Although treatment period and concentrations were comparable in both studies, further investigations are necessary to explain the contrasting findings. In the study presented here, treatment with BETi I-BET762 revealed no reduction of telomerase activity at a comparable concentration and treatment period, questioning the report that BETi treatment reduces *TERT* and telomerase activity in *TERT*-rearranged neuroblastoma cell lines (Huang, 2020). Determination of telomere length in long-term treatment experiments will contribute to our understanding of telomerase activity and the influence of HDAC and BET inhibition on telomere maintenance in high-risk neuroblastoma. Further preclinical studies are necessary to investigate whether patients with *TERT*-rearranged tumors would benefit from BET inhibitor treatment. In this study, there was no evidence that BET inhibitor treatment represses *TERT* expression or telomerase activity in models of *TERT*-rearranged high-risk neuroblastoma.

5.8 Panobinostat treatment reduces malignancy of neuroblastoma cell lines

Replicative immortality is considered as one of the hallmarks of cancer (Low, 2013). HDAC inhibition was demonstrated to reduce malignancy in high-risk neuroblastoma models (Fabian, 2014; Lodrini, 2013; Thole, 2017). The efficacy of drug treatment varies among the particular

lineages and genomic backgrounds. A panel of six cell lines representing *MYCN*-amplified, *TERT*-rearranged and cell lines lacking those alteration were investigated in this study. Panobinostat treatment was demonstrated here to have antitumoral efficacy towards neuroblastoma cells of different genetic background at low nanomolar concentrations. There was no correlation between genotype and metabolic activity, suggesting that the antitumoral efficacy of panobinostat is independent of *MYCN* and *TERT* status in the selected cell line panel.

One major characteristic of cancer cells is their potential to form colonies from single cell state. Decreasing the ability of colony formation is considered to reduce tumor cell migration and metastasis formation. This study revealed that in *TERT*-rearranged cell lines, colony formation is severely impaired after panobinostat treatment. This might partially depend on reduced *TERT*-expression induced by HDACi treatment. Reduced colony formation capacity after panobinostat treatment has been reported in many cancers including neuroblastoma, underlining the antineoplastic features of the pan-HDACi (Fabian, 2014; Helland, 2016; Shahbazi, 2016). In *TERT*-expressing melanoma and thyroid gland cancer cell line models, knockdown of *TERT* resulted in reduced colony formation (Liu, 2018). One candidate that was identified to be involved in colony formation, cell survival, proliferation, and motility in various cancers including *MYCN*-amplified neuroblastoma was the focal adhesion kinase (FAK) (Beierle, 2007; Lee, 2012; Stafman, 2019; Waters, 2014). As MYCN induces FAK expression, the repression of *MYCN* by HDAC inhibitor treatment might result in reduced FAK levels and diminish the malignant phenotype (Beierle, 2007). Future studies will be necessary to assess the role of FAK on malignancy in *TERT*-rearranged neuroblastoma cell lines, which are not *MYCN*-amplified.

In this study, it was demonstrated that panobinostat treatment reduced proliferation of *TERT*-rearranged neuroblastoma cells. In *MYCN*-amplified neuroblastoma cells, HDACi treatment resulted in reduced cell proliferation, cell cycle arrest and induction of apoptosis (Lodrini, 2013; Muhlethaler-Mottet, 2008; Subramanian, 2007). In various cancer cell lines, *TERT* was demonstrated to increase cell proliferation by promoting RNA polymerase III-mediated expression of transfer RNAs (tRNA) (Khattar, 2016), and promoted the progression of cancer by regulating MYC stability and MYC-dependent oncogenesis, independent of its reverse transcriptase activity (Koh, 2015). TERT was demonstrated to bind to the RPC32 subunit of the RNA polymerase III complex, augmenting the expression of tRNAs and subsequently increasing the protein synthesis and proliferative abilities of cancer cells (Khattar, 2016). Targeting *TERT* with the HDACi panobinostat reducing *TERT* expression might decrease tRNA

expression and cell proliferation, partially contributing to the reduction of colony formation and cell proliferation after treatment.

Various chemotherapeutics or targeted drugs applied in cancer therapy base on the induction of apoptosis by the treatment. The programmed cell death is tightly controlled with multiple checkpoints to be passed until initiation. In tumors, many genes involved in apoptosis induction and progression are repressed, disabling the induction of apoptosis. Inhibition of HDACs is associated with induction of apoptosis, autophagic cell death and necrosis (Ellis, 2009; Hsu, 2011; Kabeya, 2000; Waldeck, 2016). The induction of apoptosis in cancer cells is highly desired, since this process is not only dependent on external stimuli as the immune system, which is often impaired by the therapy itself (Gardner, 1999). The study presented here demonstrates that panobinostat treatment resulted in decreased cell viability, induction of protease-mediated apoptosis and increase in sub-G1 fraction in *TERT*-rearranged cell line models. The regulation of apoptosis by HDACi has been demonstrated to be mediated by up-regulation of the pro-apoptotic proteins Bcl-2-interacting mediator of cell death (BIM) (Zhang, 2004) and Bcl-2-modifying factor (BMF) (Inoue, 2007). In addition, downregulation of the anti-apoptotic proteins B-cell lymphoma 2 (Bcl-2) and Induced myeloid leukemia cell differentiation protein Mcl-1 (Mcl-1) (Zhang, 2004) were demonstrated. The degree of regulation is depending on the cellular context and the applied HDACi (Matthews, 2012). It remains to be explored whether panobinostat treatment influences expression of BIM, BMF, Bcl-2 and Mcl-1 in *TERT*-rearranged neuroblastoma cells, thereby decreasing their tumorigenic features.

Furthermore, treatment with panobinostat and specific telomerase inhibitors BIBR1532 and costunolide was shown here to reduce cell viability, with panobinostat treatment showing antitumoral efficacy at low nanomolar concentrations. Telomerase inhibitors BIBR1532 and costunolide were shown to induce apoptosis partially via induction of caspase-3-dependent apoptotic cell death, possibly linking the panobinostat-mediated decrease of telomerase activity to the pro-apoptotic effect of panobinostat treatment (Celeghin, 2016; Pourbagheri-Sigaroodi, 2019; Yan, 2019). Since application of these specific inhibitors of telomerase did not show convincing results in preclinical studies (Relitti, 2020), treatment with the HDACi panobinostat provides a promising option to target *TERT* and induce apoptosis in *TERT*-rearranged neuroblastoma (Waldeck, 2016). In contrast, several therapeutics from the RIST and NB2004 study protocols such as dasatinib or temozolomide showed no reduction of cell viability in *TERT*-rearranged neuroblastoma cells (data not shown). In hepatocellular cancer cells, transient

knockdown of *TERT* resulted in cell cycle arrest and induction of apoptosis (Shen, 2018). These results emphasize the crucial role of *TERT* expression for the survival and malignant properties of cancer cells and highlight the need for therapeutic intervention. Together, this study demonstrates that panobinostat reduced malignancy and induced apoptosis in *TERT*-rearranged neuroblastoma cell lines, showing antitumoral efficacy superior to several therapeutics currently applied in neuroblastoma therapy. The application of panobinostat treatment to patients presenting with *TERT*-rearranged tumors provides a promising approach to reduce the malignancy of neuroblastoma tumors and could augment current therapy schedules.

5.9 Panobinostat treatment induces changes in cell cycle profile

HDAC inhibitor treatment has been described to induce cell cycle arrest and cell death via regulation of transcription factors p53, E2F, c-Myc, NF-κB, as well as the extracellular signal-regulated kinase 1/2, Wnt signaling pathways, Notch and phosphatidylinositol 3-kinase (Zhang, 2017a). This study identified hallmarks E2F target and G2M checkpoint genes to be less expressed after panobinostat treatment in *TERT*-rearranged cell lines and xenograft tumors. In preclinical models of neuroblastoma, HDACi treatment resulted in cell cycle arrest and increase in sub-G1 fraction (Deubzer, 2008; Francisco, 2012; Kolbinger, 2018; Lodrini, 2013). Further, in hepatocellular carcinoma and *MYCN*-expressing neuroblastoma models, reduction of *TERT* levels was demonstrated to suppress cell cycle progression (Shen, 2018; Tate, 2012; Waldeck, 2016). As *TERT* is repressed after HDACi treatment, these reports sustain observations from the study presented here demonstrating changes in the cell cycle profile, and increase in sub-G1 fraction in *TERT*-rearranged neuroblastoma models after panobinostat treatment. A *TERT* expression signature was postulated to overlap with signatures of *MYCN*-amplified neuroblastoma in a cohort of neuroblastoma patient samples (Huang, 2020). Expression signatures of neuroblastoma cells with high *TERT* expression and without *MYCN* amplification showed that E2F target genes and cell cycle related genes were highly expressed (Huang, 2020). In line with this report, comparing that gene set of 50 genes identified by Huang *et al*. with the RNA expressing data of xenograft tumors from this study, an average of 62% of them were downregulated after panobinostat treatment (data not shown). This data demonstrating alterations of the cell cycle profile after panobinostat treatment was sustained by flow cytometry analysis of *TERT*-rearranged neuroblastoma cell lines treated with panobinostat, showing changes of the cell cycle profiles and increase in sub-G1 fraction. Treatment with panobinostat

reduces *TERT* expression and may point towards a central role of *TERT* in cell cycle progression of *TERT*-rearranged neuroblastoma cells.

Expression profiles of neuroblastoma reveals intratumoral heterogeneity, making it difficult to decide on treatment options (van Groningen, 2017). A general classification of neuroblastoma based on RNA expression profiling was introduced by van Groningen and colleagues. They proposed a transcription factor profile unique to adrenergic or to mesenchymal neuroblastoma cells. Expression of the homeobox transcription factor *PRRX1* reprogrammed adrenergic cell types into mesenchymal cell types, but not vice versa. Upon chemotherapy treatment, remaining cells showed increase in *PRRX1* expression and were more resistant to therapy with cisplatin, doxorubicin and etoposide (van Groningen, 2017), which are applied in the first-line therapy of neuroblastoma. The plasticity and more therapy-resistant mesenchymal cells may explain why therapies often fail and relapse occurs. In this study, RNA sequencing analysis revealed downregulation of *PRRX1* in the mesenchymal like GI-ME-N xenograft tumors after panobinostat treatment (data not shown). It would be worth investigating whether panobinostat treatment triggers the switch of mesenchymal cell types into adrenergic cell types and if panobinostat treatment further enhances cytotoxicity of antineoplastic drugs in *TERT*-rearranged neuroblastoma. Therapies targeting the mesenchymal-like cells might be a valuable option to diminish the risk of therapy resistance and relapse in neuroblastoma therapy. In summary, panobinostat treatment was demonstrated here to induce changes in the cell cycle profile and to increase sub-G1 fraction in models of *TERT*-rearranged neuroblastoma.

5.10 Panobinostat treatment triggers no major changes of epigenetic marks at *TERT* locus

In neuroblastoma, genomic rearrangements of the *TERT* locus put *TERT* expression under the control of super-enhancers elements as demonstrated in cohorts of mixed stage neuroblastoma (Peifer, 2015; Valentijn, 2015). Recent discoveries in neuroblastoma demonstrated that deregulated *TERT* expression is also achieved by integration of genomic circle DNA proximal to the *TERT* gene, resulting in transcriptional upregulation of *TERT* (Koche, 2020). The neuroblastoma cell lines GI-ME-N, CLB-GA, Kelly and possibly LAN-2 were identified to harbor a *TERT* rearrangement (Gartlgruber, 2018; Peifer, 2015). Rearrangements of the *TERT* locus were shown to occur in a region 50 kb upstream of the *TERT* gene in patient tumors (Gartlgruber, 2018; Peifer, 2015). In contrast, this study identified the breakpoint in GI-ME-N

cells to be located within the *TERT* 5'-UTR, adding more complexity to *TERT* gene regulation. Genomic *TERT* rearrangements resulting in high *TERT* expression and telomerase activity were described in several cancer entities including neuroblastoma, glioblastoma and meningioma (Diplas, 2018; Juratli, 2018; Peifer, 2015; Valentijn, 2015). Future studies applying chromosome confirmation capture technologies or ChIP sequencing are necessary to understand how the *TERT* gene is regulated and which factors drive its expression in the corresponding cellular context of a genomic *TERT* rearrangement (Gartlgruber, 2018).

Besides activating mutations in the *TERT* gene body or in the gene promotor, epigenetic modifications were identified to upregulate *TERT* expression across tumor entities (Zhao, 2009). In this study, ChIP sequencing of solvent-treated cells confirmed the epigenetic profile indicative of an active chromatin state (Gartlgruber, 2018; Peifer, 2015; Valentijn, 2015). After panobinostat treatment, this profile revealed genome-wide alterations in the analyzed histone marks, but no major changes of the epigenetic environment of the rearranged *TERT* region were detected after panobinostat treatment. The few significantly altered histone modifications in the rearranged *TERT* region are not likely to severely influence the expression of *TERT*, and cannot explain the repression of *TERT* mRNA levels after panobinostat treatment. Comparing *TERT*-rearranged tumors and cell lines with samples without a *TERT* rearrangement, histone marks H3K27ac, H3K4me1 and H3K4me3 were enriched at the transcriptional start site of *TERT*, which are all associated with actively transcribed protein-coding genes (Gartlgruber, 2018; Peifer, 2015; Valentijn, 2015). Histone mark H3K36me3 was enriched across the *TERT* gene body, an indication of actively transcribed genes (Gartlgruber, 2018; Peifer, 2015). Repressive chromatin marks H3K27me3 and H3K9me3 showed a more divergent pattern, also being enriched at *TERT* gene body and the transcriptional start site (Gartlgruber, 2018; Peifer, 2015). The parallel occurrence of activating and repressive chromatin marks at the same locus is termed a bivalent state, allowing timely gene activation or repression upon stimulation (Voigt, 2013). This epigenetic profile indicative of an actively transcribed *TERT* locus was confirmed here in solvent-treated cells and the efficacy of panobinostat treatment was ensured by technical validation of samples prior to sequencing. Sample analysis applying qRT-PCR confirmed decreasing *TERT* levels after panobinostat treatment, and pull-down efficacy of proteins was exemplarily analyzed at *GRHL1* and *MIR183* loci, demonstrating technical accuracy of sample preparation. Induction of *GRHL1* and *MIR183* was previously demonstrated in neuroblastoma cells after panobinostat treatment (Fabian, 2014; Lodrini, 2013). In this study, the six histone modifications from the publication of Peifer *et al*. were used for the analysis of histone modifications in the *TERT* region after panobinostat treatment. These histone modifications

represent prominent histone marks playing major roles in gene regulation and are commonly used for ChIP sequencing analyses (Kimura, 2013). There are additional histone marks like H3K4me2 and H3K4ac that were shown to be involved in *TERT* transcription in multiple cancers (Li, 2016a; Stern, 2015). It would be worthwhile investigating whether these histone modifications are differentially regulated after panobinostat treatment at the *TERT* locus. In addition, this study investigated chromatin marks 18 h after panobinostat treatment. This period might have been too short to induce changes in the selected chromatin marks at the *TERT* locus, although *TERT* levels are reduced to about 40% at that time point. Regulatory mechanisms such as miRNA-mediated degradation or post-transcriptional modifications mediating the early repression of *TERT* could explain the clear reduction of *TERT* mRNA level early after onset of panobinostat treatment. Looking at histone modifications at later time points might unravel an additional participation of histone marks in the regulation of *TERT* and contribute to our understanding of the epigenetic landscape at the *TERT* locus after HDACi treatment. Therefore, histone modifications participating in the regulation of the *TERT* region induced by HDACi panobinostat cannot completely be ruled out.

Global increase of histone acetylation is a well-described effect of HDACi treatment (Dias, 2018; Glick, 1999). In normal human fibroblasts and epithelial cells, HDAC inhibition induces expression of *TERT* by changing the acetylation status of nucleosomal histones resulting in an open chromatin state, but not in cancer cells (Takakura, 2001). In contrast, in breast cancer cells and other cancers, genome-wide hyperacetylation of histones was shown to be increased after panobinostat treatment (Singh, 2016; Tate, 2012). Global increase in histone mark H3K27ac was also reported here after panobinostat treatment, but the few significantly altered acetylated sites in the rearranged *TERT*-region are unlikely to explain the strong repression of *TERT*. Additional so far unknown hyperacetylated sites may participate to indirectly regulate the expression of *TERT* after panobinostat treatment.

Many oncogenes acquire close proximity to transcriptional strong enhancer elements, a process called super-enhancer hijacking (Northcott, 2014). This results in an induction of massive oncogene expression and increased expression of subsequent target genes. In *TERT*-rearranged neuroblastoma, several strong enhancer regions like EBF Transcription Factor 1 (EBF1), Membrane Associated Ring-CH-Type Finger 11 (MARCH11) and Neuropeptide Y (NPY) juxtaposed the *TERT* gene (Gartlgruber, 2018; Peifer, 2015). Further analysis of ChIP sequencing data of the *TERT*-rearranged cell line models focusing on patterns of H3K27ac and H3K4me1 histone modifications, which are known to mark active enhancers, could identify the

responsible enhancer elements driving *TERT* expression (Ernst, 2011; Heintzman, 2007). It would be interesting to assess whether panobinostat treatment influences the interaction of acquired enhancer elements and *TERT*. The *TERT* locus is transcriptionally silenced in most somatic cells and becomes (re)activated during tumorigenesis (Low, 2013). HDAC inhibition reverses this repression in normal cells (Cong, 1999; Takakura, 2001; Wang, 2003). ATAC sequencing in CLB-GA and Kelly neuroblastoma cells revealed an enrichment of peaks at the *TERT* locus and neighboring genes, indicative of open chromatin (Gartlgruber, 2018). Circularized chromosome conformation capture (4-C) sequencing analysis identifying possible regulatory elements and super-enhancers driving *TERT* expression are worthwhile investigating in *TERT*-rearranged neuroblastoma. Further investigations possibly applying ATAC-seq or DNase-footprinting could help to illuminate the regulation of the *TERT* locus after panobinostat treatment.

In addition to histone modification, DNA methylation of CpG dinucleotides can influence *TERT* gene transcription (Jie, 2019; Zhu, 2010). HDACi were demonstrated to indirectly influence DNA methylation, by downregulation of DNA methyltransferase 3 beta (DNMT3B) mRNA and protein expression in human endometrial adenocarcinoma cells (Xiong, 2005). The study presented here demonstrates that methylation is globally reduced after panobinostat treatment. The *TERT* locus was less methylated at few CpG sites after panobinostat treatment, but generally showed no major alterations at individual CpG dinucleotides. Few alternately methylated CpG sites were distributed spatially within the *TERT* region and might not be sufficient to result in transcriptional repression of *TERT* (Bird, 2004; Deaton, 2011). Methylation of CpG dinucleotides is generally considered to silence gene expression in somatic tissue (Long, 2017), and HDAC inhibition indirectly reduces methylation at CpG sites (Zopf, 2012). Further, it was shown in healthy mice that panobinostat treatment induced DNA hypomethylation (Al-Hamamah, 2019). Cancer cells display a dysregulation of CpG methylation patterns, resulting in oncogene activation (Gal-Yam, 2008). There is controversy discussion about how methylation regulates the expression of *TERT* (Jie, 2019). Increased methylation of CpG sites at the *TERT* promotor was demonstrated to repress *TERT* in teratocarcinoma cells, normal oral fibroblasts and senescent normal oral keratinocytes (Lopatina, 2003; Shin, 2003). In contrast, across tumor entities including colon, breast, prostate and brain cancer, hypermethylation of the THOR region proximal to *TERT* was described to result in upregulation of *TERT* gene expression (Lee, 2019; Seynnaeve, 2017). In non-small cell lung cancer cells, treatment with HDACi vorinostat induced reduction of telomerase activity and diminished methylation of the THOR region and expression of DNA-

methyltransferases *DNMT1* and *DNMT3b* (Li, 2011). Methylation array profiling of mixed-stage neuroblastoma revealed that *MYCN*-amplified tumors showed the highest levels of CpG methylation in the *TERT* region, followed by *TERT*-rearranged neuroblastoma (Gartlgruber, 2018; Peifer, 2015). Strongly enriched methylation of CpG site cg11625005 (chr5:1295737) close to the *TERT* promotor was observed in neuroblastoma tumors with high *TERT* expression (Gartlgruber, 2018; Peifer, 2015). In this study, the rearranged *TERT* region of the GI-ME-N cell line reveals a distinct genomic environment that is lacking the native sequence proximal to *TERT*, including the gene promotor itself. Therefore, the published epigenetic regulation of *TERT* cannot be transferred to the data presented in this study. It remains to be investigated whether structural motifs such as E-boxes, GC or ETS binding sites are proximal to *TERT*, and if they are regulated by HDACi treatment.

In telomerase-positive cells, it was shown that methylation of the *TERT* promoter was necessary for active gene transcription and that CCCTC-Binding Factor (CTCF) binding to the first exon repressed *TERT* transcription, which was abrogated when methylation of its recognition sequence was increased (Renaud, 2005; Renaud, 2007). Applying ChIP sequencing, it would be interesting to assess whether binding of the transcriptional insulator CTCF to *TERT* is increased after panobinostat treatment, possibly mediating *TERT* repression. In addition, changes in methylation of CpG dinucleotides are indirect effects mediated by HDAC inhibitors and the investigated time point of 18 h after treatment might have been too early to reveal clear changes of the methylation status in the rearranged *TERT* region. Looking at methylation patterns at later time points might unravel a possible differential methylation of CpG sites regulating *TERT* expression, and contribute to our understanding of the methylation status at the *TERT* locus after panobinostat treatment in *TERT*-rearranged neuroblastoma cells. Further analyses of the methylation status of the *TERT* region applying bisulfite cloning and sequencing might help to uncover potential changes in the methylation status of the *TERT* locus (Zhang, 2009). Therefore, regulation of the *TERT* region by alternatively methylated CpG sites induced by panobinostat treatment might possibly contribute to the repression of *TERT* at later time points. Focusing on the *TERT* locus, further analyses to investigate the chromatin state after panobinostat treatment are necessary to unravel the regulation of the locus after panobinostat treatment. This study demonstrates that panobinostat treatment revealed no major changes in the investigated epigenetic marks at the *TERT* locus in *TERT*-rearranged cells.

5.11 Panobinostat treatment reduces stability of the *TERT* mRNA transcript

Treatment with HDACi results in changes in gene expression profiles, with the regulated genes remain largely unknown (Peart, 2005). One direct effect of HDACi treatment is the increase in histone acetylation resulting in facilitated gene transcription, or in transcription factor acetylation (de Ruijter, 2003; Roth, 2001; Tate, 2012). Indirect effects of HDACi treatment include the inhibition of interactions between HDACs and non-histone proteins or the regulation of non-coding RNAs like miRNAs (Bolden, 2006; Shin, 2009). This study demonstrates that histone modifications and methylation of CpG dinucleotides in the *TERT* region are not majorly changed by panobinostat treatment in *TERT*-rearranged neuroblastoma cells at given treatment time points, whereas stability of the *TERT* mRNA was reduced upon global transcriptional inhibition. Panobinostat treatment reduced half-life of the *TERT* mRNA transcript after blocking *de novo* RNA synthesis with actinomycin D, arguing for a mechanism targeting stability of the *TERT* mRNA transcript. Depending on the cell lines used, half-life of *TERT* mRNA was assessed to about 13 h and 21 h. In contrast, stability of *TERT* mRNA has been determined with half-life of 2-6 h in cancer cells or immortalized cell lines (Emerald, 2007; Gunes, 2000; Xu, 1999; Yi, 1999). In *TERT*-rearranged neuroblastoma, *TERT* expression is higher than in all other subgroups of neuroblastoma and the *TERT* mRNA stability might be enhanced by so far unknown mechanisms in the *TERT*-rearranged cell lines. Since panobinostat treatment had no impact on *TERT* mRNA transcription of the overexpressing plasmid containing the *TERT* open reading frame, transcriptional regulators of *TERT* might target the promotor or non-coding sequence of the transcript, resulting in degradation of the mRNA or precursors.

Upon HDAC1/2 depletion, *TERT* expression was shown here to be significantly reduced. In mammalian cells, HDAC1/2 inhibition with trichostatin A resulted in accelerated poly(A) RNA degradation (Sharma, 2016). The acetylated CCR4-CAF1-NOT deadenylase complex participates in degradation of global poly(A) RNA pools and might degrade the *TERT* RNA transcript (Sharma, 2016). It will be worthwhile investigating if HDACi-induced HDAC1/2 inhibition results in acetylation of the CCR4-CAF1-NOT deadenylase complex in *TERT*-rearranged neuroblastoma cells, decreased global RNA pools and subsequent destabilization and degradation of *TERT* mRNA. This study suggest that panobinostat treatment plays an important role in modulating *TERT* mRNA stability. It remains to be elucidated which factors mediate the reduction of the *TERT* transcript stability after HDACi treatment. Whether

degradation of global poly(A) RNA pools will be more selective for targeting *TERT* remains to be demonstrated and will help to elucidate the fate of the *TERT* mRNA after HDACi treatment.

Given the broad spectrum of effects triggered upon HDAC inhibition, it is likely that multiple mechanisms mediate the HDACi-induced antitumoral phenotype, resulting in different response to treatment dependent on the cellular context (Li, 2016b). Over 1,300 miRNAs are predicted to target *TERT* and they might act in concert on the regulation of *TERT* (Agarwal, 2015). As demonstrated in neuroblastoma, miRNAs play crucial roles in mRNA expression, transcript stability and regulation of tumor suppressor expression (Lodrini, 2013; Nowak, 2018). HDACi treatment was demonstrated to alter expression profiles of miRNAs in many tumor entities (Rafehi, 2016; Shin, 2009). Nevertheless, it remains challenging to identify a link between miRNAs, HDACi and/or a specific cancer or pathway (Autin, 2019). It is assumed that HDAC inhibition re-establishes the expression of abnormally expressed miRNAs in a range of cancer types, building a rationale for miRNAs as potential drug targets (Ediriweera, 2020). In *MYCN*-amplified neuroblastoma, treatment with panobinostat triggered expression of tumor suppressive miR-183 and induced cancer cell death (Lodrini, 2013). Several miRNAs were identified to target the *TERT* RNA, resulting in transcript degradation and reduced telomerase activity. Potential candidates are miR-128, shown to suppress *TERT* expression by binding to its coding region in HeLa and teratoma cells (Guzman, 2018), as well as miR-133a and miR-138, shown to target the *TERT* 3'-UTR in HeLa cells (Hrdlickova, 2014). While the role of miR-133a remained poorly investigated in neuroblastoma, overexpression of miR-128 was demonstrated in neuroblastoma cells to alter the expression of genes implicated in cytoskeletal organization, apoptosis, cell survival and proliferation, including the anti-apoptotic factor Bcl-2 (Guidi, 2010). Further, miR-128 was demonstrated to act as a tumor suppressor to reduce neuroblastoma cell motility, invasiveness, and growth (Evangelisti, 2009). It would be interesting to assess whether panobinostat treatment induces the expression of miR-128, mediating the antitumoral phenotype and repression of *TERT* in *TERT*-rearranged neuroblastoma. Although miR-128 is reported to bind the *TERT* coding region, no influence on expression of the *TERT* overexpressing plasmid was detected here after treatment with HDACi. In human malignant neuroblastoma, tumor suppressor miR-138 is hardly expressed (Chakrabarti, 2013). In neuroblastoma cell lines, it was shown that knockdown of *TERT* indirectly increased expression of miR-138, mediating apoptosis and increasing sensitivity towards the plant-derived flavonoid apigenin (Chakrabarti, 2013). It remains to be explored whether miR-138 is induced after HDACi treatment and if this miRNA contributes to the observed induction of apoptosis and repression of *TERT* mRNA in *TERT*-rearranged

neuroblastoma cells. Given that *TERT* is repressed already after 2 h of HDACi treatment, the induction of a miRNA targeting the *TERT* mRNA at this early time point seems unlikely. In summary, the data presented here reveals evidence that the reduction of the *TERT* mRNA is mediated by a reduction of RNA stability after panobinostat treatment. It remains to be elucidated which factors mediate the reduction of the *TERT* transcript stability after HDACi treatment. Further studies focusing on posttranscriptional modifications, regulatory proteins or RNA silencing could identify a possible link of reduced *TERT* mRNA stability and HDAC inhibition with panobinostat in *TERT*-rearranged neuroblastoma.

5.12 Summary

This study demonstrates the clinically approved pan-HDAC inhibitor panobinostat as a potent antitumoral agent in models of *TERT*-rearranged high-risk neuroblastoma. Panobinostat treatment suppresses high-level *TERT* expression and telomerase activity, cell cycle progression and xenograft tumor growth and induces apoptosis in *TERT*-rearranged neuroblastoma models, suggesting indirect druggability of *TERT* and a potential novel molecular rationale for therapeutic intervention. The reduction of *TERT* mRNA expression and telomerase activity are mediated by HDAC1 and HDAC2. Analyses of histone modifications and CpG methylation in the rearranged *TERT* genomic region reveals no major changes after panobinostat treatment. Reduced stability of the *TERT* mRNA transcript was demonstrated after panobinostat treatment, suggesting reduced RNA stability as the underlying molecular mechanism. First-line chemotherapeutic agents of neuroblastoma therapy and targeted compounds in the preclinical phase have no impact on *TERT* expression and telomerase activity. Combination therapy of panobinostat and bortezomib shows strong synergistic effects in preclinical models of *TERT*-rearranged high-risk neuroblastoma, paving the way for an early clinical trial, translating recent scientific discoveries to the bedside to benefit patients. Optimization of current neuroblastoma treatment protocols including panobinostat presents a rationale for future investigations to identify synergistic therapeutic effects to reduce dose and toxicity of the treatment, and to diminish the risk of relapse in the *TERT*-rearranged high-risk patient subgroup.

6 Appendix

6.1 DNA breakpoint and rearrangement partner of the *TERT* region in GI-ME-N cells

Rearrangements of the *TERT* locus were shown to occur in a region upstream of *TERT* termed the breakpoint region (Peifer, 2015; Valentijn, 2015). In a cohort of neuroblastoma patients, the corresponding breakpoint was identified to occur not in the gene body or the promotor of *TERT*, but in a region of about 50 kb upstream of *TERT* transcriptional start site (TSS) (Peifer, 2015). To obtain the individual profile of the GI-ME-N cell line and to identify the DNA breakpoint and rearrangement partner of the *TERT* region, whole genome sequencing (WGS) was performed. Cells were harvested and each 10 x10^6 cells were snap frozen in three replicates. Sample preparation and Nanopore sequencing were performed by Rocío Chamorro González and data analysis was performed by Kerstin Haase and Konstantin Helmsauer at the *Experimental and Clinical Research Center* (ECRC), Berlin.

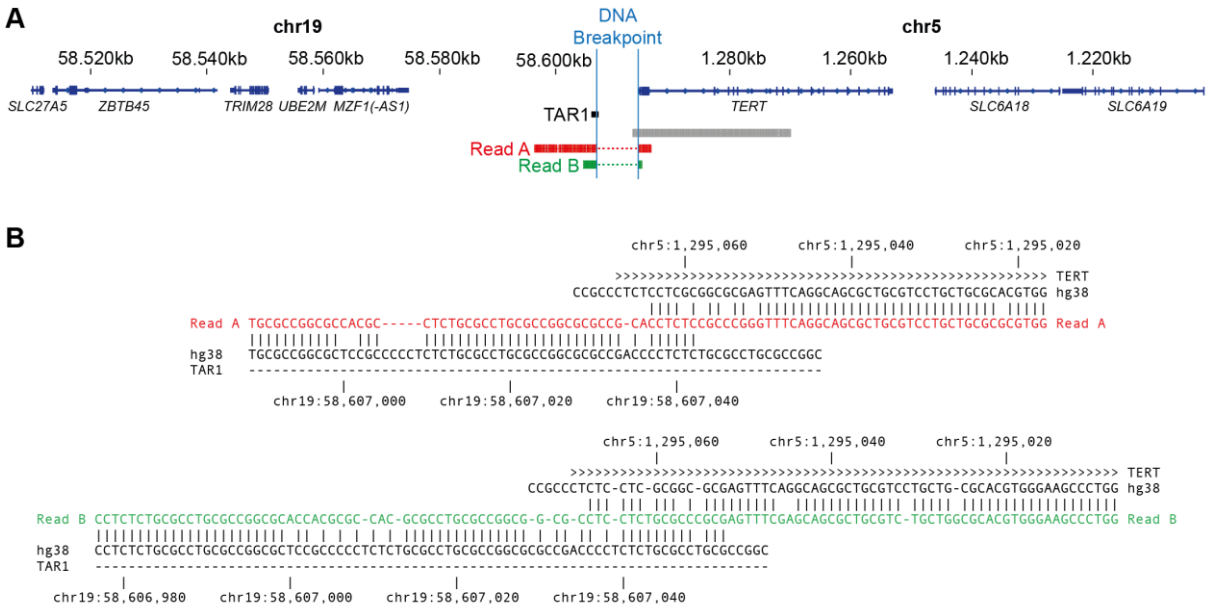

Figure 48: Low-coverage long-read sequencing localizes a candidate TERT-chr19 rearrangement.
A, Two of three long reads overlapping the *TERT* promotor indicate a rearrangement of the *TERT* promotor and a region in chr19q13.43. Read A (red) aligns to the *TERT* locus with an alignment block of length 1992 bp and mapping quality 60 and to chr19q13.43 with an alignment block of length 9625 bp and mapping quality 60. Read B (green) aligns to the *TERT* locus with an alignment block of length 488 bp and mapping quality 60 and to chr19q13.43 with an alignment block of length 2208 bp and mapping quality 0. **B,** Alignments of reads A and B to the *TERT* locus and chr19q13.43 both localize a breakpoint within the first 2-15 bases of the *TERT* 5'-untranslated region and the other breakpoint within a TAR1 repeat in chr19q13.43 with limited sequence homology near the breakpoints. Whole-genome sequencing reads aligned to hg38 genome and visualized with the Integrative Genomics Viewer (IGV). TAR1: telomere associated repeat 1; hg38: human genome 38. From K. Haase/K. Helmsauer.

Using low-coverage long-read Nanopore sequencing, the DNA breakpoint in GI-ME-N cells was located within the 5'-untranslated region (UTR) of *TERT*, fusing *TERT* to a subtelomeric locus on chromosome 19, truncating the native gene promotor from its gene (Figure 48 A). The analysis of the DNA breakpoint was sustained by re-analysis of published targeted DNA sequencing data of GI-ME-N cells (Peifer, 2015). The breakpoint for the hg38 annotation was identified as follows:

chr 19 …58607050, 58607051, 58607052 -breakpoint- 1295066, 1295065, 1295064, … chr 5

Published circular chromosome conformation capture sequencing (4C-seq) and FISH data suggest chromosome 19 as the *TERT* rearrangement partner (Gartlgruber, 2018). Low-coverage sequencing revealed two long reads, spanning the breakpoint in the repetitive area (Figure 48 B). Sequencing reveals evidence for a chr5-chr19 junction, the likely rearrangement partner was chr19:58607052 (+) which joins the *TERT* promotor chr5:1295066 (-).

6.2 Modulation of *TERT* levels in models of high-risk neuroblastoma

6.2.1 *TERT* expression is not decreased by BET inhibitor treatment

TERT is a downstream target of *MYCN* and *TERT* levels are high in *MYCN*-amplified neuroblastoma, whereas *MYCN* is expressed at comparatively low levels in *TERT*-rearranged GI-ME-N and CLB-GA cell lines (Peifer, 2015; Huang, 2020; Zhao, 2014). Bromodomain and extra-terminal motif (BET) inhibitors indirectly reduce expression of *MYCN* and *MYCN* target genes such as *TERT*, and are promising preclinical candidates for treating *MYCN*-amplified neuroblastoma (Henssen, 2016). To investigate if BET inhibitors also reduce *TERT* expression in *TERT*-rearranged neuroblastoma cells, GI-ME-N and CLB-GA cells were treated with BET inhibitors JQ1, OTX015 or I-BET762 for 48 h. Additionally, a concentration series of panobinostat was included for treatment.

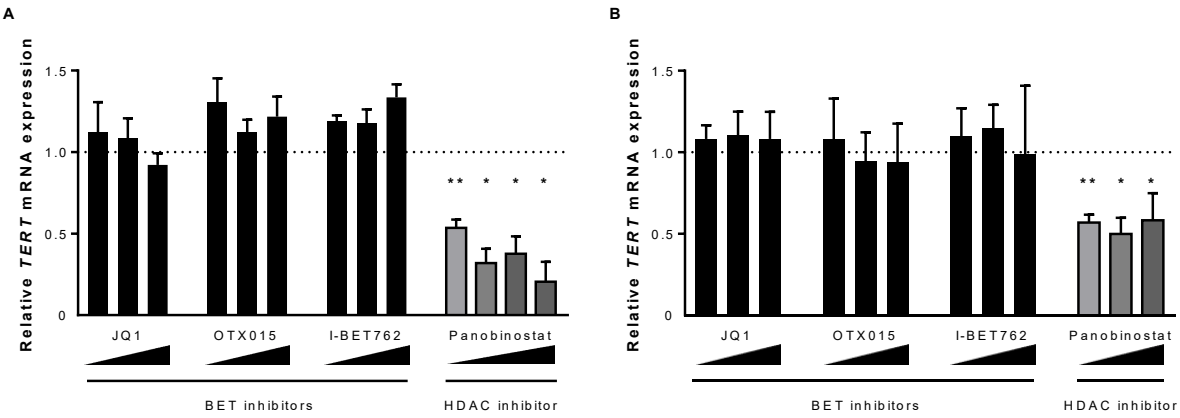

Figure 49: TERT mRNA expression is reduced by panobinostat treatment but not by BET inhibitor treatment. **A**, GI-ME-N and (**B**) CLB-GA cells were treated for 48 h with JQ1 (0.25, 0.5, 1 µM), OTX015 (0.1, 0.5, 1 µM), I-BET762 (0.25, 0.5, 1 µM) or panobinostat (5, 10, 15, 30 nM). *TERT* expression was analyzed by qRT-PCR (mean fold change over solvent ± SD; n≥3). Not significance if not indicated differently. Dotted lines indicate control value. *P≤0.05, **P≤0.01.

Due to the strong antitumoral effect of panobinostat, CLB-GA cells could not be treated with 30 nM panobinostat for 48 h. Indirect targeting of *MYCN* using BET inhibitors JQ1, OTX015 and I-BET762 had no influence on *TERT* mRNA expression in GI-ME-N (Figure 49 A) and CLB-GA cells (Figure 49 B). Panobinostat reduced *TERT* mRNA expression in a concentration-dependent manner in GI-ME-N cells (Figure 49 A), whereas *TERT* levels in CLB-GA cells showed a 2-fold decrease (Figure 49 B). Concentration of 30 nM panobinostat resulted in reduced *TERT* expression to 21% in GI-ME-N cells and of 15 nM panobinostat to 58% in CLB-GA cells.

6.2.2 *TERT* expression is increased and telomerase activity is induced after enforced *TERT* expression

To estimate the efficacy of the *TERT* plasmid after transfection, *TERT* expression was analyzed by qRT-PCR. GI-ME-N and CLB-GA cells were transfected with the *TERT* plasmid or empty vector and cells were harvested after 24-120 h.

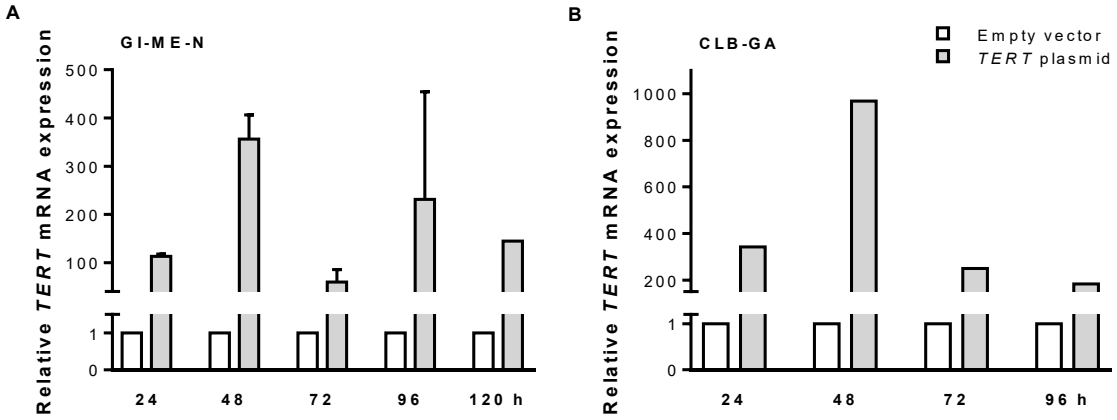

Figure 50: TERT mRNA expression is increased after transfection with TERT plasmid.
GI-ME-N and CLB-GA cells were transfected with either empty vector or *TERT* plasmid and harvested 24-120 h after transfection. *TERT* mRNA expression in (**A**) GI-ME-N and (**B**) CLB-GA cells. *TERT* expression was analyzed by qRT-PCR (mean fold change over solvent ± SD; n≥1).

The *TERT* plasmid increases *TERT* mRNA expression to a maximum of 356-fold 48 h after transfection in GI-ME-N cells (Figure 50 A) and to 969-fold after 48 h in CLB-GA cells (Figure 50 B).

Subsequently, telomerase activity was quantified by the telomerase activity assay. GI-ME-N and CLB-GA cells were transfected with the *TERT* plasmid or empty vector and cells were harvested after 24-120 h.

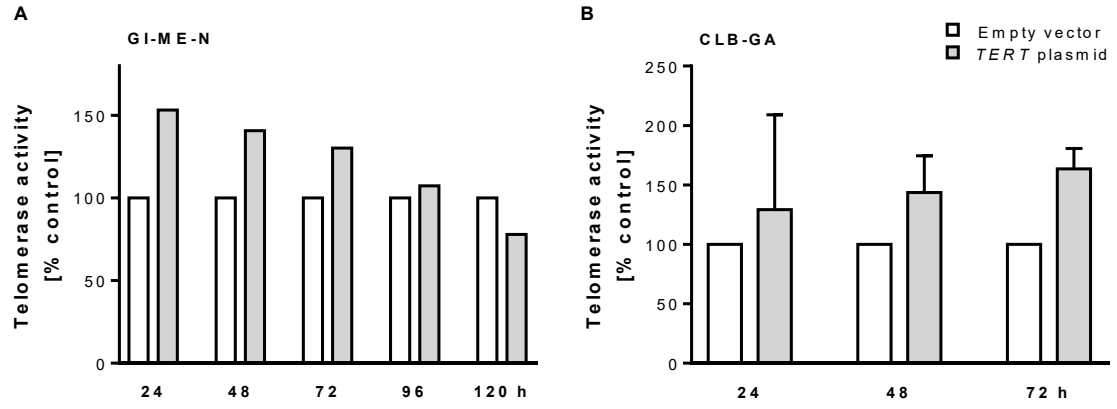

Figure 51: Telomerase activity is induced after transfection with TERT plasmid.
GI-ME-N and CLB-GA cells were transfected with either empty vector or *TERT* plasmid and harvested 24-120 h after transfection. Telomerase activity in (**A**) GI-ME-N and (**B**) CLB-GA cells. Telomerase activity was measured by ELISA (mean % over solvent ± SD; n≥1).

Telomerase activity increased to a maximum of 153% after 24 h in transfected GI-ME-N cells (Figure 51 A) and to 163% after 72 h in CLB-GA cells (Figure 51 B).

6.2.3 Panobinostat treatment reduces TERT protein levels

Treatment with panobinostat results in decreased *TERT* mRNA levels and reduced telomerase activity in *TERT*-rearranged cell lines. To investigate the effect of panobinostat on TERT at protein level, western blot analysis was performed. GI-ME-N cells were treated for 72 h with solvent or panobinostat or cells were transfected with a *TERT* overexpressing plasmid or empty vector and treated with solvent (DMSO) or panobinostat for 72 h.

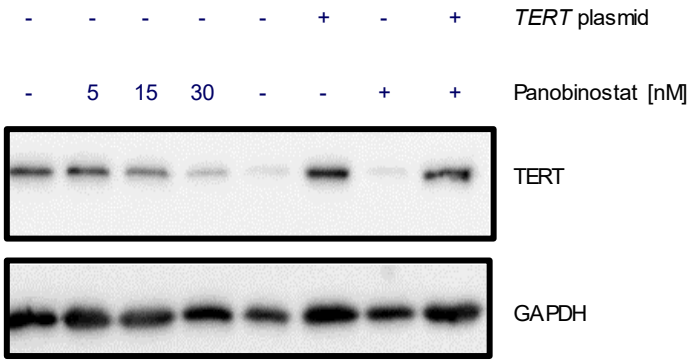

Figure 52: Panobinostat treatment reduces TERT protein levels.
Representative western blot analysis of GI-ME-N cells 72 h after panobinostat (5, 15, 30 nM) treatment (lanes 1-4). GI-ME-N cells were transfected with either empty vector or *TERT* plasmid and treated with panobinostat (5 nM) for 72 h (lanes 5-8). GAPDH served as a loading control.

Panobinostat treatment resulted in reduction of TERT in a concentration dependent manner (Figure 52). Enforced expression of *TERT* resulted in high TERT protein levels, that were not decreased by panobinostat treatment. This data suggests that not only *TERT* mRNA levels but also TERT protein levels decrease after panobinostat treatment, and that enforced expression of *TERT* remains high TERT protein levels after panobinostat treatment.

6.3 Panobinostat harbors strong antitumoral effects towards neuroblastoma cells

6.3.1 Panobinostat treatment reduces metabolic activity of neuroblastoma cells

To determine the potency of panobinostat towards neuroblastoma cell lines, the half-maximal inhibitory concentration (IC_{50}) was measured after 72 h treatment. Cells were treated with 0.001-1000 nM panobinostat. The *MYCN*-amplified neuroblastoma cell lines BE(2)-C and IMR-5/75 as well as the *TERT*-rearranged cell lines GI-ME-N and CLB-GA were included in the panel, besides the neither *TERT*-rearranged nor *MYCN*-amplified neuroblastoma cell lines LAN-6 and SK-N-FI. The water-soluble tetrazolium (WST-1) assay was performed to quantify metabolic activity after panobinostat treatment.

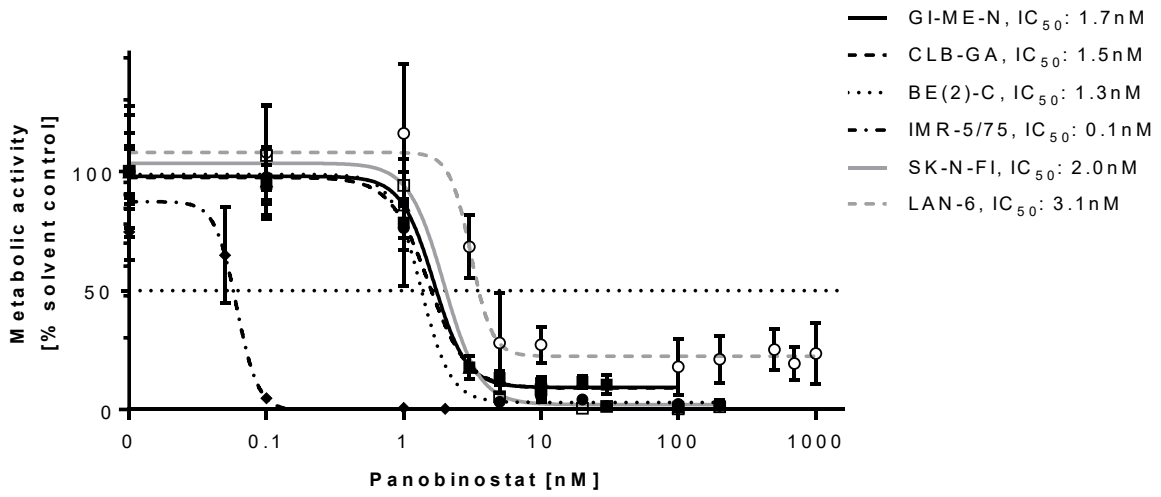

Figure 53: Metabolic activity is reduced in a panel of neuroblastoma cells treated with panobinostat.
Metabolic activity after 72 h panobinostat treatment was analyzed in a panel of neuroblastoma cell lines detected by colorimetric WST-1 assay (mean % over solvent control ± SD; n=10). IC_{50} values were determined via non-linear regression fit. Dotted line indicates half-maximal metabolic activity.

Metabolic activity was reduced at low concentrations with calculated IC_{50} values ranging from 0.1 nM - 3.1 nM (Figure 53). The *MYCN*-amplified IMR-5/75 cell line was shown to harbor high *TERT* expression levels (Peifer, 2015), but had the lowest calculated IC_{50} of 0.1 nM in the cell line panel. There was no connection of the *TERT* status and metabolic activity under panobinostat treatment, underlining the antitumoral effect of panobinostat on various neuroblastoma cells regardless of the genomic background.

6.3.2 Proliferation of neuroblastoma cells is impeded by panobinostat treatment

The expression of *TERT* mRNA decreases after 2-4 h of treatment (section 4.1.1). To assess the kinetic of panobinostat towards reduced cell proliferation, continuous impedance measurements of cell lines treated with panobinostat were performed. Calculated cell proliferation of *TERT*-rearranged GI-ME-N cells, *MYCN* amplified IMR-5/75 cells and LAN-6 cells lacking those events were investigated after several days of panobinostat treatment.

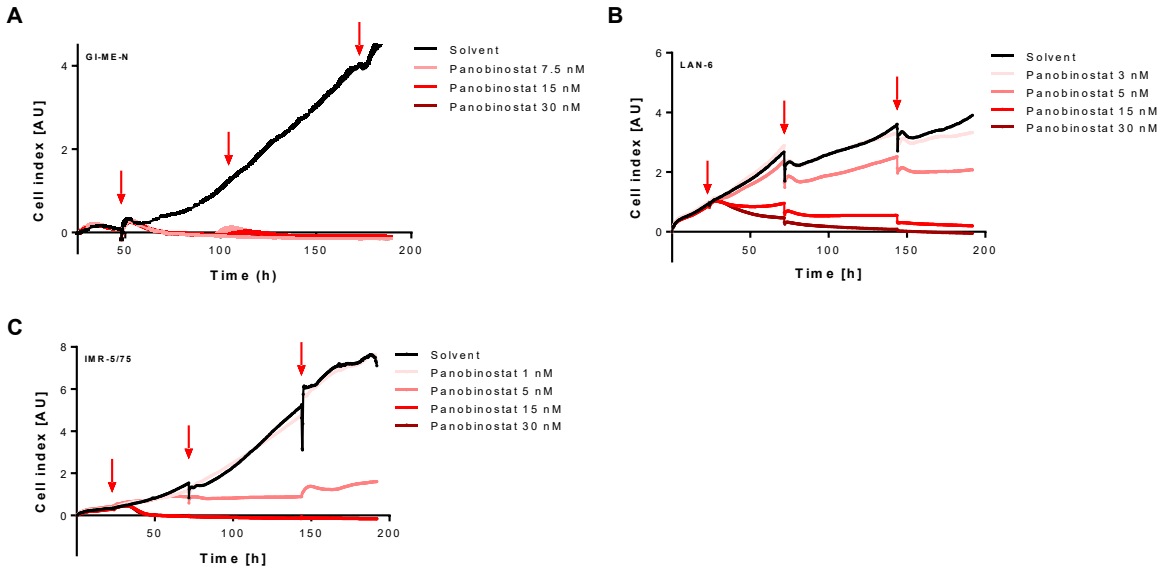

Figure 54: Panobinostat impairs cell proliferation of neuroblastoma cell lines.
Proliferation of cell lines (**A**) GI-ME-N, (**B**) LAN-6 and (**C**) IMR-5/75 treated with panobinostat for several days measured using the xCelligence™ cell impedance analyzer (mean over background, n≥2). Arrows indicate application of treatment. AU: arbitrary units.

Small dips in the proliferation curves were due to changed impedance after fresh treatment was applied, and curves equilibrated quickly to previous levels. Proliferation curves of all three cell lines showed a clear reduction of cell proliferation after panobinostat treatment, using the calculated dimension-less cell index reflecting cell growth behavior (Figure 54 A, B and C). In the GI-ME-N cell line, solvent (DMSO) treated cells continued proliferation whereas panobinostat of 7.5-30 nM completely abolished cell proliferation (Figure 54 A). The cell indices further decreased upon treatment application, indicating the detachment from cell culture plate and possible induction of cell death. In LAN-6 cells, panobinostat treatment of 15-30 nM resulted in decreased cell proliferation and detachment of treated cells from well plate (Figure 54 B). Solvent and 3 nM panobinostat treatment resulted in similar growth

behavior of LAN-6 cells, whereas a concentration of 5 nM completely arrested cell proliferation. Solvent treated IMR-5/75 cells and a concentration of 1 nM panobinostat could not affect cell proliferation rate, whereas a concentration of 5 nM panobinostat arrested cell growth of treated cells (Figure 54 C). Panobinostat applied at 15-30 nM completely arrested cell proliferation and induced detachment of treated cells from well plate (Figure 54 A, B and C). In GI-ME-N, LAN-6 and BE(2)-C cell lines, a proliferation arrest after few hours of treatment at concentrations of 15 nM panobinostat or higher was observed, accompanied with detachment of treated cells from well plate.

6.3.3 Panobinostat treatment attenuates colony formation capacity

The ability of transformed cells to form colonies and to grow independently is considered a hallmark of carcinogenesis. To investigate whether panobinostat treatment influences colony formation in *TERT*-rearranged cell lines, GI-ME-N and CLB-GA cells were treated with 0.1-10 nM panobinostat and colony formation was analyzed after nine days of treatment.

Treatment with panobinostat reduced the capacity of GI-ME-N and CLB-GA cells to form colonies in a concentration-dependent manner with 5 nM panobinostat resulting in a decrease of colony formation to 13% in GI-ME-N and 1% in CLB-GA relative to solvent treated cells (Figure 55). After treatment with 15 nM panobinostat, almost no colonies were visible (data not shown). These results demonstrate that *TERT*-rearranged neuroblastoma cells treated with panobinostat lose their ability to form colonies from single cell level.

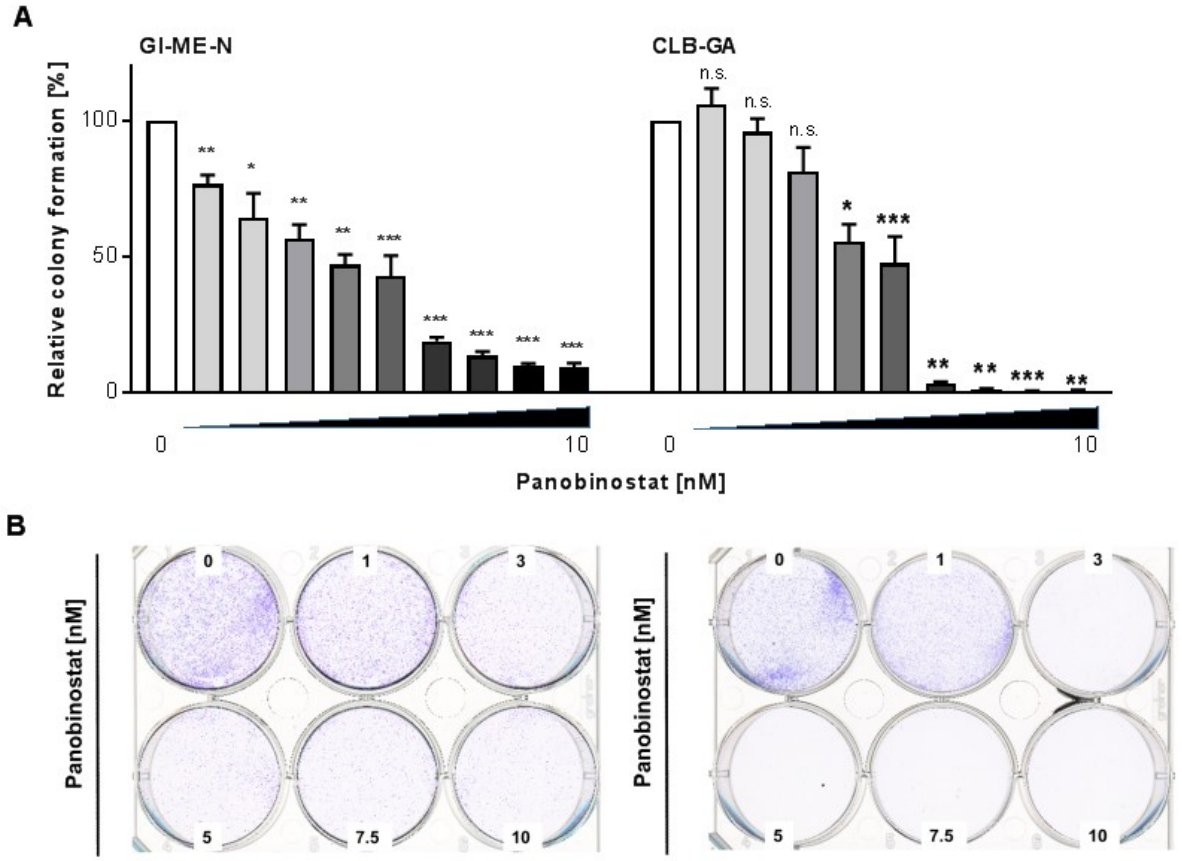

Figure 55: Panobinostat treatment reduces colony formation capacity.
Colony formation assay of GI-ME-N and CLB-GA cells treated with panobinostat. After nine days, colonies were fixed, stained and evaluated using ImageJ. **A**, Quantification of colonies (mean ± SD; n≥3). **B**, Representative pictures of stained colonies. *P≤0.05, **P≤0.01, ***P≤0.001, n.s.: not significant.

6.3.4 Panobinostat decreases cell viability in 2D and 3D models of *TERT*-rearranged neuroblastoma

To assess cell viability after and efficacy of panobinostat treatment, 2D and 3D cell culture models using clinically relevant concentrations of panobinostat were investigated. Cell culture experiments were performed by Alessandra Silvestri and Guido Gambara at CPO, Berlin to evaluate the antitumoral effects of panobinostat in GI-ME-N and CLB-GA 2D and 3D cell culture models. Adherent cells or small organoids were cultured and subsequently treated with six different concentrations of panobinostat, including the concentration of 5 ng/ml that can be achieved in patient plasma levels (Rathkopf, 2010b). A mass concentration of 5 ng/ml is equivalent to a molar concentration of about 15 nM as applied in cell culture experiments.

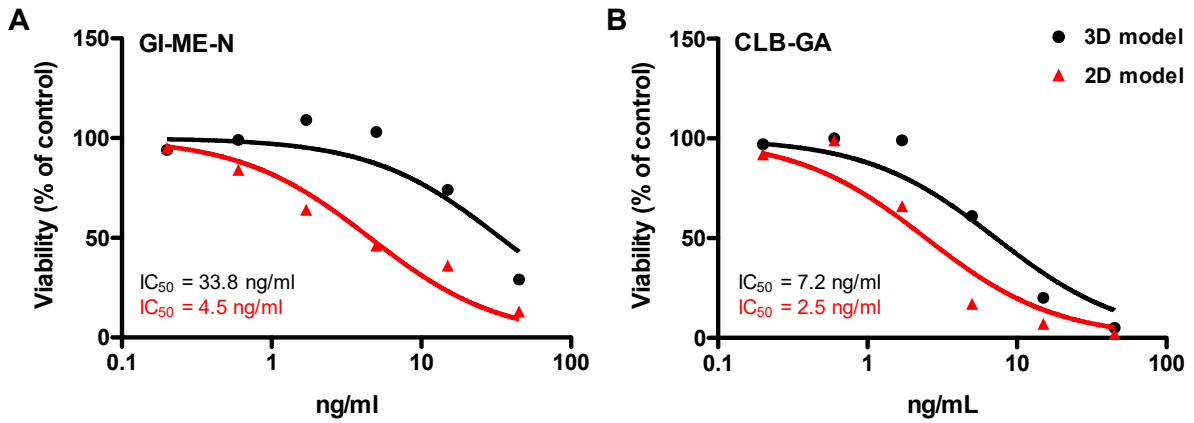

Figure 56: Panobinostat treatment reduces cell viability in 2D and 3D models of TERT-rearranged high-risk neuroblastoma.
GI-ME-N or CLB-GA cells were treated for 72 h with panobinostat. Viable cell numbers by luminescence-based assay in (**A**) GI-ME-N and (**B**) CLB-GA cell line models (mean % over solvent control; n=4). Experiments were performed by CPO. Red triangle: 2D cell culture model, black circle: 3D cell culture model.

In 3D cell culture models, IC_{50} at the patient plasma concentration of 5 ng/ml was determined to be 33.8 ng/ml and is higher than in the 2D model with an calculated IC_{50} of 4.5 ng/ml in GI-ME-N cells (Figure 56 A). Accordingly, IC_{50} in the 3D model of CLB-GA was calculated of 7.2 ng/ml, and in the 2D culture IC_{50} was 2.5 ng/ml (Figure 56 B). Small organoids in 3D models showed more resistance towards panobinostat treatment than cells growing in monolayers. Panobinostat reduced viability of GI-ME-N and CLB-GA cells in models of 2D and 3D neuroblastoma at clinically relevant low nanomolar concentrations.

6.3.5 Panobinostat treatment induces changes in cell cycle profile, increases sub-G1 fraction and triggers protease-mediated apoptosis

Histone deacetylase inhibitors were demonstrated to induce cell cycles arrest in high-risk neuroblastoma (Kolbinger, 2018; Lodrini, 2013). To estimate the effect of panobinostat treatment on cell cycle, flow cytometry was performed on *TERT*-rearranged GI-ME-N and CLB-GA cell lines. GI-ME-N cells were treated with 10.6 nM and CLB-GA cells with 5.8 nM panobinostat for 72 h. The chosen concentrations resulted from calculated IC_{50} of panobinostat treatment from previous assays (data not shown).

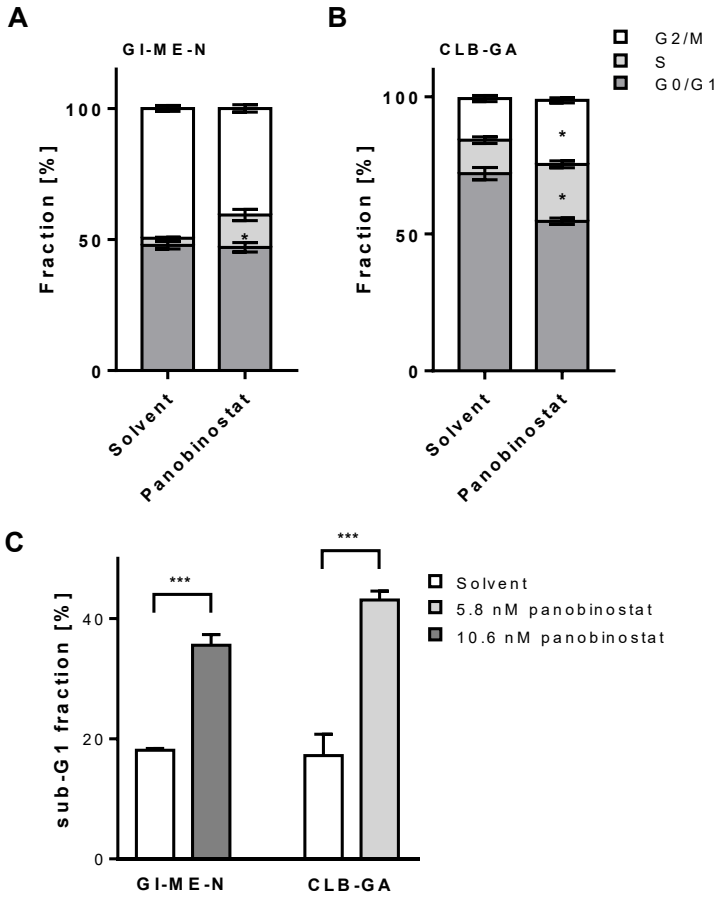

Figure 57: Panobinostat treatment induces changes in cell cycle profile and increase sub-G1 fraction in TERT-rearranged cell lines.
Cell cycle profiles of (**A**) GI-ME-N and (**B**) CLB-GA cells after panobinostat treatment analyzed by propidium iodide staining (mean % ± SD; n=3). **C**, Quantification of sub-G1 fraction after panobinostat treatment analyzed by propidium iodide staining (mean % ± SD; n=3). *P≤0.05, ***P≤0.001.

Propidium iodide (PI) staining of fixed cells was analyzed by flow cytometry and showed an increase in S-phase in GI-ME-N cells (Figure 57 A) and in S- and G2/M-phase in CLB-GA (Figure 57 B). An increase of cells in sub-G1 fraction was detected in both cell lines after panobinostat treatment (Figure 57 C).

To investigate whether protease-mediated apoptosis is induced after panobinostat treatment, PARP-1 western blot analysis was performed in CLB-GA cells. Specific fragmentation of PARP-1 is considered as indication for active caspase signaling and active proteases unique in cell death programs. The caspase inhibitor Z-VAD was used to block apoptosis induction and to serve as functional control.

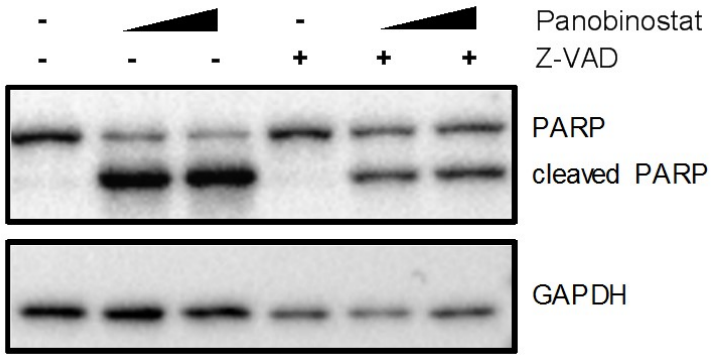

Figure 58: Panobinostat induces protease-mediated apoptosis in CLB-GA cells.
Representative western blot analysis of CLB-GA cells 48 h after solvent, panobinostat (7.5, 15 nM) or combined Z-VAD (20 µM) treatment. GAPDH served as a loading control.

CLB-GA cells treated with panobinostat showed an increase in cleaved PARP-1 protein accompanied by a decrease in PARP-1 protein level (Figure 58). Combination treatment with panobinostat and Z-VAD resulted in less reduced cleavage products of PARP-1 and less decrease of PARP-1 levels. This experiment suggests that panobinostat induces apoptosis in CLB-GA cells via active protease signaling.

6.4 Transcriptome-wide analysis of panobinostat effects in *TERT*-rearranged neuroblastoma models

To uncover the regulation after panobinostat treatment, RNA sequencing of treated GI-ME-N and CLB-GA xenograft tumors was performed. Three tumors of each condition were chosen for analyses. Library preparation and sequencing were performed at the High Throughput Sequencing Core Facility at the DKFZ, Heidelberg and data was analyzed by Benedikt Obermayer at the *Berlin Institute of Health* (BIH). Statistical analysis of the GI-ME-N model with an absolute $\log_2$ fold-change larger than 0.5 or smaller than -0.5 and an adjusted p-value smaller than 0.05 revealed that a total of 613 genes were upregulated and 480 were down-regulated after panobinostat treatment, among them *TERT* (data not shown). Analysis of the CLB-GA xenograft tumors with an absolute $\log_2$ fold-change larger than 1 or smaller than -1 and an adjusted p-value smaller than 0.05 revealed that 984 genes were upregulated and 151 genes were downregulated after panobinostat treatment, among them *TERT* (data not shown). Principal component analysis (PCA) of both models was performed to reveal the

internal structure of the data in a way that best explains the variance in the RNA expression data.

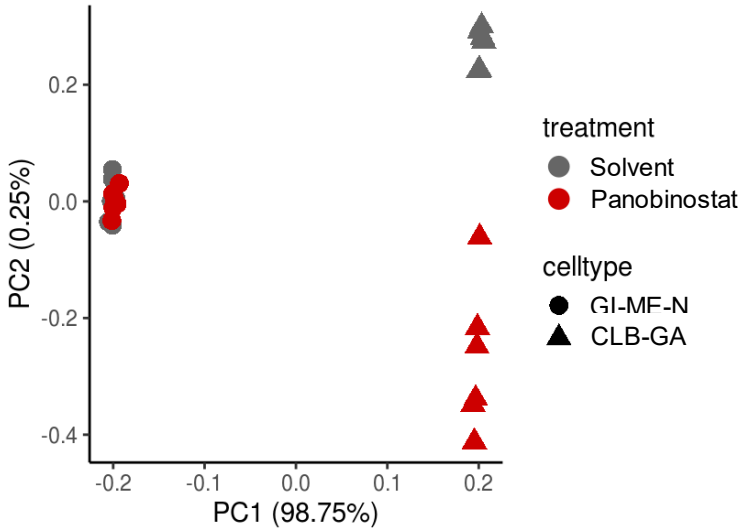

Figure 59: Panobinostat treatment reveals diversity in response to treatment in GI-ME-N and CLB-GA xenograft tumors.
Principal component analysis of RNA expression data of GI-ME-N and CLB-GA xenograft tumors. PC1 represents the variable cell line, PC2 the treatment condition.

Principal component analysis showed that the main split is between the two cell lines (99% of the variance), and then by the treatment, with stronger effects in CLB-GA than in GI-ME-N xenograft tumors (Figure 59).

Next, the differential expression of the two $\log_2$ fold-changes of GI-ME-N and CLB-GA were plotted against each other and correlation analysis was performed comparing the top differential expressed genes between the two cell lines. Gene set enrichment analysis using GAGE was plotted to analyze the distribution of $\log_2$ fold-changes in the gene sets that are significant in both contrasts.

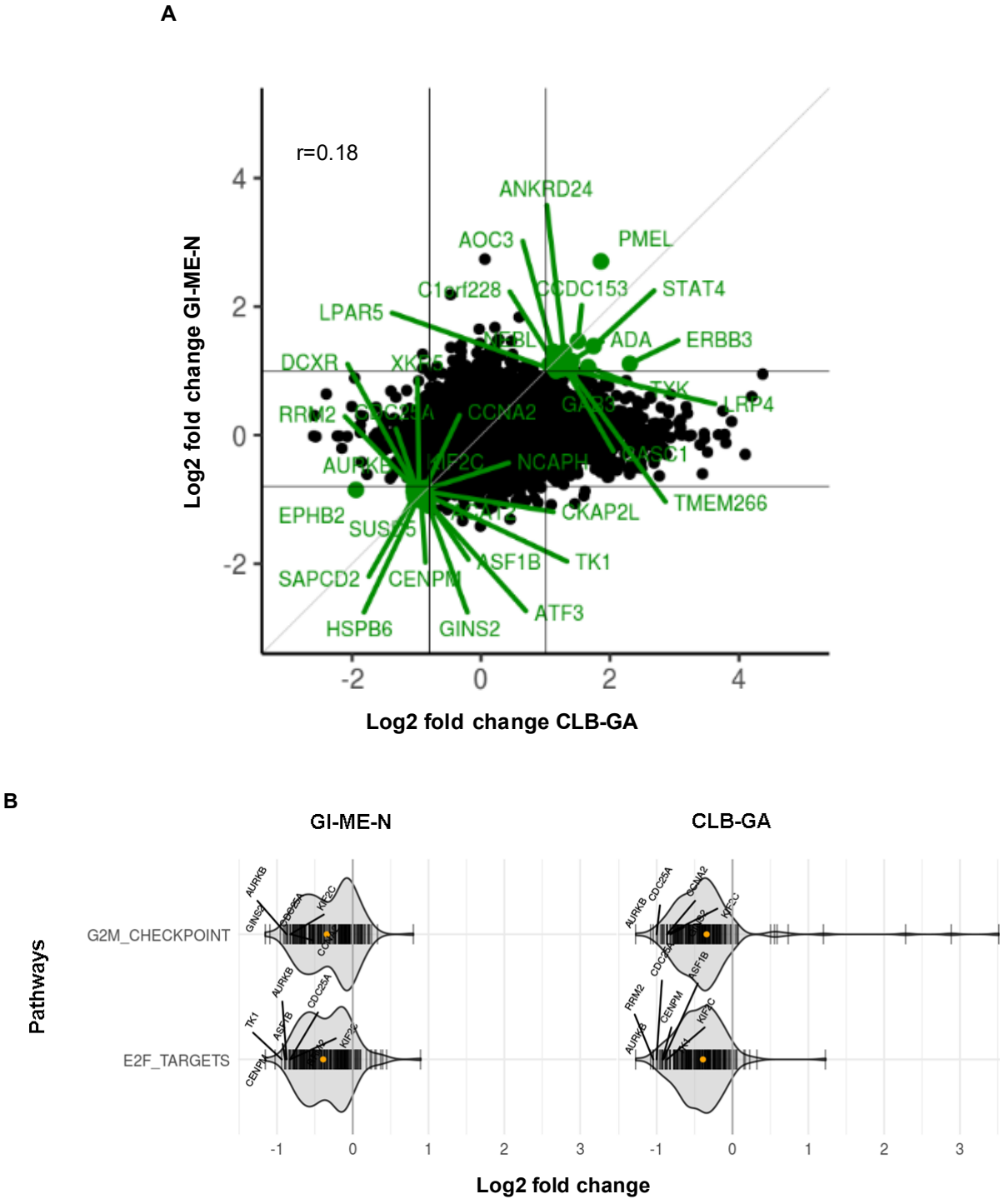

Figure 60: Panobinostat treatment reduces expression of hallmarks G2M checkpoint and E2F target genes in neuroblastoma xenograft tumors.

A, XY-plot of differential expressed genes both in GI-ME-N and CLB-GA xenograft tumors treated with panobinostat 15 mg/kg/d (n=3) or solvent (DMSO) (n=3). RNA sequencing expression data was normalized to corresponding solvent control and compared between conditions. Green circles highlight individual genes that are differentially expressed in both models. Vertical and horizontal lines indicate log_2 fold-change cutoff values.

B, Distribution plot of log_2 fold-changes of gene sets G2M checkpoint and E2F target gene expression in GI-ME-N and CLB-GA xenograft tumors. Orange circles indicate mean expression of all genes in the gene set. Adjusted P-value ≤0.05, r=0.18.

A combined analysis of GI-ME-N and CLB-GA xenograft tumors with an absolute log_2 fold-change larger than 1 or smaller than -1 and an adjusted p-value smaller than 0.05 identified 800 genes to be downregulated and 319 genes to be upregulated after panobinostat treatment in both models (data not shown). G2M checkpoint and E2F target genes were identified to be significantly less expressed in both models under panobinostat treatment (Figure 60 A). Enrichments of custom gene sets was tested using GAGE, applying gene sets listed in MSigDB. GAGE analysis of G2M checkpoint and E2F target genes revealed a significant downregulation of genes in those pathways in GI-ME-N and CLB-GA xenograft tumors (Figure 60 B).

Nine genes of these two subsets hallmarks G2M and E2F targets were selected and mRNA expression was analyzed by qRT-PCR.

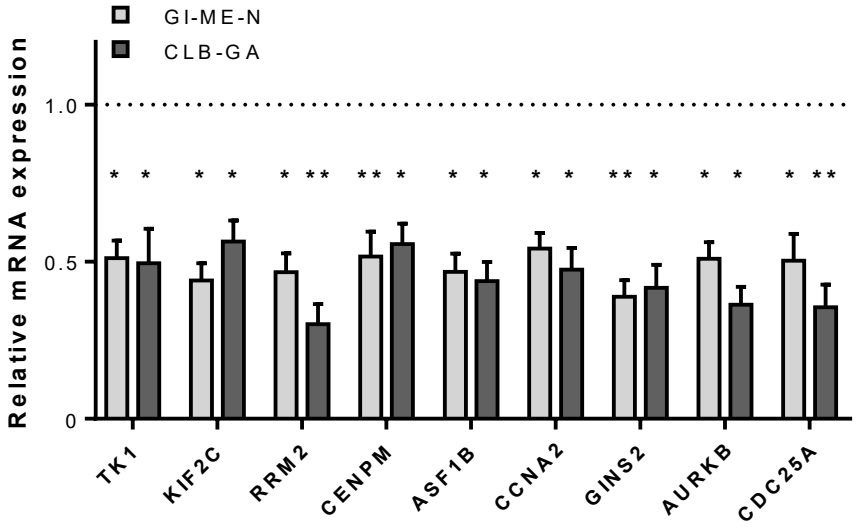

Figure 61: Panobinostat treatment reduces RNA expression of a panel of hallmarks G2M checkpoint and E2F target genes in neuroblastoma xenograft tumors.
Expression of mRNA of nine selected hallmarks G2M checkpoint and E2F target genes in GI-ME-N and CLB-GA xenograft tumors treated with panobinostat 15 mg/kg/d or solvent (DMSO). Expression was analyzed by qRT-PCR (mean fold change over solvent ± SEM; n=3). Dotted line indicates control value. *P≤0.05, **P≤0.01.

Results from RNA sequencing were validated by qRT-PCR, showing that the expression of G2M checkpoint and E2F target gene mRNA decreased to 40-50% under panobinostat treatment in both xenograft models (Figure 61).

To assess whether this observation is also true in GI-ME-N and CLB-GA cell lines, RNA expression analyses of cell lines treated with panobinostat were quantified by qRT-PCR.

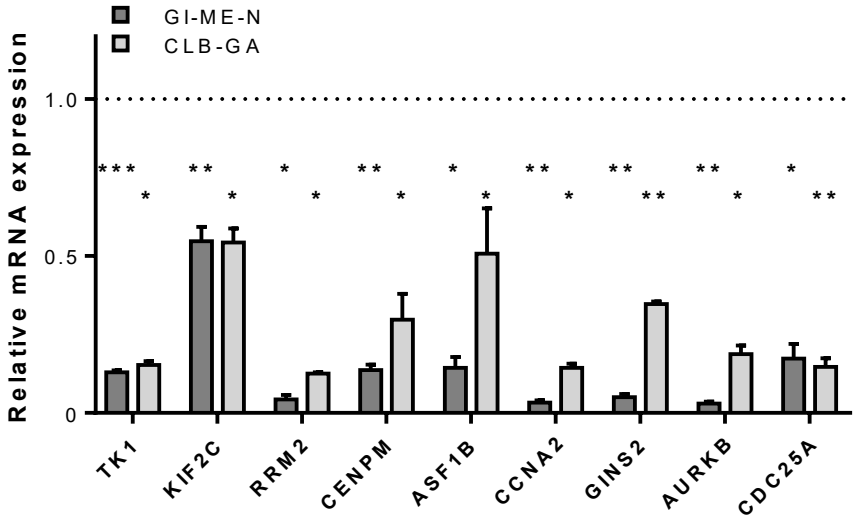

Figure 62: Panobinostat treatment reduces RNA expression of a panel of hallmarks G2M checkpoint and E2F target genes in neuroblastoma cell lines.
Expression of mRNA of nine selected hallmarks G2M checkpoint and E2F target genes in GI-ME-N and CLB-GA cells treated with panobinostat. GI-ME-N cells were treated with 30 nM panobinostat, CLB-GA cells with 15 nM panobinostat. Expression was analyzed by qRT-PCR (mean fold change over solvent ± SD; n≥2). Dotted line indicates control value. *P≤0.05, **P≤0.01, ***P≤0.001.

As in the xenograft tumors, expression of the nine selected genes of hallmarks G2M checkpoint and E2F target genes were reduced by panobinostat treatment by at least 2-fold in both cell models (Figure 62). The reduced expression was overall stronger in GI-ME-N than in CLB-GA cells. These results underline previous cell cycle analyses in GI-ME-N and CLB-GA cells (section 6.3), suggesting that panobinostat treatment induces changes in cell cycle profile in models of high-risk *TERT*-rearranged neuroblastoma by downregulating G2M checkpoint and E2F target genes.

7 References

Ackermann, S., Cartolano, M., Hero, B., Welte, A., Kahlert, Y., Roderwieser, A., Bartenhagen, C., Walter, E., Gecht, J., Kerschke, L., Volland, R., Menon, R., Heuckmann, J. M., Gartlgruber, M., Hartlieb, S., Henrich, K.-O., Okonechnikov, K., Altmüller, J., Nürnberg, P., Lefever, S., de Wilde, B., Sand, F., Ikram, F., Rosswog, C., Fischer, J., Theissen, J., Hertwig, F., Singhi, A. D., Simon, T., Vogel, W., Perner, S., Krug, B., Schmidt, M., Rahmann, S., Achter, V., Lang, U., Vokuhl, C., Ortmann, M., Büttner, R., Eggert, A., Speleman, F., O'Sullivan, R. J., Thomas, R. K., Berthold, F., Vandesompele, J., Schramm, A., Westermann, F., Schulte, J. H., Peifer, M. & Fischer, M. 2018. A mechanistic classification of clinical phenotypes in neuroblastoma. *Science* **362**, 1165-1170.

Adhikary, S. & Eilers, M. 2005. Transcriptional regulation and transformation by Myc proteins. *Nat Rev Mol Cell Biol* **6**, 635-645.

Afifi, S., Michael, A., Azimi, M., Rodriguez, M., Lendvai, N. & Landgren, O. 2015. Role of Histone Deacetylase Inhibitors in Relapsed Refractory Multiple Myeloma: A Focus on Vorinostat and Panobinostat. *Pharmacotherapy* **35**, 1173-1188.

Agarwal, M. B. 2016. Is cancer chemotherapy dying? *Asian journal of transfusion science* **10**, S1-S7.

Agarwal, V., Bell, G. W., Nam, J.-W. & Bartel, D. P. 2015. Predicting effective microRNA target sites in mammalian mRNAs. *eLife* **4**, e05005.

Ahmed, S., Passos, J. F., Birket, M. J., Beckmann, T., Brings, S., Peters, H., Birch-Machin, M. A., von Zglinicki, T. & Saretzki, G. 2008. Telomerase does not counteract telomere shortening but protects mitochondrial function under oxidative stress. *J Cell Sci* **121**, 1046-1053.

Ait-Aissa, K., Ebben, J. D., Kadlec, A. O. & Beyer, A. M. 2016. Friend or foe? Telomerase as a pharmacological target in cancer and cardiovascular disease. *Pharmacological research* **111**, 422-433.

Akincilar, S. C., Unal, B. & Tergaonkar, V. 2016. Reactivation of telomerase in cancer. *Cellular and Molecular Life Sciences* **73**, 1659-1670.

Al-Hamamah, M. A., Alotaibi, M. R., Ahmad, S. F., Ansari, M. A., Attia, M. S. M., Nadeem, A., Bakheet, S. A., As Sobeai, H. M. & Attia, S. M. 2019. Genetic and epigenetic alterations induced by the small-molecule panobinostat: A mechanistic study at the chromosome and gene levels. *DNA Repair (Amst)* **78**, 70-80.

Ali Syeda, Z., Langden, S. S. S., Munkhzul, C., Lee, M. & Song, S. J. 2020. Regulatory Mechanism of MicroRNA Expression in Cancer. *Int J Mol Sci* **21**.

Althoff, K., Beckers, A., Bell, E., Nortmeyer, M., Thor, T., Sprüssel, A., Lindner, S., De Preter, K., Florin, A., Heukamp, L. C., Klein-Hitpass, L., Astrahantseff, K., Kumps, C., Speleman, F., Eggert, A., Westermann, F., Schramm, A. & Schulte, J. H. 2015. A Cre-conditional MYCN-driven neuroblastoma mouse model as an improved tool for preclinical studies. *Oncogene* **34**, 3357-3368.

Anne, M., Sammartino, D., Barginear, M. F. & Budman, D. 2013. Profile of panobinostat and its potential for treatment in solid tumors: an update. *Onco Targets Ther* **6**, 1613-1624.

Artandi, S. E., Alson, S., Tietze, M. K., Sharpless, N. E., Ye, S., Greenberg, R. A., Castrillon, D. H., Horner, J. W., Weiler, S. R., Carrasco, R. D. & DePinho, R. A. 2002. Constitutive telomerase expression promotes mammary carcinomas in aging mice. *Proc Natl Acad Sci U S A* **99**, 8191-8196.

Artandi, S. E. & DePinho, R. A. 2010. Telomeres and telomerase in cancer. *Carcinogenesis* **31**, 9-18.

Arumugam, T., Ramachandran, V., Fournier, K. F., Wang, H., Marquis, L., Abbruzzese, J. L., Gallick, G. E., Logsdon, C. D., McConkey, D. J. & Choi, W. 2009. Epithelial to Mesenchymal Transition Contributes to Drug Resistance in Pancreatic Cancer. *Cancer Research* **69**, 5820-5828.

Aryee, M. J., Jaffe, A. E., Corrada-Bravo, H., Ladd-Acosta, C., Feinberg, A. P., Hansen, K. D. & Irizarry, R. A. 2014. Minfi: a flexible and comprehensive Bioconductor package for the analysis of Infinium DNA methylation microarrays. *Bioinformatics* **30**, 1363-1369.

Asklund, T., KVARNBRINK, S., HOLMLUND, C., WIBOM, C., BERGENHEIM, T., HENRIKSSON, R. & HEDMAN, H. 2012. Synergistic Killing of Glioblastoma Stem-like Cells by Bortezomib and HDAC Inhibitors. *Anticancer Res* **32**, 2407-2413.

Atkinson, S. P., Hoare, S. F., Glasspool, R. M. & Keith, W. N. 2005. Lack of Telomerase Gene Expression in Alternative Lengthening of Telomere Cells Is Associated with Chromatin Remodeling of the hTR and hTERT Gene Promoters. *Cancer Research* **65**, 7585-7590.

Attiyeh, E. F., London, W. B., Mosse, Y. P., Wang, Q., Winter, C., Khazi, D., McGrady, P. W., Seeger, R. C., Look, A. T., Shimada, H., Brodeur, G. M., Cohn, S. L., Matthay, K. K. & Maris, J. M. 2005. Chromosome 1p and 11q deletions and outcome in neuroblastoma. *N Engl J Med* **353**, 2243-2253.

Autin, P., Blanquart, C. & Fradin, D. 2019. Epigenetic Drugs for Cancer and microRNAs: A Focus on Histone Deacetylase Inhibitors. *Cancers (Basel)* **11**.

Bagci, O., Tumer, S., Olgun, N. & Altungoz, O. 2012. Copy number status and mutation analyses of anaplastic lymphoma kinase (ALK) gene in 90 sporadic neuroblastoma tumors. *Cancer Letters* **317**, 72-77.

Bantscheff, M., Hopf, C., Savitski, M. M., Dittmann, A., Grandi, P., Michon, A. M., Schlegl, J., Abraham, Y., Becher, I., Bergamini, G., Boesche, M., Delling, M., Dumpelfeld, B., Eberhard, D., Huthmacher, C., Mathieson, T., Poeckel, D., Reader, V., Strunk, K., Sweetman, G., Kruse, U., Neubauer, G., Ramsden, N. G. & Drewes, G. 2011. Chemoproteomics profiling of HDAC inhibitors reveals selective targeting of HDAC complexes. *Nat Biotechnol* **29**, 255-265.

Baylin, S. B. & Ohm, J. E. 2006. Epigenetic gene silencing in cancer - a mechanism for early oncogenic pathway addiction? *Nat Rev Cancer* **6**, 107-116.

Beierle, E. A., Trujillo, A., Nagaram, A., Kurenova, E. V., Finch, R., Ma, X., Vella, J., Cance, W. G. & Golubovskaya, V. M. 2007. N-MYC regulates focal adhesion kinase expression in human neuroblastoma. *J Biol Chem* **282**, 12503-12516.

Beliveau, A. & Yaswen, P. 2007. Soothing the watchman: telomerase reduces the p53-dependent cellular stress response. *Cell Cycle* **6**, 1284-1287.

Berthold, F., Spix, C., Kaatsch, P. & Lampert, F. 2017. Incidence, Survival, and Treatment of Localized and Metastatic Neuroblastoma in Germany 1979-2015. *Paediatr Drugs* **19**, 577-593.

Bird, A. & Macleod, D. 2004. Reading the DNA methylation signal. *Cold Spring Harb Symp Quant Biol* **69**, 113-118.

Bodnar, A. G., Ouellette, M., Frolkis, M., Holt, S. E., Chiu, C. P., Morin, G. B., Harley, C. B., Shay, J. W., Lichtsteiner, S. & Wright, W. E. 1998. Extension of life-span by introduction of telomerase into normal human cells. *Science* **279**, 349-352.

Boehm, J. S., Hession, M. T., Bulmer, S. E. & Hahn, W. C. 2005. Transformation of human and murine fibroblasts without viral oncoproteins. *Mol Cell Biol* **25**, 6464-6474.

Boeva, V., Louis-Brennetot, C., Peltier, A., Durand, S., Pierre-Eugene, C., Raynal, V., Etchevers, H. C., Thomas, S., Lermine, A., Daudigeos-Dubus, E., Geoerger, B.,

Orth, M. F., Grunewald, T. G. P., Diaz, E., Ducos, B., Surdez, D., Carcaboso, A. M., Medvedeva, I., Deller, T., Combaret, V., Lapouble, E., Pierron, G., Grossetete-Lalami, S., Baulande, S., Schleiermacher, G., Barillot, E., Rohrer, H., Delattre, O. & Janoueix-Lerosey, I. 2017. Heterogeneity of neuroblastoma cell identity defined by transcriptional circuitries. *Nat Genet* **49**, 1408-1413.

Boeva, V., Popova, T., Bleakley, K., Chiche, P., Cappo, J., Schleiermacher, G., Janoueix-Lerosey, I., Delattre, O. & Barillot, E. 2012. Control-FREEC: a tool for assessing copy number and allelic content using next-generation sequencing data. *Bioinformatics* **28**, 423-425.

Bolden, J. E., Peart, M. J. & Johnstone, R. W. 2006. Anticancer activities of histone deacetylase inhibitors. *Nat Rev Drug Discov* **5**, 769-784.

Boros, J., Arnoult, N., Stroobant, V., Collet, J. F. & Decottignies, A. 2014. Polycomb repressive complex 2 and H3K27me3 cooperate with H3K9 methylation to maintain heterochromatin protein 1alpha at chromatin. *Mol Cell Biol* **34**, 3662-3674.

Boumber, Y., Younes, A. & Garcia-Manero, G. 2011. Mocetinostat (MGCD0103): a review of an isotype-specific histone deacetylase inhibitor. *Expert Opin Investig Drugs* **20**, 823-829.

Bown, N., Lastowska, M., Cotterill, S., O'Neill, S., Ellershaw, C., Roberts, P., Lewis, I., Pearson, A. D., Group, U. K. C. C. & the, U. K. C. s. C. S. G. 2001. 17q gain in neuroblastoma predicts adverse clinical outcome. U.K. Cancer Cytogenetics Group and the U.K. Children's Cancer Study Group. *Medical and pediatric oncology* **36**, 14-19.

Bresler, S. C., Weiser, D. A., Huwe, P. J., Park, J. H., Krytska, K., Ryles, H., Laudenslager, M., Rappaport, E. F., Wood, A. C., McGrady, P. W., Hogarty, M. D., London, W. B., Radhakrishnan, R., Lemmon, M. A. & Mosse, Y. P. 2014. ALK mutations confer differential oncogenic activation and sensitivity to ALK inhibition therapy in neuroblastoma. *Cancer Cell* **26**, 682-694.

Brodeur, G. M. 2003. Neuroblastoma: biological insights into a clinical enigma. *Nat Rev Cancer* **3**, 203-216.

Brodeur, G. M. & Bagatell, R. 2014. Mechanisms of neuroblastoma regression. *Nature reviews. Clinical oncology* **11**, 704-713.

Brodeur, G. M., Sekhon, G. & Goldstein, M. N. 1977. Chromosomal aberrations in human neuroblastomas. *Cancer* **40**, 2256-2263.

Bruserud, O., Stapnes, C., Ersvaer, E., Gjertsen, B. T. & Ryningen, A. 2007. Histone deacetylase inhibitors in cancer treatment: a review of the clinical toxicity and the modulation of gene expression in cancer cell. *Curr Pharm Biotechnol* **8**, 388-400.

Bryan, T. M., Englezou, A., Gupta, J., Bacchetti, S. & Reddel, R. R. 1995. Telomere elongation in immortal human cells without detectable telomerase activity. *The EMBO journal* **14**, 4240-4248.

Buckingham, L. 2013. in *Pharmacogenomics* (eds Yui-Wing Francis Lam & Larisa H. Cavallari) 117-131 (Academic Press).

Bui, C. B., Le, H. K., Vu, D. M., Truong, K. D., Nguyen, N. M., Ho, M. A. N. & Truong, D. Q. 2019. ARID1A-SIN3A drives retinoic acid-induced neuroblastoma differentiation by transcriptional repression of TERT. *Mol Carcinog* **58**, 1998-2007.

Campbell, K., Gastier-Foster, J. M., Mann, M., Naranjo, A. H., Van Ryn, C., Bagatell, R., Matthay, K. K., London, W. B., Irwin, M. S., Shimada, H., Granger, M. M., Hogarty, M. D., Park, J. R. & DuBois, S. G. 2017. Association of MYCN copy number with clinical features, tumor biology, and outcomes in neuroblastoma: A report from the Children's Oncology Group. *Cancer* **123**, 4224-4235.

Cann, K. L. & Dellaire, G. 2011. Heterochromatin and the DNA damage response: the need to relax. *Biochem Cell Biol* **89**, 45-60.

Caron, H., van Sluis, P., de Kraker, J., Bokkerink, J., Egeler, M., Laureys, G., Slater, R., Westerveld, A., Voute, P. A. & Versteeg, R. 1996. Allelic loss of chromosome 1p as a predictor of unfavorable outcome in patients with neuroblastoma. *N Engl J Med* **334**, 225-230.

Carpenter, E. L. & Mosse, Y. P. 2012. Targeting ALK in neuroblastoma--preclinical and clinical advancements. *Nature reviews. Clinical oncology* **9**, 391-399.

Carroll, T. S., Liang, Z., Salama, R., Stark, R. & de Santiago, I. 2014. Impact of artifact removal on ChIP quality metrics in ChIP-seq and ChIP-exo data. *Front Genet* **5**, 75.

Cascon, A. & Robledo, M. 2012. MAX and MYC: a heritable breakup. *Cancer Res* **72**, 3119-3124.

Catley, L., Weisberg, E., Tai, Y. T., Atadja, P., Remiszewski, S., Hideshima, T., Mitsiades, N., Shringarpure, R., LeBlanc, R., Chauhan, D., Munshi, N. C., Schlossman, R., Richardson, P., Griffin, J. & Anderson, K. C. 2003. NVP-LAQ824 is a potent novel histone deacetylase inhibitor with significant activity against multiple myeloma. *Blood* **102**, 2615-2622.

Celeghin, A., Giunco, S., Freguja, R., Zangrossi, M., Nalio, S., Dolcetti, R. & De Rossi, A. 2016. Short-term inhibition of TERT induces telomere length-independent cell cycle arrest and apoptotic response in EBV-immortalized and transformed B cells. *Cell Death Dis* **7**, e2562-e2562.

Chakrabarti, M., Banik, N. L. & Ray, S. K. 2013. miR-138 overexpression is more powerful than hTERT knockdown to potentiate apigenin for apoptosis in neuroblastoma in vitro and in vivo. *Exp Cell Res* **319**, 1575-1585.

Chen, L., Lü, M. H., Zhang, D., Hao, N. B., Fan, Y. H., Wu, Y. Y., Wang, S. M., Xie, R., Fang, D. C., Zhang, H., Hu, C. J. & Yang, S. M. 2014. miR-1207-5p and miR-1266 suppress gastric cancer growth and invasion by targeting telomerase reverse transcriptase. *Cell Death Dis* **5**, e1034-e1034.

Chenette, E. J. 2009. DNA damage response: Keeping telomerase at bay. *Nat Rev Mol Cell Biol* **10**, 813.

Cheng, D., Zhao, Y., Wang, S., Zhang, F., Russo, M., McMahon, S. B. & Zhu, J. 2017a. Repression of telomerase gene promoter requires human-specific genomic context and is mediated by multiple HDAC1-containing corepressor complexes. *Faseb j* **31**, 1165-1178.

Cheng, M.-H., Wong, Y.-H., Chang, C.-M., Yang, C.-C., Chen, S.-H., Yuan, C.-L., Kuo, H.-M., Yang, C.-Y. & Chiu, H.-F. 2017b. B1, a novel HDAC inhibitor, induces apoptosis through the regulation of STAT3 and NF-κB. *Int J Mol Med* **39**, 1137-1148.

Cheung, N. K., Zhang, J., Lu, C., Parker, M., Bahrami, A., Tickoo, S. K., Heguy, A., Pappo, A. S., Federico, S., Dalton, J., Cheung, I. Y., Ding, L., Fulton, R., Wang, J., Chen, X., Becksfort, J., Wu, J., Billups, C. A., Ellison, D., Mardis, E. R., Wilson, R. K., Downing, J. R. & Dyer, M. A. 2012. Association of age at diagnosis and genetic mutations in patients with neuroblastoma. *Jama* **307**, 1062-1071.

Chiappori, A. A., Kolevska, T., Spigel, D. R., Hager, S., Rarick, M., Gadgeel, S., Blais, N., Von Pawel, J., Hart, L., Reck, M., Bassett, E., Burington, B. & Schiller, J. H. 2015. A randomized phase II study of the telomerase inhibitor imetelstat as maintenance therapy for advanced non-small-cell lung cancer. *Ann Oncol* **26**, 354-362.

Chipumuro, E., Marco, E., Christensen, C. L., Kwiatkowski, N., Zhang, T., Hatheway, C. M., Abraham, B. J., Sharma, B., Yeung, C., Altabef, A., Perez-Atayde, A., Wong, K. K., Yuan, G. C., Gray, N. S., Young, R. A. & George, R. E. 2014. CDK7 inhibition suppresses super-enhancer-linked oncogenic transcription in MYCN-driven cancer. *Cell* **159**, 1126-1139.

Choi, J., Southworth, L. K., Sarin, K. Y., Venteicher, A. S., Ma, W., Chang, W., Cheung, P., Jun, S., Artandi, M. K., Shah, N., Kim, S. K. & Artandi, S. E. 2008. TERT

promotes epithelial proliferation through transcriptional control of a Myc- and Wnt-related developmental program. *PLoS Genet* **4**, e10.

Choo, S. P., Chowbay, B., Ng, Q. S., Thng, C. H., Lim, C., Hartono, S., Koh, T. S., Huynh, H., Poon, D., Ang, M. K., Chang, S. & Toh, H. C. 2013. A Phase 1 dose-finding and pharmacodynamic study of rapamycin in combination with bevacizumab in patients with unresectable hepatocellular carcinoma. *European Journal of Cancer* **49**, 999-1008.

Christopher, L. J., Cui, D., Wu, C., Luo, R., Manning, J. A., Bonacorsi, S. J., Lago, M., Allentoff, A., Lee, F. Y. F., McCann, B., Galbraith, S., Reitberg, D. P., He, K., Barros, A., Blackwood-Chirchir, A., Humphreys, W. G. & Iyer, R. A. 2008. Metabolism and Disposition of Dasatinib after Oral Administration to Humans. *Drug Metabolism and Disposition* **36**, 1357-1364.

Ci, X., Li, B., Ma, X., Kong, F., Zheng, C., Bjorkholm, M., Jia, J. & Xu, D. 2015. Bortezomib-mediated down-regulation of telomerase and disruption of telomere homeostasis contributes to apoptosis of malignant cells. *Oncotarget* **6**, 38079-38092.

Cohn, S. L., Pearson, A. D., London, W. B., Monclair, T., Ambros, P. F., Brodeur, G. M., Faldum, A., Hero, B., Iehara, T., Machin, D., Mosseri, V., Simon, T., Garaventa, A., Castel, V. & Matthay, K. K. 2009. The International Neuroblastoma Risk Group (INRG) classification system: an INRG Task Force report. *J Clin Oncol* **27**, 289-297.

Colebatch, A. J., Dobrovic, A. & Cooper, W. A. 2019. TERT gene: its function and dysregulation in cancer. *J Clin Pathol* **72**, 281-284.

Collins, K. & Mitchell, J. R. 2002. Telomerase in the human organism. *Oncogene* **21**, 564-579.

Cong, Y.-S., Wen, J. & Bacchetti, S. 1999. The Human Telomerase Catalytic Subunit hTERT: Organization of the Gene and Characterization of the Promoter. *Human Molecular Genetics* **8**, 137-142.

Cortez-Gonzalez, X. & Zanetti, M. 2007. Telomerase immunity from bench to bedside: round one. *J Transl Med* **5**, 12.

Counter, C. M., Hahn, W. C., Wei, W., Caddle, S. D., Beijersbergen, R. L., Lansdorp, P. M., Sedivy, J. M. & Weinberg, R. A. 1998. Dissociation among in vitro telomerase activity, telomere maintenance, and cellular immortalization. *Proc Natl Acad Sci U S A* **95**, 14723-14728.

Dagogo-Jack, I., Brannon, A. R., Ferris, L. A., Campbell, C. D., Lin, J. J., Schultz, K. R., Ackil, J., Stevens, S., Dardaei, L., Yoda, S., Hubbeling, H., Digumarthy, S. R., Riester, M., Hata, A. N., Sequist, L. V., Lennes, I. T., Iafrate, A. J., Heist, R. S., Azzoli, C. G., Farago, A. F., Engelman, J. A., Lennerz, J. K., Benes, C. H., Leary, R. J., Shaw, A. T. & Gainor, J. F. 2018. Tracking the Evolution of Resistance to ALK Tyrosine Kinase Inhibitors through Longitudinal Analysis of Circulating Tumor DNA. *JCO Precis Oncol* **2018**.

Das, A., Banik, N. L. & Ray, S. K. 2009. Retinoids induce differentiation and downregulate telomerase activity and N-Myc to increase sensitivity to flavonoids for apoptosis in human malignant neuroblastoma SH-SY5Y cells. *Int J Oncol* **34**, 757-765.

Dawson, M. A. & Kouzarides, T. 2012. Cancer epigenetics: from mechanism to therapy. *Cell* **150**, 12-27.

De Coster, W., D'Hert, S., Schultz, D. T., Cruts, M. & Van Broeckhoven, C. 2018. NanoPack: visualizing and processing long-read sequencing data. *Bioinformatics* **34**, 2666-2669.

de Ruijter, A. J., van Gennip, A. H., Caron, H. N., Kemp, S. & van Kuilenburg, A. B. 2003. Histone deacetylases (HDACs): characterization of the classical HDAC family. *Biochem J* **370**, 737-749.

De Vitis, M., Berardinelli, F. & Sgura, A. 2018. Telomere Length Maintenance in Cancer: At the Crossroad between Telomerase and Alternative Lengthening of Telomeres (ALT). *Int J Mol Sci* **19**, 606.

Deaton, A. M. & Bird, A. 2011. CpG islands and the regulation of transcription. *Genes Dev* **25**, 1010-1022.

Deeg, K. I., Chung, I., Bauer, C. & Rippe, K. 2016. Cancer Cells with Alternative Lengthening of Telomeres Do Not Display a General Hypersensitivity to ATR Inhibition. *Front Oncol* **6**, 186.

Deubzer, H. E., Ehemann, V., Westermann, F., Heinrich, R., Mechtersheimer, G., Kulozik, A. E., Schwab, M. & Witt, O. 2008. Histone deacetylase inhibitor Helminthosporium carbonum (HC)-toxin suppresses the malignant phenotype of neuroblastoma cells. *Int J Cancer* **122**, 1891-1900.

Deubzer, H. E., Schier, M. C., Oehme, I., Lodrini, M., Haendler, B., Sommer, A. & Witt, O. 2013. HDAC11 is a novel drug target in carcinomas. *Int J Cancer* **132**, 2200-2208.

Dias, J. N. R., Aguiar, S. I., Pereira, D. M., André, A. S., Gano, L., Correia, J. D. G., Carrapiço, B., Rütgen, B., Malhó, R., Peleteiro, C., Goncalves, J., Rodrigues, C. M. P., Gil, S., Tavares, L. & Aires-da-Silva, F. 2018. The histone deacetylase inhibitor panobinostat is a potent antitumor agent in canine diffuse large B-cell lymphoma. *Oncotarget* **9**, 28586-28598.

Diplas, B. H., He, X., Brosnan-Cashman, J. A., Liu, H., Chen, L. H., Wang, Z., Moure, C. J., Killela, P. J., Loriaux, D. B., Lipp, E. S., Greer, P. K., Yang, R., Rizzo, A. J., Rodriguez, F. J., Friedman, A. H., Friedman, H. S., Wang, S., He, Y., McLendon, R. E., Bigner, D. D., Jiao, Y., Waitkus, M. S., Meeker, A. K. & Yan, H. 2018. The genomic landscape of TERT promoter wildtype-IDH wildtype glioblastoma. *Nat Commun* **9**, 2087.

Dobin, A., Davis, C. A., Schlesinger, F., Drenkow, J., Zaleski, C., Jha, S., Batut, P., Chaisson, M. & Gingeras, T. R. 2012. STAR: ultrafast universal RNA-seq aligner. *Bioinformatics* **29**, 15-21.

Donmez, G. & Outeiro, T. F. 2013. SIRT1 and SIRT2: emerging targets in neurodegeneration. *EMBO Mol Med* **5**, 344-352.

Du, P., Zhang, X., Huang, C.-C., Jafari, N., Kibbe, W. A., Hou, L. & Lin, S. M. 2010. Comparison of Beta-value and M-value methods for quantifying methylation levels by microarray analysis. *BMC Bioinformatics* **11**, 587.

Duan, H., Heckman, C. A. & Boxer, L. M. 2005. Histone deacetylase inhibitors down-regulate bcl-2 expression and induce apoptosis in t(14;18) lymphomas. *Mol Cell Biol* **25**, 1608-1619.

Eckschlager, T., Plch, J., Stiborova, M. & Hrabeta, J. 2017. Histone Deacetylase Inhibitors as Anticancer Drugs. *Int J Mol Sci* **18**.

Edgar, R., Domrachev, M. & Lash, A. E. 2002. Gene Expression Omnibus: NCBI gene expression and hybridization array data repository. *Nucleic Acids Res* **30**, 207-210.

Ediriweera, M. K. & Cho, S. K. 2020. Targeting miRNAs by histone deacetylase inhibitors (HDACi): Rationalizing epigenetics-based therapies for breast cancer. *Pharmacol Ther* **206**, 107437.

Ellis, L., Bots, M., Lindemann, R. K., Bolden, J. E., Newbold, A., Cluse, L. A., Scott, C. L., Strasser, A., Atadja, P., Lowe, S. W. & Johnstone, R. W. 2009. The histone deacetylase inhibitors LAQ824 and LBH589 do not require death receptor signaling or a functional apoptosome to mediate tumor cell death or therapeutic efficacy. *Blood* **114**, 380-393.

Emerald, B. S., Chen, Y., Zhu, T., Zhu, Z., Lee, K.-O., Gluckman, P. D. & Lobie, P. E. 2007. αCP1 Mediates Stabilization of hTERT mRNA by Autocrine Human Growth Hormone. *Journal of Biological Chemistry* **282**, 680-690.

Engelhardt, M., Albanell, J., Drullinsky, P., Han, W., Guillem, J., Scher, H. I., Reuter, V. & Moore, M. A. 1997. Relative contribution of normal and neoplastic cells determines telomerase activity and telomere length in primary cancers of the prostate, colon, and sarcoma. *Clin Cancer Res* **3**, 1849-1857.

Ernst, J., Kheradpour, P., Mikkelsen, T. S., Shoresh, N., Ward, L. D., Epstein, C. B., Zhang, X., Wang, L., Issner, R., Coyne, M., Ku, M., Durham, T., Kellis, M. & Bernstein, B. E. 2011. Mapping and analysis of chromatin state dynamics in nine human cell types. *Nature* **473**, 43-49.

Esteller, M. 2007. Epigenetic gene silencing in cancer: the DNA hypermethylome. *Hum Mol Genet* **16 Spec No 1**, R50-59.

Evangelisti, C., Florian, M. C., Massimi, I., Dominici, C., Giannini, G., Galardi, S., Bue, M. C., Massalini, S., McDowell, H. P., Messi, E., Gulino, A., Farace, M. G. & Ciafre, S. A. 2009. MiR-128 up-regulation inhibits Reelin and DCX expression and reduces neuroblastoma cell motility and invasiveness. *Faseb j* **23**, 4276-4287.

Fabian, J., Lodrini, M., Oehme, I., Schier, M. C., Thole, T. M., Hielscher, T., Kopp-Schneider, A., Opitz, L., Capper, D., Deimling, A. v., Wiegand, I., Milde, T., Mahlknecht, U., Westermann, F., Popanda, O., Roels, F., Hero, B., Berthold, F., Fischer, M., Kulozik, A. E., Witt, O. & Deubzer, H. E. 2014. GRHL1 Acts as Tumor Suppressor in Neuroblastoma and Is Negatively Regulated by MYCN and HDAC3. *Cancer Research* **74**, 2604-2616.

Farooqi, A. A., Mansoor, Q., Alaaeddine, N. & Xu, B. 2018. MicroRNA Regulation of Telomerase Reverse Transcriptase (TERT): Micro Machines Pull Strings of Papier-Mâché Puppets. *Int J Mol Sci* **19**, 1051.

Ficner, R. 2009. Novel structural insights into class I and II histone deacetylases. *Current topics in medicinal chemistry* **9**, 235-240.

Filippakopoulos, P., Qi, J., Picaud, S., Shen, Y., Smith, W. B., Fedorov, O., Morse, E. M., Keates, T., Hickman, T. T., Felletar, I., Philpott, M., Munro, S., McKeown, M. R., Wang, Y., Christie, A. L., West, N., Cameron, M. J., Schwartz, B., Heightman, T. D., La Thangue, N., French, C. A., Wiest, O., Kung, A. L., Knapp, S. & Bradner, J. E. 2010. Selective inhibition of BET bromodomains. *Nature* **468**, 1067-1073.

Fischer, M., Skowron, M. & Berthold, F. 2005. Reliable Transcript Quantification by Real-Time Reverse Transcriptase-Polymerase Chain Reaction in Primary Neuroblastoma Using Normalization to Averaged Expression Levels of the Control Genes HPRT1 and SDHA. *The Journal of molecular diagnostics : JMD* **7**, 89-96.

Floris, G., Debiec-Rychter, M., Sciot, R., Stefan, C., Fieuws, S., Machiels, K., Atadja, P., Wozniak, A., Faa, G. & Schöffski, P. 2009. High Efficacy of Panobinostat Towards Human Gastrointestinal Stromal Tumors in a Xenograft Mouse Model. *Clinical Cancer Research* **15**, 4066-4076.

Flynn, R. L., Cox, K. E., Jeitany, M., Wakimoto, H., Bryll, A. R., Ganem, N. J., Bersani, F., Pineda, J. R., Suvà, M. L., Benes, C. H., Haber, D. A., Boussin, F. D. & Zou, L. 2015. Alternative lengthening of telomeres renders cancer cells hypersensitive to ATR inhibitors. *Science* **347**, 273-277.

Francisco, R., Perez-Perarnau, A., Cortes, C., Gil, J., Tauler, A. & Ambrosio, S. 2012. Histone deacetylase inhibition induces apoptosis and autophagy in human neuroblastoma cells. *Cancer Lett* **318**, 42-52.

Friedman, D. L., Kadan-Lottick, N. S., Whitton, J., Mertens, A. C., Yasui, Y., Liu, Y., Meadows, A. T., Robison, L. L. & Strong, L. C. 2005. Increased risk of cancer among siblings of long-term childhood cancer survivors: a report from the childhood cancer survivor study. *Cancer Epidemiology and Prevention Biomarkers* **14**, 1922-1927.

Frumm, S. M., Fan, Z. P., Ross, K. N., Duvall, J. R., Gupta, S., VerPlank, L., Suh, B.-C., Holson, E., Wagner, F. F., Smith, W. B., Paranal, R. M., Bassil, C. F., Qi, J., Roti,

G., Kung, A. L., Bradner, J. E., Tolliday, N. & Stegmaier, K. 2013. Selective HDAC1/HDAC2 inhibitors induce neuroblastoma differentiation. *Chemistry & biology* **20**, 713-725.

Furumai, R., Matsuyama, A., Kobashi, N., Lee, K. H., Nishiyama, M., Nakajima, H., Tanaka, A., Komatsu, Y., Nishino, N., Yoshida, M. & Horinouchi, S. 2002. FK228 (depsipeptide) as a natural prodrug that inhibits class I histone deacetylases. *Cancer Res* **62**, 4916-4921.

Gal-Yam, E. N., Egger, G., Iniguez, L., Holster, H., Einarsson, S., Zhang, X., Lin, J. C., Liang, G., Jones, P. A. & Tanay, A. 2008. Frequent switching of Polycomb repressive marks and DNA hypermethylation in the PC3 prostate cancer cell line. *Proceedings of the National Academy of Sciences* **105**, 12979-12984.

Gao, L., Cueto, M. A., Asselbergs, F. & Atadja, P. 2002. Cloning and functional characterization of HDAC11, a novel member of the human histone deacetylase family. *J Biol Chem* **277**, 25748-25755.

Gardner, R. V. 1999. Long term hematopoietic damage after chemotherapy and cytokine. *Front Biosci* **4**, e47-57.

Gartlgruber, M. 2018. *Novel chromatin interactions by structural rearrangements and aberrant enhancer functions drive oncogenic programs in unfavorable neuroblastoma* http://wwwubuni-heidelbergde/archiv/25365 thesis, Universität Heidelberg,

Ghosh, A., Saginc, G., Leow, S. C., Khattar, E., Shin, E. M., Yan, T. D., Wong, M., Zhang, Z., Li, G., Sung, W.-K., Zhou, J., Chng, W. J., Li, S., Liu, E. & Tergaonkar, V. 2012a. Telomerase directly regulates NF-κB-dependent transcription. *Nat Cell Biol* **14**, 1270-1281.

Ghosh, A., Saginc, G., Leow, S. C., Khattar, E., Shin, E. M., Yan, T. D., Wong, M., Zhang, Z., Li, G., Sung, W. K., Zhou, J., Chng, W. J., Li, S., Liu, E. & Tergaonkar, V. 2012b. Telomerase directly regulates NF-kappaB-dependent transcription. *Nat Cell Biol* **14**, 1270-1281.

Glick, R. D., Swendeman, S. L., Coffey, D. C., Rifkind, R. A., Marks, P. A., Richon, V. M. & La Quaglia, M. P. 1999. Hybrid polar histone deacetylase inhibitor induces apoptosis and CD95/CD95 ligand expression in human neuroblastoma. *Cancer Res* **59**, 4392-4399.

Glozak, M. A., Sengupta, N., Zhang, X. & Seto, E. 2005. Acetylation and deacetylation of non-histone proteins. *Gene* **363**, 15-23.

Gomez, D. E., Armando, R. G., Farina, H. G., Menna, P. L., Cerrudo, C. S., Ghiringhelli, P. D. & Alonso, D. F. 2012. Telomere structure and telomerase in health and disease (review). *Int J Oncol* **41**, 1561-1569.

Gordon, D. M. & Santos, J. H. 2010. The emerging role of telomerase reverse transcriptase in mitochondrial DNA metabolism. *J Nucleic Acids* **2010**.

Greider, C. W. & Blackburn, E. H. 1985. Identification of a specific telomere terminal transferase activity in tetrahymena extracts. *Cell* **43**, 405-413.

Greig, S. L. 2016. Panobinostat: A Review in Relapsed or Refractory Multiple Myeloma. *Targeted Oncology* **11**, 107-114.

Guidi, M., Muiños-Gimeno, M., Kagerbauer, B., Martí, E., Estivill, X. & Espinosa-Parrilla, Y. 2010. Overexpression of miR-128 specifically inhibits the truncated isoform of NTRK3 and upregulates BCL2 in SH-SY5Y neuroblastoma cells. *BMC Mol Biol* **11**, 95-95.

Gunes, C., Lichtsteiner, S., Vasserot, A. P. & Englert, C. 2000. Expression of the hTERT gene is regulated at the level of transcriptional initiation and repressed by Mad1. *Cancer Res* **60**, 2116-2121.

Guzman, H., Sanders, K., Idica, A., Bochnakian, A., Jury, D., Daugaard, I., Zisoulis, D. G. & Pedersen, I. M. 2018. miR-128 inhibits telomerase activity by targeting TERT mRNA. *Oncotarget* **9**, 13244-13253.

Haas, D., Ablin, A. R., Miller, C., Zoger, S. & Matthay, K. K. 1988. Complete pathologic maturation and regression of stage IVS neuroblastoma without treatment. *Cancer* **62**, 818-825.

Haberland, M., Montgomery, R. L. & Olson, E. N. 2009. The many roles of histone deacetylases in development and physiology: implications for disease and therapy. *Nat Rev Genet* **10**.

Hahn, W. C., Counter, C. M., Lundberg, A. S., Beijersbergen, R. L., Brooks, M. W. & Weinberg, R. A. 1999. Creation of human tumour cells with defined genetic elements. *Nature* **400**, 464-468.

Hall, J. A., Dominy, J. E., Lee, Y. & Puigserver, P. 2013. The sirtuin family's role in aging and age-associated pathologies. *J Clin Invest* **123**, 973-979.

Hall, M. D., Telma, K. A., Chang, K.-E., Lee, T. D., Madigan, J. P., Lloyd, J. R., Goldlust, I. S., Hoeschele, J. D. & Gottesman, M. M. 2014. Say No to DMSO: Dimethylsulfoxide Inactivates Cisplatin, Carboplatin, and Other Platinum Complexes. *Cancer Research* **74**, 3913-3922.

Hanmod, S. S., Wang, G., Edwards, H., Buck, S. A., Ge, Y., Taub, J. W. & Wang, Z. 2015. Targeting histone deacetylases (HDACs) and Wee1 for treating high-risk neuroblastoma. *Pediatr Blood Cancer* **62**, 52-59.

Hansen, K. D. 2017. IlluminaHumanMethylationEPICanno.ilm10b4.hg19: Annotation for Illumina's EPIC methylation arrays. R package version 0.6.0.

Harley, C. B. 2008. Telomerase and cancer therapeutics. *Nature Reviews Cancer* **8**, 167-179.

Hart, L. S., Rader, J., Raman, P., Batra, V., Russell, M. R., Tsang, M., Gagliardi, M., Chen, L., Martinez, D. & Li, Y. 2017. Preclinical therapeutic synergy of MEK1/2 and CDK4/6 inhibition in neuroblastoma. *Clinical Cancer Research* **23**, 1785-1796.

Hayflick, L. 1965. THE LIMITED IN VITRO LIFETIME OF HUMAN DIPLOID CELL STRAINS. *Exp Cell Res* **37**, 614-636.

He, L. Z., Tolentino, T., Grayson, P., Zhong, S., Warrell, R. P., Jr., Rifkind, R. A., Marks, P. A., Richon, V. M. & Pandolfi, P. P. 2001. Histone deacetylase inhibitors induce remission in transgenic models of therapy-resistant acute promyelocytic leukemia. *J Clin Invest* **108**, 1321-1330.

Heidenreich, B. & Kumar, R. 2017. TERT promoter mutations in telomere biology. *Mutat Res* **771**, 15-31.

Heintzman, N. D., Stuart, R. K., Hon, G., Fu, Y., Ching, C. W., Hawkins, R. D., Barrera, L. O., Van Calcar, S., Qu, C., Ching, K. A., Wang, W., Weng, Z., Green, R. D., Crawford, G. E. & Ren, B. 2007. Distinct and predictive chromatin signatures of transcriptional promoters and enhancers in the human genome. *Nat Genet* **39**, 311-318.

Helland, Ø., Popa, M., Bischof, K., Gjertsen, B. T., McCormack, E. & Bjørge, L. 2016. The HDACi Panobinostat Shows Growth Inhibition Both In Vitro and in a Bioluminescent Orthotopic Surgical Xenograft Model of Ovarian Cancer. *PLoS One* **11**, e0158208.

Hennika, T., Hu, G., Olaciregui, N. G., Barton, K. L., Ehteda, A., Chitranjan, A., Chang, C., Gifford, A. J., Tsoli, M., Ziegler, D. S., Carcaboso, A. M. & Becher, O. J. 2017. Pre-Clinical Study of Panobinostat in Xenograft and Genetically Engineered Murine Diffuse Intrinsic Pontine Glioma Models. *PLoS One* **12**, e0169485.

Henrich, K.-O., Bender, S., Saadati, M., Dreidax, D., Gartlgruber, M., Shao, C., Herrmann, C., Wiesenfarth, M., Parzonka, M., Wehrmann, L., Fischer, M., Duffy, D. J., Bell, E., Torkov, A., Schmezer, P., Plass, C., Höfer, T., Benner, A., Pfister, S. M. & Westermann, F. 2016. Integrative Genome-Scale Analysis Identifies Epigenetic

Mechanisms of Transcriptional Deregulation in Unfavorable Neuroblastomas. *Cancer Research* **76**, 5523-5537.

Henssen, A., Althoff, K., Odersky, A., Beckers, A., Koche, R., Speleman, F., Schäfers, S., Bell, E., Nortmeyer, M., Westermann, F., Preter, K. D., Florin, A., Heukamp, L., Spruessel, A., Astrahanseff, K., Lindner, S., Sadowski, N., Schramm, A., Astorgues-Xerri, L., Riveiro, M. E., Eggert, A., Cvitkovic, E. & Schulte, J. H. 2016. Targeting MYCN-Driven Transcription By BET-Bromodomain Inhibition. *Clinical Cancer Research* **22**, 2470-2481.

Henssen, A. G., Reed, C., Jiang, E., Garcia, H. D., von Stebut, J., MacArthur, I. C., Hundsdoerfer, P., Kim, J. H., de Stanchina, E., Kuwahara, Y., Hosoi, H., Ganem, N. J., Dela Cruz, F., Kung, A. L., Schulte, J. H., Petrini, J. H. & Kentsis, A. 2017. Therapeutic targeting of PGBD5-induced DNA repair dependency in pediatric solid tumors. *Sci Transl Med* **9**.

Hideshima, T., Bradner, J. E., Wong, J., Chauhan, D., Richardson, P., Schreiber, S. L. & Anderson, K. C. 2005. Small-molecule inhibition of proteasome and aggresome function induces synergistic antitumor activity in multiple myeloma. *Proc Natl Acad Sci U S A* **102**, 8567-8572.

Hiyama, E., Hiyama, K., Yokoyama, T., Matsuura, Y., Piatyszek, M. A. & Shay, J. W. 1995. Correlating telomerase activity levels with human neuroblastoma outcomes. *Nat Med* **1**, 249-255.

Hoffmeyer, K., Raggioli, A., Rudloff, S., Anton, R., Hierholzer, A., Del Valle, I., Hein, K., Vogt, R. & Kemler, R. 2012. Wnt/β-Catenin Signaling Regulates Telomerase in Stem Cells and Cancer Cells. *Science* **336**, 1549-1554.

Hrdlickova, R., Nehyba, J., Bargmann, W. & Bose, H. R., Jr. 2014. Multiple tumor suppressor microRNAs regulate telomerase and TCF7, an important transcriptional regulator of the Wnt pathway. *PLoS One* **9**, e86990.

Hsu, Y. F., Sheu, J. R., Hsiao, G., Lin, C. H., Chang, T. H., Chiu, P. T., Wang, C. Y. & Hsu, M. J. 2011. p53 in trichostatin A induced C6 glioma cell death. *Biochim Biophys Acta* **1810**, 504-513.

Hu, J., Hwang, S. S., Liesa, M., Gan, B., Sahin, E., Jaskelioff, M., Ding, Z., Ying, H., Boutin, A. T., Zhang, H., Johnson, S., Ivanova, E., Kost-Alimova, M., Protopopov, A., Wang, Y. A., Shirihai, O. S., Chin, L. & DePinho, R. A. 2012. Antitelomerase therapy provokes ALT and mitochondrial adaptive mechanisms in cancer. *Cell* **148**, 651-663.

Hu, Y., Shi, G., Zhang, L., Li, F., Jiang, Y., Jiang, S., Ma, W., Zhao, Y., Songyang, Z. & Huang, J. 2016. Switch telomerase to ALT mechanism by inducing telomeric DNA damages and dysfunction of ATRX and DAXX. *Sci Rep* **6**, 32280.

Huang, M., Zeki, J., Sumarsono, N., Coles, G. L., Taylor, J. S., Danzer, E., Bruzoni, M., Hazard, F. K., Lacayo, N. J., Sakamoto, K. M., Dunn, J. C. Y., Spunt, S. L. & Chiu, B. 2020. Epigenetic targeting of TERT-associated gene expression signature in human neuroblastoma with TERT overexpression. *Cancer Res*.

Ianevski, A., He, L., Aittokallio, T. & Tang, J. 2017. SynergyFinder: a web application for analyzing drug combination dose-response matrix data. *Bioinformatics* **33**, 2413-2415.

Iannilli, F., Zalfa, F., Gartner, A., Bagni, C. & Dotti, C. G. 2013. Cytoplasmic TERT Associates to RNA Granules in Fully Mature Neurons: Role in the Translational Control of the Cell Cycle Inhibitor p15INK4B. *PLoS One* **8**, e66602.

Indran, I. R., Hande, M. P. & Pervaiz, S. 2011. hTERT overexpression alleviates intracellular ROS production, improves mitochondrial function, and inhibits ROS-mediated apoptosis in cancer cells. *Cancer Res* **71**, 266-276.

Infarinato, N. R., Park, J. H., Krytska, K., Ryles, H. T., Sano, R., Szigety, K. M., Li, Y., Zou, H. Y., Lee, N. V., Smeal, T., Lemmon, M. A. & Mosse, Y. P. 2016. The

ALK/ROS1 Inhibitor PF-06463922 Overcomes Primary Resistance to Crizotinib in ALK-Driven Neuroblastoma. *Cancer Discov* **6**, 96-107.

Inoue, S., Riley, J., Gant, T. W., Dyer, M. J. & Cohen, G. M. 2007. Apoptosis induced by histone deacetylase inhibitors in leukemic cells is mediated by Bim and Noxa. *Leukemia* **21**, 1773-1782.

INRG. *The International Neuroblastoma Risk Group Classification System*, www.inrg.org (2020).

Ito, T., Watanabe, H., Yamamichi, N., Kondo, S., Tando, T., Haraguchi, T., Mizutani, T., Sakurai, K., Fujita, S., Izumi, T., Isobe, T. & Iba, H. 2008. Brm transactivates the telomerase reverse transcriptase (TERT) gene and modulates the splicing patterns of its transcripts in concert with p54nrb. *Biochemical Journal* **411**, 201-209.

Jagadeeshan, S., Prasad, M., Ortiz-Cuaran, S., Gregoire, V., Saintigny, P. & Elkabets, M. 2019. Adaptive Responses to Monotherapy in Head and Neck Cancer: Interventions for Rationale-Based Therapeutic Combinations. *Trends in Cancer* **5**, 365-390.

Janyst, K., Janyst, M., Siernicka, M. & Lasek, W. 2018. Synergistic antitumor effects of histone deacetylase inhibitor scriptaid and bortezomib against ovarian cancer cells. *Oncol Rep* **39**, 1999-2005.

Jie, M.-M., Chang, X., Zeng, S., Liu, C., Liao, G.-B., Wu, Y.-R., Liu, C.-H., Hu, C.-J., Yang, S.-M. & Li, X.-Z. 2019. Diverse regulatory manners of human telomerase reverse transcriptase. *Cell Communication and Signaling* **17**, 63.

Jung, A. R., Yoo, J. E., Shim, Y. H., Choi, Y. N., Jeung, H. C., Chung, H. C., Rha, S. Y. & Oh, B. K. 2013. Increased alternative lengthening of telomere phenotypes of telomerase-negative immortal cells upon trichostatin--a treatment. *Anticancer Res* **33**, 821-829.

Jung, J., Seol, H. S. & Chang, S. 2018. The Generation and Application of Patient-Derived Xenograft Model for Cancer Research. *Cancer research and treatment : official journal of Korean Cancer Association* **50**, 1-10.

Juratli, T. A., McCabe, D., Nayyar, N., Williams, E. A., Silverman, I. M., Tummala, S. S., Fink, A. L., Baig, A., Martinez-Lage, M., Selig, M. K., Bihun, I. V., Shankar, G. M., Penson, T., Lastrapes, M., Daubner, D., Meinhardt, M., Hennig, S., Kaplan, A. B., Fujio, S., Kuter, B. M., Bertalan, M. S., Miller, J. J., Batten, J. M., Ely, H. A., Christiansen, J., Baretton, G. B., Stemmer-Rachamimov, A. O., Santagata, S., Rivera, M. N., Barker, F. G., 2nd, Schackert, G., Wakimoto, H., Iafrate, A. J., Carter, S. L., Cahill, D. P. & Brastianos, P. K. 2018. DMD genomic deletions characterize a subset of progressive/higher-grade meningiomas with poor outcome. *Acta Neuropathol* **136**, 779-792.

Kabeya, Y., Mizushima, N., Ueno, T., Yamamoto, A., Kirisako, T., Noda, T., Kominami, E., Ohsumi, Y. & Yoshimori, T. 2000. LC3, a mammalian homologue of yeast Apg8p, is localized in autophagosome membranes after processing. *EMBO J* **19**, 5720-5728.

Kang, H. J., Choi, Y. S., Hong, S. B., Kim, K. W., Woo, R. S., Won, S. J., Kim, E. J., Jeon, H. K., Jo, S. Y., Kim, T. K., Bachoo, R., Reynolds, I. J., Gwag, B. J. & Lee, H. W. 2004. Ectopic expression of the catalytic subunit of telomerase protects against brain injury resulting from ischemia and NMDA-induced neurotoxicity. *The Journal of neuroscience : the official journal of the Society for Neuroscience* **24**, 1280-1287.

Kazanets, A., Shorstova, T., Hilmi, K., Marques, M. & Witcher, M. 2016. Epigenetic silencing of tumor suppressor genes: Paradigms, puzzles, and potential. *Biochimica et Biophysica Acta (BBA) - Reviews on Cancer* **1865**, 275-288.

Kelly, R. D. & Cowley, S. M. 2013. The physiological roles of histone deacetylase (HDAC) 1 and 2: complex co-stars with multiple leading parts. *Biochem Soc Trans* **41**, 741-749.

Khan, N., Jeffers, M., Kumar, S., Hackett, C., Boldog, F., Khramtsov, N., Qian, X., Mills, E., Berghs, S., Carey, N., Finn, P., Collins, L., Tumber, A., Ritchie, J., Jensen, P.,

Lichenstein, H. & Sehested, M. 2008a. Determination of the class and isoform selectivity of small-molecule histone deacetylase inhibitors. *The Biochemical journal* **409**, 581-589.

Khan, N., Jeffers, M., Kumar, S., Hackett, C., Boldog, F., Khramtsov, N., Qian, X., Mills, E., Berghs, S. C., Carey, N., Finn, P. W., Collins, L. S., Tumber, A., Ritchie, J. W., Jensen, P. B., Lichenstein, H. S. & Sehested, M. 2008b. Determination of the class and isoform selectivity of small-molecule histone deacetylase inhibitors. *Biochem J* **409**, 581-589.

Kharbanda, S., Kumar, V., Dhar, S., Pandey, P., Chen, C., Majumder, P., Yuan, Z. M., Whang, Y., Strauss, W., Pandita, T. K., Weaver, D. & Kufe, D. 2000. Regulation of the hTERT telomerase catalytic subunit by the c-Abl tyrosine kinase. *Current Biology* **10**, 568-575.

Khattar, E., Kumar, P., Liu, C. Y., Akıncılar, S. C., Raju, A., Lakshmanan, M., Maury, J. J. P., Qiang, Y., Li, S., Tan, E. Y., Hui, K. M., Shi, M., Loh, Y. H. & Tergaonkar, V. 2016. Telomerase reverse transcriptase promotes cancer cell proliferation by augmenting tRNA expression. *J Clin Invest* **126**, 4045-4060.

Khattar, E. & Tergaonkar, V. 2017. Transcriptional Regulation of Telomerase Reverse Transcriptase (TERT) by MYC. *Front Cell Dev Biol* **5**, 1.

Killela, P. J., Reitman, Z. J., Jiao, Y., Bettegowda, C., Agrawal, N., Diaz, L. A., Friedman, A. H., Friedman, H., Gallia, G. L., Giovanella, B. C., Grollman, A. P., He, T.-C., He, Y., Hruban, R. H., Jallo, G. I., Mandahl, N., Meeker, A. K., Mertens, F., Netto, G. J., Rasheed, B. A., Riggins, G. J., Rosenquist, T. A., Schiffman, M., Shih, I.-M., Theodorescu, D., Torbenson, M. S., Velculescu, V. E., Wang, T.-L., Wentzensen, N., Wood, L. D., Zhang, M., McLendon, R. E., Bigner, D. D., Kinzler, K. W., Vogelstein, B., Papadopoulos, N. & Yan, H. 2013. TERT promoter mutations occur frequently in gliomas and a subset of tumors derived from cells with low rates of self-renewal. *Proceedings of the National Academy of Sciences* **110**, 6021-6026.

Kim, J. H., Park, S.-M., Kang, M. R., Oh, S.-Y., Lee, T. H., Muller, M. T. & Chung, I. K. 2005a. Ubiquitin ligase MKRN1 modulates telomere length homeostasis through a proteolysis of hTERT. *Genes & Development* **19**, 776-781.

Kim, N., Piatyszek, M., Prowse, K., Harley, C., West, M., Ho, P., Coviello, G., Wright, W., Weinrich, S. & Shay, J. 1994a. Specific association of human telomerase activity with immortal cells and cancer. *Science* **266**, 2011-2015.

Kim, N. W., Piatyszek, M. A., Prowse, K. R., Harley, C. B., West, M. D., Ho, P. L., Coviello, G. M., Wright, W. E., Weinrich, S. L. & Shay, J. W. 1994b. Specific association of human telomerase activity with immortal cells and cancer. *Science* **266**, 2011-2015.

Kim, T. H., Barrera, L. O., Zheng, M., Qu, C., Singer, M. A., Richmond, T. A., Wu, Y., Green, R. D. & Ren, B. 2005b. A high-resolution map of active promoters in the human genome. *Nature* **436**, 876-880.

Kimura, H. 2013. Histone modifications for human epigenome analysis. *Journal Of Human Genetics* **58**, 439.

Koche, R. P., Rodriguez-Fos, E., Helmsauer, K., Burkert, M., MacArthur, I. C., Maag, J., Chamorro, R., Munoz-Perez, N., Puiggròs, M., Dorado Garcia, H., Bei, Y., Röefzaad, C., Bardinet, V., Szymansky, A., Winkler, A., Thole, T., Timme, N., Kasack, K., Fuchs, S., Klironomos, F., Thiessen, N., Blanc, E., Schmelz, K., Künkele, A., Hundsdörfer, P., Rosswog, C., Theissen, J., Beule, D., Deubzer, H., Sauer, S., Toedling, J., Fischer, M., Hertwig, F., Schwarz, R. F., Eggert, A., Torrents, D., Schulte, J. H. & Henssen, A. G. 2020. Extrachromosomal circular DNA drives oncogenic genome remodeling in neuroblastoma. *Nature Genetics* **52**, 29-34.

Koh, C. M., Khattar, E., Leow, S. C., Liu, C. Y., Muller, J., Ang, W. X., Li, Y., Franzoso, G., Li, S., Guccione, E. & Tergaonkar, V. 2015. Telomerase regulates MYC-driven

oncogenesis independent of its reverse transcriptase activity. *J Clin Invest* **125**, 2109-2122.

Kolbinger, F. R., Koeneke, E., Ridinger, J., Heimburg, T., Müller, M., Bayer, T., Sippl, W., Jung, M., Gunkel, N., Miller, A. K., Westermann, F., Witt, O. & Oehme, I. 2018. The HDAC6/8/10 inhibitor TH34 induces DNA damage-mediated cell death in human high-grade neuroblastoma cell lines. *Arch Toxicol* **92**, 2649-2664.

Kramer, O. H., Gottlicher, M. & Heinzel, T. 2001. Histone deacetylase as a therapeutic target. *Trends Endocrinol Metab* **12**, 294-300.

Krennhrubec, K., Marshall, B. L., Hedglin, M., Verdin, E. & Ulrich, S. M. 2007. Design and evaluation of 'Linkerless' hydroxamic acids as selective HDAC8 inhibitors. *Bioorg Med Chem Lett* **17**, 2874-2878.

Kyo, S., Takakura, M., Taira, T., Kanaya, T., Itoh, H., Yutsudo, M., Ariga, H. & Inoue, M. 2000. Sp1 cooperates with c-Myc to activate transcription of the human telomerase reverse transcriptase gene (hTERT). *Nucleic Acids Res* **28**, 669-677.

Lavanya, C., Venkataswamy, M. M., Sibin, M. K., Srinivas Bharath, M. M. & Chetan, G. K. 2018. Down regulation of human telomerase reverse transcriptase (hTERT) expression by BIBR1532 in human glioblastoma LN18 cells. *Cytotechnology* **70**, 1143-1154.

Le Douarin, N. M. & Dupin, E. 2012. The neural crest in vertebrate evolution. *Curr Opin Genet Dev* **22**, 381-389.

LeBoeuf, M., Terrell, A., Trivedi, S., Sinha, S., Epstein, J. A., Olson, E. N., Morrisey, E. E. & Millar, S. E. 2010. Hdac1 and Hdac2 act redundantly to control p63 and p53 functions in epidermal progenitor cells. *Dev Cell* **19**, 807-818.

Lee, D. D., Leao, R., Komosa, M., Gallo, M., Zhang, C. H., Lipman, T., Remke, M., Heidari, A., Nunes, N. M., Apolonio, J. D., Price, A. J., De Mello, R. A., Dias, J. S., Huntsman, D., Hermanns, T., Wild, P. J., Vanner, R., Zadeh, G., Karamchandani, J., Das, S., Taylor, M. D., Hawkins, C. E., Wasserman, J. D., Figueiredo, A., Hamilton, R. J., Minden, M. D., Wani, K., Diplas, B., Yan, H., Aldape, K., Akbari, M. R., Danesh, A., Pugh, T. J., Dirks, P. B., Castelo-Branco, P. & Tabori, U. 2019. DNA hypermethylation within TERT promoter upregulates TERT expression in cancer. *J Clin Invest* **129**, 223-229.

Lee, J., Sung, Y. H., Cheong, C., Choi, Y. S., Jeon, H. K., Sun, W., Hahn, W. C., Ishikawa, F. & Lee, H. W. 2008. TERT promotes cellular and organismal survival independently of telomerase activity. *Oncogene* **27**, 3754-3760.

Lee, S., Qiao, J., Paul, P., O'Connor, K. L., Evers, M. B. & Chung, D. H. 2012. FAK is a critical regulator of neuroblastoma liver metastasis. *Oncotarget* **3**, 1576-1587.

Lee, T. I., Johnstone, S. E. & Young, R. A. 2006. Chromatin immunoprecipitation and microarray-based analysis of protein location. *Nat Protoc* **1**, 729-748.

Li, C.-T., Hsiao, Y.-M., Wu, T.-C., Lin, Y.-w., Yeh, K.-T. & Ko, J.-L. 2011. Vorinostat, SAHA, represses telomerase activity via epigenetic regulation of telomerase reverse transcriptase in non-small cell lung cancer cells. *Journal of Cellular Biochemistry* **112**, 3044-3053.

Li, H. 2018. Minimap2: pairwise alignment for nucleotide sequences. *Bioinformatics* **34**, 3094-3100.

Li, H. & Durbin, R. 2009. Fast and accurate short read alignment with Burrows-Wheeler transform. *Bioinformatics* **25**, 1754-1760.

Li, Y., Cheng, H., Chang, W. & Tergaonkar, V. 2016a. Activation of mutant TERT promoter by RAS-ERK signaling is a key step in malignant progression of BRAF-mutant human melanomas. *Proceedings of the National Academy of Sciences* **113**, 14402-14407.

Li, Y. & Seto, E. 2016b. HDACs and HDAC Inhibitors in Cancer Development and Therapy. *Cold Spring Harbor Perspectives in Medicine* **6**, a026831.

Liao, Y., Smyth, G. K. & Shi, W. 2013. featureCounts: an efficient general purpose program for assigning sequence reads to genomic features. *Bioinformatics* **30**, 923-930.

Liao, Y., Smyth, G. K. & Shi, W. 2019. The R package Rsubread is easier, faster, cheaper and better for alignment and quantification of RNA sequencing reads. *Nucleic Acids Res* **47**, e47.

Liberzon, A., Birger, C., Thorvaldsdottir, H., Ghandi, M., Mesirov, J. P. & Tamayo, P. 2015. The Molecular Signatures Database (MSigDB) hallmark gene set collection. *Cell Syst* **1**, 417-425.

Listerman, I., Sun, J., Gazzaniga, F. S., Lukas, J. L. & Blackburn, E. H. 2013. The major reverse transcriptase-incompetent splice variant of the human telomerase protein inhibits telomerase activity but protects from apoptosis. *Cancer Res* **73**, 2817-2828.

Liu, C., Fang, X., Ge, Z., Jalink, M., Kyo, S., Björkholm, M., Gruber, A., Sjöberg, J. & Xu, D. 2007. The Telomerase Reverse Transcriptase (hTERT) Gene Is a Direct Target of the Histone Methyltransferase SMYD3. *Cancer Research* **67**, 2626-2631.

Liu, L., Saldanha, S. N., Pate, M. S., Andrews, L. G. & Tollefsbol, T. O. 2004. Epigenetic regulation of human telomerase reverse transcriptase promoter activity during cellular differentiation. *Genes Chromosomes Cancer* **41**, 26-37.

Liu, R., Zhang, T., Zhu, G. & Xing, M. 2018. Regulation of mutant TERT by BRAF V600E/MAP kinase pathway through FOS/GABP in human cancer. *Nature Communications* **9**, 579.

Lodrini, M., Oehme, I., Schroeder, C., Milde, T., Schier, M. C., Kopp-Schneider, A., Schulte, J. H., Fischer, M., De Preter, K., Pattyn, F., Castoldi, M., Muckenthaler, M. U., Kulozik, A. E., Westermann, F., Witt, O. & Deubzer, H. E. 2013. MYCN and HDAC2 cooperate to repress miR-183 signaling in neuroblastoma. *Nucleic Acids Research* **41**, 6018-6033.

London, W. B., Castleberry, R. P., Matthay, K. K., Look, A. T., Seeger, R. C., Shimada, H., Thorner, P., Brodeur, G., Maris, J. M., Reynolds, C. P. & Cohn, S. L. 2005. Evidence for an age cutoff greater than 365 days for neuroblastoma risk group stratification in the Children's Oncology Group. *J Clin Oncol* **23**, 6459-6465.

Long, M. D., Smiraglia, D. J. & Campbell, M. J. 2017. The Genomic Impact of DNA CpG Methylation on Gene Expression; Relationships in Prostate Cancer. *Biomolecules* **7**.

Lopatina, N. G., Poole, J. C., Saldanha, S. N., Hansen, N. J., Key, J. S., Pita, M. A., Andrews, L. G. & Tollefsbol, T. O. 2003. Control mechanisms in the regulation of telomerase reverse transcriptase expression in differentiating human teratocarcinoma cells. *Biochem Biophys Res Commun* **306**, 650-659.

Love, M. I., Huber, W. & Anders, S. 2014. Moderated estimation of fold change and dispersion for RNA-seq data with DESeq2. *Genome Biology* **15**, 550.

Loven, J., Hoke, H. A., Lin, C. Y., Lau, A., Orlando, D. A., Vakoc, C. R., Bradner, J. E., Lee, T. I. & Young, R. A. 2013. Selective inhibition of tumor oncogenes by disruption of super-enhancers. *Cell* **153**, 320-334.

Low, K. C. & Tergaonkar, V. 2013. Telomerase: central regulator of all of the hallmarks of cancer. *Trends Biochem Sci* **38**, 426-434.

Lu, M. H., Tang, B., Zeng, S., Hu, C. J., Xie, R., Wu, Y. Y., Wang, S. M., He, F. T. & Yang, S. M. 2016. Long noncoding RNA BC032469, a novel competing endogenous RNA, upregulates hTERT expression by sponging miR-1207-5p and promotes proliferation in gastric cancer. *Oncogene* **35**, 3524-3534.

Luo, W., Friedman, M. S., Shedden, K., Hankenson, K. D. & Woolf, P. J. 2009. GAGE: generally applicable gene set enrichment for pathway analysis. *BMC Bioinformatics* **10**, 161.

Ma, P., Pan, H., Montgomery, R. L., Olson, E. N. & Schultz, R. M. 2012. Compensatory functions of histone deacetylase 1 (HDAC1) and HDAC2 regulate transcription and

apoptosis during mouse oocyte development. *Proceedings of the National Academy of Sciences* **109**, E481-E489.

Mac, S. M., D'Cunha, C. A. & Farnham, P. J. 2000. Direct recruitment of N-myc to target gene promoters. *Mol Carcinog* **29**, 76-86.

Mandriota, S. J., Valentijn, L. J., Lesne, L., Betts, D. R., Marino, D., Boudal-Khoshbeen, M., London, W. B., Rougemont, A. L., Attiyeh, E. F., Maris, J. M., Hogarty, M. D., Koster, J., Molenaar, J. J., Versteeg, R., Ansari, M. & Gumy-Pause, F. 2015. Ataxia-telangiectasia mutated (ATM) silencing promotes neuroblastoma progression through a MYCN independent mechanism. *Oncotarget* **6**, 18558-18576.

Maris, J. M. 2010. Recent Advances in Neuroblastoma. *New England Journal of Medicine* **362**, 2202-2211.

Maris, J. M., Hogarty, M. D., Bagatell, R. & Cohn, S. L. 2007. Neuroblastoma. *Lancet* **369**, 2106-2120.

Masutomi, K., Possemato, R., Wong, J. M., Currier, J. L., Tothova, Z., Manola, J. B., Ganesan, S., Lansdorp, P. M., Collins, K. & Hahn, W. C. 2005. The telomerase reverse transcriptase regulates chromatin state and DNA damage responses. *Proc Natl Acad Sci U S A* **102**, 8222-8227.

Matthay, K. K., Maris, J. M., Schleiermacher, G., Nakagawara, A., Mackall, C. L., Diller, L. & Weiss, W. A. 2016. Neuroblastoma. *Nat Rev Dis Primers* **2**, 16078.

Matthews, G. M., Newbold, A. & Johnstone, R. W. 2012. Intrinsic and extrinsic apoptotic pathway signaling as determinants of histone deacetylase inhibitor antitumor activity. *Adv Cancer Res* **116**, 165-197.

Medvedeva, Y. A., Khamis, A. M., Kulakovskiy, I. V., Ba-Alawi, W., Bhuyan, M. S. I., Kawaji, H., Lassmann, T., Harbers, M., Forrest, A. R. R., Bajic, V. B. & consortium, F. 2014. Effects of cytosine methylation on transcription factor binding sites. *BMC genomics* **15**, 119-119.

Mei, S., Ho, A. D. & Mahlknecht, U. 2004. Role of histone deacetylase inhibitors in the treatment of cancer (Review). *Int J Oncol* **25**, 1509-1519.

Melo, M., da Rocha, A. G., Vinagre, J., Batista, R., Peixoto, J., Tavares, C., Celestino, R., Almeida, A., Salgado, C., Eloy, C., Castro, P., Prazeres, H., Lima, J., Amaro, T., Lobo, C., Martins, M. J., Moura, M., Cavaco, B., Leite, V., Cameselle-Teijeiro, J. M., Carrilho, F., Carvalheiro, M., Maximo, V., Sobrinho-Simoes, M. & Soares, P. 2014. TERT promoter mutations are a major indicator of poor outcome in differentiated thyroid carcinomas. *J Clin Endocrinol Metab* **99**, E754-765.

Menyhárt, O., Harami-Papp, H., Sukumar, S., Schäfer, R., Magnani, L., de Barrios, O. & Győrffy, B. 2016. Guidelines for the selection of functional assays to evaluate the hallmarks of cancer. *Biochimica et Biophysica Acta (BBA) - Reviews on Cancer* **1866**, 300-319.

Miyazaki, M., Otomo, R., Matsushima-Hibiya, Y., Suzuki, H., Nakajima, A., Abe, N., Tomiyama, A., Ichimura, K., Matsuda, K., Watanabe, T., Ochiya, T., Nakagama, H., Sakai, R. & Enari, M. 2018. The p53 activator overcomes resistance to ALK inhibitors by regulating p53-target selectivity in ALK-driven neuroblastomas. *Cell Death Discovery* **4**, 56.

Molenaar, J. J., Koster, J., Zwijnenburg, D. A., van Sluis, P., Valentijn, L. J., van der Ploeg, I., Hamdi, M., van Nes, J., Westerman, B. A., van Arkel, J., Ebus, M. E., Haneveld, F., Lakeman, A., Schild, L., Molenaar, P., Stroeken, P., van Noesel, M. M., Ora, I., Santo, E. E., Caron, H. N., Westerhout, E. M. & Versteeg, R. 2012. Sequencing of neuroblastoma identifies chromothripsis and defects in neuritogenesis genes. *Nature* **483**, 589-593.

Monclair, T., Brodeur, G. M., Ambros, P. F., Brisse, H. J., Cecchetto, G., Holmes, K., Kaneko, M., London, W. B., Matthay, K. K., Nuchtern, J. G., von Schweinitz, D.,

Simon, T., Cohn, S. L. & Pearson, A. D. 2009. The International Neuroblastoma Risk Group (INRG) staging system: an INRG Task Force report. *J Clin Oncol* **27**, 298-303.

Montgomery, R. L., Davis, C. A., Potthoff, M. J., Haberland, M., Fielitz, J., Qi, X., Hill, J. A., Richardson, J. A. & Olson, E. N. 2007. Histone deacetylases 1 and 2 redundantly regulate cardiac morphogenesis, growth, and contractility. *Genes Dev* **21**, 1790-1802.

Moreno, L., Caron, H., Geoerger, B., Eggert, A., Schleiermacher, G., Brock, P., Valteau-Couanet, D., Chesler, L., Schulte, J. H., De Preter, K., Molenaar, J., Schramm, A., Eilers, M., Van Maerken, T., Johnsen, J. I., Garrett, M., George, S. L., Tweddle, D. A., Kogner, P., Berthold, F., Koster, J., Barone, G., Tucker, E. R., Marshall, L., Herold, R., Sterba, J., Norga, K., Vassal, G. & Pearson, A. D. 2017. Accelerating drug development for neuroblastoma - New Drug Development Strategy: an Innovative Therapies for Children with Cancer, European Network for Cancer Research in Children and Adolescents and International Society of Paediatric Oncology Europe Neuroblastoma project. *Expert Opin Drug Discov* **12**, 801-811.

Mosse, Y. P. 2016. Anaplastic Lymphoma Kinase as a Cancer Target in Pediatric Malignancies. *Clin Cancer Res* **22**, 546-552.

Mossé, Y. P., Laudenslager, M., Longo, L., Cole, K. A., Wood, A., Attiyeh, E. F., Laquaglia, M. J., Sennett, R., Lynch, J. E., Perri, P., Laureys, G., Speleman, F., Kim, C., Hou, C., Hakonarson, H., Torkamani, A., Schork, N. J., Brodeur, G. M., Tonini, G. P., Rappaport, E., Devoto, M. & Maris, J. M. 2008. Identification of ALK as a major familial neuroblastoma predisposition gene. *Nature* **455**, 930-935.

Muhlethaler-Mottet, A., Meier, R., Flahaut, M., Bourloud, K. B., Nardou, K., Joseph, J. M. & Gross, N. 2008. Complex molecular mechanisms cooperate to mediate histone deacetylase inhibitors anti-tumour activity in neuroblastoma cells. *Mol Cancer* **7**, 55.

Mukherjee, S., Firpo, E. J., Wang, Y. & Roberts, J. M. 2011. Separation of telomerase functions by reverse genetics. *Proc Natl Acad Sci U S A* **108**, E1363-1371.

Munakata, K., Mochida, H., Kondo, S. & Suzuki, Y. 1980. Mutagenicity of N-acylglycinhydroxamic acids and related compounds. *Journal of Pharmacobio-Dynamics* **3**, 557-561.

Muñoz-Lorente, M. A., Cano-Martin, A. C. & Blasco, M. A. 2019. Mice with hyper-long telomeres show less metabolic aging and longer lifespans. *Nature Communications* **10**, 4723.

Mustafi, S., Camarena, V., Qureshi, R., Yoon, H., Volmar, C. H., Huff, T. C., Sant, D. W., Zheng, L., Brothers, S. P., Wahlestedt, C., Slingerland, J. & Wang, G. 2019. Vitamin C supplementation expands the therapeutic window of BETi for triple negative breast cancer. *EBioMedicine* **43**, 201-210.

Naiditch, J. A., Jie, C., Lautz, T. B., Yu, S., Clark, S., Voronov, D., Chu, F. & Madonna, M. B. 2015. Mesenchymal change and drug resistance in neuroblastoma. *Journal of Surgical Research* **193**, 279-288.

Nakamura, M., Saito, H., Ebinuma, H., Wakabayashi, K., Saito, Y., Takagi, T., Nakamoto, N. & Ishii, H. 2001. Reduction of telomerase activity in human liver cancer cells by a histone deacetylase inhibitor. *J Cell Physiol* **187**, 392-401.

Nelms, B. L. & Labosky, P. A. 2010. in *Transcriptional Control of Neural Crest Development* (Morgan & Claypool Life Sciences).

Nie, D., Huang, K., Yin, S., Li, Y., Xie, S., Ma, L., Wang, X., Wu, Y. & Xiao, J. 2012. Synergistic/additive interaction of valproic acid with bortezomib on proliferation and apoptosis of acute myeloid leukemia cells. *Leuk Lymphoma* **53**, 2487-2495.

NIH. *National Institute of Health*, http://clinicaltrials.gov (2020).

Northcott, P. A., Lee, C., Zichner, T., Stütz, A. M., Erkek, S., Kawauchi, D., Shih, D. J. H., Hovestadt, V., Zapatka, M., Sturm, D., Jones, D. T. W., Kool, M., Remke, M., Cavalli, F. M. G., Zuyderduyn, S., Bader, G. D., VandenBerg, S., Esparza, L. A.,

Ryzhova, M., Wang, W., Wittmann, A., Stark, S., Sieber, L., Seker-Cin, H., Linke, L., Kratochwil, F., Jäger, N., Buchhalter, I., Imbusch, C. D., Zipprich, G., Raeder, B., Schmidt, S., Diessl, N., Wolf, S., Wiemann, S., Brors, B., Lawerenz, C., Eils, J., Warnatz, H.-J., Risch, T., Yaspo, M.-L., Weber, U. D., Bartholomae, C. C., von Kalle, C., Turányi, E., Hauser, P., Sanden, E., Darabi, A., Siesjö, P., Sterba, J., Zitterbart, K., Sumerauer, D., van Sluis, P., Versteeg, R., Volckmann, R., Koster, J., Schuhmann, M. U., Ebinger, M., Grimes, H. L., Robinson, G. W., Gajjar, A., Mynarek, M., von Hoff, K., Rutkowski, S., Pietsch, T., Scheurlen, W., Felsberg, J., Reifenberger, G., Kulozik, A. E., von Deimling, A., Witt, O., Eils, R., Gilbertson, R. J., Korshunov, A., Taylor, M. D., Lichter, P., Korbel, J. O., Wechsler-Reya, R. J. & Pfister, S. M. 2014. Enhancer hijacking activates GFI1 family oncogenes in medulloblastoma. *Nature* **511**, 428-434.

Nowak, I., Boratyn, E., Durbas, M., Horwacik, I. & Rokita, H. 2018. Exogenous expression of miRNA-3613-3p causes APAF1 downregulation and affects several proteins involved in apoptosis in BE(2)-C human neuroblastoma cells. *Int J Oncol* **53**, 1787-1799.

Oehme, I., Deubzer, H. E., Lodrini, M., Milde, T. & Witt, O. 2009a. Targeting of HDAC8 and investigational inhibitors in neuroblastoma. *Expert Opinion on Investigational Drugs* **18**, 1605-1617.

Oehme, I., Deubzer, H. E., Wegener, D., Pickert, D., Linke, J. P., Hero, B., Kopp-Schneider, A., Westermann, F., Ulrich, S. M., von Deimling, A., Fischer, M. & Witt, O. 2009b. Histone deacetylase 8 in neuroblastoma tumorigenesis. *Clin Cancer Res* **15**, 91-99.

Oehme, I., Linke, J. P., Bock, B. C., Milde, T., Lodrini, M., Hartenstein, B., Wiegand, I., Eckert, C., Roth, W., Kool, M., Kaden, S., Grone, H. J., Schulte, J. H., Lindner, S., Hamacher-Brady, A., Brady, N. R., Deubzer, H. E. & Witt, O. 2013. Histone deacetylase 10 promotes autophagy-mediated cell survival. *Proc Natl Acad Sci U S A* **110**, E2592-2601.

Okamoto, K. & Seimiya, H. 2019. Revisiting Telomere Shortening in Cancer. *Cells* **8**, 107.

Olovnikov, A. M. 1996. Telomeres, telomerase, and aging: origin of the theory. *Exp Gerontol* **31**, 443-448.

Olzscha, H., Bekheet, M. E., Sheikh, S. & La Thangue, N. B. 2016. HDAC Inhibitors. *Methods Mol Biol* **1436**, 281-303.

Palmqvist, R., Zhang, A., Xu, D., Golovleva, I., Norrback, K. F., Gruber, A., Oberg, A., Stenling, R. & Roos, G. 2005. hTERT gene copy number is not associated with hTERT RNA expression or telomerase activity in colorectal cancer. *Int J Cancer* **116**, 395-400.

Park, J. I., Venteicher, A. S., Hong, J. Y., Choi, J., Jun, S., Shkreli, M., Chang, W., Meng, Z., Cheung, P., Ji, H., McLaughlin, M., Veenstra, T. D., Nusse, R., McCrea, P. D. & Artandi, S. E. 2009. Telomerase modulates Wnt signalling by association with target gene chromatin. *Nature* **460**, 66-72.

Pavlik, C. M., Wong, C. Y. B., Ononye, S., Lopez, D. D., Engene, N., McPhail, K. L., Gerwick, W. H. & Balunas, M. J. 2013. Santacruzamate A, a potent and selective histone deacetylase inhibitor from the Panamanian marine cyanobacterium cf. Symploca sp. *Journal of natural products* **76**, 2026-2033.

Peart, M. J., Smyth, G. K., van Laar, R. K., Bowtell, D. D., Richon, V. M., Marks, P. A., Holloway, A. J. & Johnstone, R. W. 2005. Identification and functional significance of genes regulated by structurally different histone deacetylase inhibitors. *Proc Natl Acad Sci U S A* **102**, 3697-3702.

Pediatric Treatment Editorial Board, P. D. Q. 2002. in *PDQ Cancer Information Summaries* (National Cancer Institute (US)).

Peifer, M., Hertwig, F., Roels, F., Dreidax, D., Gartlgruber, M., Menon, R., Krämer, A., Roncaioli, J. L., Sand, F., Heuckmann, J. M., Ikram, F., Schmidt, R., Ackermann, S., Engesser, A., Kahlert, Y., Vogel, W., Altmüller, J., Nürnberg, P., Thierry-Mieg, J., Thierry-Mieg, D., Mariappan, A., Heynck, S., Mariotti, E., Henrich, K.-O., Gloeckner, C., Bosco, G., Leuschner, I., Schweiger, M. R., Savelyeva, L., Watkins, S. C., Shao, C., Bell, E., Höfer, T., Achter, V., Lang, U., Theissen, J., Volland, R., Saadati, M., Eggert, A., de Wilde, B., Berthold, F., Peng, Z., Zhao, C., Shi, L., Ortmann, M., Büttner, R., Perner, S., Hero, B., Schramm, A., Schulte, J. H., Herrmann, C., O'Sullivan, R. J., Westermann, F., Thomas, R. K. & Fischer, M. 2015. Telomerase activation by genomic rearrangements in high-risk neuroblastoma. *Nature* **526**, 700-704.

Peters, T. J., Buckley, M. J., Statham, A. L., Pidsley, R., Samaras, K., R, V. L., Clark, S. J. & Molloy, P. L. 2015. De novo identification of differentially methylated regions in the human genome. *Epigenetics Chromatin* **8**, 6.

Pezzolo, A., Pistorio, A., Gambini, C., Haupt, R., Ferraro, M., Erminio, G., De Bernardi, B., Garaventa, A. & Pistoia, V. 2015. Intratumoral diversity of telomere length in individual neuroblastoma tumors. *Oncotarget* **6**, 7493-7503.

Pidsley, R., Zotenko, E., Peters, T. J., Lawrence, M. G., Risbridger, G. P., Molloy, P., Van Djik, S., Muhlhausler, B., Stirzaker, C. & Clark, S. J. 2016. Critical evaluation of the Illumina MethylationEPIC BeadChip microarray for whole-genome DNA methylation profiling. *Genome Biol* **17**, 208.

Pilchova, I., Klacanova, K., Dibdiakova, K., Saksonova, S., Stefanikova, A., Vidomanova, E., Lichardusova, L., Hatok, J. & Racay, P. 2017. Proteasome Stress Triggers Death of SH-SY5Y and T98G Cells via Different Cellular Mechanisms. *Neurochem Res* **42**, 3170-3185.

Pinto, N. R., Applebaum, M. A., Volchenboum, S. L., Matthay, K. K., London, W. B., Ambros, P. F., Nakagawara, A., Berthold, F., Schleiermacher, G., Park, J. R., Valteau-Couanet, D., Pearson, A. D. & Cohn, S. L. 2015. Advances in Risk Classification and Treatment Strategies for Neuroblastoma. *J Clin Oncol* **33**, 3008-3017.

Populo, H., Boaventura, P., Vinagre, J., Batista, R., Mendes, A., Caldas, R., Pardal, J., Azevedo, F., Honavar, M., Guimaraes, I., Manuel Lopes, J., Sobrinho-Simoes, M. & Soares, P. 2014. TERT promoter mutations in skin cancer: the effects of sun exposure and X-irradiation. *J Invest Dermatol* **134**, 2251-2257.

Pourbagheri-Sigaroodi, A., Bashash, D., Safaroghli-Azar, A., Farshi-Paraasghari, M., Momeny, M., Mansoor, F. N. & Ghaffari, S. H. 2019. Contributory role of microRNAs in anti-cancer effects of small molecule inhibitor of telomerase (BIBR1532) on acute promyelocytic leukemia cell line. *European Journal of Pharmacology* **846**, 49-62.

Prince, H. M., Bishton, M. J. & Johnstone, R. W. 2009. Panobinostat (LBH589): a potent pan-deacetylase inhibitor with promising activity against hematologic and solid tumors. *Future Oncol* **5**, 601-612.

Provost, C., Prignon, A., Cazes, A., Combaret, V., Delattre, O., Janoueix-Lerosey, I., Montravers, F. & Talbot, J. N. 2016. 68Ga-DOTATOC and FDG PET Imaging of Preclinical Neuroblastoma Models. *Anticancer Res* **36**, 4459-4466.

Pugh, T. J., Morozova, O., Attiyeh, E. F., Asgharzadeh, S., Wei, J. S., Auclair, D., Carter, S. L., Cibulskis, K., Hanna, M., Kiezun, A., Kim, J., Lawrence, M. S., Lichenstein, L., McKenna, A., Pedamallu, C. S., Ramos, A. H., Shefler, E., Sivachenko, A., Sougnez, C., Stewart, C., Ally, A., Birol, I., Chiu, R., Corbett, R. D., Hirst, M., Jackman, S. D., Kamoh, B., Khodabakshi, A. H., Krzywinski, M., Lo, A., Moore, R. A., Mungall, K. L., Qian, J., Tam, A., Thiessen, N., Zhao, Y., Cole, K. A.,

Diamond, M., Diskin, S. J., Mosse, Y. P., Wood, A. C., Ji, L., Sposto, R., Badgett, T., London, W. B., Moyer, Y., Gastier-Foster, J. M., Smith, M. A., Auvil, J. M. G., Gerhard, D. S., Hogarty, M. D., Jones, S. J. M., Lander, E. S., Gabriel, S. B., Getz, G., Seeger, R. C., Khan, J., Marra, M. A., Meyerson, M. & Maris, J. M. 2013. The genetic landscape of high-risk neuroblastoma. *Nature Genetics* **45**, 279-284.

Puissant, A., Frumm, S. M., Alexe, G., Bassil, C. F., Qi, J., Chanthery, Y. H., Nekritz, E. A., Zeid, R., Gustafson, W. C., Greninger, P., Garnett, M. J., McDermott, U., Benes, C. H., Kung, A. L., Weiss, W. A., Bradner, J. E. & Stegmaier, K. 2013. Targeting MYCN in neuroblastoma by BET bromodomain inhibition. *Cancer Discov* **3**, 308-323.

Qing, H., Aono, J., Findeisen, H. M., Jones, K. L., Heywood, E. B. & Bruemmer, D. 2016. Differential Regulation of Telomerase Reverse Transcriptase Promoter Activation and Protein Degradation by Histone Deacetylase Inhibition. *J Cell Physiol* **231**, 1276-1282.

Rafehi, H. & El-Osta, A. 2016. HDAC Inhibition in Vascular Endothelial Cells Regulates the Expression of ncRNAs. *Non-coding RNA* **2**, 4.

Rahman, R., Osteso-Ibanez, T., Hirst, R. A., Levesley, J., Kilday, J. P., Quinn, S., Peet, A., O'Callaghan, C., Coyle, B. & Grundy, R. G. 2010. Histone deacetylase inhibition attenuates cell growth with associated telomerase inhibition in high-grade childhood brain tumor cells. *Mol Cancer Ther* **9**, 2568-2581.

Ramirez, F., Dundar, F., Diehl, S., Gruning, B. A. & Manke, T. 2014. deepTools: a flexible platform for exploring deep-sequencing data. *Nucleic Acids Res* **42**, W187-191.

Ramunas, J., Yakubov, E., Brady, J. J., Corbel, S. Y., Holbrook, C., Brandt, M., Stein, J., Santiago, J. G., Cooke, J. P. & Blau, H. M. 2015. Transient delivery of modified mRNA encoding TERT rapidly extends telomeres in human cells. *Faseb j* **29**, 1930-1939.

Rathkopf, D., Wong, B. Y., Ross, R. W., Anand, A., Tanaka, E., Woo, M. M., Hu, J., Dzik-Jurasz, A., Yang, W. & Scher, H. I. 2010a. A phase I study of oral panobinostat alone and in combination with docetaxel in patients with castration-resistant prostate cancer. *Cancer Chemotherapy and Pharmacology* **66**, 181-189.

Rathkopf, D., Wong, B. Y., Ross, R. W., Anand, A., Tanaka, E., Woo, M. M., Hu, J., Dzik-Jurasz, A., Yang, W. & Scher, H. I. 2010b. A phase I study of oral panobinostat alone and in combination with docetaxel in patients with castration-resistant prostate cancer. *Cancer Chemother Pharmacol* **66**, 181-189.

Recagni, M., Bidzinska, J., Zaffaroni, N. & Folini, M. 2020. The Role of Alternative Lengthening of Telomeres Mechanism in Cancer: Translational and Therapeutic Implications. *Cancers (Basel)* **12**.

Regairaz, M., Munier, F., Sartelet, H., Castaing, M., Marty, V., Renauleaud, C., Doux, C., Delbe, J., Courty, J., Fabre, M., Ohta, S., Vielh, P., Michiels, S., Valteau-Couanet, D. & Vassal, G. 2016. Mutation-Independent Activation of the Anaplastic Lymphoma Kinase in Neuroblastoma. *Am J Pathol* **186**, 435-445.

Relitti, N., Saraswati, A. P., Federico, S., Khan, T., Brindisi, M., Zisterer, D., Brogi, S., Gemma, S., Butini, S. & Campiani, G. 2020. Telomerase-based cancer therapeutics: a review on their clinical trials. *Curr Top Med Chem*.

Ren, J. G., Xia, H. L., Tian, Y. M., Just, T., Cai, G. P. & Dai, Y. R. 2001. Expression of telomerase inhibits hydroxyl radical-induced apoptosis in normal telomerase negative human lung fibroblasts. *FEBS Lett* **488**, 133-138.

Renaud, S., Loukinov, D., Abdullaev, Z., Guilleret, I., Bosman, F. T., Lobanenkov, V. & Benhattar, J. 2007. Dual role of DNA methylation inside and outside of CTCF-binding regions in the transcriptional regulation of the telomerase hTERT gene. *Nucleic Acids Res* **35**, 1245-1256.

Renaud, S., Loukinov, D., Bosman, F. T., Lobanenkov, V. & Benhattar, J. 2005. CTCF binds the proximal exonic region of hTERT and inhibits its transcription. *Nucleic Acids Res* **33**, 6850-6860.

Reynolds, C. P., Matthay, K. K., Villablanca, J. G. & Maurer, B. J. 2003. Retinoid therapy of high-risk neuroblastoma. *Cancer Lett* **197**, 185-192.

Richardson, P. G., Hungria, V. T., Yoon, S. S., Beksac, M., Dimopoulos, M. A., Elghandour, A., Jedrzejczak, W. W., Guenther, A., Nakorn, T. N., Siritanaratkul, N., Schlossman, R. L., Hou, J., Moreau, P., Lonial, S., Lee, J. H., Einsele, H., Sopala, M., Bengoudifa, B. R., Corrado, C., Binlich, F. & San-Miguel, J. F. 2016. Panobinostat plus bortezomib and dexamethasone in previously treated multiple myeloma: outcomes by prior treatment. *Blood* **127**, 713-721.

Ropero, S. & Esteller, M. 2007. The role of histone deacetylases (HDACs) in human cancer. *Mol Oncol* **1**, 19-25.

Rosato, R. R., Almenara, J. A. & Grant, S. 2003. The histone deacetylase inhibitor MS-275 promotes differentiation or apoptosis in human leukemia cells through a process regulated by generation of reactive oxygen species and induction of p21CIP1/WAF1 1. *Cancer Res* **63**, 3637-3645.

Roth, S. Y., Denu, J. M. & Allis, C. D. 2001. Histone acetyltransferases. *Annu Rev Biochem* **70**, 81-120.

Rubis, B., Holysz, H., Gladych, M., Toton, E., Paszel, A., Lisiak, N., Kaczmarek, M., Hofmann, J. & Rybczynska, M. 2013. Telomerase downregulation induces proapoptotic genes expression and initializes breast cancer cells apoptosis followed by DNA fragmentation in a cell type dependent manner. *Mol Biol Rep* **40**, 4995-5004.

Saeboe-Larssen, S., Fossberg, E. & Gaudernack, G. 2006. Characterization of novel alternative splicing sites in human telomerase reverse transcriptase (hTERT): analysis of expression and mutual correlation in mRNA isoforms from normal and tumour tissues. *BMC Mol Biol* **7**, 26.

Salloum, R., Hummel, T. R., Kumar, S. S., Dorris, K., Li, S., Lin, T., Daryani, V. M., Stewart, C. F., Miles, L., Poussaint, T. Y., Stevenson, C., Goldman, S., Dhall, G., Packer, R., Fisher, P., Pollack, I. F., Fouladi, M., Boyett, J. & Drissi, R. 2016. A molecular biology and phase II study of imetelstat (GRN163L) in children with recurrent or refractory central nervous system malignancies: a pediatric brain tumor consortium study. *J Neurooncol* **129**, 443-451.

Samy, M., Gattolliat, C.-H., Pendino, F., Hillion, J., Nguyen, E., Bombard, S., Douc-Rasy, S., Bénard, J. & Ségal-Bendirdjian, E. 2012. Loss of the Malignant Phenotype of Human Neuroblastoma Cells by a Catalytically Inactive Dominant-Negative hTERT Mutant. *Molecular Cancer Therapeutics* **11**, 2384-2393.

Sanaei, M. & Kavoosi, F. 2019. Histone Deacetylases and Histone Deacetylase Inhibitors: Molecular Mechanisms of Action in Various Cancers. *Advanced Biomedical Research* **8**, 63-63.

Sarin, K. Y., Cheung, P., Gilison, D., Lee, E., Tennen, R. I., Wang, E., Artandi, M. K., Oro, A. E. & Artandi, S. E. 2005. Conditional telomerase induction causes proliferation of hair follicle stem cells. *Nature* **436**, 1048-1052.

Sauerwald, A., Sandin, S., Cristofari, G., Scheres, S. H., Lingner, J. & Rhodes, D. 2013. Structure of active dimeric human telomerase. *Nat Struct Mol Biol* **20**, 454-460.

Sausen, M., Leary, R. J., Jones, S., Wu, J., Reynolds, C. P., Liu, X., Blackford, A., Parmigiani, G., Diaz, L. A., Jr., Papadopoulos, N., Vogelstein, B., Kinzler, K. W., Velculescu, V. E. & Hogarty, M. D. 2013. Integrated genomic analyses identify ARID1A and ARID1B alterations in the childhood cancer neuroblastoma. *Nat Genet* **45**, 12-17.

Schneider, A., Chatterjee, S., Bousiges, O., Selvi, B. R., Swaminathan, A., Cassel, R., Blanc, F., Kundu, T. K. & Boutillier, A. L. 2013. Acetyltransferases (HATs) as targets for neurological therapeutics. *Neurotherapeutics* **10**, 568-588.

Schulte, J. H. & Eggert, A. 2015. Neuroblastoma. *Crit Rev Oncog* **20**, 245-270.

Seeger, R. C., Brodeur, G. M., Sather, H., Dalton, A., Siegel, S. E., Wong, K. Y. & Hammond, D. 1985. Association of multiple copies of the N-myc oncogene with rapid progression of neuroblastomas. *N Engl J Med* **313**, 1111-1116.

Seto, E. & Yoshida, M. 2014. Erasers of histone acetylation: the histone deacetylase enzymes. *Cold Spring Harbor perspectives in biology* **6**, a018713-a018713.

Seynnaeve, B., Lee, S., Borah, S., Park, Y., Pappo, A., Kirkwood, J. M. & Bahrami, A. 2017. Genetic and Epigenetic Alterations of TERT Are Associated with Inferior Outcome in Adolescent and Young Adult Patients with Melanoma. *Sci Rep* **7**, 45704.

Shahbazi, J., Liu, P. Y., Atmadibrata, B., Bradner, J. E., Marshall, G. M., Lock, R. B. & Liu, T. 2016. The Bromodomain Inhibitor JQ1 and the Histone Deacetylase Inhibitor Panobinostat Synergistically Reduce N-Myc Expression and Induce Anticancer Effects. *Clinical Cancer Research* **22**, 2534-2544.

Sharma, S., Poetz, F., Bruer, M., Ly-Hartig, Thi Bach N., Schott, J., Séraphin, B. & Stoecklin, G. 2016. Acetylation-Dependent Control of Global Poly(A) RNA Degradation by CBP/p300 and HDAC1/2. *Molecular Cell* **63**, 927-938.

Shay, J. & Bacchetti, S. 1997. A survey of telomerase activity in human cancer. *European Journal of Cancer* **33**, 787-791.

Shay, J. W., Pereira-Smith, O. M. & Wright, W. E. 1991. A role for both RB and p53 in the regulation of human cellular senescence. *Exp Cell Res* **196**, 33-39.

Shay, J. W., Reddel, R. R. & Wright, W. E. 2012. Cancer and Telomeres—An ALTernative to Telomerase. *Science* **336**, 1388-1390.

Shen, S. & Kozikowski, A. P. 2016. Why Hydroxamates May Not Be the Best Histone Deacetylase Inhibitors--What Some May Have Forgotten or Would Rather Forget? *ChemMedChem* **11**, 15-21.

Shen, Y., Xi, F., Li, H., Luo, Y., Chen, C. & Wang, L. 2018. Telomerase reverse transcriptase suppression inhibits cell proliferation and promotes cell apoptosis in hepatocellular cancer. *IUBMB Life* **70**, 642-648.

Shibue, T. & Weinberg, R. A. 2017. EMT, CSCs, and drug resistance: the mechanistic link and clinical implications. *Nature reviews. Clinical oncology* **14**, 611-629.

Shin, K. H., Kang, M. K., Dicterow, E. & Park, N. H. 2003. Hypermethylation of the hTERT promoter inhibits the expression of telomerase activity in normal oral fibroblasts and senescent normal oral keratinocytes. *Br J Cancer* **89**, 1473-1478.

Shin, S., Lee, E. M., Cha, H. J., Bae, S., Jung, J. H., Lee, S. M., Yoon, Y., Lee, H., Kim, S., Kim, H., Lee, S. J., Park, I. C., Jin, Y. W. & An, S. 2009. MicroRNAs that respond to histone deacetylase inhibitor SAHA and p53 in HCT116 human colon carcinoma cells. *Int J Oncol* **35**, 1343-1352.

Shirakawa, K., Chavez, L., Hakre, S., Calvanese, V. & Verdin, E. 2013. Reactivation of latent HIV by histone deacetylase inhibitors. *Trends in Microbiology* **21**, 277-285.

Sidell, N. 1982. Retinoic Acid-Induced Growth Inhibition and Morphologic Differentiation of Human Neuroblastoma Cells In Vitro2. *JNCI: Journal of the National Cancer Institute* **68**, 589-596.

Singh, A., Patel, V. K., Jain, D. K., Patel, P. & Rajak, H. 2016. Panobinostat as Pan-deacetylase Inhibitor for the Treatment of Pancreatic Cancer: Recent Progress and Future Prospects. *Oncology and therapy* **4**, 73-89.

Singhapol, C., Pal, D., Czapiewski, R., Porika, M., Nelson, G. & Saretzki, G. C. 2013. Mitochondrial Telomerase Protects Cancer Cells from Nuclear DNA Damage and Apoptosis. *PLoS One* **8**, e52989.

Slatkin, M. 2009. Epigenetic inheritance and the missing heritability problem. *Genetics* **182**, 845-850.

Smyth, G. K. 2005. in *Bioinformatics and Computational Biology Solutions Using R and Bioconductor* 397-420 (Springer New York).

Spitz, R., Hero, B., Simon, T. & Berthold, F. 2006. Loss in chromosome 11q identifies tumors with increased risk for metastatic relapses in localized and 4S neuroblastoma. *Clin Cancer Res* **12**, 3368-3373.

Stafman, L. L., Williams, A. P., Marayati, R., Aye, J. M., Markert, H. R., Garner, E. F., Quinn, C. H., Lallani, S. B., Stewart, J. E., Yoon, K. J., Whelan, K. & Beierle, E. A. 2019. Focal Adhesion Kinase Inhibition Contributes to Tumor Cell Survival and Motility in Neuroblastoma Patient-Derived Xenografts. *Sci Rep* **9**, 13259.

Stern, J. L., Theodorescu, D., Vogelstein, B., Papadopoulos, N. & Cech, T. R. 2015. Mutation of the TERT promoter, switch to active chromatin, and monoallelic TERT expression in multiple cancers. *Genes & Development* **29**, 2219-2224.

Subramanian, C., Jarzembowski, J. A., Opipari, A. W., Jr., Castle, V. P. & Kwok, R. P. 2007. CREB-binding protein is a mediator of neuroblastoma cell death induced by the histone deacetylase inhibitor trichostatin A. *Neoplasia* **9**, 495-503.

Suenaga, M., Soda, H., Oka, M., Yamaguchi, A., Nakatomi, K., Shiozawa, K., Kawabata, S., Kasai, T., Yamada, Y., Kamihira, S., Tei, C. & Kohno, S. 2002. Histone deacetylase inhibitors suppress telomerase reverse transcriptase mrna expression in prostate cancer cells. *International Journal of Cancer* **97**, 621-625.

Takakura, M., Kyo, S., Sowa, Y., Wang, Z., Yatabe, N., Maida, Y., Tanaka, M. & Inoue, M. 2001. Telomerase activation by histone deacetylase inhibitor in normal cells. *Nucleic Acids Research* **29**, 3006-3011.

Tamakawa, R. A., Fleisig, H. B. & Wong, J. M. 2010. Telomerase inhibition potentiates the effects of genotoxic agents in breast and colorectal cancer cells in a cell cycle-specific manner. *Cancer Res* **70**, 8684-8694.

Tan, C. R. C., Abdul-Majeed, S., Cael, B. & Barta, S. K. 2018. Clinical Pharmacokinetics and Pharmacodynamics of Bortezomib. *Clinical Pharmacokinetics*.

Tate, C. R., Rhodes, L. V., Segar, H. C., Driver, J. L., Pounder, F. N., Burow, M. E. & Collins-Burow, B. M. 2012. Targeting triple-negative breast cancer cells with the histone deacetylase inhibitor panobinostat. *Breast Cancer Research* **14**, R79.

Thiele, C. J., Reynolds, C. P. & Israel, M. A. 1985. Decreased expression of N-myc precedes retinoic acid-induced morphological differentiation of human neuroblastoma. *Nature* **313**, 404-406.

Thole, T. M., Lodrini, M., Fabian, J., Wuenschel, J., Pfeil, S., Hielscher, T., Kopp-Schneider, A., Heinicke, U., Fulda, S., Witt, O., Eggert, A., Fischer, M. & Deubzer, H. E. 2017. Neuroblastoma cells depend on HDAC11 for mitotic cell cycle progression and survival. *Cell Death Dis* **8**, e2635.

Thole, T. M., Toedling, J., Sprussel, A., Pfeil, S., Savelyeva, L., Capper, D., Messerschmidt, C., Beule, D., Groeneveld-Krentz, S., Eckert, C., Gambara, G., Henssen, A. G., Finkler, S., Schulte, J. H., Sieber, A., Bluethgen, N., Regenbrecht, C. R. A., Kunkele, A., Lodrini, M., Eggert, A. & Deubzer, H. E. 2020. Reflection of neuroblastoma intratumor heterogeneity in the new OHC-NB1 disease model. *Int J Cancer* **146**, 1031-1041.

Thompson, P. A., Drissi, R., Muscal, J. A., Panditharatna, E., Fouladi, M., Ingle, A. M., Ahern, C. H., Reid, J. M., Lin, T., Weigel, B. J. & Blaney, S. M. 2013. A phase I trial of imetelstat in children with refractory or recurrent solid tumors: a Children's Oncology Group Phase I Consortium Study (ADVL1112). *Clin Cancer Res* **19**, 6578-6584.

Thorvaldsdottir, H., Robinson, J. T. & Mesirov, J. P. 2013. Integrative Genomics Viewer (IGV): high-performance genomics data visualization and exploration. *Brief Bioinform* **14**, 178-192.

Tonini, G. P., Nakagawara, A. & Berthold, F. 2012. Towards a turning point of neuroblastoma therapy. *Cancer Letters* **326**, 128-134.

Touleimat, N. & Tost, J. 2012. Complete pipeline for Infinium((R)) Human Methylation 450K BeadChip data processing using subset quantile normalization for accurate DNA methylation estimation. *Epigenomics* **4**, 325-341.

Trigg, R. M. & Turner, S. D. 2018. ALK in Neuroblastoma: Biological and Therapeutic Implications. *Cancers (Basel)* **10**, 113.

Turtoi, A., Peixoto, P., Castronovo, V. & Bellahcene, A. 2015. Histone deacetylases and cancer-associated angiogenesis: current understanding of the biology and clinical perspectives. *Crit Rev Oncog* **20**, 119-137.

Valentijn, L. J., Koster, J., Zwijnenburg, D. A., Hasselt, N. E., van Sluis, P., Volckmann, R., van Noesel, M. M., George, R. E., Tytgat, G. A. M., Molenaar, J. J. & Versteeg, R. 2015. TERT rearrangements are frequent in neuroblastoma and identify aggressive tumors. *Nature Genetics* **47**, 1411.

van Groningen, T., Koster, J., Valentijn, L. J., Zwijnenburg, D. A., Akogul, N., Hasselt, N. E., Broekmans, M., Haneveld, F., Nowakowska, N. E., Bras, J., van Noesel, C. J. M., Jongejan, A., van Kampen, A. H., Koster, L., Baas, F., van Dijk-Kerkhoven, L., Huizer-Smit, M., Lecca, M. C., Chan, A., Lakeman, A., Molenaar, P., Volckmann, R., Westerhout, E. M., Hamdi, M., van Sluis, P. G., Ebus, M. E., Molenaar, J. J., Tytgat, G. A., Westerman, B. A., van Nes, J. & Versteeg, R. 2017. Neuroblastoma is composed of two super-enhancer-associated differentiation states. *Nat Genet* **49**, 1261-1266.

Van Veggel, M., Westerman, E. & Hamberg, P. 2018. Clinical Pharmacokinetics and Pharmacodynamics of Panobinostat. *Clin Pharmacokinet* **57**, 21-29.

VanGuilder, H. D., Vrana, K. E. & Freeman, W. M. 2008. Twenty-five years of quantitative PCR for gene expression analysis. *Biotechniques* **44**, 619-626.

Voigt, P., Tee, W.-W. & Reinberg, D. 2013. A double take on bivalent promoters. *Genes & Development* **27**, 1318-1338.

Wala, J. A., Bandopadhayay, P., Greenwald, N. F., O'Rourke, R., Sharpe, T., Stewart, C., Schumacher, S., Li, Y., Weischenfeldt, J., Yao, X., Nusbaum, C., Campbell, P., Getz, G., Meyerson, M., Zhang, C. Z., Imielinski, M. & Beroukhim, R. 2018. SvABA: genome-wide detection of structural variants and indels by local assembly. *Genome Res* **28**, 581-591.

Waldeck, K., Cullinane, C., Ardley, K., Shortt, J., Martin, B., Tothill, R. W., Li, J., Johnstone, R. W., McArthur, G. A., Hicks, R. J. & Wood, P. J. 2016. Long term, continuous exposure to panobinostat induces terminal differentiation and long term survival in the TH-MYCN neuroblastoma mouse model. *Int J Cancer* **139**, 194-204.

Walsh, M. F., Sacca, R., Wildman, T., Amoroso, K., Kennedy, J., Zhang, L., Birsoy, O., Mandelker, D., Steinsnyder, Z., Latham, A., Carlo, M. I., Cadoo, K., Kemel, Y., Robson, M., Stadler, Z. K. & Offit, K. 2019. Pathogenic Loss-of-Function Germline TERT Mutations in Patients With Solid Tumors. *JCO Precis Oncol*, 1-5.

Wang, C. Y. 1977. Mutagenicity of hydroxamic acids for Salmonella typhimurium. *Mutation Research/Fundamental and Molecular Mechanisms of Mutagenesis* **56**, 7-12.

Wang, G., Edwards, H., Caldwell, J. T., Buck, S. A., Qing, W. Y., Taub, J. W., Ge, Y. & Wang, Z. 2013. Panobinostat synergistically enhances the cytotoxic effects of cisplatin, doxorubicin or etoposide on high-risk neuroblastoma cells. *PLoS One* **8**, e76662.

Wang, J., Jiang, J., Chen, H., Wang, L., Guo, H., Yang, L., Xiao, D., Qing, G. & Liu, H. 2019. FDA-approved drug screen identifies proteasome as a synthetic lethal target in MYC-driven neuroblastoma. *Oncogene*.

Wang, N., Kjellin, H., Sofiadis, A., Fotouhi, O., Juhlin, C. C., Bäckdah, M., Zedenius, J., Xu, D., Lehtiö, J. & Larsson, C. 2016. Genetic and epigenetic background and protein expression profiles in relation to telomerase activation in medullary thyroid carcinoma. *Oncotarget* **7**.

Wang, S., Pike, A. M., Lee, S. S., Strong, M. A., Connelly, C. J. & Greider, C. W. 2017. BRD4 inhibitors block telomere elongation. *Nucleic Acids Research* **45**, 8403-8410.

Wang, S. & Zhu, J. 2003. Evidence for a relief of repression mechanism for activation of the human telomerase reverse transcriptase promoter. *J Biol Chem* **278**, 18842-18850.

Waters, A. M. & Beierle, E. A. 2014. The interaction between FAK, MYCN, p53 and Mdm2 in neuroblastoma. *Anticancer Agents Med Chem* **14**, 46-51.

Weaver, T. M., Morrison, E. A. & Musselman, C. A. 2018. Reading More than Histones: The Prevalence of Nucleic Acid Binding among Reader Domains. *Molecules* **23**.

Weiss, C., Uziel, O., Wolach, O., Nordenberg, J., Beery, E., Bulvick, S., Kanfer, G., Cohen, O., Ram, R., Bakhanashvili, M., Magen-Nativ, H., Shilo, N. & Lahav, M. 2012. Differential downregulation of telomerase activity by bortezomib in multiple myeloma cells-multiple regulatory pathways in vitro and ex vivo. *Br J Cancer* **107**, 1844-1852.

Wikibooks, E. *Telomerase*, https://commons.wikimedia.org/wiki/File:Telemerase.JPG (2008).

Witt, O., Deubzer, H. E., Lodrini, M., Milde, T. & Oehme, I. 2009a. Targeting histone deacetylases in neuroblastoma. *Curr Pharm Des* **15**, 436-447.

Witt, O., Deubzer, H. E., Milde, T. & Oehme, I. 2009b. HDAC family: what are the cancer relevant targets? *Cancer Lett* **277**.

Wong, M., Sun, Y., Xi, Z., Milazzo, G., Poulos, R. C., Bartenhagen, C., Bell, J. L., Mayoh, C., Ho, N., Tee, A. E., Chen, X., Li, Y., Ciaccio, R., Liu, P. Y., Jiang, C. C., Lan, Q., Jayatilleke, N., Cheung, B. B., Haber, M., Norris, M. D., Zhang, X. D., Marshall, G. M., Wang, J. Y., Hüttelmaier, S., Fischer, M., Wong, J. W. H., Xu, H., Perini, G., Dong, Q., George, R. E. & Liu, T. 2019. JMJD6 is a tumorigenic factor and therapeutic target in neuroblastoma. *Nature Communications* **10**, 3319.

Wong, M. S., Chen, L., Foster, C., Kainthla, R., Shay, J. W. & Wright, W. E. 2013. Regulation of telomerase alternative splicing: a target for chemotherapy. *Cell Rep* **3**, 1028-1035.

Wright, W., Piatyszek, M., Rainey, W., Byrd, W. & Shay, J. 1996. Telomerase activity in human germline and embryonic tissues and cells. *Developmental Genetics* **18**, 173-179.

Wu, R., Lu, Z., Cao, Z. & Zhang, Y. 2011. Zinc chelation with hydroxamate in histone deacetylases modulated by water access to the linker binding channel. *Journal of the American Chemical Society* **133**, 6110-6113.

Wyce, A., Ganji, G., Smitheman, K. N., Chung, C. W., Korenchuk, S., Bai, Y., Barbash, O., Le, B., Craggs, P. D., McCabe, M. T., Kennedy-Wilson, K. M., Sanchez, L. V., Gosmini, R. L., Parr, N., McHugh, C. F., Dhanak, D., Prinjha, R. K., Auger, K. R. & Tummino, P. J. 2013. BET inhibition silences expression of MYCN and BCL2 and induces cytotoxicity in neuroblastoma tumor models. *PLoS One* **8**, e72967.

Xiong, Y., Dowdy, S. C., Podratz, K. C., Jin, F., Attewell, J. R., Eberhardt, N. L. & Jiang, S. W. 2005. Histone deacetylase inhibitors decrease DNA methyltransferase-3B messenger RNA stability and down-regulate de novo DNA methyltransferase activity in human endometrial cells. *Cancer Res* **65**, 2684-2689.

Xu, D., Gruber, A., Björkholm, M., Peterson, C. & Pisa, P. 1999. Suppression of telomerase reverse transcriptase (hTERT) expression in differentiated HL-60 cells: regulatory mechanisms. *British journal of cancer* **80**, 1156-1161.

Yamaguchi, T., Cubizolles, F., Zhang, Y., Reichert, N., Kohler, H., Seiser, C. & Matthias, P. 2010. Histone deacetylases 1 and 2 act in concert to promote the G1-to-S progression. *Genes Dev* **24**, 455-469.

Yan, Z., Xu, T., An, Z., Hu, Y., Chen, W., Ma, J., Shao, C. & Zhu, F. 2019. Costunolide induces mitochondria-mediated apoptosis in human gastric adenocarcinoma BGC-823 cells. *BMC Complement Altern Med* **19**, 151.

Yang, X. J. & Seto, E. 2008a. Lysine acetylation: codified crosstalk with other posttranslational modifications. *Mol Cell* **31**.

Yang, X. J. & Seto, E. 2008b. The Rpd3/Hda1 family of lysine deacetylases: from bacteria and yeast to mice and men. *Nat Rev Mol Cell Biol* **9**.

Ye, X. & Weinberg, R. A. 2015. Epithelial-Mesenchymal Plasticity: A Central Regulator of Cancer Progression. *Trends Cell Biol* **25**, 675-686.

Yi, X., Tesmer, V. M., Savre-Train, I., Shay, J. W. & Wright, W. E. 1999. Both transcriptional and posttranscriptional mechanisms regulate human telomerase template RNA levels. *Mol Cell Biol* **19**, 3989-3997.

Yu, A. L., Gilman, A. L., Ozkaynak, M. F., London, W. B., Kreissman, S. G., Chen, H. X., Smith, M., Anderson, B., Villablanca, J. G. & Matthay, K. K. 2010. Anti-GD2 antibody with GM-CSF, interleukin-2, and isotretinoin for neuroblastoma. *New England Journal of Medicine* **363**, 1324-1334.

Yuan, X., Larsson, C. & Xu, D. 2019. Mechanisms underlying the activation of TERT transcription and telomerase activity in human cancer: old actors and new players. *Oncogene* **38**, 6172-6183.

Zage, P. E. 2018. Novel Therapies for Relapsed and Refractory Neuroblastoma. *Children (Basel, Switzerland)* **5**, 148.

Zareifar, S., Shakibazad, N., Zekavat, O. R., Bordbar, M. & Shahriari, M. 2019. Successful treatment of refractory metastatic neuroblastoma with panobinostat in combination with chemotherapy agents and iodine-131-meta-iodobenzylguanidine therapy. *J Oncol Pharm Pract*, 1078155219852670.

Zhang, D., Xiao, Y. F., Zhang, J. W., Xie, R., Hu, C. J., Tang, B., Wang, S. M., Wu, Y. Y., Hao, N. B. & Yang, S. M. 2015. miR-1182 attenuates gastric cancer proliferation and metastasis by targeting the open reading frame of hTERT. *Cancer Lett* **360**, 151-159.

Zhang, H., Shang, Y.-P., Chen, H.-y. & Li, J. 2017a. Histone deacetylases function as novel potential therapeutic targets for cancer. *Hepatology Research* **47**, 149-159.

Zhang, J. & Zhong, Q. 2014. Histone deacetylase inhibitors and cell death. *Cell Mol Life Sci* **71**, 3885-3901.

Zhang, Y., Adachi, M., Zhao, X., Kawamura, R. & Imai, K. 2004. Histone deacetylase inhibitors FK228, N-(2-aminophenyl)-4-[N-(pyridin-3-yl-methoxycarbonyl)amino-methyl]benzamide and m-carboxycinnamic acid bis-hydroxamide augment radiation-induced cell death in gastrointestinal adenocarcinoma cells. *Int J Cancer* **110**, 301-308.

Zhang, Y., Rohde, C., Tierling, S., Stamerjohanns, H., Reinhardt, R., Walter, J. & Jeltsch, A. 2009. DNA methylation analysis by bisulfite conversion, cloning, and sequencing of individual clones. *Methods Mol Biol* **507**, 177-187.

Zhang, Y., Toh, L., Lau, P. & Wang, X. 2012. Human Telomerase Reverse Transcriptase (hTERT) Is a Novel Target of the Wnt/β-Catenin Pathway in Human Cancer. *Journal of Biological Chemistry* **287**, 32494-32511.

Zhang, Z., Yu, L., Dai, G., Xia, K., Liu, G., Song, Q., Tao, C., Gao, T. & Guo, W. 2017b. Telomerase reverse transcriptase promotes chemoresistance by suppressing cisplatin-dependent apoptosis in osteosarcoma cells. *Sci Rep* **7**, 7070-7070.

Zhao, Q., Zhai, Y. X., Liu, H. Q., Shi, Y. A. & Li, X. B. 2015. MicroRNA-491-5p suppresses cervical cancer cell growth by targeting hTERT. *Oncol Rep* **34**, 979-986.

Zhao, Y., Cheng, D., Wang, S. & Zhu, J. 2014. Dual roles of c-Myc in the regulation of hTERT gene. *Nucleic Acids Res* **42**, 10385-10398.

Zhao, Y., Wang, S., Popova, E. Y., Grigoryev, S. A. & Zhu, J. 2009. Rearrangement of upstream sequences of the hTERT gene during cellular immortalization. *Genes Chromosomes Cancer* **48**, 963-974.

Zhu, J., Zhao, Y. & Wang, S. 2010. Chromatin and epigenetic regulation of the telomerase reverse transcriptase gene. *Protein & Cell* **1**, 22-32.

Zopf, S., Ocker, M., Neureiter, D., Alinger, B., Gahr, S., Neurath, M. F. & Di Fazio, P. 2012. Inhibition of DNA methyltransferase activity and expression by treatment with the pan-deacetylase inhibitor panobinostat in hepatocellular carcinoma cell lines. *BMC Cancer* **12**, 386.

8 Publications

Thole, T. M., Toedling, J., Sprussel, A., Pfeil, S., Savelyeva, L., Capper, D., Messerschmidt, C., Beule, D., Groeneveld-Krentz, S., Eckert, C., Gambara, G., Henssen, A. G., **Finkler, S.**, Schulte, J. H., Sieber, A., Bluethgen, N., Regenbrecht, C. R. A., Kunkele, A., Lodrini, M., Eggert, A. & Deubzer, H. E. 2020. Reflection of neuroblastoma intratumor heterogeneity in the new OHC-NB1 disease model. Int J Cancer 146, 1031-1041.

Arlt, B., Zasada, C., Baum, K., Wuenschel, J., Mastrobuoni, G., Lodrini, M., Astrahantseff, K., Winkler, A., Schulte, J.H., **Finkler, S.**, Forbes, M., Hundsdoerfer, P., Guergen, D., Hoffmann, J., Wolf, J., Eggert, A., Kempa, S., Deubzer, H.E. 2020. Inhibiting phosphoglycerate dehydrogenase counteracts chemotherapeutic efficacy against MYCN-amplified neuroblastoma. Int J Cancer 148, 1219-1232.

9 Acknowledgements

First, I would like to thank the European Union's Horizon 2020 Research and Innovation Program, the Berlin Institute of Health, and the German Cancer Aid for funding of this project, and all patients participating in clinical studies and donating sample material for research.

I would like to thank Prof. Dr. Angelika Eggert for giving me the opportunity to join her department, for constructive scientific discussions and for believing that chemists can do more than just drug synthesis.

My sincere gratitude to my supervisor and mentor PD Dr. Hedwig Deubzer for the continuous support of my doctoral studies, for enabling to participate in outstanding international meetings, for her clear vision of the project, experienced council and for her continuous encouragement throughout the entire PhD project.

I would like to thank Prof. Dr. Nils Blüthgen for supervising my thesis, for his advice and fruitful discussion of the project.

A big thank you to Marco Lodrini for his patience, motivation, and for sharing his immense knowledge. Your guidance helped me all the times to find my way and kept inspiring me for new ideas. Thank you for your open door and all the hours you invested in discussing scientific and non-scientific questions. I could never have imagined having a better advisor for my PhD study and your enormous support of this project cannot be appreciated highly enough.

My great thankfulness to our collaboration partners that advised and supported us, for their expertise and interest in this project. Thanks to the research groups of Matthias Fischer, Anton Henssen, Johannes Schulte and Dieter Beule, and to CPO, EPO, iPATH and the DKFZ core facility Genomics and Proteomics for their outstanding technical support. For bioinformatic support and data analyses, I am especially grateful to PD Dr. January Weiner, Dr. Benedikt Obermayer, Konstantin Helmsauer and Dr. Kerstin Haase. Many thanks to Rocío Chamorro González for her help with the DNA sequencing, and to Daniel Konietzko from the Charité purchasing department, for making things possible shortly before deadlines.

I especially want to thank Daniela, Jasmin and Jeannette for their excellent technical support and helping hands, for their patience and for all the hours we spent together in the lab. Thanks to Annika Sprüssel for her outstanding support with the mouse experiments and to Annika Winkler, who can do magic in gene technology.

Many thanks to all previous and current members of Hedi's research group, for their warm welcome, positive working atmosphere, legendary nights at the Schurkenkeller and the countless hours with coffee and chocolate that we spent together in our office. Thank you Theresa, Annika, Sebastian, Birte, Jasmin, Daniela, Jeannette, Inas, Rasmus, Constantin, Marco, Maddalena and Martin.

Especially I want to thank my partners in crime: Annabell, Birte, Kerstin, Mareike, Lena and Laura for being such good company during our PhD time and for sharing all the ups and downs. Thank you for your humor, your understanding, your energy and your encouraging words! Thanks for giving my partly-Kölsche soul a place with celebrating Karneval here in Berlin or in the "Stadt met K".

Thank you to my fellow lab mates at the Forum 4 and the ECRC for building a fruitful ground to grow on and for creating an open and kind working atmosphere. I will never forget our summer retreats, our motivated teams at the annual relay race, and the enjoyable lunch breaks at our small patio. Particularly, I would like to thank Anton, Anika, Mella, Steffen, Silke, Iris, Jutta and Nicole. I want to thank Jörn, Falk and Matthias for their critical questions and interest in this project, and Kathy Astrahantseff for her scientific input and for reviewing the manuscripts.

My deepest gratitude to my family, my family-in-law and to my friends, for their continuous encouragement, good companionship and supply with delicious food. To my parents Elisabeth and Bernd for their love and unconditional support, and to my grandparents and Norbert, who sadly can't witness my graduation anymore. Thank you for your love, faith and company and for being proud, whatever I am doing.

Finally, I would like to thank Rafael for his love, care and motivation especially during the last months and for reminding me of what matters beside science. Dziękuję bardzo!

10 Declaration

Declaration:

I hereby declare that I completed the doctoral thesis independently based on the stated resources and aids.

I have not applied for a doctoral degree elsewhere and do not have a corresponding doctoral degree.

I have not submitted the doctoral thesis, or parts of it, to another academic institution and the thesis has not been accepted or rejected. I declare that I have acknowledged the Doctoral Degree Regulations which underlie the procedure of the Faculty of Life Sciences of Humboldt-Universität zu Berlin, as amended on 5th March 2015. Furthermore, I declare that no collaboration with commercial doctoral degree supervisors took place, and that the principles of Humboldt-Universität zu Berlin for ensuring good academic practice were abided by.

Erklärung:

Hiermit erkläre ich, die Dissertation selbstständig und nur unter Verwendung der angegebenen Hilfen und Hilfsmittel angefertigt zu haben.

Ich habe mich anderwärts nicht um einen Doktorgrad beworben und besitze keinen entsprechenden Doktorgrad.

Ich erkläre, dass ich die Dissertation oder Teile davon nicht bereits bei einer anderen wissenschaftlichen Einrichtung eingereicht habe und dass sie dort weder angenommen noch abgelehnt wurde. Ich erkläre die Kenntnisnahme der dem Verfahren zugrundeliegenden Promotionsordnung der Lebenswissenschaftlichen Fakultät der Humboldt-Universität zu Berlin vom 5. März 2015. Weiterhin erkläre ich, dass keine Zusammenarbeit mit gewerblichen Promotionsbearbeiterinnen/Promotionsberatern stattgefunden hat und dass die Grundsätze der Humboldt-Universität zu Berlin zur Sicherung guter wissenschaftlicher Praxis eingehalten wurden.

Place, Date Sabine Finkler